



**University
of Antwerp**

Faculty of Medicine and Health Sciences
Ophthalmology

**Complications of Laser Refractive Surgery:
Prevention, Diagnosis, and Treatment**

PhD thesis submitted for the degree of Doctor of Medical Sciences
at the University of Antwerp to be defended by Nanji Lu

Supervisors:
Prof. Dr. Dr. Carina Koppen
Prof. Dr. Dr. Farhad Hafezi
Prof. Dr. Dr. Jos J. Rozema

Antwerp, 2023

Disclaimer

The author allows to consult and copy parts of this work for personal use. Further reproduction or transmission in any form or by any means, without the prior permission of the author is strictly forbidden.

**Complicaties van Refractieve Laserchirurgie:
Preventie, Diagnose en Behandeling**

PhD thesis submitted for the degree of Doctor of Medical Sciences
at the University of Antwerp 2023

Supervisors:

Prof. Dr. Dr. Carina KOPPEN
University of Antwerp, Antwerp, Belgium
Prof. Dr. Dr. Farhad HAFEZI
University of Zurich, Zurich, Switzerland
Prof. Dr. Dr. Jos ROZEMA
University of Antwerp, Antwerp, Belgium

Members of the Examination Committee:

Prof. Dr. Dr. Erika VLIEGHE
University of Antwerp, Antwerp, Belgium
Prof. Dr. Dr. Samuel COENEN
University of Antwerp, Antwerp, Belgium
Prof. Dr. Dr. Jesper HJORTDAL
Aarhus University, Aarhus, Denmark
Prof. Dr. Dr. Vincent BORDERIE
Sorbonne Université, Paris, France
Prof. Dr. Dr. Carina KOPPEN
University of Antwerp, Antwerp, Belgium
Prof. Dr. Dr. Farhad HAFEZI
University of Zurich, Zurich, Switzerland
Prof. Dr. Dr. Jos ROZEMA
University of Antwerp, Antwerp, Belgium

Table of Contents

Chapter 1 General Introduction and Thesis Outline	7
---	---

Part 1 Laser Refractive Surgery Complications: Prevention and Diagnosis

Chapter 2 A Novel Keratoconus Staging System Based on Optical Coherence Tomography	43
---	----

Chapter 3 A Novel Artificial Intelligence-Assisted Keratoconus Diagnostic Index Based on Optical Coherence Tomography	65
--	----

Chapter 4 Combining Spectral-Domain OCT and Air-puff Tonometry Analysis to Diagnose Keratoconus	87
--	----

Chapter 5 Combinations of Scheimpflug Tomography, Ocular Coherence Tomography and Air-puff Tonometry Improve the Detection of Keratoconus	109
---	-----

Chapter 6 Performance of a New Biomechanical Index for Post-Laser Vision Correction Ectasia Diagnosis	133
--	-----

Part 2 Laser Refractive Surgery Complications: Treatment

Chapter 7 Epithelium-on CXL Provides a Similar Biomechanical Effect as Accelerated Epithelium-off CXL	149
--	-----

Chapter 8 The Antibacterial Efficacy of High-Fluence PACK Cross-Linking can be Accelerated	163
---	-----

Chapter 9 High-Fluence Accelerated PACK-CXL for Bacterial	179
---	-----

Keratitis Using Riboflavin/UV-A or Rose Bengal/Green
in the Ex-Vivo Porcine Cornea

Chapter 10 Summary, Discussion and Future Directions	195
English Abstract	207
Dutch Abstract	211
List of Abbreviations	215
Appendix CV and Publication Lists	221
Acknowledgements	229

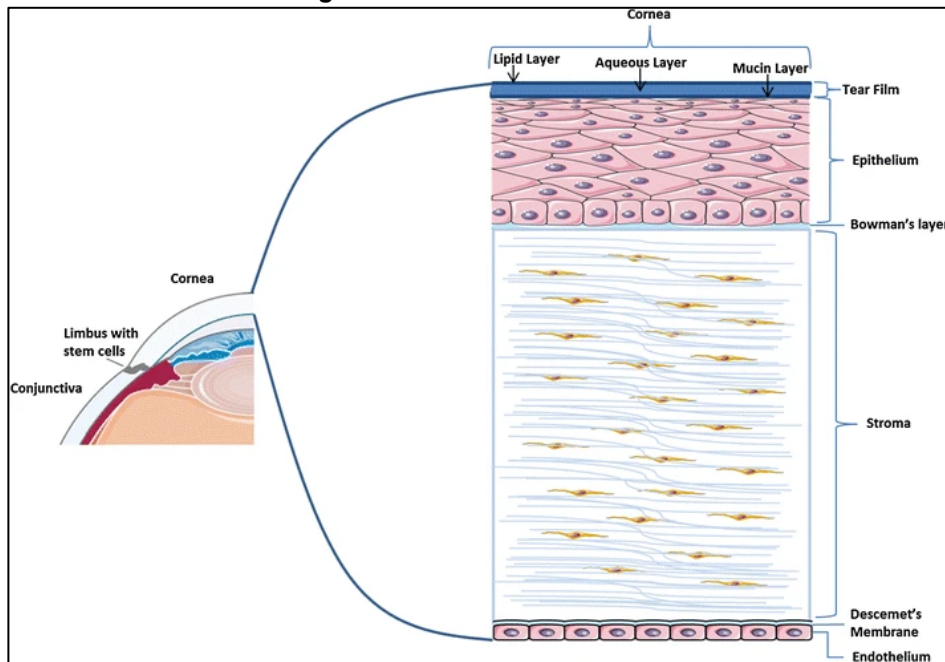
Chapter 1

General Introduction and Thesis Outline

THE HUMAN CORNEA

The cornea is located at the front of the eyeball. In adults, the cornea's diameter is around 12 mm in the horizontal meridian and 11 mm in the vertical meridian. The corneal thickness gradually increases from the center towards the periphery ¹.

Figure 1: Corneal structure ²



The cornea is transparent and avascular. Two thirds of the eye's total refractive power is made up of the cornea and tear film, which together make a positive lens with a refraction of around 43 diopters (D) ³. As a result, the cornea allows the passage of outside light into the eye and helps it focus on the retina. Therefore, any change in the anatomic structures and shape of the cornea will cause a change in its refractive state. Histologically, five layers of the cornea can be distinguished, from the anterior to posterior these layers are the corneal epithelium, Bowman's layer, stroma, Descemet membrane, and endothelium (Figure 1).

Epithelium and Tear Film

The corneal epithelium is covered by the tear film, which nourishes the anterior cornea, excretes metabolic products, smoothens irregularities of the cornea surface, and acts as a protective barrier ⁴. The composition of tears mainly includes lipid, water, and mucus ⁵. Any abnormality in the amount or composition of tears will lead to dry eye.

The corneal epithelium consists of 5-6 layers of three types of epithelial cells, called superficial cells, wing cells, and basal cells, and different forms of tight junctions between corneal epithelial cells ⁶. The epithelial cells can regenerate and renew continuously: the limbus stem cells asymmetrically proliferate to yield the basal cells, which differentiate into wing cells and subsequently into superficial cells and gradually emerging from the base to the surface ^{7,8}.

The corneal epithelium is approximately 50-60 μm thick ⁹, or around 10% of the total corneal thickness, and provides more than 10% of the whole cornea refraction power due to its high refractive index ¹⁰. In normal individuals, the epithelial thickness is thin centrally and thick peripherally ⁹. This profile can change according to the morphology of the underlying corneal stroma to smooth the cornea surface for providing better refraction status ¹¹.

Bowman's Layer

Lying between the epithelium and cornea stroma, Bowman's layer is 8-12 μm thick and becomes thinner with age ¹². Bowman's layer is acellular and composed of a random arrangement of collagen fibrils and proteoglycans. The collagen fibrils in Bowman's layer are mainly collagen types I and III ¹³.

The function of Bowman's layer is not yet determined. Patients that have undergone photorefractive keratectomy (PRK) do not experience adverse effects when removing the central 6-7 mm of Bowman's layer (based on the optical zone) ¹⁴. It also does not contribute to corneal biomechanics in *ex-vivo* experiments ¹⁵. Although Bowman's layer cannot regenerate after an injury, a Bowman's-like layer may reappear after PRK ¹³.

Stroma

The stroma comprises 90% of total corneal thickness (which is approximately 450-480 μm thick in average) and therefore provides the main characteristics of the cornea ¹⁶. The stroma predominantly consists of keratocytes, which synthesize and digest the stromal extracellular matrix (ECM). Keratocytes are normally quiet but could be activated and transformed to myofibroblasts and express α -smooth muscle actin in response to injury and infection ¹⁷. Both keratocytes and other cells in the stroma secrete cytokines and growth factors, such as transforming growth factor (TGF)- β and tumor necrosis factor (TNF)- α , which play a key role in the healing of the corneal stroma and the formation of the corneal scars ^{18, 19}.

The stroma is mainly composed of collagen, which is mostly type I with small amounts of types III, V, VI, and *etc.* ²⁰. Proteoglycans are distributed among the collagen fibrils, which are composed of core protein and glycosaminoglycan chains, are thought to regulate collagen fibril spacing ²¹. The diameter of collagen fibrils and the distance between collagen fibrils in the corneal stroma are both highly uniform, which makes the transparency of the cornea. Besides, the diameter and the distance between collagen fibrils are less than half of the wavelength of human visible light (400-700 nm), which allow light to pass through the cornea without interference. The collagen fibrils align with the same orientation and form in collagen lamellae. The collagen lamellae are parallel to each other but in different directions. There are around 300 collagen lamellae in the central cornea and 500 close to the limbus, which vary in width and thickness ²². The width of collagen lamellae gradually increases from the anterior to posterior stroma, which forms the anterior corneal curvature ²³. In addition, the stroma is not regenerable, so the ablation of the cornea during laser refractive surgery takes place in the stroma.

The cornea is one of the most highly innervated and sensitive organs in the body. The ciliary nerve of the trigeminal nerve's ophthalmic branch (fifth pair of cerebral nerves) is the origin of the majority of sensory nerves in the cornea.

These nerve fibers penetrate the cornea radially in the deeper part of the peripheral stroma and then travel forward to form the terminal subepithelial plexus. After into the cornea for a short distance, the nerve fibers lose their myelin sheath, penetrate Bowman's layer, and terminate at the level of the wing cells of the epithelium²⁴. Any damages to the corneal epithelium and stroma, such as trauma and laser refractive surgery, will expose the nerve endings and consequently cause severe pain. Meanwhile, any factor that causes damage to the corneal nerve, such as herpes simplex virus infection and laser refractive surgery^{25, 26}, will cause reduced corneal tear secretion due to decreased corneal sensation, which will lead to dry eye, epithelium defection and even corneal ulcer formation.

Descemet Membrane

Descemet membrane lies behind the stroma, which serves as the basement membrane of the endothelium. Its thickness increases from birth (3 μm) until adulthood (8-10 μm)²⁷. Two layers of the Descemet membrane can be identified in the histological analysis: the anterior banded zone that is produced during development and the posterior non-banded zone that is produced during life²⁸. The Descemet membrane is composed mainly of collagen types IV and VIII²⁹.

Recently, the existence of an additional corneal layer between the stroma and the Descemet membrane, called Dua's layer, has been claimed³⁰, but the existence of this non-cellular pre-Descemet membrane is still controversial and its function is unclear.

Endothelium

The endothelium is the most posterior layer of the cornea, which lies directly behind the Descemet membrane and is in contact with the aqueous humor of the anterior chamber. The corneal endothelium is a monolayer with evenly arranged cells that are hexagonal in shape³¹. The density of the endothelial cells is around 3500 cells/ mm^2 in young adults and decreases with age³². The density and shape of these cells are important for evaluating their function and status³³. Corneal endothelium prevents corneal edema and helps maintain the

transparency and partially dehydrated state of the cornea. Its cells contain an ion transport system (Na^+/K^+ -ATPase) that forms an osmotic gradient between the stroma and the aqueous humor, leading to passive water diffusion from the relatively hypotonic stroma to the relatively hypertonic aqueous humor ³⁴. Moreover, the endothelium acts as a permeability barrier to allow nutrients drift from the anterior chamber into the stroma ³².

Although the corneal endothelial cells possess proliferative capacity, the process of proliferation is slow ³⁵. Therefore, any damage to corneal endothelial cells, such as anterior chamber inflammation or anterior segment surgery, will affect its normal function. When the corneal endothelial cell density decreases to the point of loss of compensation, corneal edema will develop, resulting in impaired vision.

LASER REFRACTIVE SURGERY

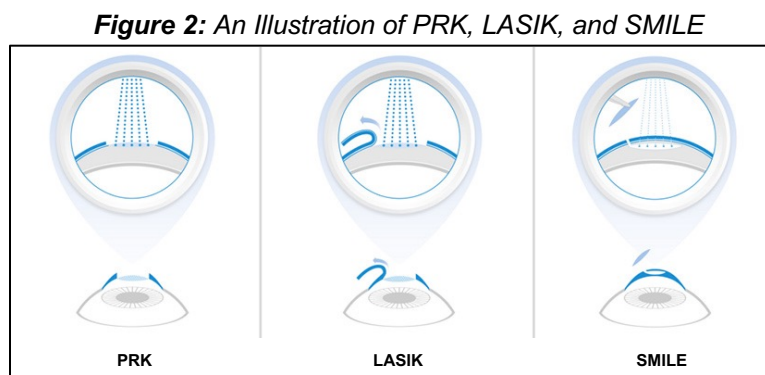
Laser refractive surgery refers to the application of laser techniques to correct refractive errors, such as myopia, hyperopia, presbyopia, or astigmatism ³⁶. There is growing evidence that myopia is on the rise around the world, with a recent study estimating that an average of 30% of the world's population is myopia currently and that the number of myopic people will be closer to 50% by 2050 ³⁷. Therefore, as a method of correcting myopia, the volume of laser refractive surgery is also increasing due to the increase in the prevalence of myopia.

The excimer laser was developed in the early 1970s and was the first laser technique modified for laser refractive surgery usage in the early 1980s ^{38, 39}. The excimer laser applies 193 nm wavelength ultraviolet light to break corneal molecular bonds, which accurately removes corneal tissue to sculpt the cornea into the desired shape while the collateral thermal damage in adjacent tissue is negligible ⁴⁰⁻⁴². Experiments were first performed conducted in animals and the Munnerlyn formula was introduced to define ablation profile ⁴³. The concept of sculpting the cornea, photorefractive keratotomy (PRK), was proposed and successfully applied in humans in the early 1990s ⁴⁴. Each excimer laser uses

a different configuration of spot sizes and ablation frequencies, and these modalities are revised continuously to improve surgical outcome ⁴⁵⁻⁴⁷.

The femtosecond laser is a focused infrared laser with a wavelength of 1053 nm that applies ultrafast pulses with a duration of 100 femtoseconds ⁴⁸. Its surgical effect is achieved by photo disruption: as the laser pulse vaporizes corneal tissue, it creates a cavitation bubble of carbon dioxide gas and water that blasts the corneal tissue ⁴⁹. While the excimer laser is a surface ablation process that ablates the corneal tissue from the top, the femtosecond laser can cut the corneal tissue at a specific depth by using an applanation cone to flatten the cornea.

Currently, there are two main types of laser refractive surgery (**Figure 2**). The first type contains surface procedures without the creation of a corneal flap or corneal cap, in which the stroma, with or without the corneal epithelium, is ablated by an excimer laser (e.g., PRK and transepithelial PRK - TransPRK). The second type consists of flap or lamellar procedures that form a corneal flap or cap after which the corneal stroma is removed by an excimer laser or a specialized instrument (e.g., laser-assisted in situ keratomileusis - LASIK, or small incision lenticule extraction - SMILE).



For PRK, surface ablation without the flap creation is performed; LASIK, the corneal flap following laser ablation is conducted; SMILE: a femtosecond laser is applied to create the lenticule

Table 1: The comparisons of three laser refractive surgery manners

Comparisons	TransPRK	LASIK	SMILE
Year Started to Clinical Practice	2013	1994	2011
Technique and Platform	Excimer laser	Excimer laser (femtosecond laser for the flap creation)	Femtosecond laser
Technique and Platform	Corneal thinnest thickness should be at least 480 mm; More suitable for thin corneas and relative irregular corneas	Corneal thinnest thickness should be at least 500 mm	Corneal thinnest thickness should be at least 550 mm
Correction Range (Usually recommended)	Myopia: Up to -10 D; Hyperopia: Up to + 4 D; Astigmatism: Up to 5 D	Myopia: Up to - 8 D; Hyperopia: Up to + 4 D; Astigmatism: Up to 5 D	Myopia: - 2.5 to - 8 D; Hyperopia: NA; Astigmatism: Up to 2.5 D
Corneal Flap and Suction	No flap; "No Touch No Suction"	With negative suction pressure, flap can be made by a mechanical blade or femtosecond laser	No flap; lamellar lenticule is created by a femtosecond laser
Corneal Biomechanics	Less corneal biomechanical loss	Under the same ablation volume, its lost the highest corneal biomechanical properties	Under the same ablation volume, its lost higher than PRK but lower than LASIK
Healing and Visual Recovery	Corneal epithelium recovery in 3 to 7 days; around 1 months postoperatively, targeted vision can be achieved	Targeted vision usually can be achieved at the second day postoperatively	Targeted vision usually can be achieved 2-3 days to 1 week postoperatively
Intraoperative Complications	Very rare	Flap-related complications	Rare: suction loss
Post-ectasia Risk	Very low	Low	Very low
Postoperative Infectious Keratitis	Rare but with open epithelium during the recovery period, the risk is the highest	Rare	Rare
Dry Eye Risk	Less likely	More likely	Less likely

TransPRK, trans-epithelium photorefractive keratotomy; LASIK, laser-assisted in situ keratomileusis; SMILE, small incision lenticule extraction; D, diopters; NA, not available

PRK

As mentioned before, PRK was the first laser refractive surgery. To start the procedure, the corneal epithelium is usually soaked by 20% ethanol and removed using a hockey knife. Next, the stroma is ablated by computer-controlled excimer laser. A bandage contact lens is placed on the cornea after the surgery until the epithelium is fully recovered, which usually requires around 3 days. Compared to flap or lamellar procedures, the slow recovery of vision and postoperative pain are regarded as the main disadvantages of PRK.

After the corneal epithelium profile could be routinely and easily measured in clinical, TransPRK, which also calls all surface laser ablation (ASLA), applies the excimer laser to replace 20% ethanol and hockey knife for precisely removing the epithelium. As a result, the whole surgery process is computer-controlled laser ablation⁵⁰. In addition, with the application of static cyclotorsion compensation and smart pulse technology during the surgery, the safety of the procedure and the quality of vision in the early postoperative period are further improved^{51, 52}.

LASIK

Since its launch in the early 1990s, LASIK has become one of the major laser refractive surgeries to correct refractive errors. Traditional LASIK applies a microkeratome to create a hinged corneal flap (lamellar flap), exposing the stroma to subsequent excimer laser for the ablation of the target refraction⁵³. With the development of the femtosecond laser, the corneal flap can now be formed with greater accuracy and safety, thus decreasing the occurrence of complications⁵⁴.

The corneal flap is a partial resection of the cornea; the segment of the corneal flap that attaches to the cornea is called the hinge. The most common location for the hinge is either the superior or the nasal position. There are advantages and disadvantages for both hinge positions. The main advantages of the superior hinge flap are: 1) the natural movement of the upper lid does not risk the displacement of the flap; and 2) a larger effective optical zone during the

large horizontal astigmatic ablation. In contrast, the major advantage of creating a nasal hinge flap is preserving the nasal innervation of the cornea. In principle, since the corneal nerves predominantly enter the cornea in the horizontal direction (three o'clock and nine o'clock), the superior hinge flap will transect both sides of corneal innervation ⁵⁵.

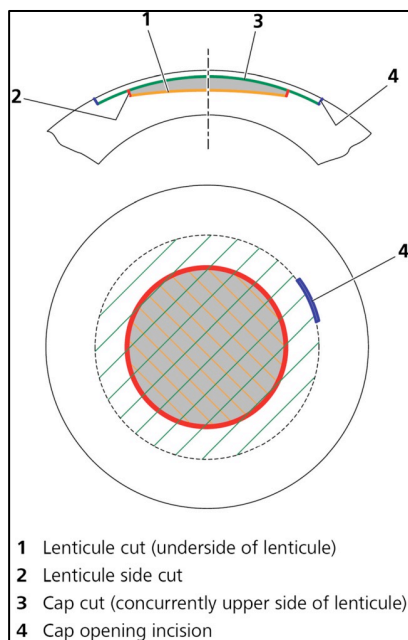
The corneal flap thickness can be modified but must remain below Bowman's layer to avoid the scarring the membrane. The corneal flap must therefore be thicker than 85 µm and is typically around 110-120 µm. The creation of thin flaps (< 110 µm) has the advantage of preserving the integrity of the corneal biomechanics ⁵⁶, but comes with a higher risk of intraoperative complications, especially when using a microkeratome. Thin corneal flaps also carry the risk of postoperative haze formation ⁵⁷.

Compared with PRK and SMILE, LASIK has the highest reduction in corneal biomechanics (evaluated by elastic modulus) for the same correction ^{58, 59}. However, due to the rapid recovery of postoperative vision and minimal discomfort, LASIK is more in accordance with patient expectations. For hyperopic corrections, LASIK has less regression and longer stable results compared with PRK ⁶⁰. Therefore, LASIK remains one of the most popular laser refractive surgery today.

SMILE

SMILE, which is developed from femtosecond lenticule extraction (FLEx) ⁶¹, is a relatively new laser refractive surgery procedure designed to treat refractive errors. Different from PRK and LASIK, it does not use an excimer laser but uses a femtosecond laser instead to create a target corneal lenticule (lamellar lenticule) in the stroma that is extracted whole through a small tunnel incision (2-3 mm, usually at super-temporal site) ⁶². Because of the dissection and extraction of the lamellar lenticule involved, SMILE has a steeper learning curve compared to PRK and LASIK.

Figure 3: Incision geometry of the SMILE ⁶²



During the creation of corneal lenticule, the cornea is sucked by a negative pressure suction port to fixate the eye for the cutting of femtosecond laser. To obtain a corneal lenticule, some cuts need to be formed in sequence: 1) the lower interface of the corneal lenticule; 2) the side cut of corneal lenticule; 3) the upper interface of the corneal lenticule; and 4) the tunnel incision connected to the upper interface of the corneal lenticule. The upper interface of the corneal lenticule and its anterior remaining cornea form the corneal cap (**Figure 3**). Compared to the corneal flap in LASIK, the corneal cap better preserves the complete structure of the cornea, which helps to maintain the innervation and biomechanical properties of the cornea. Similar to the design of the corneal flap in LASIK, the corneal cap in SMILE can be designed by the surgeons, including the cap thickness (110-130 μm is commonly used), cap diameter, and cap side cut angle. The pros and cons of corneal caps with different thicknesses and designs still need further research.

The safety and predictability of SMILE has been reported ⁶³, showing that the visual and refractive outcomes of SMILE is similar to LASIK ⁶⁴.

Main Complications

The complications of laser refractive surgery can occur both intra- and postoperatively. Unlike the patients of other corneal surgeries, for all laser refractive surgery candidates, the cornea is in a healthy state. Therefore, the prevention and management of the complications are particularly important. With the development of laser techniques and the improvement of operating skills, the incidence and severity of laser refractive surgery complications have dramatically decreased. In the following part, the most common and severe complications of laser refractive surgery will be described.

Intraoperative complications

For TransPRK, intraoperative complications are extremely rare because of the simplicity of the “untouched” laser procedure as well as the laser technology has dimensional eye-tracking system to compensate for quick eye movements during the surgery ⁶⁵. For LASIK, the most common intraoperative complication is the corneal flap complications, including buttonhole and irregular flaps, thin flaps, and free flaps. However, as the femtosecond laser gradually replaces the microkeratome to make the corneal flaps, the occurrences of flap-related complications is less ⁶⁶. For SMILE, the suction loss during the femtosecond laser process is one of the primary intraoperative complications ⁶⁷. Most commonly, suction loss is caused by the patients rather than the surgeons or the devices. The unintentional movement brought on by the Bell's response of the patients or the patients' improperly tracking the green light are two main reasons. Another primary intraoperative complication is the complications occurred during the lenticule dissection and extraction. The occurrences of an opaque bubble layer and black spots during the femtosecond laser process can cause difficulties during the lenticule dissection and extraction ⁶⁸.

Postoperative complications **refractive imprecision**

The most common complication in any laser refractive surgery is the inability to obtain an accurate target refractive result for the patient ⁶⁹. This complication can occur for a variety of reasons, primarily due to inaccuracy of the

preoperative subjective refraction, especially in patients with low refractive errors. This refractive imprecision is different from refractive regression as the former refers to patients who never reach their targeted refraction after surgery, while the latter refers to those who do achieve their target initially, later lose it due to the remodeling of the corneal epithelium and stroma⁷⁰. Such regressions usually occur in patients with high preoperative refractive errors.

The most common and meaningful way to prevent refractive imprecision is to perform multiple refractive examinations before the surgery. Ophthalmologists could also apply aberrometers to obtain objective refractive information of the patients and compare it with subjective refractive information before deciding on the surgical parameters. The managements of refractive imprecision mainly include the correction of spectacles and contact lenses (CLs), and the application of enhancement laser refractive surgery. For PRK and LASIK, customized ablation can be performed⁷¹⁻⁷³; For SMILE, depending on the thickness of the cap, either a topical LASIK or a PRK enhancement could be considered^{72, 74}.

post-laser refractive surgery ectasia

Ectasia after laser refractive surgery was firstly documented by Seiler *et al.* in 1998. They described three high myopic patients with preoperative thin corneas after LASIK had a rapid progression of steepening cornea and myopia⁷⁵. After this initial report, other kinds of post-laser refractive surgery ectasia were also reported, including post-PRK and post-SMILE ectasia after the myopic corrections^{76, 77}, and ectasia after the hyperopic corrections⁷⁸. Based on the reported cases, the most common post-laser refractive surgery ectasia is post-LASIK ectasia, following with post-PRK ectasia. Although the actual incidence of post-laser refractive surgery is unknown, it has been estimated to be 0.01-0.94%⁷⁹.

Currently, the etiology of post-laser refractive surgery ectasia is attributed to two kinds of reasons: 1) a loss of corneal structural integrity after the excessive laser ablation leading to the decompensation of corneal biomechanics; 2) the

preoperative presence of undetected subclinical keratoconus, the cornea in a weakened biomechanics state and takes the laser ablation, thus this two-hit causes the corneal biomechanical decompensation⁸⁰. The result of biomechanical decompensation is that the damaged cornea deforms due to continued intraocular pressure. Ideally, patients at risk for post-laser refractive surgery ectasia would be identified before laser refractive surgery and classified as unsuitable. Various risk factors have been noted to be associated with post-laser refractive surgery ectasia. Randleman *et al.* proposed the ectasia risk score system (ERSS), which is a preoperative screening system to evaluate the risk of post-LASIK ectasia⁸¹. The system with risk scales was based upon the preoperative parameters of the candidates, including the shape of corneal topography, the residual stroma thickness, surgical age, thinnest corneal thickness, and attempted refractive correction. Santhiago *et al.* established the percent tissue altered (PTA) among the laser refractive surgery candidates with or without suspicious preoperative topography^{82,83}. While other potential factors also play a role in the risk of post-laser refractive surgery ectasia, the screening of preoperative corneal morphology is the key for all risk evaluation system.

Keratoconus

The main purpose of preoperative corneal morphology screening is to diagnose early-stage keratoconus⁸⁴. Keratoconus is a bilateral disease that reduces corneal stiffness and viscosity, leading to progressive local thinning and steepening of the cornea⁸⁵. As the disease progresses, corneal hydrops occurs, resulting in further vision impairment and eventually in corneal blindness⁸⁶. Due to the limitations of diagnostic methods and the inappropriateness of the methodology applied in the previous prevalence study surveys, keratoconus was previously considered as a rare disease and its prevalence has been underestimated⁸⁷. In a study conducted in the Netherlands, the results showed that both the annual incidence and the prevalence of keratoconus were 5-fold to 10-fold higher than previously reported⁸⁸. According to estimates, the prevalence and incidence rates of keratoconus are between 0.2 and 4,790 per 100,000 persons and 1.5 and 25 cases per 100,000 persons/year, respectively, with the highest rates occurring in Middle Eastern and Asian ethnicities⁸⁹.

Typically, the onset of keratoconus is in early adolescence and progresses into 20s to 30s ⁹⁰.

Given the association with other genetic syndromes, such as Down syndrome, keratoconus is thought to be influenced by genetic factors; nonetheless, currently, no definitive causative genetic targets have been identified and multiple genetic factors located at different positions are thought to play a key role in different aspects of keratoconus development. These genes include those involved in the synthesis of collagen fibers and fibronectin extracellular matrix proteins, cross-linking between collagens, etc ⁹¹. Several environmental and familial factors were found to be associated with the risk of developing keratoconus, including the patients who have the family history of keratoconus, eye rubbing history, allergy, and atopy ⁹². However, some patients who clearly have no family history, eye rubbing history, or allergic history still develop keratoconus.

Early screening for keratoconus patients can help ophthalmologists exclude those patients from being candidates for laser refractive surgery and thus prevent triggering the keratoconus pathological process, which presents as post-refractive surgery ectasia. The diagnostic methods and tools for keratoconus change with the advancement of technology: keratoconus was first diagnosed by observations through a slit lamp. Later, Placido-disc based topography was used, which provides precise information on anterior corneal surface curvature ⁹³. However, Placido topography cannot provide information on corneal thickness and posterior surface curvature, while its measurements' repeatability is influenced by *e.g.*, dry eyes and corneal scars. This issue was solved by Scheimpflug tomography, which provides both anterior and posterior cornea curvatures, as well as the thickness of cornea ⁹⁴. The remodeling of the corneal epithelium thickness is the early reaction of corneal stroma remodeling in keratoconus, which can help the early diagnosis of keratoconus ⁹⁵. Very high frequency (VHF) digital ultrasound is the first approach that can measure the corneal epithelium profile ⁹⁶. Compared to VHF digital ultrasound, non-contact optical coherence tomography (OCT) can obtain the profile of corneal

epithelium and a high resolution of cornea sectional structure ⁹⁷. Since the pathological process of keratoconus starts with a decrease in corneal biomechanics, and the remodeling of the corneal structure is its reflection ⁹⁸. Therefore, directly capturing the corneal biomechanical properties can help diagnose keratoconus at the source. The corneal biomechanical properties could be determined by coupling a calibrated non-contact tonometer with an ultra-high-speed Scheimpflug camera and then numerically assessing the dynamic changes in corneal deformation ⁹⁹.

All these devices generate various parameters that describe corneal characteristics from a different perspective. Although the number of parameters increases, ophthalmologists prefer using as few parameters as possible to make the correct diagnosis. Hence machine learning (ML) can be applied to these parameters to generate an index with high diagnostic accuracy for keratoconus ^{100, 101}. Machine learning may be divided into supervised learning (SL) and unsupervised learning (USL) ¹⁰². SL usually analyzes and clusters labeled datasets, logistic regression (LR), random forest (RF), and neural network (NN) belong to SL, while USL usually analyzes and clusters unlabeled datasets, k-nearest neighbors (KNN) and principal component analysis (PCA) belong to USL. With the application of artificial intelligence, in the current clinical practice based on the commercially available devices, the Screening Corneal Objective Risk of Ectasia (SCORE) Analyzer is one of most widely used keratoconus diagnostic system based on Placido-based topography ¹⁰³. Belin/Ambrósio enhanced ectasia display (BADD) and Pentacam random forest index (PRFI) are the two most common applied parameters established through Scheimpflug-based tomography ¹⁰⁴. The Corvis Biomechanical Index (CBI) is the first corneal biomechanical comprehensive index to diagnose keratoconus ¹⁰⁵. By combining different measuring principles, some other parameters were established, including Root Mean Square (RMS) and Asphericity Asymmetry Index (AAI) based on the combination of Placido-based topography and Scheimpflug-based tomography ¹⁰⁶, and the Tomographic and Biomechanical Index (TBI) based on the combination of Scheimpflug-based tomography and an air-puff device ⁹⁹. While for each parameter it is claimed that they can achieve

a perfect diagnostic accuracy, the independent validation studies showed that these parameters are sometimes less diagnostic of early-stage keratoconus, which indicates further optimized work and inspire us to establish a new diagnostic index through OCT with a high-resolution measurement of the corneal structure in the future ^{107, 108}.

Table 2: The Amsler-Krumeich (AK) staging system

Grades	Characteristics
Stage 1	Eccentric steeping Myopia and astigmatism < 5.00 D Mean central K readings < 48.00 D
Stage 2	Myopia and astigmatism from 5.00 to 8.00 D Mean central K readings < 53.00 D Absence of scarring Minimum corneal thickness > 400 μm
Stage 3	Myopia and astigmatism from 8.00 to 10.00 D Mean central K readings > 53.00 D Absence of scarring Minimum corneal thickness from 300 to 400 μm
Stage 4	Refraction not measurable Mean central K readings > 55.00 D Central corneal scarring Minimum corneal thickness < 300 μm

D, diopters; K, keratometry

Keratoconus classification systems

During the diagnostic process, there are always borderline (suspect) cases between keratoconus and normal corneas. In order to more intuitively and objectively evaluate normal, borderline and different degrees of keratoconus to make correct surgery decisions, the keratoconus staging (classification) system was proposed. In reviewing the existing keratoconus staging systems, the first staging system was proposed by Amsler ¹⁰⁹, Krumeich *et al.* updated it to the Amsler-Krumeich (AK) staging system (**Table 1**) ¹¹⁰, although helpful for more advanced keratoconus, it lacks early diagnostic ability. Alió and Shabayek later introduced the corneal coma-like aberrations to the AK staging system ¹¹¹, while

Ishii *et al.* integrated six front surface parameters into the AK staging system ¹¹². Belin *et al.* established the Belin ABCD staging system (**Table 2**) by expanding the AK staging system into 5 stages, adding the posterior surface curvature, switching the corneal central thickness to the corneal thinnest thickness, and modifying the values of all the objective parameters in the mildest stage based on the results of ROC analyses ¹¹³. Sandali *et al.* firstly established an OCT-based structural staging system by describing the corneal structural remodeling through the sectional scan observation ¹¹⁴. Beyond these systems which based on corneal structure, the staging systems based on corneal biomechanics was also established ^{115, 116}.

Table 3: The Belin ABCD staging system

Criteria	A	B	C	D	
	ARC (3 mm Zone)	PRC (3mm Zone)	Thinnest Pachymetry	BDVA	Scarring
Stage O	>7.25 mm (<46.5 D)	>5.90 mm (<57.25 D)	>490 µm	= 20/20 (= 1.0)	-
Stage I	>7.05 mm (<48.0 D)	>5.70 mm (<59.25 D)	>450 µm	<20/20 (<1.0)	-. +, ++
Stage II	>6.35 mm (<53.0 D)	>5.15 mm (<65.5 D)	>400 µm	<20/40 (<0.5)	-. +, ++
Stage III	>6.15 mm (<55.0 D)	>4.95 mm (<68.5 D)	>300 µm	<20/100 (<0.2)	-. +, ++
Stage IV	<6.15 mm (>55.0 D)	<4.95 mm (>68.5 D)	≤ 300 µm	<20/400 (<0.05)	-. +, ++

ARC, anterior radius of curvature; PRC, posterior radius of curvature; D, diopters

Treatment of corneal ectasia

Primarily, the management of post-laser refractive surgery ectasia includes the correction of spectacles and CLs at the early stage, when post-laser refractive surgery ectasia progresses into the late stage, lamellar keratoplasty (LK) and penetrating keratoplasty (PK) are conducted ¹¹⁷. Corneal cross-linking (CXL) was introduced as the most common treatment for post-refractive surgery ectasia in early stage ¹¹⁸. This is because CXL avoids the occurrence of the

complications of keratoplasty and also helps the prevention of the ectasia progression. As the corneal biomechanics of post-refractive surgery ectasia is impaired, CXL uses riboflavin (acts as the chromophore) and 365 nm ultraviolet-A (UV-A) light to generate oxygen free radicals and activate various pathways that create covalent bonds between collagen fibers to improve corneal biomechanical properties ¹¹⁹.

The protocols of CXL are composed with irradiation intensity, irradiation time and total irradiation energy. The first established CXL protocol was the Dresden protocol designed for keratoconus treatment, which removes epithelium (epithelium-off), drops 0.1% riboflavin to saturate the cornea, and applies 3 mW/cm² UV-A light for continuous 30 minutes irradiation (in total energy of 5.4 J/cm²) ¹²⁰. The long-term success rate of the Dresden protocol is high, which is currently regarded as the standard protocol of CXL ¹²¹. However, the Dresden protocol is time-consuming and limited to the application of corneas with a stromal thickness of more than 400 μm ¹²². Since the efficiency of CXL is oxygen dependent ¹²³, other accelerated epithelium-off CXL protocols were reasonably developed (*e.g.*, 9 mW/cm², 10 minutes, 5.4 J/cm²) while the effect of oxygen consumption limitation is considered ¹²⁴. Due to the removal of epithelium during CXL, the complications, such as serious postoperative pain, delayed epithelium recovery, haze, and infection, may occur ^{125, 126}. Therefore, the protocols of CXL without epithelium removal (epithelium-on) were accordingly proposed ¹²⁷. However, the remaining epithelial cells consume more oxygen and the tight junctions of epithelial cells also limit riboflavin infiltration ¹²⁸; accordingly, the epithelium-on CXL protocols with the additional support of iontophoresis, modified riboflavin solution, the supplement of oxygen were established ¹²⁹⁻¹³¹. However, these modified epithelium-on protocols require additional devices and different riboflavin solutions, which make the epithelium-on CXL more difficult to operate, so a new, uniform, and easy-to-perform epithelium-on protocol is needed.

Infectious Keratitis

Any surgery or operation carries the risk of infection. Laser refractive surgery, especially for PRK that corneal epithelium is removed during the surgery, also has the risk of postoperative infection, although it is low¹³². Based on a large clinical retrospective study, the incidence of infectious keratitis after LASIK was 0.03%. In comparison, the infection rate after PRK was relatively high at 0.20%^{133, 134}. Compared with PRK and LASIK, SMILE has a relative short clinical application history, no large scale-based post-SMILE infectious keratitis is reported till now. However, in theory, while LASIK and SMILE could be categorized as lamellar procedures, since the cap side cut of SMILE is smaller, and the corneal pocket is relatively closed; therefore, the rate of post-SMILE infection should be relatively lower than LASIK.

Any pathogenic microorganism can cause infectious keratitis after laser refractive surgery, including bacteria, fungi, and acanthamoeba^{135, 136}, but the most common pathogenic microorganism is still bacteria, including *Staphylococcus epidermidis* and *Pseudomonas aeruginosa*, and methicillin-resistant *Staphylococcus aureus* (MRSA) might be one of the most challenging resistant patterns^{133, 137, 138}.

For infectious keratitis after laser refractive surgery, in addition, due to the thin corneal thickness after laser refractive surgery, it more requires timely and effectively treatment to prevent corneal penetration. However, the timely identification of the causative organism(s) and selection of the most appropriate antimicrobial agent(s) sometimes can be challenging. Unfortunately, antimicrobial resistance (AMR) continues to increase, which reduces the effectiveness of treatment and leads to a growing need for new treatments overcoming the challenges¹³⁹. Photoactivated chromophore for keratitis-corneal cross-linking (PACK-CXL) represents one such approach: chromophore photoactivation can function similarly to a disinfectant by lowering the bacteria load¹⁴⁰. In detail, for the mechanism of PACK-CXL, while CXL can improve corneal biomechanics to decrease the risk of corneal penetration, it also acts from other aspects, including: 1) directly killing effect on

microorganisms from UV-A light; 2) increasing steric hindrance and altering access to metalloproteinase cleavage sites render the corneal stroma more resistant to enzymatic digestion; and (3) producing oxidative stress to cause direct damage on the cell membranes and nucleic acids of any microorganisms¹⁴¹.

PACK-CXL has been successfully applied for bacterial and fungal keratitis in *in-vitro* experiments^{142, 143}, it has also been shown to be effective alone, and in combination with standard-of-care antimicrobial therapy in clinical practices: in the Bacterial Keratitis Preferred Practice Pattern recommended by the American Academy of Ophthalmology, in most cases, topical antibiotic eye drops (e.g., Cefazolin or vancomycin with Tobramycin for no organism identified or multiple types of organisms, Cefazolin for Gram-positive cocci, Tobramycin for Gram-negative rods, Ceftriaxone for Gram-negative cocci, Amikacin for Gram-positive rods, and Sulfacetamide for Gram-positive rods) are the first-line preferred form of treatment since they can reach high tissue levels¹⁴⁴⁻¹⁴⁶.

Currently, PACK-CXL mainly includes two types of chromophore and light source combinations: riboflavin with UV-A light and rose bengal with green light (in wavelength of 522 nm)¹⁴⁷. Similar to CXL treats for corneal ectasia disease, PACK-CXL also involves the designs of CXL protocols. However, the CXL protocols now commonly used in PACK-CXL are directly derived from the CXL protocols designed for corneal ectasia disease with the combined application of antibiotics/antifungals or not: most of the clinical studies still maintained to apply the Dresden protocol for bacterial/fungus keratitis¹⁴⁸, for example in a prospective randomized phase 3 trial, a total fluence of 5.4 J/cm² or 7.2 J/cm² (0.1% riboflavin with UV-A light, 9 mW/cm², 10 mins or 13 mins or 20 seconds, respectively) was applied for infectious keratitis of presumed bacterial, fungal, or mixed origin¹⁴⁹; Therefore, the PACK-CXL protocols should be updated for the purpose of infectious keratitis treatment. Recently, the CXL light source device was miniaturized and can be applied on the slit lamp¹⁵⁰. Thus, if the PACK-CXL can be accelerated while maintaining its pathogen-killing effect, the

PACK-CXL can be applied in a timely manner on the slit lamp for patients with a more comfortable surgical experience.

Haze

Corneal haze is a clouding of the cornea, which usually referees to a cloudy or opaque appearance under the clear corneal epithelium. Corneal haze can be seen following PRK/TransPRK and thin-flap LASIK ⁵⁷, which represents subepithelial corneal fibrosis, a manifestation of the side effects of the cornea's wound healing process: after laser refractive surgery, in response to the initially apoptosis of keratocytes, TGF- β , interleukin (IL)-1 α /IL-1 β , and other molecules arisen from the wounded epithelium, mediate the transformation of some keratocytes into myofibroblasts ¹⁵¹. Myofibroblasts have contractile properties that are intended to help close wounds, but they are not as transparent as normal keratocytes ¹⁵². These myofibroblasts are not only more numerous, but also demonstrate greater reflectivity of their cell bodies and nuclei. In addition, the extracellular matrix produced by myofibroblasts is disorganized and denser than the usual matrix, which consequently causes more light to scatter ^{153, 154}.

The risk and severity of corneal haze coincide with the total corneal ablation volume ¹⁵⁵. High UV-radiation environments also increase the risk of late-onset corneal haze after PRK, and thus sunglasses is suggested for post-PRK patients ¹⁵⁶. In general, the incidence of corneal haze has declined because of the development of the excimer laser, the advances in laser ablation profile design, and the prophylactic application of mitomycin C (MMC) during the surgery ¹⁵⁷. MMC is a potent mitotic inhibitor that preferentially affects rapidly proliferating cells such as keratocytes and consequently reduces the myofibroblasts' generation, and thus the form of corneal haze decreases ¹⁵⁸.

Dry Eye

Most of patients after laser refractive surgery could experience dry eye symptoms and relieve themselves 6-12 months after surgery ^{159, 160}. Only a few of patients have persistent dry eye symptoms and continue to need artificial

tears, while these patients usually also have symptoms of dry eye before surgery.

Before laser refractive surgery, the evaluation of the patient's ocular surface status and dry eye is the most important method to prevent postoperative dry eye ¹⁶¹. The preoperative evaluation includes tear film breakup time, Schirmer test, the function of the meibomian glands, and the exclusion of systematic diseases. All patients with dry eye syndrome, especially with the signs of corneal or conjunctival staining, should be treated to stabilize the ocular surface prior to surgery ¹⁶². For the laser refractive surgery candidates who have high possibilities of postoperative dry eye, PRK or SMILE but not LASIK should be considered ¹⁶³.

AIM AND THESIS OUTLINE

This thesis investigates new approaches to the prevention and treatment of two most serious complications, post-ectasia and infectious keratitis, after laser refractive surgery. Compared to other major complications, these two complications can seriously impair vision and even lead to corneal blindness. By using current art to prevent and treat these two complications, we investigate the following objectives:

The first five chapters focus on the diagnosis and management of KC to prevent post-refractive surgery ectasia after laser refractive surgery. In **Chapter 2**, we innovatively establish a numerical spectral-domain OCT based KC staging system and compare it with existing KC staging systems. In **Chapter 3**, we proposed a new OCT-based index by including both information of stroma and epithelium to diagnose keratoconus. In **Chapter 4**, we propose a brand-new approach, combining OCT and air-puff device facilitated by AI, to diagnose KC. In **Chapter 5**, we comprehensively investigate whether the combinations of devices with different measuring principles, supported by AI, can improve the diagnosis of different stages' KC. In **Chapter 6**, we try to investigate the performance of a new biomechanical index for post-laser refractive surgery ectasia diagnosis.

The subsequent four chapters focus on innovative treatment methods for the complications of laser refractive surgery. In **Chapter 7**, we propose a revolutionary new epithelium-on CXL protocol combining the application of epithelium penetration enhancer to treat KC and post-laser refractive surgery ectasia. In addition, we *ex-vivo* compare its biomechanical stiffening effect with an accelerated epithelium-off CXL protocol. In **Chapter 8**, we try to determine whether high-fluence PAK-CXL can be accelerated while maintain its bacterial killing effect in the *in-vitro* settings. In **Chapter 9**, we establish a stable *ex-vivo* bacterial infectious keratitis model and investigate the bacterial killing effect of two high-fluence PAK-CXL protocols with different chromophores.

REFERENCES

1. Fares U, Otri AM, Al-Aqaba MA, Dua HS. Correlation of central and peripheral corneal thickness in healthy corneas. *Cont Lens Anterior Eye* 2012;35:39-45.
2. Rowsey TG, Karamichos D. The role of lipids in corneal diseases and dystrophies: a systematic review. *Clinical and Translational Medicine* 2017;6:30.
3. Courville CB, Smolek MK, Klyce SD. Contribution of the ocular surface to visual optics. *Experimental Eye Research* 2004;78:417-425.
4. Tiffany JM. Tears in health and disease. *Eye* 2003;17:923-926.
5. Hodges RR, Dartt DA. Tear film mucins: front line defenders of the ocular surface; comparison with airway and gastrointestinal tract mucins. *Exp Eye Res* 2013;117:62-78.
6. Sridhar MS. Anatomy of cornea and ocular surface. *Indian J Ophthalmol* 2018;66:190-194.
7. Dua HS, Azuara-Blanco A. Limbal stem cells of the corneal epithelium. *Surv Ophthalmol* 2000;44:415-425.
8. Blanpain C, Horsley V, Fuchs E. Epithelial stem cells: turning over new leaves. *Cell* 2007;128:445-458.
9. Reinstein DZ, Archer TJ, Gobbe M, Silverman RH, Coleman DJ. Epithelial thickness in the normal cornea: three-dimensional display with Artemis very high-frequency digital ultrasound. *J Refract Surg* 2008;24:571-581.
10. Patel S, Tutchenko L. The refractive index of the human cornea: A review. *Cont Lens Anterior Eye* 2019;42:575-580.
11. Rocha KM, Perez-Straziota CE, Stulting RD, Randleman JB. Epithelial and stromal remodeling after corneal collagen cross-linking evaluated by spectral-domain OCT. *J Refract Surg* 2014;30:122-127.
12. Germundsson J, Karanis G, Fagerholm P, Lagali N. Age-Related Thinning of Bowman's Layer in the Human Cornea In Vivo. *Investigative Ophthalmology & Visual Science* 2013;54:6143-6149.
13. Wilson SE. Bowman's layer in the cornea- structure and function and regeneration. *Exp Eye Res* 2020;195:108033.
14. Marshall J. The 2014 Bowman Lecture—Bowman's and Bruch's: a tale of two membranes during the laser revolution. *Eye* 2015;29:46-64.
15. Torres-Netto EA, Hafezi F, Spuru B, et al. Contribution of Bowman layer to corneal biomechanics. *J Cataract Refract Surg* 2021;47:927-932.
16. Chen S, Mienaltowski MJ, Birk DE. Regulation of corneal stroma extracellular matrix assembly. *Exp Eye Res* 2015;133:69-80.
17. Torricelli AA, Wilson SE. Cellular and extracellular matrix modulation of corneal stromal opacity. *Exp Eye Res* 2014;129:151-160.

18. Saika S. TGF-beta signal transduction in corneal wound healing as a therapeutic target. *Cornea* 2004;23:S25-30.
19. Vesaluoma M, Teppo A-M, Grönhagen-Riska C, Tervo T. Increased release of tumour necrosis factor- α in human tear fluid after excimer laser induced corneal wound. *British Journal of Ophthalmology* 1997;81:145-149.
20. Meek KM. Corneal collagen-its role in maintaining corneal shape and transparency. *Biophys Rev* 2009;1:83-93.
21. Hassell JR, Birk DE. The molecular basis of corneal transparency. *Exp Eye Res* 2010;91:326-335.
22. BRON AJ. The architecture of the corneal stroma. *British Journal of Ophthalmology* 2001;85:379-381.
23. Morishige N, Takagi Y, Chikama T-i, Takahara A, Nishida T. Three-Dimensional Analysis of Collagen Lamellae in the Anterior Stroma of the Human Cornea Visualized by Second Harmonic Generation Imaging Microscopy. *Investigative Ophthalmology & Visual Science* 2011;52:911-915.
24. Yang AY, Chow J, Liu J. Corneal Innervation and Sensation: The Eye and Beyond. *Yale J Biol Med* 2018;91:13-21.
25. Moein HR, Kheirkhah A, Muller RT, Cruzat AC, Pavan-Langston D, Hamrah P. Corneal nerve regeneration after herpes simplex keratitis: A longitudinal in vivo confocal microscopy study. *Ocul Surf* 2018;16:218-225.
26. Lee BH, McLaren JW, Erie JC, Hodge DO, Bourne WM. Reinnervation in the Cornea after LASIK. *Investigative Ophthalmology & Visual Science* 2002;43:3660-3664.
27. de Oliveira RC, Wilson SE. Descemet's membrane development, structure, function and regeneration. *Exp Eye Res* 2020;197:108090.
28. Johnson DH, Bourne WM, Campbell RJ. The ultrastructure of Descemet's membrane. I. Changes with age in normal corneas. *Arch Ophthalmol* 1982;100:1942-1947.
29. Fitch JM, Birk DE, Linsenmayer C, Linsenmayer TF. The spatial organization of Descemet's membrane-associated type IV collagen in the avian cornea. *J Cell Biol* 1990;110:1457-1468.
30. Dua HS, Faraj LA, Said DG, Gray T, Lowe J. Human corneal anatomy redefined: a novel pre-Descemet's layer (Dua's layer). *Ophthalmology* 2013;120:1778-1785.
31. Waring GO, 3rd, Bourne WM, Edelhauser HF, Kenyon KR. The corneal endothelium. Normal and pathologic structure and function. *Ophthalmology* 1982;89:531-590.
32. Bourne WM. Biology of the corneal endothelium in health and disease. *Eye* 2003;17:912-918.
33. Mishima S. Clinical investigations on the corneal endothelium-XXXVIII Edward Jackson Memorial Lecture. *Am J Ophthalmol* 1982;93:1-29.
34. Edelhauser HF. The Balance between Corneal Transparency and Edema The Proctor

- Lecture. *Investigative Ophthalmology & Visual Science* 2006;47:1755-1767.
35. Joyce NC. Proliferative capacity of the corneal endothelium. *Prog Retin Eye Res* 2003;22:359-389.
 36. Kim T-i, Alió del Barrio JL, Wilkins M, Cochener B, Ang M. Refractive surgery. *The Lancet* 2019;393:2085-2098.
 37. Holden BA, Fricke TR, Wilson DA, et al. Global Prevalence of Myopia and High Myopia and Temporal Trends from 2000 through 2050. *Ophthalmology* 2016;123:1036-1042.
 38. Trokel SL, Srinivasan R, Braren B. Excimer Laser Surgery of the Cornea. *American Journal of Ophthalmology* 1983;96:710-715.
 39. Krueger RR, Rabinowitz YS, Binder PS. The 25th Anniversary of Excimer Lasers in Refractive Surgery: Historical Review. *Journal of Refractive Surgery* 2010;26:749-760.
 40. Seiler T, Wollensak J. In vivo experiments with the excimer laser--technical parameters and healing processes. *Ophthalmologica* 1986;192:65-70.
 41. Seiler T, Bende T, Winckler K, Wollensak J. Side effects in excimer corneal surgery. DNA damage as a result of 193 nm excimer laser radiation. *Graefes Arch Clin Exp Ophthalmol* 1988;226:273-276.
 42. Bende T, Seiler T, Wollensak J. Side effects in excimer corneal surgery. Corneal thermal gradients. *Graefes Arch Clin Exp Ophthalmol* 1988;226:277-280.
 43. Munnerlyn CR, Koons SJ, Marshall J. Photorefractive keratectomy: a technique for laser refractive surgery. *J Cataract Refract Surg* 1988;14:46-52.
 44. Seiler T, Kahle G, Kriegerowski M. Excimer laser (193 nm) myopic keratomileusis in sighted and blind human eyes. *Refract Corneal Surg* 1990;6:165-173.
 45. Pidro A, Biscevic A, Pjano MA, Mravicic I, Bejdic N, Bohac M. Excimer Lasers in Refractive Surgery. *Acta Inform Med* 2019;27:278-283.
 46. Müller B, Boeck T, Hartmann C. Effect of excimer laser beam delivery and beam shaping on corneal sphericity in photorefractive keratectomy. *J Cataract Refract Surg* 2004;30:464-470.
 47. Gottsch JD, Rencs EV, Cambier JL, Hall D, Azar DT, Stark WJ. Excimer laser calibration system. *J Refract Surg* 1996;12:401-411.
 48. Kymionis G, Kankariya V, Plaka A, Reinstein D. Femtosecond Laser Technology in Corneal Refractive Surgery: A Review. *Journal of refractive surgery (Thorofare, NJ : 1995)* 2012;28:912-920.
 49. Soong HK, Malta JB. Femtosecond lasers in ophthalmology. *Am J Ophthalmol* 2009;147:189-197.e182.
 50. Aslanides IM, Padroni S, Arba Mosquera S, Ioannides A, Mukherjee A. Comparison of single-step reverse transepithelial all-surface laser ablation (ASLA) to alcohol-assisted photorefractive keratectomy. *Clin Ophthalmol* 2012;6:973-980.
 51. Aslanides IM, Toliou G, Padroni S, Arba Mosquera S, Kolli S. The effect of static

- cyclotorsion compensation on refractive and visual outcomes using the Schwind Amaris laser platform for the correction of high astigmatism. *Cont Lens Anterior Eye* 2011;34:114-120.
52. Aslanides IM, Kymionis GD. Trans advanced surface laser ablation (TransPRK) outcomes using SmartPulseTechnology. *Cont Lens Anterior Eye* 2017;40:42-46.
 53. Reinstein DZ, Archer TJ, Gobbe M. The history of LASIK. *J Refract Surg* 2012;28:291-298.
 54. Kahuam-López N, Navas A, Castillo-Salgado C, Graue-Hernandez EO, Jimenez-Corona A, Ibarra A. *Femtosecond laser versus mechanical microkeratome use for laser-assisted in - situ keratomileusis (LASIK)*. Cochrane Database Syst Rev. 2018 Feb 8;2018(2):CD012946. doi: 10.1002/14651858.CD012946. eCollection 2018.; 2018.
 55. Donnenfeld ED, Solomon K, Perry HD, et al. The effect of hinge position on corneal sensation and dry eye after LASIK. *Ophthalmology* 2003;110:1023-1029; discussion 1029-1030.
 56. Medeiros FW, Sinha-Roy A, Alves MR, Dupps WJ, Jr. Biomechanical corneal changes induced by different flap thickness created by femtosecond laser. *Clinics (Sao Paulo)* 2011;66:1067-1071.
 57. Hafezi F, Seiler T. Persistent subepithelial haze in thin-flap LASIK. *J Refract Surg* 2010;26:222-225.
 58. Spuru B, Kling S, Hafezi F, Sekundo W. Biomechanical Properties of Human Cornea Tested by Two-Dimensional Extensiometry Ex Vivo in Fellow Eyes: Femtosecond Laser-Assisted LASIK Versus SMILE. *J Refract Surg* 2018;34:419-423.
 59. Torres-Netto EA, Spuru B, Kling S, et al. Similar Biomechanical Cross-linking Effect After SMILE and PRK in Human Corneas in an Ex Vivo Model for Postoperative Ectasia. *J Refract Surg* 2020;36:49-54.
 60. Spadea L, Sabetti L, D'Alessandri L, Balestrazzi E. Photorefractive keratectomy and LASIK for the correction of hyperopia: 2-year follow-up. *J Refract Surg* 2006;22:131-136.
 61. Ang M, Mehta JS, Chan C, Htoon HM, Koh JC, Tan DT. Refractive lenticule extraction: transition and comparison of 3 surgical techniques. *J Cataract Refract Surg* 2014;40:1415-1424.
 62. Reinstein DZ, Archer TJ, Gobbe M. Small incision lenticule extraction (SMILE) history, fundamentals of a new refractive surgery technique and clinical outcomes. *Eye Vis (Lond)* 2014;1:3.
 63. Ivarsen A, Asp S, Hjortdal J. Safety and complications of more than 1500 small-incision lenticule extraction procedures. *Ophthalmology* 2014;121:822-828.
 64. Lau YT-Y, Shih KC, Tse RH-K, Chan TC-Y, Jhanji V. Comparison of Visual, Refractive and Ocular Surface Outcomes Between Small Incision Lenticule Extraction and Laser-Assisted In Situ Keratomileusis for Myopia and Myopic Astigmatism. *Ophthalmology and Therapy* 2019;8:373-386.

65. Adib-Moghaddam S, Soleyman-Jahi S, Tofighi S, et al. Factors Associated With Ocular Cyclotorsion Detected by High-Speed Dual-Detection Eye Tracker During Single-Step Transepithelial Photorefractive Keratectomy. *Journal of Refractive Surgery* 2018;34:736-744.
66. Moshirfar M, Gardiner JP, Schliesser JA, et al. Laser in situ keratomileusis flap complications using mechanical microkeratome versus femtosecond laser: retrospective comparison. *J Cataract Refract Surg* 2010;36:1925-1933.
67. Wong CW, Chan C, Tan D, Mehta JS. Incidence and management of suction loss in refractive lenticule extraction. *J Cataract Refract Surg* 2014;40:2002-2010.
68. Krueger RR, Meister CS. A review of small incision lenticule extraction complications. *Curr Opin Ophthalmol* 2018;29:292-298.
69. Jabbur NS, Sakatani K, O'Brien TP. Survey of complications and recommendations for management in dissatisfied patients seeking a consultation after refractive surgery. *J Cataract Refract Surg* 2004;30:1867-1874.
70. Moshirfar M, Desautels JD, Walker BD, Murri MS, Birdsong OC, Hoopes PCS. Mechanisms of Optical Regression Following Corneal Laser Refractive Surgery: Epithelial and Stromal Responses. *Med Hypothesis Discov Innov Ophthalmol* 2018;7:1-9.
71. Moshirfar M, Jehangir N, Fenzl CR, McCaughey M. LASIK Enhancement: Clinical and Surgical Management. *J Refract Surg* 2017;33:116-127.
72. Moshirfar M, Basharat NF, Kelkar N, Bundogji N, Ronquillo YC, Hoopes PC. Visual Outcomes of Photorefractive Keratectomy Enhancement After Primary LASIK. *J Refract Surg* 2022;38:733-740.
73. Moshirfar M, Villarreal A, Thomson AC, et al. PRK Enhancement for Residual Refractive Error After Primary PRK: A Retrospective Study. *Ophthalmol Ther* 2021;10:175-185.
74. Reinstein DZ, Carp GI, Archer TJ, Vida RS. Outcomes of Re-treatment by LASIK After SMILE. *J Refract Surg* 2018;34:578-588.
75. Seiler T, Koufala K, Richter G. Iatrogenic keratectasia after laser in situ keratomileusis. *J Refract Surg* 1998;14:312-317.
76. Malecaze F, Couillet J, Calvas P, Fournié P, Arné JL, Brodaty C. Corneal ectasia after photorefractive keratectomy for low myopia. *Ophthalmology* 2006;113:742-746.
77. El-Naggar MT. Bilateral ectasia after femtosecond laser-assisted small-incision lenticule extraction. *J Cataract Refract Surg* 2015;41:884-888.
78. Randleman JB, Banning CS, Stulting RD. Corneal ectasia after hyperopic LASIK. *J Refract Surg* 2007;23:98-102.
79. Moshirfar M, Tukan AN, Bundogji N, et al. Ectasia After Corneal Refractive Surgery: A Systematic Review. *Ophthalmol Ther* 2021;10:753-776.
80. Roberts CJ, Dupps WJ, Jr. Biomechanics of corneal ectasia and biomechanical treatments. *J Cataract Refract Surg* 2014;40:991-998.

81. Randleman JB, Russell B, Ward MA, Thompson KP, Stulting RD. Risk factors and prognosis for corneal ectasia after LASIK. *Ophthalmology* 2003;110:267-275.
82. Santhiago MR, Smadja D, Gomes BF, et al. Association between the percent tissue altered and post-laser in situ keratomileusis ectasia in eyes with normal preoperative topography. *Am J Ophthalmol* 2014;158:87-95.e81.
83. Santhiago MR, Smadja D, Wilson SE, Krueger RR, Monteiro ML, Randleman JB. Role of percent tissue altered on ectasia after LASIK in eyes with suspicious topography. *J Refract Surg* 2015;31:258-265.
84. Ambrósio R, Jr., Randleman JB. Screening for ectasia risk: what are we screening for and how should we screen for it? *J Refract Surg* 2013;29:230-232.
85. Mas Tur V, MacGregor C, Jayaswal R, O'Brart D, Maycock N. A review of keratoconus: Diagnosis, pathophysiology, and genetics. *Survey of Ophthalmology* 2017;62:770-783.
86. Rabinowitz YS. Keratoconus. *Surv Ophthalmol* 1998;42:297-319.
87. Chan E, Chong EW, Lee SS-Y, et al. Incidence and Prevalence of Keratoconus Based on Scheimpflug Imaging. *Ophthalmology* 2023;130:445-448.
88. Godefrooij DA, de Wit GA, Uiterwaal CS, Imhof SM, Wisse RP. Age-specific Incidence and Prevalence of Keratoconus: A Nationwide Registration Study. *Am J Ophthalmol* 2017;175:169-172.
89. Santodomingo-Rubido J, Carracedo G, Suzaki A, Villa-Collar C, Vincent SJ, Wolffsohn JS. Keratoconus: An updated review. *Cont Lens Anterior Eye* 2022;45:101559.
90. Vazirani J, Basu S. Keratoconus: current perspectives. *Clin Ophthalmol* 2013;7:2019-2030.
91. Mathan JJ, Gokul A, Simkin SK, Meyer JJ, Patel DV, McGhee CNJ. Topographic screening reveals keratoconus to be extremely common in Down syndrome. *Clinical & Experimental Ophthalmology* 2020;48:1160-1167.
92. Bykhovskaya Y, Rabinowitz YS. Update on the genetics of keratoconus. *Experimental Eye Research* 2021;202:108398.
93. Wilson SE, Klyce SD. Screening for Corneal Topographic Abnormalities before Refractive Surgery. *Ophthalmology* 1994;101:147-152.
94. Oliveira CM, Ribeiro C, Franco S. Corneal imaging with slit-scanning and Scheimpflug imaging techniques. *Clinical and Experimental Optometry* 2011;94:33-42.
95. Reinstein DZ, Archer TJ, Gobbe M. Corneal epithelial thickness profile in the diagnosis of keratoconus. *J Refract Surg* 2009;25:604-610.
96. Reinstein DZ, Silverman RH, Rondeau MJ, Coleman DJ. Epithelial and Corneal Thickness Measurements by High-frequency Ultrasound Digital Signal Processing. *Ophthalmology* 1994;101:140-146.
97. Reinstein DZ, Yap TE, Archer TJ, Gobbe M, Silverman RH. Comparison of Corneal Epithelial Thickness Measurement Between Fourier-Domain OCT and Very High-Frequency Digital Ultrasound. *J Refract Surg* 2015;31:438-445.

98. Esporcatte LPG, Salomão MQ, Lopes BT, et al. Biomechanical diagnostics of the cornea. *Eye and Vision* 2020;7:9.
99. Ambrósio R, Jr., Lopes BT, Faria-Correia F, et al. Integration of Scheimpflug-Based Corneal Tomography and Biomechanical Assessments for Enhancing Ectasia Detection. *J Refract Surg* 2017;33:434-443.
100. Maeda N, Klyce SD, Smolek MK. Neural network classification of corneal topography. Preliminary demonstration. *Invest Ophthalmol Vis Sci* 1995;36:1327-1335.
101. Smolek MK, Klyce SD. Current keratoconus detection methods compared with a neural network approach. *Invest Ophthalmol Vis Sci* 1997;38:2290-2299.
102. Alzubaidi L, Zhang J, Humaidi AJ, et al. Review of deep learning: concepts, CNN architectures, challenges, applications, future directions. *Journal of Big Data* 2021;8:53.
103. Saad A, Gatinel D. Validation of a New Scoring System for the Detection of Early Forme of Keratoconus. *International Journal of Keratoconus and Ectatic Corneal Diseases* 2012;1:100-108.
104. Lopes BT, Ramos IC, Salomão MQ, et al. Enhanced Tomographic Assessment to Detect Corneal Ectasia Based on Artificial Intelligence. *Am J Ophthalmol* 2018;195:223-232.
105. Vinciguerra R, Ambrósio R, Jr., Elsheikh A, et al. Detection of Keratoconus With a New Biomechanical Index. *J Refract Surg* 2016;32:803-810.
106. Doctor K, Vunnava KP, Shroff R, et al. Simplifying and understanding various topographic indices for keratoconus using Scheimpflug based topographers. *Indian J Ophthalmol* 2020;68:2732-2743.
107. Shetty R, Rao H, Khamar P, et al. Keratoconus Screening Indices and Their Diagnostic Ability to Distinguish Normal From Ectatic Corneas. *Am J Ophthalmol* 2017;181:140-148.
108. Wang YM, Chan TCY, Yu M, Jhanji V. Comparison of Corneal Dynamic and Tomographic Analysis in Normal, Forme Fruste Keratoconic, and Keratoconic Eyes. *J Refract Surg* 2017;33:632-638.
109. Amsler M. [Classic keratocene and crude keratocene; Unitary arguments]. *Ophthalmologica* 1946;111:96-101.
110. Krumeich JH, Daniel J, Knülle A. Live-epikeratophakia for keratoconus. *J Cataract Refract Surg* 1998;24:456-463.
111. Alió JL, Shabayek MH. Corneal higher order aberrations: a method to grade keratoconus. *J Refract Surg* 2006;22:539-545.
112. Ishii R, Kamiya K, Igarashi A, Shimizu K, Utsumi Y, Kumanomido T. Correlation of corneal elevation with severity of keratoconus by means of anterior and posterior topographic analysis. *Cornea* 2012;31:253-258.
113. Belin MW, Duncan JK. Keratoconus: The ABCD Grading System. *Klin Monbl Augenheilkd* 2016;233:701-707.

114. Sandali O, El Sanharawi M, Temstet C, et al. Fourier-domain optical coherence tomography imaging in keratoconus: a corneal structural classification. *Ophthalmology* 2013;120:2403-2412.
115. Herber R, Pillunat LE, Raiskup F. Development of a classification system based on corneal biomechanical properties using artificial intelligence predicting keratoconus severity. *Eye Vis (Lond)* 2021;8:21.
116. Flockerzi E, Vinciguerra R, Belin MW, Vinciguerra P, Ambrósio R, Jr., Seitz B. Combined biomechanical and tomographic keratoconus staging: Adding a biomechanical parameter to the ABCD keratoconus staging system. *Acta Ophthalmol* 2022;100:e1135-e1142.
117. McAllum PJ, Segev F, Herzig S, Rootman DS. Deep anterior lamellar keratoplasty for post-LASIK ectasia. *Cornea* 2007;26:507-511.
118. Richoz O, Mavrakanas N, Pajic B, Hafezi F. Corneal collagen cross-linking for ectasia after LASIK and photorefractive keratectomy: long-term results. *Ophthalmology* 2013;120:1354-1359.
119. Randleman JB, Khandelwal SS, Hafezi F. Corneal cross-linking. *Survey of Ophthalmology* 2015;60:509-523.
120. Wollensak G, Spoerl E, Seiler T. Riboflavin/ultraviolet-a-induced collagen crosslinking for the treatment of keratoconus. *Am J Ophthalmol* 2003;135:620-627.
121. Raiskup F, Theuring A, Pillunat LE, Spoerl E. Corneal collagen crosslinking with riboflavin and ultraviolet-A light in progressive keratoconus: ten-year results. *J Cataract Refract Surg* 2015;41:41-46.
122. Hafezi F, Kling S, Gilardoni F, et al. Individualized Corneal Cross-linking With Riboflavin and UV-A in Ultrathin Corneas: The Sub400 Protocol. *Am J Ophthalmol* 2021;224:133-142.
123. Richoz O, Hammer A, Tabibian D, Gatziofias Z, Hafezi F. The Biomechanical Effect of Corneal Collagen Cross-Linking (CXL) With Riboflavin and UV-A is Oxygen Dependent. *Transl Vis Sci Technol* 2013;2:6.
124. Mazzotta C, Raiskup F, Hafezi F, et al. Long term results of accelerated 9 mW corneal crosslinking for early progressive keratoconus: the Siena Eye-Cross Study 2. *Eye Vis (Lond)* 2021;8:16.
125. Murchison CE, Petroll WM, Robertson DM. Infectious keratitis after corneal crosslinking: systematic review. *J Cataract Refract Surg* 2021;47:1075-1080.
126. Agarwal R, Jain P, Arora R. Complications of corneal collagen cross-linking. *Indian J Ophthalmol* 2022;70:1466-1474.
127. Leccisotti A, Islam T. Transepithelial corneal collagen cross-linking in keratoconus. *Journal of Refractive Surgery* 2010;26:942-948.
128. Hafezi F. Corneal Cross-Linking: Epi-On. *Cornea* 2022;41:1203-1204.

129. Lombardo M, Giannini D, Lombardo G, Serrao S. Randomized Controlled Trial Comparing Transepithelial Corneal Cross-linking Using Iontophoresis with the Dresden Protocol in Progressive Keratoconus. *Ophthalmology* 2017;124:804-812.
130. Hersh PS, Lai MJ, Gelles JD, Lesniak SP. Transepithelial corneal crosslinking for keratoconus. *Journal of Cataract & Refractive Surgery* 2018;44:313-322.
131. Matthys A, Cassagne M, Galiacy SD, El Hout S, Fournié P, Malecaze F. Transepithelial Corneal Cross-linking With Supplemental Oxygen in Keratoconus: 1-Year Clinical Results. *J Refract Surg* 2021;37:42-48.
132. Schallhorn JM, Schallhorn SC, Hettinger K, Hannan S. Infectious keratitis after laser vision correction: Incidence and risk factors. *J Cataract Refract Surg* 2017;43:473-479.
133. Llovet F, de Rojas V, Interlandi E, et al. Infectious keratitis in 204 586 LASIK procedures. *Ophthalmology* 2010;117:232-238.e231-234.
134. de Rojas V, Llovet F, Martínez M, et al. Infectious keratitis in 18,651 laser surface ablation procedures. *J Cataract Refract Surg* 2011;37:1822-1831.
135. Sridhar MS, Garg P, Bansal AK, Sharma S. Fungal keratitis after laser in situ keratomileusis. *J Cataract Refract Surg* 2000;26:613-615.
136. Garg P, Chaurasia S, Vaddavalli PK, Muralidhar R, Mittal V, Gopinathan U. Microbial keratitis after LASIK. *J Refract Surg* 2010;26:209-216.
137. Ortega-Usobiaga J, Llovet-Osuna F, Djodeyre MR, Llovet-Rausell A, Beltran J, Baviera J. Incidence of corneal infections after laser in situ keratomileusis and surface ablation when moxifloxacin and tobramycin are used as postoperative treatment. *Journal of Cataract & Refractive Surgery* 2015;41:1210-1216.
138. Solomon R, Donnenfeld ED, Perry HD, et al. Methicillin-Resistant Staphylococcus aureus Infectious Keratitis Following Refractive Surgery. *American Journal of Ophthalmology* 2007;143:629-634.
139. Willcox MDP. Antibiotics and Microbial Keratitis: Do We Need to Test for Resistance? *Eye Contact Lens* 2020;46:1-2.
140. Hafezi F, Randleman JB. PACK-CXL: defining CXL for infectious keratitis. *J Refract Surg* 2014;30:438-439.
141. Kumar V, Lockerbie O, Keil SD, et al. Riboflavin and UV-light based pathogen reduction: extent and consequence of DNA damage at the molecular level. *Photochem Photobiol* 2004;80:15-21.
142. Kling S, Hufschmid FS, Torres-Netto EA, et al. High Fluence Increases the Antibacterial Efficacy of PACK Cross-Linking. *Cornea* 2020;39:1020-1026.
143. Martins SA, Combs JC, Noguera G, et al. Antimicrobial efficacy of riboflavin/UVA combination (365 nm) in vitro for bacterial and fungal isolates: a potential new treatment for infectious keratitis. *Invest Ophthalmol Vis Sci* 2008;49:3402-3408.
144. Knyazer B, Krakauer Y, Tailakh MA, et al. Accelerated Corneal Cross-linking as an

- Adjunct Therapy in the Management of Presumed Bacterial Keratitis: A Cohort Study. *J Refract Surg* 2020;36:258-264.
145. Hafezi F, Hosny M, Shetty R, et al. PACK-CXL vs. antimicrobial therapy for bacterial, fungal, and mixed infectious keratitis: a prospective randomized phase 3 trial. *Eye Vis (Lond)* 2022;9:2.
 146. Lin A, Rhee MK, Akpek EK, et al. Bacterial Keratitis Preferred Practice Pattern®. *Ophthalmology* 2019;126:P1-P55.
 147. Arboleda A, Miller D, Cabot F, et al. Assessment of rose bengal versus riboflavin photodynamic therapy for inhibition of fungal keratitis isolates. *Am J Ophthalmol* 2014;158:64-70.e62.
 148. Manns RPC, Achiron A, Knyazer B, et al. Use of corneal cross-linking beyond keratoconus: a systemic literature review. *Graefe's Archive for Clinical and Experimental Ophthalmology* 2023.
 149. Hafezi F, Hosny M, Shetty R, et al. PACK-CXL vs. antimicrobial therapy for bacterial, fungal, and mixed infectious keratitis: a prospective randomized phase 3 trial. *Eye and Vision* 2022;9:2.
 150. Hafezi F, Richoz O, Torres-Netto EA, Hillen M, Hafezi NL. Corneal Cross-linking at the Slit Lamp. *J Refract Surg* 2021;37:78-82.
 151. Wilson SE. Interleukin-1 and Transforming Growth Factor Beta: Commonly Opposing, but Sometimes Supporting, Master Regulators of the Corneal Wound Healing Response to Injury. *Investigative Ophthalmology & Visual Science* 2021;62:8-8.
 152. Shu DY, Lovicu FJ. Myofibroblast transdifferentiation: The dark force in ocular wound healing and fibrosis. *Prog Retin Eye Res* 2017;60:44-65.
 153. Moller-Pedersen T, Cavanagh HD, Petroll WM, Jester JV. Stromal wound healing explains refractive instability and haze development after photorefractive keratectomy: a 1-year confocal microscopic study. *Ophthalmology* 2000;107:1235-1245.
 154. Wilson SE. Biology of keratorefractive surgery- PRK, PTK, LASIK, SMILE, inlays and other refractive procedures. *Exp Eye Res* 2020;198:108136.
 155. Møller-Pedersen T, Cavanagh HD, Petroll WM, Jester JV. Corneal haze development after PRK is regulated by volume of stromal tissue removal. *Cornea* 1998;17:627-639.
 156. Stojanovic A, Nitter TA. Correlation between ultraviolet radiation level and the incidence of late-onset corneal haze after photorefractive keratectomy. *J Cataract Refract Surg* 2001;27:404-410.
 157. Majmudar PA, Schallhorn SC, Cason JB, et al. Mitomycin-C in corneal surface excimer laser ablation techniques: a report by the American Academy of Ophthalmology. *Ophthalmology* 2015;122:1085-1095.
 158. Teus MA, de Benito-Llopis L, Alió JL. Mitomycin C in corneal refractive surgery. *Surv Ophthalmol* 2009;54:487-502.

159. Hovanesian JA, Shah SS, Maloney RK. Symptoms of dry eye and recurrent erosion syndrome after refractive surgery. *J Cataract Refract Surg* 2001;27:577-584.
160. Murakami Y, Manche EE. Prospective, randomized comparison of self-reported postoperative dry eye and visual fluctuation in LASIK and photorefractive keratectomy. *Ophthalmology* 2012;119:2220-2224.
161. Toda I. Dry Eye After LASIK. *Investigative Ophthalmology & Visual Science* 2018;59:DES109-DES115.
162. Behrens A, Doyle JJ, Stern L, et al. Dysfunctional tear syndrome: a Delphi approach to treatment recommendations. *Cornea* 2006;25:900-907.
163. Denoyer A, Landman E, Trinh L, Faure JF, Auclin F, Baudouin C. Dry eye disease after refractive surgery: comparative outcomes of small incision lenticule extraction versus LASIK. *Ophthalmology* 2015;122:669-676.

Chapter 2

A Novel Keratoconus Staging System Based on Optical Coherence Tomography

Nan-Ji Lu, Farhad Hafezi, Carina Koppen, Jorge L. Alió del Barrio, Ioannis M. Aslanides, Shady T. Awwad, Sorcha Ní Dhubhghaill, Roberto Pineda II, Emilio A. Torres-Netto, Lin Wang, Qin-Mei Wang, Le-Le Cui, Jos J. Rozema

E-published in Journal of Cataract and Refractive Surgery 2023 August 1st

ABSTRACT

Purpose: To establish a numerical spectral-domain optical coherence tomography (SD-OCT)-based keratoconus (KC) staging system and compare it with existing KC staging systems.

Setting: Eye Hospital of Wenzhou Medical University, Wenzhou, China

Designs: Retrospective case-control study.

Methods: Scheimpflug tomography, air-puff tonometry, and SD-OCT were performed on 236 normal and 331 KC eyes. All SD-OCT-derived parameters of the corneal epithelium and stroma were evaluated based on their receiver operating characteristic (ROC) curves, area under the curve (AUC), sensitivity, and specificity to discriminate between normal and KC eyes. The best performing parameters were subsequently used to create an OCT-based staging system, which was compared with existing tomographic and biomechanical staging systems.

Results: Two hundred and thirty-six eyes from 236 normal patients and 331 eyes from 331 KC patients of different stages were included. The highest ranked AUC ROC SD-OCT parameters, derived from stroma and epithelium, were stroma overall minimum thickness ('ST', AUC 0.836, sensitivity 90%, specificity 67%) and epithelium overall standard deviation ('EP', AUC 0.835, sensitivity 75%, specificity 78%). A numerical SD-OCT staging system called STEP including 2 parameters - 'ST' and 'EP'- with 5 stages was proposed.

Conclusions: The new SD-OCT-based KC staging system is the first to take the epithelium with its sublayer stroma information into account, showing a strong compatibility to the existing staging systems. This system could be incorporated into daily practice, potentially leading to an overall improvement in KC treatment and follow-up management.

INTRODUCTION

Keratoconus (KC) is a bilateral corneal ectatic disorder characterized by local biomechanical weakness, corneal thinning, and protrusion ¹. This can result in increasing myopia, irregular astigmatism, corneal scarring, and loss of vision ². Existing studies indicate that early diagnosis with timely corneal cross-linking (CXL) can slow or halt the KC progression ³, and that early diagnosis can also prevent inappropriate refractive laser treatment in cases of subclinical disease.

Placido topography is typically used to assess the corneal curvature for signs of KC, while Scheimpflug tomography added corneal elevation and more complex parameters for KC diagnosis and staging. By training new algorithms and adding automation to the analysis, our ability to diagnose KC early, accurately, and efficiently could be significantly improved ⁴. In the past, the maximum keratometry (K_{\max}) was regarded as a simple and useful index to assess KC severity, and many still use it to monitor progression ⁵. However, K_{\max} is a single-point measurement, which has a low repeatability in advanced KC cases ^{6,7}. The Belin ABCD staging system was introduced to provide a more robust KC progression and staging method ⁵. These tomographic techniques, however, omit a key feature of KC, namely a change in corneal biomechanics. Combining an air-puff tonometer with high-speed Scheimpflug imaging (Corvis, Oculus Optikgeräte, Wetzlar, Germany) captures this aspect, and by analyzing dynamic corneal response parameters, the Corvis Biomechanical Index (CBI) has been proposed as a means of augmenting early KC diagnosis ^{8,9}. The linear form of the CBI has recently been used to generate an 'Elastic' staging system ¹⁰⁻¹², that was later combined with the Belin ABCD staging system ¹¹.

Compared with Scheimpflug technology, anterior segment optical coherence tomography (AS-OCT) provides yet greater image resolution. AS-OCT can differentiate the corneal epithelium and other corneal layers with a resolution that Scheimpflug technology cannot deliver ¹³. The corneal epithelial profile had been proven to benefit early-stage KC detection ¹⁴⁻¹⁷ although it was first described and measured using very high-frequency (VHF) digital ultrasound ¹⁸, which is not routinely used clinically.

Ideally, a disease staging system should have some key features, including: (1) the ability to diagnose early to assist in the follow up of patients in a timely manner; (2) objective numeric parameters that change linearly as the disease progresses to assess the disease severity; (3) as few parameters as possible to evaluate the disease in multiple dimensions and to facilitate clinical application; and (4) be platform independent and not limited to a specific device or algorithm^{19, 20}. However, to date, the corneal epithelium and its underlying stromal layer have not been considered in a data-driven KC staging system.

The aim of this study is to use AS-OCT to create a KC staging system that includes the epithelium with its sublayer stroma information, based on a large population of both normal and KC patients, with an emphasis on integration into clinical practice. We also aimed to compare it with existing tomographic and biomechanical KC staging systems to evaluate its performance relative to the current standard.

METHODS

This retrospective study was conducted with the approval of the ethics committee of the Eye Hospital of Wenzhou Medical University between 2018 June to 2023 March.

Patients Inclusion and Database

This study included two groups of patients, the healthy group (people without ocular pathology other than ametropia) and the KC group. Prior to the examination, patients were asked to discontinue soft contact lens wear for at least 2 weeks, or at least 4 weeks for rigid gas-permeable contact lenses. All measurements were taken in a consistent dimly lit examination room by experienced technicians prior to the instillation of fluorescein.

The healthy patient group was recruited from those seeking laser vision correction (LVC) in the Eye Hospital of Wenzhou Medical University. The

inclusion criteria comprised the absence of ocular or systemic abnormalities and a negative history of ocular surgery, a stable corrected distance visual acuity (CDVA) $\geq 20/20$ for 2 years before surgery with Scheimpflug tomography (Pentacam HR, Oculus Optikgeräte, Wetzlar, Germany), and confirmed by four cornea specialists. To avoid the inclusion of forme fruste KC in the normal group, a minimum of 3-years follow-up was required after LVC to exclude possible iatrogenic ectasia. For the normal group, only one randomly selected eye was included per person.

In the KC group, the diagnosis of KC was also confirmed by four cornea specialists. The diagnosis typically required 2 typical signs of KC on Scheimpflug tomography, such as abnormal corneal thickness distribution and thinnest pachymetry, abnormal posterior elevation, skewed asymmetric bowtie/inferior steepening [SAB/IS] or increased inferior steepness, and/ or 1 classic slit lamp finding (Fleischer ring, Vogt striae, or central thinning).

After the confirmation of the KC diagnosis, for each KC patient, only the eye with the mildest KC manifestation was selected and included. As a result of selecting the less affected side, these cases included some KC eyes that did not manifest any slit lamp findings. They were further categorized into three sub-groups: the forme fruste KC (FFKC), early-stage KC (EKC), and advanced KC (AKC) sub-groups²¹. The criteria of the FFKC sub-group comprised of best CDVA $\geq 20/20$, no KC signs at slit-lamp, $K_{\max} < 47.4$ diopters (D), thinnest pachymetry $\geq 480 \mu\text{m}$, "normal" tomography with the difference between the K_{\max} values in the inferior and superior areas at 3 mm (IS-Value) < 1.4 D, and no SAB/IS^{4, 22, 23}. For the EKC sub-group, the criteria were: $K_{\max} < 48.5$ D, smallest thickness $> 480 \mu\text{m}$, best CDVA $\geq 16/20$, no central scars and fewer than two slit lamp findings. The criteria for the AKC sub-group were KC eyes with parameters exceeding those of the FFKC and EKC sub-groups.

Scheimpflug Tomography

Tomography measurements were obtained using a Pentacam HR (software version 1.25r12). Only eyes with "OK" quality measurements were included.

The following parameters were recorded: K_1 , K_2 , K_{max} , corneal thinnest pachymetry, IS-Value, and the values of 'A', 'B' and 'C' read from the Belin ABCD staging, where 'A' and 'B' stand for the anterior and posterior radius of curvature for a 3.0 mm zone centered on the thinnest point and the 'C' stands for the thinnest pachymetry; while 'D' refers to CDVA, a subjective parameter that was not included in current analysis. The Scheimpflug tomography was only used to set up the new OCT-based system, but is not included in the new OCT-based system itself.

Corneal Biomechanics Using High-speed Dynamic Scheimpflug Imaging

The corneal biomechanical properties were measured by Corvis (software version 1.6r2503), and only measurements with an acceptable quality were included for analysis. The data recorded included the Stress-Strain Index (SSI)²⁴, CBI⁹, the Tomographic and Biomechanical Index (TBI)²³, the Corvis Biomechanical Factor (CBiF)¹², and 'Elastic' stage¹¹.

Spectral-Domain OCT

AS-OCT measurements were performed with the RTVue-XR Spectral-Domain OCT (SD-OCT, OptoVue, Inc., Fremont, CA, USA) in Pachymetry-Wide scan pattern, which is known to provide an excellent repeatability²⁵. For each eye, 3 continuous scans were conducted. The whole cornea, epithelium, and stromal thickness maps were recorded in the central (2 mm diameter), paracentral (2 to 5 mm), midperipheral (5 to 7 mm), and peripheral regions (7 to 9 mm). In the latter three regions, the thickness was monitored in 8 equally spaced points along the median circumference of the area, including the temporal (T), superior-temporal (ST), superior (S), superior-nasal (SN), nasal (N), inferior-nasal (IN), inferior (I), and inferior-temporal (IT) positions.

All parameters derived from the measured thickness of the three different corneal layers by the OCT software (ReVue version 2018.0.04; Optovue, Inc.). These measurements included: (1) Pachymetric/ Epithelial/ Stromal Minimum Thickness: the minimum thickness in the whole cornea/epithelium/stroma layer; (2) Pachymetric/ Epithelial/ Stromal Min-Max: the minimum thickness in the

whole Cornea/ Epithelium/ Stroma minus the maximum thickness in the whole cornea/epithelium/stroma; (3) Pachymetric/ Epithelial/ Stromal 5mm/7mm SN-IT/ST-IN/S-I: the average thickness of the whole cornea/epithelium/stroma in SN/ST/S area respectively minus that of the whole cornea/epithelium/stroma in IT/IN/I area between the paracentral/midperipheral regions; (4) Pachymetric/ Epithelial/ Stromal overall standard deviation: the standard deviation of the whole cornea/epithelium/stroma thickness.

SD-OCT-Based Staging System Building

The software R (version 4.2.0, R Foundation for Statistical Computing, Vienna, Austria; <https://www.R-project.org/>) was used to perform feature selection on the OCT parameters using the *Boruta* package (Version 7.0.0)²⁶. Next, receiver operating characteristic (ROC) curve analyses were performed to identify those parameters that discriminate best between normal and KC eyes. The 5 best performing stromal and epithelial parameters with the highest area under the curve (AUC) values, along with their cutoff values, were then recorded.

To build the staging system, the highest ranked AUC ROC SD-OCT parameter of stroma (**ST**) and epithelium (**EP**) was selected to form the new **STEP** staging system. All cases with ST and EP values above or below the AUC-based cutoffs were defined as Stage 0 (normal), while cases with Stage > 0 were considered as KC. The lower and upper limits to the scale for ST and EP parameters were set at the lower and upper boundary of the 95% range (*i.e.*, mean \pm 1.96 x the standard deviation), respectively, to avoid including outliers. The remaining range from the AUC-based cutoffs to the lower or upper limit to the scale was then divided into 4 quartiles in accordance with the existing tomographic and biomechanical systems, thus forming the cutoff values of each stage. Finally, to optimize and finalize the staging system for a translation to the clinic, discussions were held among experts (consisting of 10 international members, including corneal specialists, each with more than 15 years of experience in KC diagnosis and management) in virtual meetings and multiple rounds of emails. The discussions pertained to the adjustment and determination of cutoff values

in each stage of two parameters, the confirmation and explanation of practical clinical utility of the current novel OCT-based staging methods proposed here.

Staging Systems Distributions and Comparisons

The distribution of each parameter from the current new staging system was assessed. Based on cross-tabulation, the staging system was compared to the distributions of the tomographic Belin ABC and the biomechanical Corvis Elastic staging systems using heat maps. For an independent validation of the two different staging systems, a new dataset was established.

STATISTICAL ANALYSIS

The statistical analysis was performed in SPSS (version 24; IBM Corporation, Armonk, New York, USA) and R. The normality of the data was verified using the Shapiro-Wilk test. Descriptive statistics were presented as mean \pm standard deviation. For continuous variables, analyses of Student's t-test and Mann-Whitney U-test were conducted to analyze the differences between the groups. A value of $P < 0.05$ was considered statistically significant for all tests. For categorical variables, analyses of chi-square test were applied to analyze the differences between the groups. To determine the optimal cut-off values, sensitivity, and specificity, ROC curves and AUC were applied as accuracy measures. The cut-off values were determined by Youden's index. Whereas an AUC value of 1.0 indicates perfect discrimination, values of ≤ 0.5 show that the assessed parameter has no diagnostic ability. Values between 0.5 and 1.0 refer to a significant difference between the distributions of the considered variables in two groups.

RESULTS

Demographics

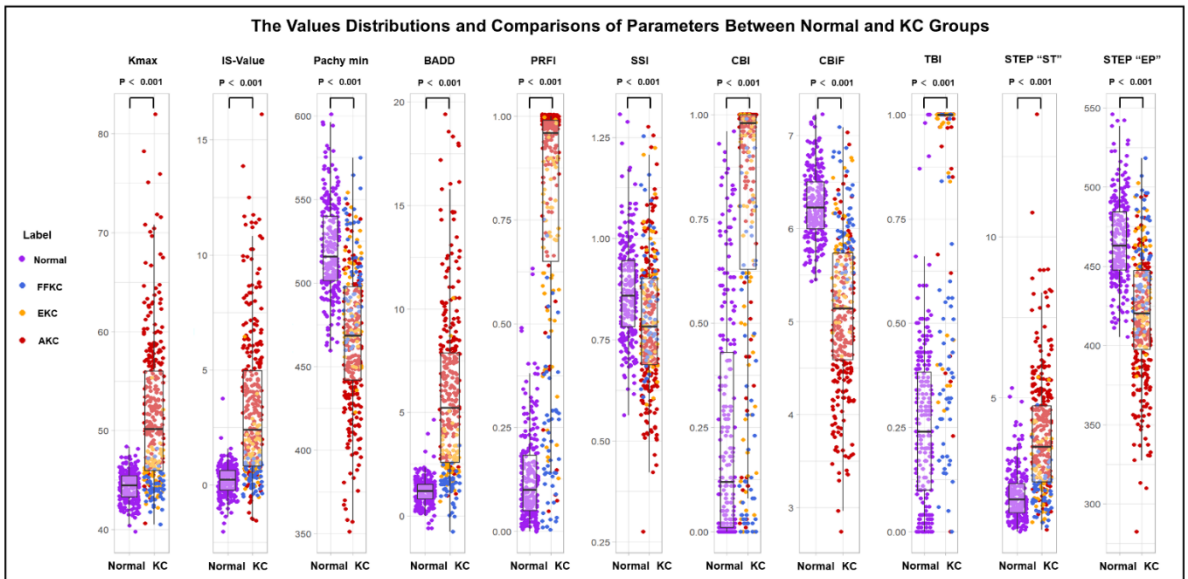
This retrospective study included 567 eyes of 567 patients for whom the basic demographic information is shown in **Table 1**. The distribution of the parameter values and comparisons between the healthy and KC groups are shown in **Figure 1**. For the KC group, there were a total of 331 eyes of 331 KC patients, including 50 FFKC eyes of 50 patients, 56 EKC eyes of 56 patients, and 225

Table 1: Basic demographic information

Parameter	Unit	Normal	Keratoconus	P Values
Original database to build the system				
Number	(OD/OS)	117/119	171/160	0.624
Gender	(M/F)	106/130	239/92	< 0.001
Age	Years	22.12±6.22	22.18±6.40	0.832
K ₁	Diopter	42.45±1.52	44.19±3.16	< 0.001
K ₂	Diopter	43.68±1.63	47.05±4.02	< 0.001
K _{max}	Diopter	44.36±1.49	51.56±7.12	< 0.001
IS-Value	Diopter	0.20±0.66	3.29±3.11	< 0.001
Pachy min	µm	538.83±30.48	484.82±40.95	< 0.001
BADD	-	1.18±0.64	5.76±3.85	< 0.001
PRFI	-	0.13±0.11	0.78±0.31	< 0.001
SSI	-	0.87±0.12	0.80±0.16	< 0.001
CBI	-	0.23±0.27	0.77±0.34	< 0.001
CBiF	-	6.25±0.37	5.14±0.81	< 0.001
TBI	-	0.26±0.19	0.87±0.27	< 0.001
Validation database				
Number	(OD/OS)	26/21	37/34	/
Gender	(M/F)	30/17	53/18	/
Age	Years	21.87±3.83	21.13±7.37	0.525
K ₁	Diopter	42.07±1.18	44.51±4.55	< 0.001
K ₂	Diopter	43.50±1.29	47.37±5.44	< 0.001
K _{max}	Diopter	44.11±1.31	51.55±8.55	< 0.001
IS-Value	Diopter	0.11±0.58	3.07±3.21	< 0.001
Pachy min	µm	548.60±29.42	487.85±52.00	< 0.001
BADD	-	0.92±0.52	5.61±5.25	< 0.001
PRFI	-	0.08±0.08	0.69±0.37	< 0.001
SSI	-	0.90±0.13	0.83±0.16	0.014
CBI	-	0.30±0.21	0.78±0.28	< 0.001
CBiF	-	6.41±0.35	5.30±1.03	< 0.001
TBI	-	0.13±0.13	0.79±0.33	< 0.001

M, male; F, female; IS-Value, the difference between average inferior and superior corneal powers 3 mm from the center of the cornea; Pachy min, corneal thinnest pachymetry measured by OCT; BADD, the Belin-Ambrósio Deviation Index; PRFI, the Pentacam Random Forest Index; SSI, the Stress-Strain Index; CBI, the Corvis Biomechanical Index; CBiF, the Corvis Biomechanical Factor; TBI, the Tomographic and Biomechanical Index

Figure 1: Values distributions and comparisons between Normal and KC groups



KC, keratoconus; FFKC, forme fruste KC; EKC, early-stage KC; AKC, advanced KC; IS-Value, the difference between average inferior and superior corneal powers 3 mm from the center of the cornea; Pachy min, corneal thinnest pachymetry measured by OCT; BADD, the Belin-Ambrósio Deviation Index; PRFI, the Pentacam Random Forest Index; SSI, the Stress-Strain Index; CBI, the Corvis Biomechanical Index; CBiF, the Corvis Biomechanical Factor; TBI, the Tomographic and Biomechanical Index; STEP 'ST', stroma overall minimum thickness; STEP 'EP', epithelium overall standard deviation

AKC eyes of 225 patients. There were no significant differences in age between the two groups ($P = 0.832$).

The Top AUC Parameters and Staging System

Comparing between the normal and KC groups, the greatest 5 AUC stromal and epithelial corneal parameters are shown in **Table 2** (all P values < 0.001). For the stromal parameters, the top AUC ROC ranked parameter was Stroma Overall Minimum Thickness (cutoff value = 436.89, AUC = 0.836); For the epithelial parameters, the top AUC ROC ranked parameter was Epithelium Overall Standard Deviation (cutoff value = 2.34, AUC = 0.835). The cutoff values of the stages were discussed and modified by the experts, leading to the staging system shown in **Table 3**.

Table 2: The top 5 AUC SD-OCT-based parameters from stroma and epithelium layers

Feature	Normal	KC	AUC	95%CI	Cutoff Value	Sn	Sp
a: The top 5 AUC stroma parameters							
Stroma Overall Min Thickness	466.20±26.93	419.88±38.76	0.836	0.804-0.868	436.89	0.903	0.671
Stroma 5mm IT Thickness	483.87±28.12	445.92±33.43	0.809	0.774-0.844	458.36	0.847	0.665
Stroma Min-Med Thickness	-48.32±6.09	-65.08±20.81	0.798	0.762-0.834	-58.48	0.970	0.547
Stroma 2mm Thickness	473.13±27.10	436.17±35.37	0.793	0.757-0.829	444.46	0.886	0.607
Stroma 9mm S Thickness	621.76±36.46	584.61±41.24	0.756	0.717-0.795	598.17	0.754	0.671
b: The top 5 AUC epithelium parameters							
Epithelium Overall Standard Deviation	1.99±0.77	3.76±1.80	0.835	0.803-0.868	2.34	0.750	0.779
Epithelium 5mm SN-IT Thickness	-0.79±1.87	4.33±5.42	0.826	0.793-0.860	1.37	0.911	0.674
Epithelium Overall Min-Max Thickness	-9.86±3.63	-17.35±7.92	0.813	0.778-0.847	-13.89	0.898	0.616
Epithelium 5mm IT Thickness	54.41±3.46	50.21±4.73	0.778	0.740-0.816	51.83	0.809	0.668
Epithelium 5mm S-I Thickness	-1.91±2.22	1.68±4.86	0.747	0.707-0.787	1.25	0.936	0.514

SD-OCT, spectral-domain optical coherence tomography; KC, keratoconus; AUC, area under the curve; CI, confidence interval; Sn, Sensitivity; Sp, specificity; Min, minimum; Med, median; Max, maximum; T, temporal; S, superior; N, nasal; I, inferior; SN, superior-nasal; IT, inferior-temporal

Table 3: The SD-OCT-based staging system: STEP

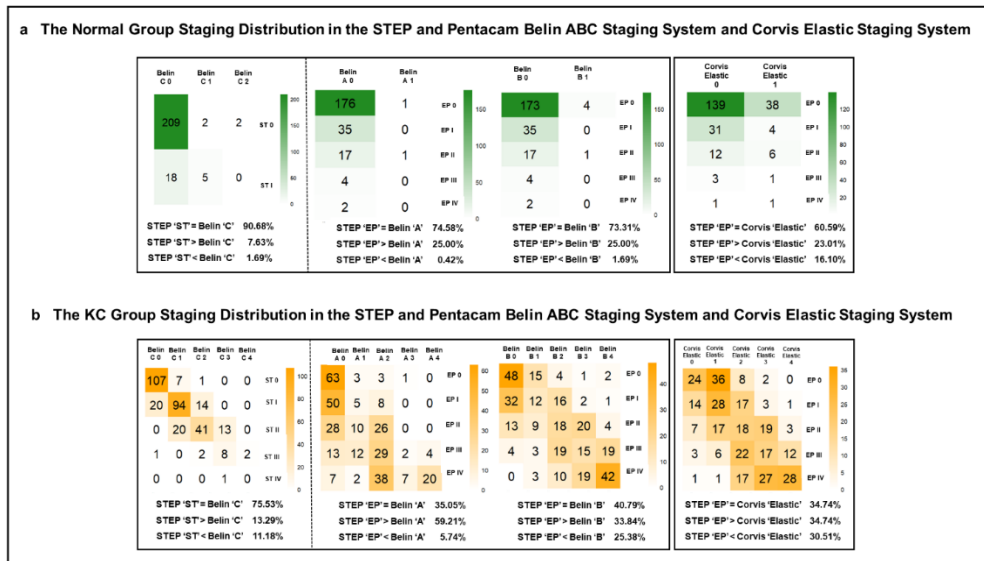
Criteria	Stage 0	Stage I	Stage II	Stage III	Stage IV
ST	≥ 435 μm	> 400 μm	> 350 μm	> 300 μm	≤ 300 μm
EP	≤ 2.30 μm	< 3.00 μm	< 4.00 μm	< 5.00 μm	≥ 5.00 μm

SD-OCT, spectral-domain optical coherence tomography; ST, stroma overall minimum thickness; EP, epithelium overall standard deviation

Distributions and Comparisons

The detailed cross-tabulation of staging distributions between the STEP and Belin ABC staging systems and between the STEP and Corvis Elastic staging systems in the normal and KC groups are shown in **Figures 2a** and **2b**, respectively. Below the figures, the corresponding relative frequencies of the STEP system compared with Belin ‘ABC’ and Corvis ‘Elastic’ staging systems were also calculated and compared to summarize the consistency of staging distributions. Two representative cases of KC in different stages are shown in **Figures 3** and **4**.

Figure 2: The normal group (a) and KC group (b) Staging distribution in the STEP and Belin ABC staging system and Corvis elastic staging system



KC, keratoconus; STEP 'ST', stroma overall minimum thickness; STEP 'EP', epithelium overall standard deviation. The numbers on the left diagonal represent eyes at the same stages in two staging systems, indicated by '=' in the statistics below; The numbers below the left diagonal represent eyes that are more severely staged in the STEP staging system than in another staging system, indicated by '>' in the statistics below; The numbers above the left diagonal represent eyes that are less severely staged in the STEP staging system than in another staging system, indicated by '<' in the statistics below

Figure 3: The right eye is EKC and the left eye is AKC, the Dresden protocol may not be considered for the left eye as the STEP 'ST' is located at Stage II

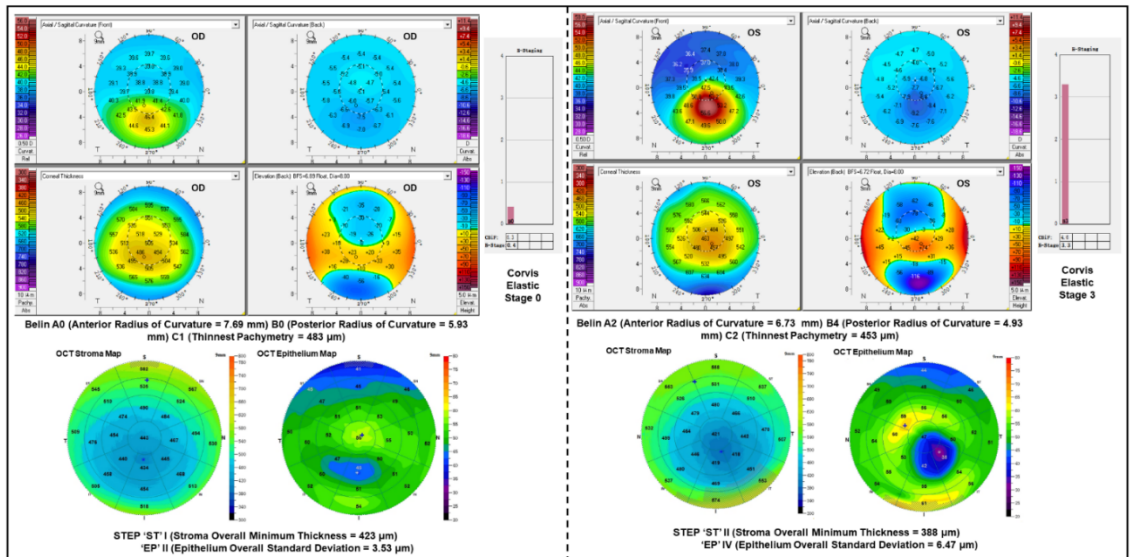
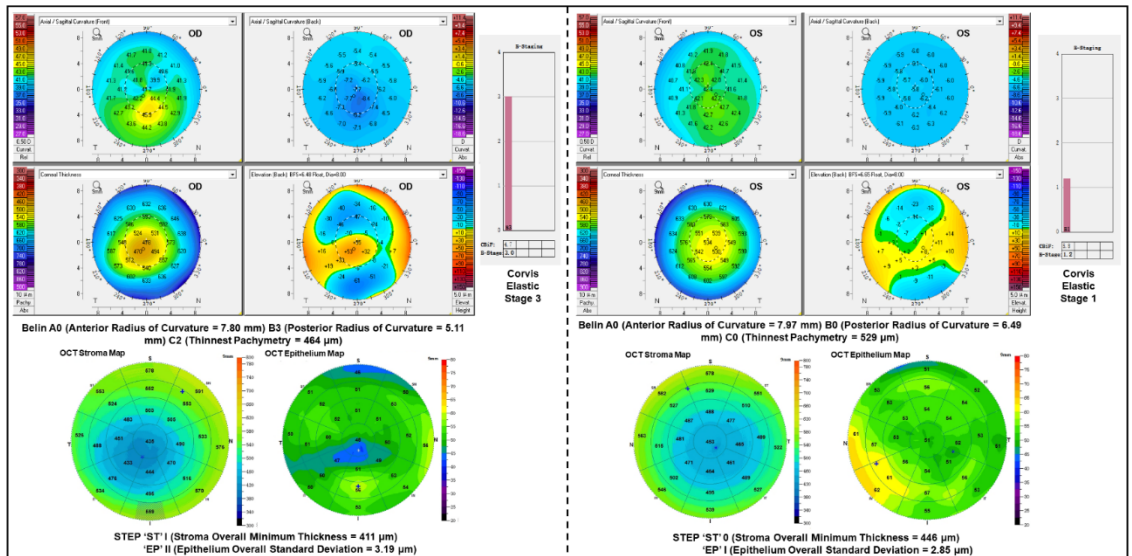


Figure 4: The right eye is AKC and the left eye is FFKC



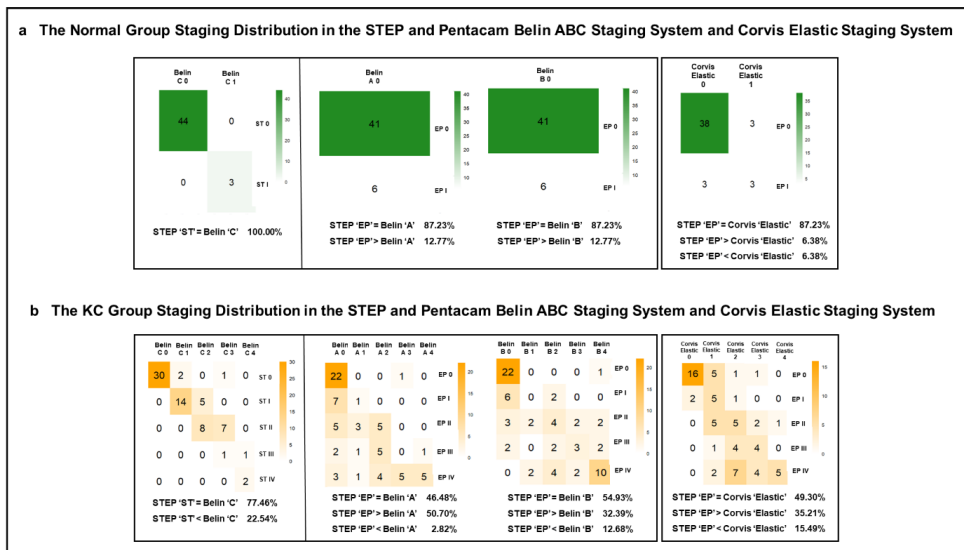
Due to similar origins, STEP 'ST' could only be compared with 'C' from the Belin ABC staging system, showing a good agreement for both normal and KC groups (90.68% normal eyes and 75.53% KC eyes were located at the same stage). Meanwhile STEP 'EP' was compared with 'A' and 'B' from the Belin ABC staging

system, as well as Corvis ‘Elastic’. In the normal group, 74.58% of eyes were of the same stage for STEP ‘EP’ and Belin ‘A’, 73.31% for STEP ‘EP’ and Belin ‘B’, and 60.59% for STEP ‘EP’ and Corvis ‘Elastic’. In the KC group, the agreement was relatively high, ranging between 35% and 41%, while inconsistencies of ≥ 2 stages between STEP 'EP' and Belin 'B' and the inconsistency of ≥ 2 stages between STEP 'EP' and Corvis 'Elastic' (e.g., eyes of stage 3 in STEP ‘EP’ and stages 0/1 in Corvis 'Elastic') was both limited to 15%.

Independent Validation

For the validation of the STEP system, a total of 47 normal eyes from 47 healthy patients and 71 eyes from 71 patients with different stages of KC (including 27 FFKC, 10 EKC, and 34 AKC) were included. The demographic information and the comparison between the two groups are shown in **Table I**. The cross-tabulation of staging distributions between the staging systems in two groups

Figure 5: In the validation study, the Normal group (a) and KC group (b) staging distribution in the STEP and Belin ABC staging system and Corvis elastic staging system



KC, keratoconus; STEP 'ST', stroma overall minimum thickness; STEP 'EP', epithelium overall standard deviation

are shown in **Figure 5**. In the normal group, the STEP system agreed very well with the Belin ABC and Corvis Elastic staging systems, more than 85% of patients were in the same stage in all the comparisons. In the KC group, the staging agreement was still relatively high (ranging between 47% and 77%).

DISCUSSION

The current study describes the establishment of a comprehensive numeric SD-OCT-based KC staging system. This OCT-based KC staging system is named STEP as it is based on two parameters, Stromal Overall Minimum Thickness (ST) and Epithelium Overall Standard Deviation (EP).

STEP is the first approach to incorporate both corneal epithelial and stromal information into a KC staging system. One practical application of STEP 'ST' could be to facilitate the decision process of CXL protocols. For example, in advanced KC cases the classic Dresden protocol is often not appropriate if the stromal pachymetry is below 400 μm (STEP 'ST' > Stage I). In such cases, the sub400 or other alternative CXL protocols might be indicated²⁷. For STEP 'EP', when the epithelium becomes more asymmetric to smoothen the irregular stromal surface during KC progression, STEP 'EP' which reflects remodeling increases correspondingly. It also indicates the degree of epithelial redistribution. Furthermore, it could potentially act as a tool for evaluating CXL effectiveness evaluation and follow-up, as the difference in epithelium thickness distribution was shown to become less in post-CXL stable post-ectasia and KC patients^{28, 29}.

Our outcomes aligned well with previous studies using an alternative SD-OCT device (MS-39, CSO Italia, Firenze, Italy), where the authors demonstrated a good correlation between the degree of visual limitation (and KC severity staging) and stromal and epithelial thickness parameters³⁰. In these studies, the "superior-inferior ratio" at 6 and 8mm played a major role, reflecting the performance of STEP 'EP' for the irregular distribution of the epithelial thickness throughout the cornea; although an OCT-based KC staging system was not developed in their studies.

In reviewing the existing KC staging systems, the first KC staging system was proposed by Amsler³¹, which Krumeich *et al.* updated to the Amsler-Krumeich (AK) staging system³². Alió and Shabayek later introduced the corneal coma-like aberrations to the AK staging system³³, while Ishii *et al.* integrated 6 front surface parameters into the AK staging system³⁴. Belin *et al.* established the Belin ABCD system by expanding the AK staging system into 5 stages, adding the posterior surface curvature, switching from the corneal central thickness to the corneal thinnest thickness, and modifying the values of all the objective parameters in the mildest stage based on the results of ROC analyses³⁵. Sandali *et al.* firstly established an OCT-based structural staging system by describing the corneal structural remodeling through the sectional scan observation³⁶. However, the descriptions are not numerical, which makes it prone to potential discrepancies in clinical practice. While the STEP system overcomes this limitation, Sandali's structural staging system still could be used to augment the STEP system by providing visualized structural information. Furthermore, ocular surface disorders such as severe dry eye, epithelial basement membrane dystrophy, and contact lens-induced epithelial remodeling warpage can affect the epithelium profile measurement, thus reducing the accuracy of STEP³⁷. The system should therefore be combined with a clinical slit lamp examination to distinguish such ocular surface disorders from KC. Caution is especially warranted in applying STEP to KC patients simultaneously suffering for these ocular surface disorders³⁸. Recently, Yousefi *et al.* firstly built a numeric OCT-based staging system by principal component analysis³⁹. While interesting, such a system does not explicitly present stromal and epithelial information, making clinical interpretation difficult. The two machine-derived parameters of STEP system, on the other hand, are far easier to interpret.

For the agreement between the STEP system and the Belin ABCD staging system, the validation study showed a similar result with the original dataset which currently used for the STEP system establishment: when compared with the Belin ABCD staging system, STEP 'ST' agreed well with Belin 'C' due to the similar description, but STEP 'EP' agreed less with Belin 'A' and 'B' in the KC

group, especially with the former. This could be explained by the fact that the epithelium remodeling occurs before the change in corneal curvature ⁴⁰. However, we should note that a good disease grading system should classify most normal patients as stage 0-1 and classify the affected patients as higher than stage 0, as we see with the STEP staging system. AS-OCT can also detect the anterior and posterior corneal curvatures simultaneously with good accuracy in both normal and KC patients ⁴¹. Therefore, the STEP staging system has the potential advantage of integrating the Belin ABCD staging system or regard it as a simultaneous reference.

There are some limitations of our study, one of which is that no progressive cases were evaluated with STEP. Furthermore, current analysis does not validate the universal application of STEP for other types of OCT systems that may lead to slightly different thickness of the corneal layers. Further investigation on this matter is required. In addition, since the STEP system includes an index that relies on a single point measurement (ST), potential future improvements of commercial AS-OCT systems allowing to determine the profiles of the epithelium and stroma could further improve the reliability of STEP.

In conclusion, we propose a digital, automated, and comprehensive OCT-based KC staging system that is compatible with existing KC staging systems and offers additional clinical relevance. This system could be incorporated into daily clinical practice and in research, as it has the potential to help treatment decision-making and monitor KC progression.

REFERENCES

1. Krachmer JH, Feder RS, Belin MW. Keratoconus and related noninflammatory corneal thinning disorders. *Surv Ophthalmol* 1984;28:293-322.
2. Rabinowitz YS. Keratoconus. *Surv Ophthalmol* 1998;42:297-319.
3. Wollensak G, Spoerl E, Seiler T. Riboflavin/ultraviolet-a-induced collagen crosslinking for the treatment of keratoconus. *Am J Ophthalmol* 2003;135:620-627.
4. Lopes BT, Ramos IC, Salomão MQ, et al. Enhanced Tomographic Assessment to Detect Corneal Ectasia Based on Artificial Intelligence. *Am J Ophthalmol* 2018;195:223-232.
5. Vinciguerra R, Belin MW, Borgia A, et al. Evaluating keratoconus progression prior to crosslinking: maximum keratometry vs the ABCD grading system. *J Cataract Refract Surg* 2021;47:33-39.
6. Asroui L, Mehanna CJ, Salloum A, Chalhoub RM, Roberts CJ, Awwad ST. Repeatability of Zone Averages Compared to Single-Point Measurements of Maximal Curvature in Keratoconus. *Am J Ophthalmol* 2021;221:226-234.
7. Jiménez-García M, Kreps EO, S ND, Koppen C, Rozema JJ. Determining the Most Suitable Tomography-Based Parameters to Describe Progression in Keratoconus. The Retrospective Digital Computer Analysis of Keratoconus Evolution Project. *Eye Contact Lens* 2021;47:486-493.
8. Vinciguerra R, Ambrósio R, Jr., Roberts CJ, Azzolini C, Vinciguerra P. Biomechanical Characterization of Subclinical Keratoconus Without Topographic or Tomographic Abnormalities. *J Refract Surg* 2017;33:399-407.
9. Vinciguerra R, Ambrósio R, Elsheikh A, et al. Detection of Keratoconus With a New Biomechanical Index. *Journal of Refractive Surgery* 2016;32:803-810.
10. Koh S, Inoue R, Ambrósio RJ, Maeda N, Miki A, Nishida K. Correlation Between Corneal Biomechanical Indices and the Severity of Keratoconus. *Cornea* 2020;39:215-221.
11. Flockerzi E, Vinciguerra R, Belin MW, Vinciguerra P, Ambrósio R, Jr., Seitz B. Combined biomechanical and tomographic keratoconus staging: Adding a biomechanical parameter to the ABCD keratoconus staging system. *Acta Ophthalmol* 2021.
12. Flockerzi E, Vinciguerra R, Belin MW, Vinciguerra P, Ambrósio R, Jr., Seitz B. Correlation of the Corvis Biomechanical Factor with tomographic parameters in keratoconus. *J Cataract Refract Surg* 2022;48:215-221.
13. Li Y, Tan O, Brass R, Weiss JL, Huang D. Corneal epithelial thickness mapping by Fourier-domain optical coherence tomography in normal and keratoconic eyes. *Ophthalmology* 2012;119:2425-2433.
14. Reinstein DZ, Archer TJ, Gobbe M. Corneal epithelial thickness profile in the diagnosis of keratoconus. *J Refract Surg* 2009;25:604-610.
15. Temstet C, Sandali O, Bouheraoua N, et al. Corneal epithelial thickness mapping using

Fourier-domain optical coherence tomography for detection of forme fruste keratoconus. *J Cataract Refract Surg* 2015;41:812-820.

16. Li Y, Chamberlain W, Tan O, Brass R, Weiss JL, Huang D. Subclinical keratoconus detection by pattern analysis of corneal and epithelial thickness maps with optical coherence tomography. *J Cataract Refract Surg* 2016;42:284-295.

17. Pavlatos E, Chen S, Yang Y, Wang Q, Huang D, Li Y. A Coincident Thinning Index for Keratoconus Identification Using OCT Pachymetry and Epithelial Thickness Maps. *Journal of Refractive Surgery* 2020;36:757-765.

18. Reinstein DZ, Silverman RH, Trokel SL, Coleman DJ. Corneal pachymetric topography. *Ophthalmology* 1994;101:432-438.

19. Gonnella JS, Hornbrook MC, Louis DZ. Staging of disease. A case-mix measurement. *Jama* 1984;251:637-644.

20. Ting DSW, Peng L, Varadarajan AV, et al. Deep learning in ophthalmology: The technical and clinical considerations. *Prog Retin Eye Res* 2019;72:100759.

21. Lu N-J, Elsheikh A, Rozema JJ, et al. Combining Spectral-Domain OCT and Air-Puff Tonometry Analysis to Diagnose Keratoconus. *Journal of Refractive Surgery* 2022;38:374-380.

22. Henriquez MA, Hadid M, Izquierdo L, Jr. A Systematic Review of Subclinical Keratoconus and Forme Fruste Keratoconus. *J Refract Surg* 2020;36:270-279.

23. Ambrósio R, Lopes BT, Faria-Correia F, et al. Integration of Scheimpflug-Based Corneal Tomography and Biomechanical Assessments for Enhancing Ectasia Detection. *Journal of Refractive Surgery* 2017;33:434-443.

24. Eliasy A, Chen K-J, Vinciguerra R, et al. Determination of Corneal Biomechanical Behavior in-vivo for Healthy Eyes Using CorVis ST Tonometry: Stress-Strain Index. *Frontiers in Bioengineering and Biotechnology* 2019;7.

25. Lu N-J, Chen D, Cui L-L, Wang L, Chen S-H, Wang Q-M. Repeatability of Cornea and Sublayer Thickness Measurements Using Optical Coherence Tomography in Corneas of Anomalous Refractive Status. *Journal of Refractive Surgery* 2019;35:600-605.

26. Kursa MB, Rudnicki WR. Feature Selection with the Boruta Package. *Journal of Statistical Software* 2010;36:1-13.

27. Hafezi F, Kling S, Gilardoni F, et al. Individualized Corneal Cross-linking With Riboflavin and UV-A in Ultrathin Corneas: The Sub400 Protocol. *Am J Ophthalmol* 2021;224:133-142.

28. Reinstein D, Gobbe M, Archer T, Couch D. Epithelial Thickness Profile as a Method to Evaluate the Effectiveness of Collagen Cross-Linking Treatment After Corneal Ectasia. *Journal of refractive surgery (Thorofare, NJ : 1995)* 2010;27:356-363.

29. Rocha KM, Perez-Straziota CE, Stulting RD, Randleman JB. Epithelial and stromal remodeling after corneal collagen cross-linking evaluated by spectral-domain OCT. *J*

Refract Surg 2014;30:122-127.

30. Vega-Estrada A, Mimouni M, Espla E, Alió Del Barrio J, Alio JL. Corneal Epithelial Thickness Intrasubject Repeatability and its Relation With Visual Limitation in Keratoconus. *Am J Ophthalmol* 2019;200:255-262.

31. Amsler M. Kératocône classique et kératocône fruste; arguments unitaires. *Ophthalmologica* 1946;111:96-101.

32. Krumeich JH, Daniel J, Knülle A. Live-epikeratophakia for keratoconus. *J Cataract Refract Surg* 1998;24:456-463.

33. Alió JL, Shabayek MH. Corneal higher order aberrations: a method to grade keratoconus. *J Refract Surg* 2006;22:539-545.

34. Ishii R, Kamiya K, Igarashi A, Shimizu K, Utsumi Y, Kumanomido T. Correlation of corneal elevation with severity of keratoconus by means of anterior and posterior topographic analysis. *Cornea* 2012;31:253-258.

35. Belin MW, Duncan JK. Keratoconus: The ABCD Grading System. *Klin Monbl Augenheilkd* 2016;233:701-707.

36. Sandali O, El Sanharawi M, Temstet C, et al. Fourier-domain optical coherence tomography imaging in keratoconus: a corneal structural classification. *Ophthalmology* 2013;120:2403-2412.

37. Levy A, Georgeon C, Knoeri J, et al. Corneal Epithelial Thickness Mapping in the Diagnosis of Ocular Surface Disorders Involving the Corneal Epithelium: A Comparative Study. *Cornea* 2022;41:1353-1361.

38. Venkateswaran N, Galor A, Wang J, Karp CL. Optical coherence tomography for ocular surface and corneal diseases: a review. *Eye Vis (Lond)* 2018;5:13.

39. Yousefi S, Yousefi E, Takahashi H, et al. Keratoconus severity identification using unsupervised machine learning. *PLOS ONE* 2018;13:e0205998.

40. Reinstein DZ, Archer TJ, Urs R, Gobbe M, RoyChoudhury A, Silverman RH. Detection of Keratoconus in Clinically and Algorithmically Topographically Normal Fellow Eyes Using Epithelial Thickness Analysis. *J Refract Surg* 2015;31:736-744.

41. Tang M, Chen A, Li Y, Huang D. Corneal power measurement with Fourier-domain optical coherence tomography. *Journal of cataract and refractive surgery* 2010;36:2115-2122.

Chapter 3

A Novel Artificial Intelligence-Assisted Keratoconus Diagnostic Index Based on Optical Coherence Tomography

Nan-Ji Lu, Carina Koppen, Sorcha Ní Dhubhghaill, Xin-Yi Chen, Qin-Mei Wang, Le-Le Cui, Jos J. Rozema

In preparation

ABSTRACT

Purpose: To establish a new spectral-domain optical coherence tomography (SD-OCT)-based keratoconus (KC) diagnostic index by artificial intelligence and compare it with existing parameters.

Methods: SD-OCT and Scheimpflug-based tomography were performed on cohorts of normal and KC eyes. Multiple SD-OCT machine-derived parameters of whole cornea, stroma, and epithelium were evaluated. For SD-OCT machine-derived parameters, receiver operating characteristic (ROC) curves were performed to determine area under the curve (AUC), sensitivity, and specificity. Principal component analysis and multinomial logistic regression after features selection were conducted to establish a new diagnostic index (whole information of stroma and epithelium, 'WISE'). WISE was then compared with existing tomography-based diagnostic parameters.

Results: We included 306 normal eyes, 101 forme fruste KC (FFKC) eyes, 86 early KC (EKC) eyes, and 161 advanced KC eyes. The highest ranked SD-OCT parameters to discriminate FFKC and EKC from normal eyes were Epithelium_5mm_SN-IT (AUC = 0.65) and Pachymetry_9mm_N (AUC = 0.77), respectively. The proposed WISE index had AUC = 0.78 and 0.96 for FFKC and EKC, respectively, similar to Belin-Ambrósio Deviation ($P = 0.058$ and 0.462 for FFKC and EKC, respectively) and Pentacam Random Forest Index ($P = 0.060$ and 0.725 for FFKC and EKC, respectively) evaluated by a DeLong's test.

Conclusions: A single OCT-based machine-derived parameter does not have sufficient power to discriminate FFKC and EKC from normal corneas, but this may be improved by combining OCT-based information from stroma and epithelium as in this new diagnostic index. The discrimination accuracy of the OCT-based WISE index was comparable to Scheimpflug-based indices.

INTRODUCTION

Keratoconus (KC) is a bilateral corneal ectatic disorder, characterized by local biomechanical weakness with asymmetric corneal involvement. As the disease progresses, the cornea becomes thinner and begins to protrude, leading to increasing myopia, irregular astigmatism, corneal scarring, and reduction of vision ¹. Early diagnosis allows for a closer follow-up of the disease so that in cases of KC progression, corneal cross-linking (CXL) can be applied promptly to stop or delay its progression ^{2,3}. Moreover, early diagnosis can also help screen laser vision correction (LVC) candidates to prevent post-LVC ectasia as an exacerbation of an unrecognized subclinical KC ^{4,5}.

KC is typically diagnosed clinically augmented by clinical devices that assess the corneal shape, such as Placido-based topography to measure the corneal anterior curvature. Later, Scheimpflug-based tomography added the posterior corneal curvature and elevation. Applying artificial intelligence (AI) methods to the vast array of parameters obtained from Placido- or Scheimpflug-based systems has significantly improved our ability to diagnose early-stage KC ^{6,7}. The newest advancement in corneal imaging, anterior segment optical coherence tomography (AS-OCT), can differentiate the corneal epithelium, Bowman's layer, and stroma with a high level of granularity beyond the capabilities of Scheimpflug-based imaging ⁸, which offer an opportunity for further improving KC detection.

In the pathophysiology of KC, the cornea reshapes in response to a local decrease in stiffness ⁹, causing stromal thinning and steepening, while the corneal epithelium remodels to smooth the corneal surface. Previous OCT studies showed that individual corneal, stromal, and epithelial parameters, sometimes combined with AI methods, facilitate early-stage KC detection ¹⁰⁻¹⁵. But such parameters only cover individual aspects of the corneal reshaping, rather than providing a global overview of all changes ¹⁶.

The aim of this study was to develop a novel OCT-based KC diagnostic index that includes whole corneal as well as unique stromal and upper-layer epithelial

information derived by OCT. Once the index was developed, we compared it with existing tomography diagnostic parameters to evaluate its performance.

METHODS

This retrospective study was conducted with the approval of the ethics committee of Eye Hospital of Wenzhou Medical University. The data was collected between 2018 July to 2022 December. All participants signed an informed consent before their data was included for analysis.

Patients Inclusion Criteria and Group Settings

This study included four groups of patients: a normal control group and three KC groups. Prior to the examination, patients were strictly asked to discontinue soft contact lens wear for at least 2 weeks, or at least 4 weeks for rigid gas-permeable contact lenses.

The normal patients were recruited from those seeking laser vision correction (LVC) in Eye Hospital of Wenzhou Medical University. The inclusion criteria were the absence of ocular/ systemic abnormalities, no history of ocular surgery, a stable corrected distance visual acuity (CDVA) $\geq 20/20$ for 2 years before surgery. After LVC, all patients had a minimum of 3-years of follow-up to exclude the inclusion of forme fruste KC. Only one eye per person was randomly included in the normal group.

For KC patients, the diagnosis was confirmed by four cornea specialists. The diagnosis usually required 2 classic signs of KC on Scheimpflug-based tomography (Pentacam HR, Oculus Optikgeräte, Wetzlar, Germany), such as abnormal corneal thickness distribution and thinnest pachymetry, abnormal posterior elevation, skewed asymmetric bowtie/inferior steep [SAB/IS] or increased inferior steepness, and/ or 1 classic slit lamp finding (Fleischer ring, Vogt striae or central thinning). After the confirmation of the KC diagnosis, only one eye with the milder impairment in each KC patient was selected, resulting in KC eyes with varying degrees of impairment being included.

According to the degree of KC severity, the included KC eyes were further divided into the forme fruste KC (FFKC), early KC (EKC), and advanced KC (AKC) groups^{17, 18}. For the FFKC group, contralateral to eyes with confirmed KC, where the inclusion criteria comprised of best CDVA \geq 20/20, no KC signs at slit-lamp, Kmax < 47.4 diopters (D), thinnest pachymetry \geq 480 μ m, “normal” tomography with the difference between the Kmax values in the inferior and superior areas at 3 mm (IS-Value) < 1.4 D, and no SAB/IS¹⁹. For the EKC group, the criteria were: Kmax < 48.5 D, thinnest pachymetry > 480 μ m, best CDVA \geq 16/20, no central scars and fewer than two slit lamp findings. The criteria for the AKC group were KC eyes with parameters exceeding those of the FFKC and EKC groups.

Spectral-Domain OCT

Spectral-domain OCT (SD-OCT) were performed using the RTVue-XR OCT (OptoVue, Inc., Fremont, CA, USA) in the Pachymetry-Wide scan pattern, which is known to provide excellent repeatability²⁰. For each eye, 3 continuous scans were conducted. The whole cornea, stromal, and epithelial thickness maps were recorded in the central (2 mm diameter), paracentral (2 to 5 mm), midperipheral (5 to 7 mm), and peripheral regions (7 to 9 mm). In the latter three regions, the thickness was monitored in 8 equally spaced points along the median circumference of the area, including the temporal (T), superior-temporal (ST), superior (S), superior-nasal (SN), nasal (N), inferior-nasal (IN), inferior (I) and inferior-temporal (IT) positions.

All machine-derived parameters based on the measured thickness of the three different corneal layers, were automatically generated through the device software (ReVue version 2018.0.04) and recorded. These measurements included: (1) Pachymetric/Stromal/Epithelial Minimum Thickness: the minimum thickness in the whole cornea/stroma/epithelium layer; (2) Pachymetric/Stromal/Epithelial Min-Max: the minimum thickness in the whole cornea/stroma/epithelium minus the maximum thickness in the whole cornea/stroma/epithelium; (3) Pachymetric/Stromal/Epithelial 5mm/7mm SN-

IT/ST-IN/S-I: the average thickness of the whole cornea/stroma/ epithelium in SN/ST/S area respectively minus that of the whole cornea/stroma/ epithelium in IT/IN/I area between the paracentral/midperipheral regions; (4) Pachymetric/Stromal/Epithelial standard deviation: the standard deviation of the whole cornea/stroma/epithelium thickness.

Scheimpflug-based Tomography

Corneal Scheimpflug-based tomography were measured using the Pentacam HR (software version 1.25r12). Only measurements with acceptable quality (marked "OK") were included in the analyses. The following tomographic parameters were recorded: K_1 , K_2 , K_{max} , IS-Value, thinnest pachymetry, and two KC diagnostic parameters - the Belin-Ambrósio Deviation (BADD) and the Pentacam Random Forest Index (PRFI)^{6, 21}.

OCT-Based Diagnostic Index Building

To evaluate the diagnostic ability of all independent machine-derived OCT parameters, receiver operating characteristic (ROC) curve analyses were performed between the normal group and three KC groups separately. The corneal, stromal, and epithelial parameters with the highest area under the curve (AUC) values were recorded.

The software R (v4.2.0, R Foundation for Statistical Computing, Vienna, Austria) and the *Boruta* package (v7.0.0)²² were used to perform feature selection on the exported machine-derived parameters. Principal component analysis (PCA) was used to reduce dimensions and eliminate the strong multicollinearity between the OCT-derived parameters after being chosen by feature selection. PCA was performed using the *nsprcomp* package (Version 4.0) in R²³. Principal Components (PCs) were recorded and picked until the cumulative proportion of PCs explained 95% of parameter variability.

Normal patients were differentiated from FFKC and EKC patients by generating a combined dataset of these three groups, and randomly dividing this into a training set and a validation set. The training set constituted 70% of the total

dataset and was used to train the model of multinomial logistic regression (MLR), while the remaining 30% of the total dataset formed the validation set, used to evaluate the model's accuracy. PCs obtained from PCA were applied as the multiple predictor variables for MLR. Then, MLR with stepwise inclusion of PCs was performed to determine the optimal combination of the best predictor variables. Finally, a new SD-OCT-based diagnostic index was formed called **WISE**, which stands for Whole Information of the Stroma and Epithelium.

KC Diagnostic Parameters Comparisons

The validation set was used to determine the ability of WISE to discriminate FFKC and EKC patients from normal patients. The accuracy was obtained through 10-fold cross-validation, which was compared to existing Scheimpflug-based tomographic KC diagnostic parameters (BADD and PRFI) using ROC curve analyses and DeLong's test ²⁴.

STATISTICAL ANALYSIS

The statistical analysis was performed in R. The normality of the data was verified using the Shapiro-Wilk test. Descriptive statistics were presented as mean \pm standard deviation. For continuous variables, analyses of Mann-Whitney U-test were conducted to analyze the differences between the groups. A value of $P < 0.05$ was considered statistically significant for all tests. To determine optimal cut-off values, sensitivity, and specificity, ROC curves and AUC were applied as accuracy measures, and the cut-off values were determined by Youden's index. AUC values range between 0-1.0, with 1.0 corresponding with perfect discrimination and ≤ 0.5 with a lack of diagnostic ability.

RESULTS

Demographics

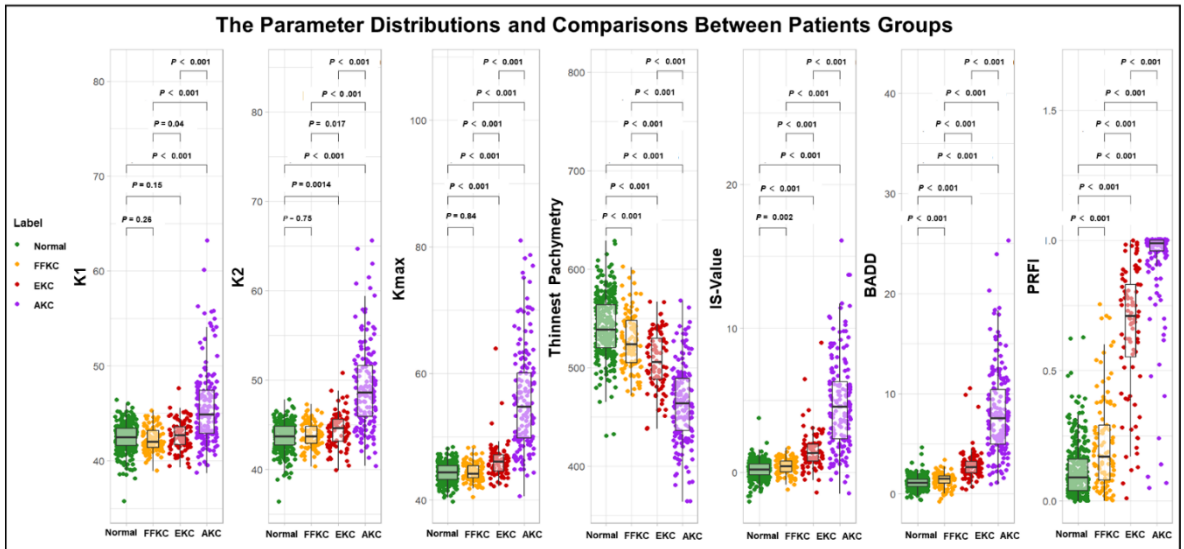
This retrospective diagnostic study included 306 normal eyes from 306 normal patients and 348 KC eyes from 348 KC patients. The demographic information for these patients is shown in **Table 1**. In the KC groups, 101 FFKC eyes from 101 patients, 86 EKC eyes from 86 patients, and 161 AKC eyes from 161

Table 1: Basic demographic information

	Unit	Normal	FFKC	EKC	AKC
Number	(OD/OS)	153/153	50/51	43/43	75/86
Age	Years	22.25 ± 5.92	23.74 ± 6.56	22.57 ± 7.19	21.82 ± 6.29
K ₁	Dioptr	42.39 ± 1.47	42.30 ± 1.25	42.73 ± 1.56	45.68 ± 4.04
K ₂	Dioptr	43.63 ± 1.57	43.78 ± 1.36	44.38 ± 1.91	49.18 ± 4.69
K _{max}	Dioptr	44.31 ± 1.48	44.39 ± 1.43	46.19 ± 2.82	55.95 ± 8.11
Thinnest Pachymetry	µm	541.15 ± 30.23	526.82 ± 29.37	507.13 ± 29.29	463.32 ± 39.43
IS-Value	Dioptr	0.19 ± 0.63	0.38 ± 0.53	1.51 ± 1.40	4.76 ± 3.20
BADD	-	1.13 ± 0.61	1.37 ± 0.69	2.90 ± 1.58	8.11 ± 4.38
PRFI	-	0.12 ± 0.10	0.22 ± 0.18	0.65 ± 0.25	0.93 ± 0.18

FFKC, forme fruste keratoconus; EKC, early keratoconus; AKC, advanced keratoconus; IS-Value, difference between average inferior and superior corneal powers 3 mm from the center of the cornea; BADD, Belin-Ambrósio Deviation; PRFI, Pentacam Random Forest Index

Figure 1: Values distributions and comparisons of basic parameters among the Normal and three KC groups



FFKC, forme fruste keratoconus; EKC, early keratoconus; AKC, advanced keratoconus; IS-Value, difference between average inferior and superior corneal powers 3 mm from the center of the cornea; BADD, Belin-Ambrósio Deviation Index; PRFI, Pentacam Random Forest Index

patients were included in the FFKC, EKC, and AKC groups, respectively. There were no significant differences in age between groups ($P = 0.104$). The distributions and comparisons between groups are shown in **Figure 1**. There was no statistical difference between the training and validation datasets.

Table 2: The Top AUC parameters in all comparisons from OCT

Variable	Layer Information	AUC	95% CI	Cut-off Value	Sn	Sp
The Normal group vs. The AKC group						
Pachymetry Overall Min-Med	Whole Cornea	0.945	0.920-0.970	-33.755	0.958	0.857
Pachymetry Overall Min	Whole Cornea	0.942	0.918-0.966	482.410	0.941	0.845
Stroma Overall Min	Stroma	0.934	0.908-0.959	434.495	0.925	0.845
Stroma 5mm IT	Stroma	0.895	0.864-0.926	458.355	0.859	0.807
EPI Overall StdDev	Epithelium	0.908	0.878-0.937	2.525	0.901	0.775
EPI Overall Min-Max	Epithelium	0.900	0.869-0.932	-14.340	0.876	0.814
The Normal group vs. The EKC group						
Pachymetry Overall Min	Whole Cornea	0.762	0.706-0.819	490.095	0.905	0.477
Pachymetry 5mm IT	Whole Cornea	0.762	0.705-0.818	514.88	0.833	0.558
Stroma 5mm IT	Stroma	0.749	0.691-0.807	455.255	0.892	0.500
Stroma Overall Min	Stroma	0.747	0.688-0.805	437.615	0.895	0.465
EPI 5mm SN-IT	Epithelium	0.771	0.711-0.832	1.325	0.905	0.558
EPI 5mm Superior-Inferior	Epithelium	0.722	0.656-0.789	-0.200	0.778	0.558
The Normal group vs. The FFKC group						
Pachymetry 9mm N	Whole Cornea	0.645	0.581-0.710	637.285	0.598	0.663
Pachymetry 7mm N	Whole Cornea	0.645	0.580-0.710	588.385	0.641	0.624
Stroma 9mm S	Stroma	0.640	0.572-0.708	597.840	0.765	0.554
Stroma 7mm N	Stroma	0.640	0.574-0.706	529.445	0.693	0.584
EPI 5mm Superior-Inferior	Epithelium	0.598	0.531-0.664	-0.605	0.690	0.485
EPI 5mm SN-IT	Epithelium	0.597	0.531-0.663	0.405	0.797	0.396

AUC, area under the curve; OCT, optical coherence tomography; Sn, sensitivity; Sp, specificity; AKC, advanced keratoconus; EKC, early keratoconus; FFKC, forme fruste keratoconus; EPI, epithelium; Min, minimum; Med, median; ST, superior-temporal; S, superior; SN, superior-nasal; N, nasal; IN, inferior-nasal; I, inferior; IT, inferior-temporal; StdDev, standard deviation

Feature Selection and PCA

There were 136 available parameters exported from the SD-OCT, describing the cornea as a whole, stromal thickness, and epithelial thickness. The six highest-ranked parameters (according to their AUC) distinguishing the normal group from the three KC groups, using the whole cornea, stroma, and epithelium are shown in **Table 2**.

The feature selection confirmed 62 relevant parameters and the results are provided in **Supplemental Materials I**. Nine PCs were required to explain 95% of the variability of parameters chosen by feature selection. The specific composite parameters and the coefficients of these PCs and the variance proportion of these PCs are shown in **Supplemental Materials II**.

Supplemental Materials I: Confirmed features from OCT by feature selection

Feature	Mean Imp	Median Imp	Min Imp	Max Imp	Norm Hits	Decision
a: Selected features from whole cornea layer						
Pachymetry Overall Min-Median	15.46	15.49	12.77	17.52	1.00	Confirmed
Pachymetry Overall Min	11.17	11.18	9.26	13.15	1.00	Confirmed
Pachymetry 5mm IT	8.30	8.32	6.60	10.10	1.00	Confirmed
Pachymetry Overall yMin	7.94	7.93	5.69	9.83	1.00	Confirmed
Pachymetry 9mm SN	6.94	6.94	4.79	8.41	1.00	Confirmed
Pachymetry Overall I 2-5mm	6.22	6.22	4.98	7.81	1.00	Confirmed
Pachymetry Overall Min-Max	5.80	5.80	3.56	7.97	1.00	Confirmed
Pachymetry 9mm ST	5.93	5.95	3.91	7.66	1.00	Confirmed
Pachymetry 9mm S	6.00	6.00	4.03	7.55	1.00	Confirmed
Pachymetry 5mm I	6.16	6.17	4.77	7.52	1.00	Confirmed
Pachymetry Overall StdDev	5.70	5.71	3.56	7.79	0.99	Confirmed
Pachymetry 9mm N	4.99	5.00	3.29	6.77	0.97	Confirmed
Pachymetry 5mm IN	4.68	4.72	3.07	6.63	0.96	Confirmed
Pachymetry Overall Median	4.41	4.45	2.78	5.79	0.94	Confirmed
Pachymetry 7mm IT	3.91	3.94	2.00	5.68	0.85	Confirmed
Pachymetry 9mm S-I	4.13	4.13	1.58	6.19	0.84	Confirmed
Pachymetry 5mmN	3.90	3.89	2.31	5.51	0.84	Confirmed
Pachymetry 9mm Superior-Inferior	3.82	3.86	1.08	6.03	0.79	Confirmed

Supplemental Materials I: Confirmed features from OCT by feature selection

Feature	Mean	Median	Min	Max	Norm	Decision
	Imp	Imp	Imp	Imp	Hits	
Pachymetry 7mm N	3.52	3.52	1.70	5.29	0.73	Confirmed
Pachymetry 9mm T	3.24	3.27	1.00	5.22	0.62	Confirmed
Pachymetry 7mm T	3.14	3.19	0.83	5.19	0.59	Confirmed
b: Selected features from stroma layer						
Stroma Min-Median	9.62	9.61	7.65	11.70	1.00	Confirmed
Stroma Overall Min	9.47	9.47	7.80	10.95	1.00	Confirmed
Stroma 2mm	6.92	6.90	5.51	8.40	1.00	Confirmed
Stroma 5mm IT	6.74	6.75	5.24	8.35	1.00	Confirmed
Stroma 9mm SN	6.74	6.77	5.03	8.14	1.00	Confirmed
Stroma yMin	5.54	5.54	3.15	7.41	0.99	Confirmed
Stroma 9mm S	5.50	5.50	3.24	7.09	0.99	Confirmed
Stroma 9mm ST	5.33	5.35	3.48	7.16	0.99	Confirmed
Stroma 5mm I	5.27	5.30	3.41	6.74	0.98	Confirmed
Stroma 9mm N	4.80	4.80	2.80	6.63	0.97	Confirmed
Stroma 5mm T	4.70	4.75	2.81	6.39	0.96	Confirmed
Stroma 5mm IN	4.44	4.43	2.30	5.99	0.93	Confirmed
Stroma 5mm N	4.20	4.24	2.65	5.56	0.90	Confirmed
Stroma 9mm S-I	3.96	4.01	1.26	6.04	0.83	Confirmed
Stroma 9mm Superior-Inferior	3.74	3.78	1.09	5.76	0.78	Confirmed
Stroma 7mm IT	3.57	3.58	1.01	5.38	0.75	Confirmed
Stroma I 2-7mm	3.41	3.46	1.09	5.32	0.70	Confirmed
Stroma 5mm ST	3.33	3.36	0.81	5.37	0.67	Confirmed
Stroma 7mm N	3.30	3.32	1.23	4.70	0.67	Confirmed
Stroma7mmT	3.20	3.20	0.76	5.19	0.62	Confirmed
Stroma Min-Max	3.29	3.32	0.26	5.38	0.62	Confirmed
Stroma9mmT	3.24	3.26	0.64	5.36	0.62	Confirmed
Stroma StdDev	3.33	3.34	0.24	6.31	0.61	Confirmed
Stroma 5mm S	3.11	3.10	-0.19	4.97	0.60	Confirmed
c: Selected features from epithelium cornea						
EPI 5mm SN-IT	12.35	12.34	10.76	14.56	1.00	Confirmed
EPI 5mm Superior-Inferior	10.10	10.13	8.05	11.85	1.00	Confirmed
EPI 5mm ST-IN	9.14	9.15	6.98	10.84	1.00	Confirmed
EPI 5mm IT	8.90	8.91	7.05	10.82	1.00	Confirmed
EPI 5mm S-I	8.92	8.95	6.62	10.79	1.00	Confirmed

Supplemental Materials I: Confirmed features from OCT by feature selection

Feature	Mean Imp	Median Imp	Min Imp	Max Imp	Norm Hits	Decision
EPI Overall StdDev	8.31	8.34	6.59	10.05	1.00	Confirmed
EPI Overall Min-Max	6.23	6.22	4.21	8.07	1.00	Confirmed
EPI Overall yMin	6.47	6.51	4.33	8.12	1.00	Confirmed
EPI 5mm I	6.03	6.06	4.38	7.85	1.00	Confirmed
EPI Overall Min	5.49	5.54	3.10	7.42	0.99	Confirmed
EPI 2mm	4.94	4.97	3.08	6.56	0.97	Confirmed
EPI Overall Min-Median	4.22	4.21	1.70	6.61	0.87	Confirmed
EPI 5mm T	4.05	4.08	1.92	6.18	0.87	Confirmed
EPI Overall Max	3.80	3.81	1.40	6.31	0.79	Confirmed
EPI Overall I 2-7mm	3.42	3.51	0.67	5.41	0.69	Confirmed
EPI 7mm IT	3.24	3.32	-0.28	5.23	0.62	Confirmed
EPI 5mm S	3.25	3.28	0.36	5.91	0.60	Confirmed

Mean Imp, mean importance; Median Imp, median importance; MinImp-MaxImp, between minimum and maximum importance; Norm Hits, fraction of random forest runs; EPI, epithelium; SD, standard deviation; T, temporal; ST, superior-temporal; S, superior; SN, superior-nasal; N, nasal; IN, inferior-nasal; I, inferior; IT, inferior-temporal

Supplemental Material II: The composite parameters and the coefficients of the PCs

Feature	PC1	PC2	PC3	PC4	PC5	PC6	PC7	PC8	PC9
Pachymetry 5mm N	0.97	0.04	0	0.04	-0.06	-0.01	0.22	-0.01	0.02
Pachymetry 5mm IN	0.96	0.2	-0.04	0.03	-0.09	0.01	0.15	0.01	-0.01
Pachymetry 5mm I	0.95	0.28	-0.06	0.02	-0.05	-0.02	0.03	0.02	-0.02
Pachymetry 5mm IT	0.96	0.24	-0.05	0.03	0.03	-0.1	-0.06	-0.01	-0.03
Pachymetry 7mm T	0.95	0	0.01	0.08	0.06	-0.16	-0.23	-0.07	-0.02
Pachymetry 7mm N	0.94	-0.03	0.02	0.04	-0.15	0.12	0.25	0	0.04
Pachymetry 7mm IT	0.94	0.24	-0.05	0.06	-0.09	-0.05	-0.19	-0.02	-0.02
Pachymetry 9mm T	0.91	-0.07	0.01	0.1	0.03	-0.09	-0.33	-0.08	0.01
Pachymetry 9mm ST	0.89	-0.29	0.06	0.03	0.16	0	-0.21	-0.01	-0.03
Pachymetry 9mm S	0.84	-0.38	0.07	-0.03	0.19	0.16	-0.06	0.11	-0.1
Pachymetry 9mm SN	0.86	-0.32	0.05	0.01	0.06	0.25	0.13	0.08	0.03
Pachymetry 9mm N	0.88	-0.06	0.02	0.05	-0.18	0.24	0.26	0.04	0.07
Pachymetry 9mm S-I	0.09	-0.69	0.17	-0.2	0.57	0.09	0.04	0.16	-0.17
Pachymetry 9mm	0.09	-0.74	0.16	-0.16	0.58	0.06	0.04	0.11	-0.1

Superior-Inferior

Supplemental Material II: The composite parameters and the coefficients of the PCs

Feature	PC1	PC2	PC3	PC4	PC5	PC6	PC7	PC8	PC9
Pachy Overall Min	0.96	0.2	-0.05	0	0.14	-0.11	0.09	0.02	0
Pachy Overall yMin	0.15	0.59	-0.15	-0.21	-0.18	0.39	-0.2	0.44	-0.11
Pachy Overall Median	0.99	0.07	-0.01	0.05	0.03	-0.09	0.06	-0.02	0
Pachy Overall Min-Med	-0.04	0.66	-0.23	-0.24	0.54	-0.08	0.13	0.19	0.01
Pachy Overall Min-Max	-0.13	0.87	-0.23	-0.18	0.23	-0.14	0.05	0.07	-0.04
Pachy Overall StdDev	0.15	-0.86	0.23	0.15	-0.26	0.16	0.03	-0.07	0.07
Pachy Overall 2-5mm	0.95	0.28	-0.06	0.02	-0.05	-0.02	0.03	0.02	-0.02
EPI 2mm	0.18	0.42	0.73	0.19	0.22	0.05	0.02	0.1	0.15
EPI 5mm T	0.12	0.38	0.78	0.25	0.16	-0.01	-0.03	0.05	0.1
EPI 5mm S	-0.01	0.34	0.63	0.64	0.14	0.06	0	0.11	0.05
EPI 5mm I	0.2	0.45	0.82	0.01	0.08	0.15	-0.01	-0.03	0.02
EPI 5mm IT	0.21	0.48	0.8	0	0.17	0.12	-0.05	0.03	0.07
EPI 7mm IT	0.1	0.35	0.85	0.13	0.02	0.04	-0.02	-0.08	-0.03
EPI 5mm SN-IT	-0.26	-0.27	-0.22	0.74	-0.14	-0.12	0.13	0.09	0.01
EPI 5mm S-I	-0.29	-0.2	-0.35	0.8	0.06	-0.13	0.01	0.19	0.04
EPI 5mmST-IN	-0.19	-0.17	-0.23	0.72	0.17	-0.21	-0.09	0.25	0.09
EPI 5mm Sup-Inf	-0.28	-0.25	-0.29	0.84	0.03	-0.17	0.03	0.19	0.05
EPI Overall Min	0.04	0.55	0.16	0.48	0.33	0.48	-0.02	-0.26	-0.03
EPI Overall yMin	0.19	0.05	0.17	-0.45	0.08	-0.17	-0.1	0.13	0.76
EPI Overall Min-Median	-0.07	0.24	-0.64	0.21	0.27	0.49	-0.05	-0.3	-0.06
EPI Overall Max	0.02	0.25	0.85	0.27	-0.07	-0.05	0.03	-0.04	-0.18
EPI Overall Min-Max	0.01	0.23	-0.68	0.16	0.35	0.47	-0.05	-0.19	0.15
EPI Overall StdDev	-0.01	-0.17	0.7	-0.22	-0.37	-0.38	0.09	0.08	-0.24
EPI Overall 2-7mm	0.12	0.38	0.85	0.11	0.02	0.09	0.02	-0.11	-0.03
Stroma 2mm	0.97	0.06	-0.11	0.02	0.06	-0.15	0.1	-0.03	-0.02
Stroma 5mm T	0.96	0.03	-0.1	0.04	0.09	-0.2	-0.08	-0.06	-0.04
Stroma 5mm ST	0.95	-0.14	-0.04	0.03	0.11	-0.19	-0.03	-0.07	-0.01
Stroma 5mm S	0.96	-0.19	-0.02	0.01	0.07	-0.12	0.05	-0.05	0.01
Stroma 5mm N	0.97	0	-0.09	0.01	-0.06	-0.02	0.21	-0.01	0.01
Stroma 5mm IN	0.96	0.16	-0.13	0.02	-0.1	-0.01	0.14	0.01	-0.01
Stroma 5mm I	0.95	0.23	-0.16	0.02	-0.06	-0.04	0.03	0.03	-0.02
Stroma 5mm IT	0.96	0.19	-0.15	0.03	0.01	-0.12	-0.06	-0.01	-0.04
Stroma 7mm T	0.95	-0.03	-0.07	0.05	0.05	-0.16	-0.23	-0.07	-0.02
Stroma 7mm N	0.94	-0.06	-0.06	0.01	-0.15	0.11	0.24	0	0.04
Stroma 7mm IT	0.94	0.2	-0.14	0.05	-0.09	-0.06	-0.19	-0.01	-0.01

Supplemental Material II: The composite parameters and the coefficients of the PCs

Feature	PC1	PC2	PC3	PC4	PC5	PC6	PC7	PC8	PC9
Stroma 9mm T	0.91	-0.09	-0.05	0.07	0.02	-0.1	-0.32	-0.07	0.01
Stroma 9mm ST	0.89	-0.31	0.04	-0.01	0.15	-0.04	-0.21	0.01	-0.02
Stroma 9mm S	0.84	-0.41	0.05	-0.07	0.17	0.13	-0.06	0.13	-0.07
Stroma 9mm SN	0.86	-0.35	0.03	-0.04	0.05	0.22	0.14	0.09	0.05
Stroma 9mm N	0.89	-0.09	-0.03	0.02	-0.19	0.22	0.26	0.04	0.07
Stroma 5mm S-I	0.04	-0.84	0.28	-0.02	0.27	-0.17	0.04	-0.14	0.07
Stroma 9mm Sup-Inf	0.1	-0.74	0.21	-0.18	0.56	0.02	0.06	0.11	-0.07
Stroma OverallMin	0.96	0.15	-0.15	0	0.11	-0.12	0.09	0.01	-0.02
Stroma yMin	0.12	0.64	-0.19	-0.13	-0.25	0.35	-0.21	0.42	-0.1
Stroma Min-Median	-0.21	0.64	-0.24	-0.11	0.52	-0.27	0.25	0.09	-0.06
Stroma Min-Max	-0.21	0.82	-0.26	-0.02	0.13	-0.29	0.12	-0.15	0
Stroma StdDev	0.26	-0.81	0.26	0	-0.2	0.33	-0.05	0.05	0.09
Stroma I 2-7mm	0.94	0.24	-0.16	0.04	-0.14	0.01	-0.01	0.03	0
Proportion Variation	0.47	0.16	0.12	0.06	0.05	0.04	0.02	0.02	0.01
Cumulative Variation	0.47	0.63	0.76	0.82	0.87	0.90	0.92	0.94	0.95

PC, principal component; EPI, epithelium; SD, standard deviation; T, temporal; ST, superior-temporal; S, superior; SN, superior-nasal; N, nasal; IN, inferior-nasal; I, inferior; IT, inferior-temporal

New OCT-Based KC Diagnostic Index

The MLR with stepwise inclusion, based on the training database, created the **WISE** index with the following formula to distinguish the normal eyes from FFKC and EKC eyes:

$$WISE = EXP(\alpha) / [1 + EXP(\alpha)]$$

where

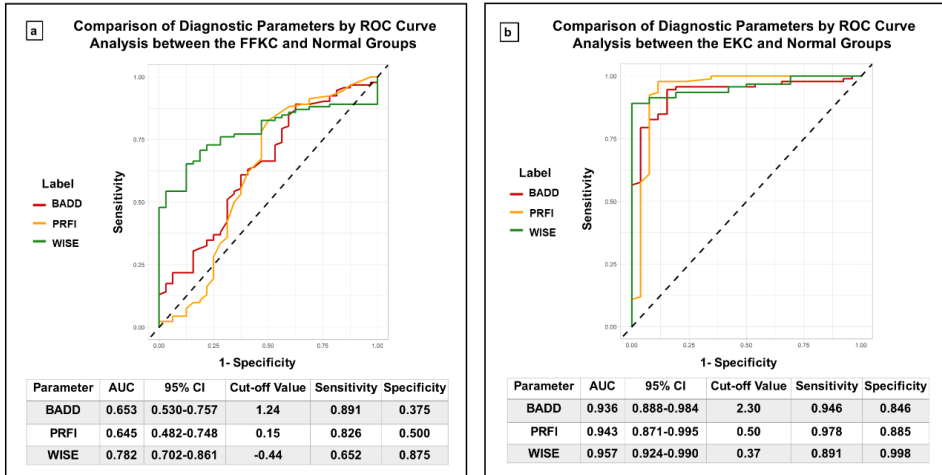
$$\alpha = -0.4771706 - 0.1775261 \times PC1 + 0.1577272 \times PC2 + 0.1937721 \times PC4 - 0.4417837 \times PC5 + 0.4560705 \times PC6 + 0.3411148 \times PC8$$

All coefficients in the formula were statistically significant (all $P < 0.01$).

Diagnostic Parameters' Comparisons

In the validation dataset, WISE was compared with the existing KC diagnostic parameters using ROC curves, AUC, sensitivity, and specificity (**Figure 2**). For the results of the DeLong's test, WISE has a similar diagnostic ability as BADD

Figure 2: Comparisons of diagnostic parameters by Receiver Operating Characteristic (ROC) curve analysis between the (a) FFKC and (b) EKC with the Normal groups



FFKC, forme fruste keratoconus; EKC, early keratoconus; AUC, area under the curve; CI, confidence intervals; BADD, Belin-Ambrósio deviation index; PRFI, Pentacam Random Forest Index; WISE, current new OCT-based index

to discriminate FFKC and EKC patients from normal controls ($P = 0.058$ and 0.462 , respectively). WISE also had an equivalent diagnostic ability as PRFI at $P = 0.060$ and 0.725 for FFKC and EKC, respectively.

DISCUSSION

This study established a comprehensive OCT-based KC diagnostic index with the assistance of AI. This new OCT-based KC diagnostic index, called WISE, includes stromal and epithelial information that may be more sensitive to the early internal remodeling of the cornea due to KC. We used machine-derived OCT-based parameters accurately detect AKC eyes, EKC with a decreased accuracy, and FFKC with a low accuracy. These results agree with previous studies' findings, as well as clinical experience, that no single SD-OCT parameter can effectively distinguish between early-stage KC and normal eyes

14, 25, 26

A literature review identified seven studies that applied only AS-OCT parameters to detect KC in its early stages (**Table 3**), including five original studies and the two validation studies ^{27, 28}. In the original studies, Temstet and Li noted the importance of epithelial distribution remodeling for early-stage KC diagnosis ^{11, 12}, while Pavlatos *et al.* suggested that the position of thinnest point between corneal layers was especially important ¹³, though that the repeatability still requires verification. Toprak and Yang *et al.* identified the parameters with the highest diagnostic ability for KC based on ROC curves, including pachymetric minimum thickness, pachymetric min-med, pachymetric SN-IT, epithelial SN-IT, and epithelial standard deviation, and applied the logistic regression and decision-tree to further improve the diagnostic ability ^{14, 15}.

Although these studies provide valid ideas to apply OCT in the early diagnosis of KC, they have several limitations in common. First, all focused on exacting those parameters deemed useful while discarding the diagnostic information that might be contained in the other parameters. Keratoconic remodeling patterns are influenced by the size and location of keratoconus, KC stage, and corneal thickness distribution. Individual parameters may only partially interpret such corneal remodeling characteristics, so a combination like the principal components used here may be preferred. In addition, the number of early-stage KC eyes included in those studies was low and the inclusion criteria for early-stage KC varied, limiting the accuracy of their analyses. To mitigate these issues, the inclusion criteria of FFKC and EKC in this work were consistent with the current most widely adopted definition, and WISE was developed using a large number of FFKC and EKC eyes, while incorporating diagnostic characteristics of all meaningful parameters through feature selection and PCA.

The WISE index obtained a high diagnostic ability comparable to those of BADD and PRFI but had the highest specificity ability to diagnose FFKC and EKC. Although the algorithms of BADD and PRFI are proprietary, the literature suggests it includes information on the corneal thickness, elevation and posterior surface ^{6, 21}. The latter two were not included in the WISE index, which may suggest that corneal elevation and posterior surface information does not

Table 3: Recent studies using AS-OCT to Diagnose the early-stage KC eyes

Lead Author and Year	OCT Devices (Analyzed Parameters)	Eyes Included	AI Application	Performance
Temstet <i>et al.</i> 2015 ¹¹	Optovue OCT (machine-derived parameters)	36 FFKC eyes and 42 normal eyes	-	72.2% sensitivity for FFKC and 83.3% sensitivity for subclinical KC
Li <i>et al.</i> 2016 ¹²	Optovue OCT (an epithelial pattern standard deviation parameter)	50 subclinical KC eyes and 150 normal eyes	-	Highest AUC = 0.985 for subclinical KC eyes
Pavlatos <i>et al.</i> 2020 ¹³	Optovue OCT (a new established coincident thinning index)	26 FFKC eyes, 16 subclinical KC eyes, and 82 normal eyes	Repeated five-fold cross-validation	56% sensitivity for FFKC and 100% sensitivity for subclinical KC
Toprak <i>et al.</i> 2021 ¹⁴	MS-39 OCT (3 machine-derived parameters)	27 FFKC eyes, 50 subclinical KC eyes, and 66 normal eyes	Binary logistic regression	75% sensitivity and 94.3% specificity for FFKC
Yang <i>et al.</i> 2021 ¹⁵	Optovue OCT (4 machine-derived parameters)	19 FFKC eyes, 12 subclinical KC, and 54 normal eyes	Two-step decision-tree	73.7% sensitivity for FFKC
Yücekul <i>et al.</i> 2022 ²⁷	Cirrus OCT (4 machine-derived parameters)	21 subclinical KC eyes and 172 normal eyes	Two-step decision-tree	90.4% sensitivity for subclinical KC
Salomão <i>et al.</i> 2023 ²⁸	Optovue OCT (an epithelial pattern standard deviation parameter)	61 VAE-NT eyes, 11 VAE-E eyes, and 101 normal eyes	-	49.1% sensitivity and 84.3% specificity for VAE-NT

AS-OCT, anterior segment optical coherence tomography; KC, keratoconus; AI: artificial intelligence; AUC, area under the curve; FFKC, forme fruste keratoconus; NN, neutral network; RF, random forest; VAE-NT, very asymmetric ectasia-normal tomography; VAE-E, very asymmetric ectasia-keratoconus

play a key role in the earlier stages KC. In addition, the training of BADD and PRFI included algorithm-based parameters to describe the morphology of the cornea, such as the maximum Ambrósio relational thickness (ART Max) ²⁹.

Meanwhile, WISE was based on either simple parameters obtained directly from OCT, or simple statistics based on the measured parameters. Including more reliable, complex parameters that describe morphological characteristics in the future, such as parameters describing the relationship between the corneal epithelium and stroma, may further improve the performance of subsequent WISE iterations.

Limitations of our study include the relatively low number of FFKC eyes considered. Although current study analyzed the largest number of FFKC patients compared to the literature, more FFKC eyes could further help to optimize the algorithm, given that this is one of the most difficult KC manifestations to detect. Moreover, the current analysis also lacks an external validation dataset, especially for ethnically diverse patient populations, as well as a validation of the capabilities of WISE on other OCT systems. Further investigation needs to be conducted in this regard.

In conclusion, this work confirmed that single OCT-based parameters have a suboptimal discriminative capacity to diagnose FFKC and EKC. The proposed WISE index largely improves the diagnostic ability for FFKC and EKC and is comparable with existing Scheimpflug-based tomographic parameters.

REFERENCES

1. Rabinowitz YS. Keratoconus. *Surv Ophthalmol* 1998;42:297-319.
2. Randleman JB, Khandelwal SS, Hafezi F. Corneal cross-linking. *Surv Ophthalmol* 2015;60:509-523.
3. Raiskup F, Herber R, Lenk J, et al. Corneal Crosslinking With Riboflavin and UVA Light in Progressive Keratoconus: Fifteen-Year Results. *Am J Ophthalmol* 2023;250:95-102.
4. Ambrósio R, Jr., Randleman JB. Screening for ectasia risk: what are we screening for and how should we screen for it? *J Refract Surg* 2013;29:230-232.
5. Asroui L, Dupps WJ, Randleman JB. Determining the Utility of Epithelial Thickness Mapping in Refractive Surgery Evaluations. *Am J Ophthalmol* 2022.
6. Lopes BT, Ramos IC, Salomão MQ, et al. Enhanced Tomographic Assessment to Detect Corneal Ectasia Based on Artificial Intelligence. *Am J Ophthalmol* 2018;195:223-232.
7. Saad A, Gatinel D. Topographic and tomographic properties of forme fruste keratoconus corneas. *Invest Ophthalmol Vis Sci* 2010;51:5546-5555.
8. Li Y, Tan O, Brass R, Weiss JL, Huang D. Corneal epithelial thickness mapping by Fourier-domain optical coherence tomography in normal and keratoconic eyes. *Ophthalmology* 2012;119:2425-2433.
9. Roberts CJ, Dupps WJ, Jr. Biomechanics of corneal ectasia and biomechanical treatments. *J Cataract Refract Surg* 2014;40:991-998.
10. Reinstein DZ, Archer TJ, Gobbe M. Corneal epithelial thickness profile in the diagnosis of keratoconus. *J Refract Surg* 2009;25:604-610.
11. Temstet C, Sandali O, Bouheraoua N, et al. Corneal epithelial thickness mapping using Fourier-domain optical coherence tomography for detection of forme fruste keratoconus. *J Cataract Refract Surg* 2015;41:812-820.
12. Li Y, Chamberlain W, Tan O, Brass R, Weiss JL, Huang D. Subclinical keratoconus detection by pattern analysis of corneal and epithelial thickness maps with optical coherence tomography. *J Cataract Refract Surg* 2016;42:284-295.
13. Pavlatos E, Chen S, Yang Y, Wang Q, Huang D, Li Y. A Coincident Thinning Index for Keratoconus Identification Using OCT Pachymetry and Epithelial Thickness Maps. *Journal of Refractive Surgery* 2020;36:757-765.
14. Toprak I, Vega A, Alió Del Barrio JL, Espla E, Cavas F, Alió JL. Diagnostic Value of Corneal Epithelial and Stromal Thickness Distribution Profiles in Forme Fruste Keratoconus and Subclinical Keratoconus. *Cornea* 2021;40:61-72.
15. Yang Y, Pavlatos E, Chamberlain W, Huang D, Li Y. Keratoconus detection using OCT corneal and epithelial thickness map parameters and patterns. *J Cataract Refract Surg* 2021;47:759-766.

16. Rabinowitz YS, Yang H, Brickman Y, et al. Videokeratography database of normal human corneas. *Br J Ophthalmol* 1996;80:610-616.
17. Lu N-J, Elsheikh A, Rozema JJ, et al. Combining Spectral-Domain OCT and Air-Puff Tonometry Analysis to Diagnose Keratoconus. *Journal of Refractive Surgery* 2022;38:374-380.
18. Lu N-J, Koppen C, Hafezi F, et al. Combinations of Scheimpflug tomography, ocular coherence tomography and air-puff tonometry improve the detection of keratoconus. *Contact Lens and Anterior Eye* 2023;101840.
19. Henriquez MA, Hadid M, Izquierdo L, Jr. A Systematic Review of Subclinical Keratoconus and Forme Fruste Keratoconus. *J Refract Surg* 2020;36:270-279.
20. Lu N-J, Chen D, Cui L-L, Wang L, Chen S-H, Wang Q-M. Repeatability of Cornea and Sublayer Thickness Measurements Using Optical Coherence Tomography in Corneas of Anomalous Refractive Status. *Journal of Refractive Surgery* 2019;35:600-605.
21. Ambrósio R, Jr., Nogueira LP, Caldas DL, et al. Evaluation of corneal shape and biomechanics before LASIK. *Int Ophthalmol Clin* 2011;51:11-38.
22. Kursu MB, Rudnicki WR. Feature Selection with the Boruta Package. *Journal of Statistical Software* 2010;36:1-13.
23. Sigg CD, Buhmann JM. Expectation-maximization for sparse and non-negative PCA. *Proceedings of the 25th international conference on Machine learning*. Helsinki, Finland: Association for Computing Machinery; 2008:960-967.
24. DeLong ER, DeLong DM, Clarke-Pearson DL. Comparing the areas under two or more correlated receiver operating characteristic curves: a nonparametric approach. *Biometrics* 1988;44:837-845.
25. Hwang ES, Perez-Straziota CE, Kim SW, Santhiago MR, Randleman JB. Distinguishing Highly Asymmetric Keratoconus Eyes Using Combined Scheimpflug and Spectral-Domain OCT Analysis. *Ophthalmology* 2018;125:1862-1871.
26. Vega-Estrada A, Mimouni M, Espla E, Alió Del Barrio J, Alió JL. Corneal Epithelial Thickness Intrasubject Repeatability and its Relation With Visual Limitation in Keratoconus. *Am J Ophthalmol* 2019;200:255-262.
27. Yücekul B, Dick HB, Taneri S. Systematic detection of keratoconus in OCT: corneal and epithelial thickness maps. *J Cataract Refract Surg* 2022;48:1360-1365.
28. Salomão MQ, Hofling-Lima AL, Gomes Esporcatte LP, et al. Corneal ectasia detection by epithelial pattern standard deviation from OCT. *J Cataract Refract Surg* 2023;49:190-194.
29. Jr R, Canedo A, Guerra F, et al. Novel Pachymetric Parameters Based on Corneal Tomography for Diagnosing Keratoconus. *Journal of refractive surgery (Thorofare, NJ : 1995)* 2011;27:753-758.

Chapter 4

Combining Spectral-Domain OCT and Air-puff Tonometry Analysis to Diagnose Keratoconus

Nan-Ji Lu, Ahmed Elsheikh, Jos J. Rozema, Nikki Hafezi, Ioannis M. Aslanides, Mark Hillen, Daniel Eckert, Christian Funck, Carina Koppen, Le-Le Cui, Farhad Hafezi

J Refract Surg. 2022 Jun;38(6):374-380

ABSTRACT

Purpose: To investigate the diagnostic capacity of SD-OCT combined with air-puff tonometry using artificial intelligence (AI) in differentiating between normal and KC eyes.

Methods: Patients who had either: undergone uneventful LVC with at least 3 years of stable follow-up, forme fruste keratoconus (FFKC), early keratoconus (EKC), or advanced keratoconus (AKC) were included. SD-OCT and biomechanical information from air-puff tonometry was divided into training and validation sets. AI models based on random forest (RF) or neural networks (NN) were trained to distinguish FFKC from normal eyes. Model accuracy was independently tested in FFKC and normal eyes. Receiver operating characteristic (ROC) curves were generated to determine area under the curve (AUC), sensitivity, and specificity values.

Results: 223 normal eyes from 223 patients, 69 FFKC eyes from 69 patients, 72 EKC eyes from 72 patients, and 258 AKC eyes from 258 patients were included. The top AUC ROC values (normal eyes compared with AKC and EKC) were Pentacam Random Forest Index (PRFI) (AUC=0.985 and 0.958), Tomographic and Biomechanical Index (TBI) (AUC=0.983 and 0.925), and Belin-Ambrósio Deviation Index (BAD-D) (AUC=0.981 and 0.922). When SD-OCT and air-puff tonometry data were combined, the RF AI model provided the highest accuracy with 99% AUC for FFKC (75.00% sensitivity; 94.74% specificity).

Conclusions: Currently, AI parameters accurately diagnose AKC and EKC, but have a limited ability to diagnose FFKC. AI-assisted diagnostic technology that utilizes both SD-OCT and air-puff tonometry may overcome this limitation, leading to improved management of patients with KC.

INTRODUCTION

Keratoconus (KC) is a relatively common bilateral corneal ectasia disease ¹, characterized by local biomechanical weakness with possible asymmetric binocular involvement. As the disease develops, the weakening cornea becomes increasingly unable to resist the distension caused by intraocular pressure. This may lead to the development of a cone-shaped protrusion that causes increasing myopia and irregular astigmatism. Early screening for KC is important for laser vision correction (LVC) to prevent triggering the KC pathological process in susceptible patients. In addition, the timely diagnosis with close follow-ups enables the early application of corneal cross-linking (CXL) to halt disease progression and vision loss.

Nowadays, there are three types of non-contact clinical instruments used to diagnose KC. The first type uses the Placido or Scheimpflug techniques to obtain shape parameters that include corneal curvature, thickness, and surface elevations. The second is anterior segment optical coherence tomography (AS-OCT), which provides measures of corneal epithelium thickness alongside corneal curvature and thickness ². The third is air-puff tonometry, which the pathological impact KC has on corneal biomechanical integrity. To date, most researchers have applied these methods separately to diagnose early-stage KC. Although each instrument is continually optimized through software updates, the diagnostic efficiency of each individual instrument is limited by its technical specifications. Since these methods are complementary, it would be important to consider a clinical approach that combines the contributions of multiple instrument types. To this end, Hwang *et al.* ³ recently combined AS-OCT with Scheimpflug-based tomography to detect highly asymmetric KC. However, this combination was restricted to structural diagnoses, which may not enable the full spectrum of patients with KC to be diagnosed. Indeed, others have shown using air-puff technology that corneal biomechanical strength deteriorates in patients with KC, before evidence of topographic anomalies can be observed ⁴, ⁵. In line with this finding, Ambrósio *et al.* combined Scheimpflug-based tomography with an air-puff device to detect subclinical ectasia ⁶; but the study did not record any information on the state of the epithelium. Finally, irregular

epithelial profiles can influence tomographic measurements ^{7, 8}, further highlighting the utility of using complementary techniques.

Inspired by these examples, the present study explores the diagnostic capability of combining AS-OCT with air-puff tonometry to differentiate between normal and KC corneas. If successful, the combination may provide an improved approach to diagnose early-stage and forme fruste KC.

METHODS

This diagnostic study was conducted with the approval of the Ethics Committee of the Eye Hospital of Wenzhou Medical University between 2018 June to 2021 March. The study adhered to the tenets of the Declaration of Helsinki and its statement of ethical principles guiding the conduct of medical research involving human subjects. All participants signed informed consent.

Patients Groups

This study considered four groups of volunteers: a normal/control group, a group with forme fruste KC (FFKC), a group with early-stage KC (EKC), and a group with advanced KC (AKC), each defined according to the criteria described below. Given the large correlation between the fellow eyes of healthy participants, one randomly selected eye was included per person in the normal group. For the FFKC and EKC groups, only the eye that met the inclusion criteria was analyzed. The exception was in the AKC group where the contralateral eye from the FFKC and EKC patients were included if they meet the AKC group criteria.

The volunteers in the normal group were recruited from patients presenting for LVC in the Eye Hospital of Wenzhou Medical University, using the inclusion criteria of no ocular or systemic abnormalities, no ocular surgery history, a stable corrected distance visual acuity (CDVA) \geq 20/20 for 2 years before surgery and a 3-year follow-up after LVC to exclude those with no clinical or tomographic signs of iatrogenic ectasia ⁹.

The diagnosis of KC required at least 1 slit-lamp finding (Fleischer ring, Vogt striae or central thinning) and 2 signs of KC on Scheimpflug topography (Pentacam HR, Oculus Optikgeräte, Wetzlar, Germany), such as decreased thinnest pachymetry, skewed asymmetric bowtie/inferior steep [SAB/IS] or increased inferior steepness.

For the FFKC group, the inclusion criteria were: 1) the contralateral eye was diagnosed with KC according to the criteria above, 2) best CDVA $\geq 20/20$, 3) no KC signs in the slit-lamp, 4) $K_{\max} < 47.4$ D, 5) thinnest pachymetry ≥ 480 μm obtained in Pentacam HR, and 6) “normal” topography with the difference between the K_{\max} values in the inferior and superior areas at 3 mm (I-S value) < 1.4 D, no AB/IS, and keratoconus percentage index (KISA%) < 60 .

The inclusion criteria for the EKC group were based on severity 1 in the Amsler-Krumeich classification of KC: 1) $K_{\max} < 48.5$ D and smallest thickness > 480 μm , 2) best CDVA $\geq 16/20$, and 3) no central scars and fewer than two slit-lamp findings.

Finally, the AKC group included all those keratoconic eyes with parameters exceeding the criteria of the FFKC and EKC groups (*i.e.*, $K_{\max} \geq 48.5$ D, smallest thickness < 480 μm , best CDVA $< 16/20$, with at least one slit-lamp finding).

Data Acquisition and Evaluated Parameters

Participants were asked to discontinue wearing soft contact lenses for at least 2 weeks before the examination, or at least 4 weeks of rigid gas-permeable contact lenses wear.

Pentacam HR Scheimpflug Topography Data

In order to classify the patients, tomography measurements were obtained with a Pentacam HR (Oculus Optikgeräte, Wetzlar, Germany, software version 1.21r59). Only eyes with a good quality score were considered, using the following parameters to assign the eyes to a severity group: K_1 , K_2 , K_{\max} ,

thinnest pachymetry, the difference between average inferior and superior corneal powers within 3 mm from the corneal center (IS-Value), and two artificial intelligence (AI) parameters - the Belin-Ambrósio deviation index (BADD) and the Pentacam Random Forest Index (PRFI). The Pentacam data were only used for the initial classification and were not included in the feature selection or AI training.

RTVue-XR Spectral-Domain OCT Data

First, a measurement was performed with the RTVue-XR Spectral-Domain OCT (Optovue, Inc., Fremont, CA, USA), which is known to provide repeatable thickness maps of anomalous corneas ¹⁰. This provided thickness maps for the whole cornea (CT), the corneal epithelium (ET), and stroma (ST) in the central (2 mm diameter), paracentral (2 to 5 mm), midperipheral (5 to 7 mm), and peripheral regions (7 to 9 mm). In the latter three regions, the thickness was monitored in 8 equally spaced points along the median circumference of the region, including the temporal (T), superior-temporal (ST), superior (S), superior-nasal (SN), nasal (N), inferior-nasal (IN), inferior (I) and inferior-temporal (IT) positions.

Corvis ST Biomechanical Data

Finally, Corvis ST (software version 1.21r59, Oculus Optikgeräte) measurements were performed, which recorded 41 parameters in two categories: (1) independent parameters, such as intraocular pressure (IOP), biomechanically-corrected IOP (bIOP), pachymetry, and 35 dynamic corneal response (DCR) parameters. The latter group included the ratio between the central deformation and the average of peripheral deformation at either 1.0 mm or 2.0 mm from center (DA ratio 1 mm/2 mm), peripheral corneal thickness increase (Pachy Slope), the Ambrósio's relational thickness to the horizontal profile (ARTh), the reciprocal of the radius during the concave state of the cornea (integrated radius), and the stiffness parameter at first applanation (SPA1) ¹¹. (2) Three other parameters were also recorded: the Stress-Strain Index (SSI); two AI parameters - the Corvis Biomechanical Index (CBI) developed from DCR parameters, and the Tomographic and Biomechanical

Index (TBI) developed from DCR and topography parameters. Only measurements with a good quality score were considered for analysis.

Artificial Intelligence

We used R (version 4.0.4, R Foundation for Statistical Computing, Vienna, Austria; <https://www.R-project.org/>) to develop two AI models based on Random Forests (RF) and Neural Networks (NN). RF and NN are currently the two most common and efficient AI methods: RF is based on decision trees and is arranged in a random manner. After obtaining the forest, every time a new input sample enters, let each decision tree in the forest judge separately to see which category this sample should belong to, and then see which category is selected the most, predict which category this sample belongs to; NN simulates the connection and information transmission mechanism between neurons in the biological nervous system. It consists of multiple neurons (nodes) and the connections between them. Each neuron receives input from other neurons and processes the input through an activation function to produce an output. The structure of the NN can be divided into input layer, hidden layer, and output layer. The input layer receives external input data, the hidden layer is used to extract and transform data features, and the output layer produces the final prediction result.

In the current study, before the AI models were trained based on SD-OCT and/or Corvis ST, feature selection was required among the parameters exported from SD-OCT and Corvis ST using the Boruta package (Version 7.0.0)¹² for two reasons: (1) surgeons often prefer the use of minimal-optimal parameters for KC diagnosis; (2) large features slow down AI models' algorithms, particularly in NN, and will simultaneously decrease the models' best possible performance¹³.

Models

Following feature selection, RF and NN models were developed based on the selected features from SD-OCT and/or Corvis ST to distinguish the FFKC group from the normal group using the randomForest (RF, Version 4.6-14) and

neuralnet (Version 1.44.2) packages. Parameters exported from Pentacam, PRFI, TBI, and BADD were not included in the training. In brief, for the RF model, 500 decision trees were grown and combined to converge the out-of-bag error and improve the prediction performance¹⁴. For the NN model, an artificial neural network was built on multi-layers of interconnected nodes, including two hidden layers and four hidden neurons, using a supervised learning algorithm¹⁵.

Validation

The total dataset was randomly divided into a training and a validation set to determine the clinical validity of the two models and their ability to correctly analyze new data: the training data constituted 70% of the total data set and was used to train the models, whilst the remaining data formed the validation set used to evaluate the models' accuracy. The average value of the classification accuracy obtained after executing a 10-fold cross-validation was recorded.

STATISTICAL ANALYSIS

The statistical analysis was performed in SPSS (version 24; IBM Corporation, Armonk, New York, USA) and R (version 4.0.4). The normality of the data was verified using the Shapiro-Wilk test. Descriptive statistics were presented as mean \pm standard deviation. For continuous variables, analysis of variance (ANOVA) and Kruskal-Wallis H test were conducted to analyze the differences between the four groups, and post-hoc tests were performed with a Bonferroni correction. The 95% confidence intervals (CI) were calculated by the Binomial exact. A value of $P < 0.05$ was considered statistically significant for all tests. To determine the optimal cut-off values, sensitivity, and specificity, we used receiver operating characteristic (ROC) curves and area under the curve (AUC) as accuracy measures. Whereas an AUC value of 1.0 indicates perfect discrimination, values of 0.5 or less show that the assessed parameter has no diagnostic ability. Values between 0.5 and 1.0 refer to a significant difference between the distributions of the considered variables in the compared groups. The top 10 AUC values and existing AI parameters' ROC result of all compared groups were taken and sorted from high to low.

RESULTS

Demographics

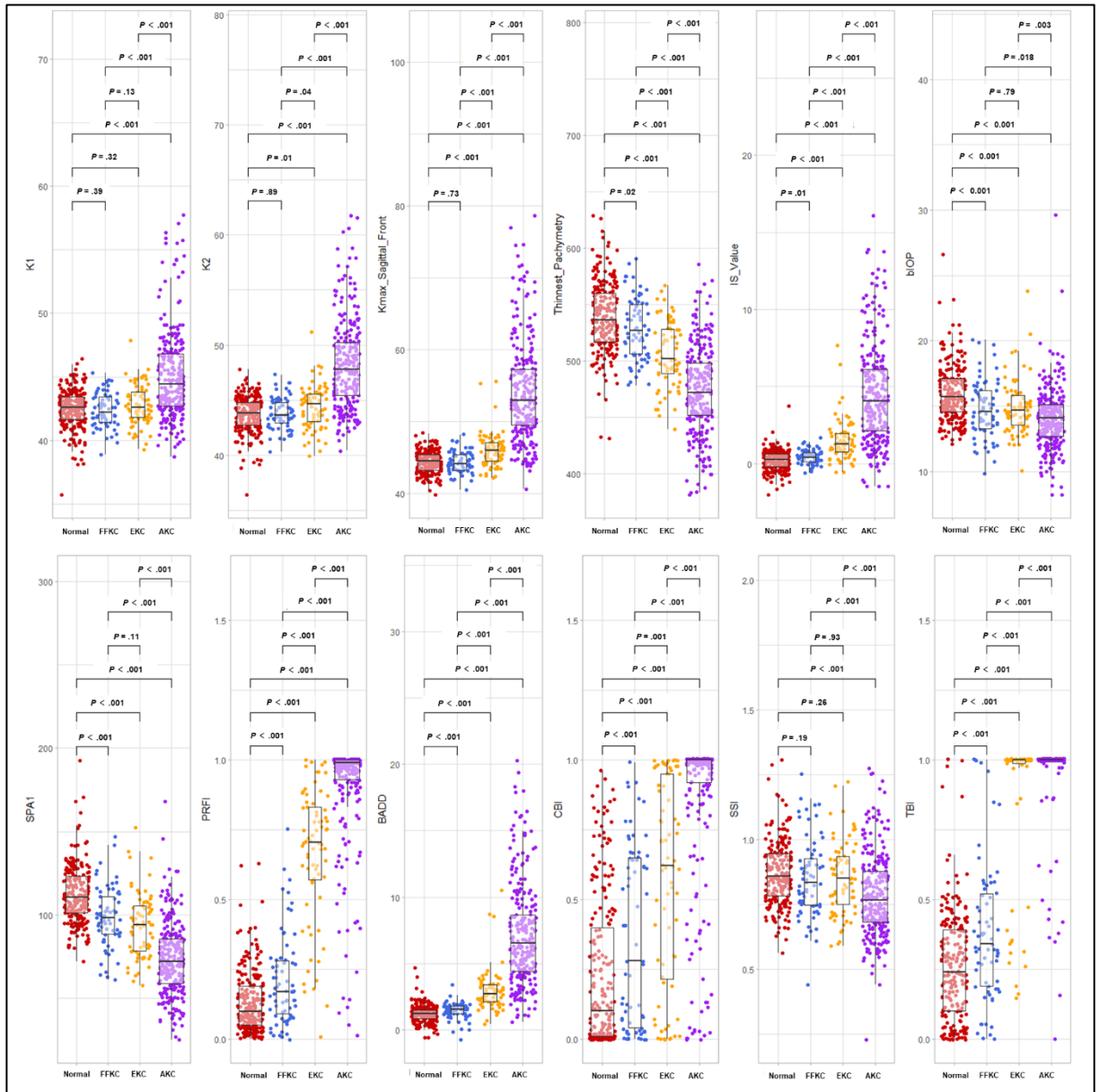
This retrospective study included 622 eyes of 481 patients for whom the demographic information is shown in **Table 1**; and the parameter distributions and comparisons between groups are shown in **Figure 1**. There were significant age differences between groups ($P = 0.017$), especially between the FFKC and normal groups, and the FFKC and AKC groups ($P = 0.004$ and 0.005 , respectively). There were no significant differences in sex distribution and OD:OS ratios (both $P > 0.05$) between the groups.

Table 1: Basic demographic information

	Unit	Normal	FFKC	EKC	AKC
Number	(OD/OS)	110/113	36/33	35/37	128/130
Age	Years	22.07 ± 6.32	24.55 ± 5.34	23.25 ± 6.86	22.19 ± 6.18
Gender	(M/F)	111/112	34/35	38/34	132/126
K_{max}	Diopter	44.38 ± 1.48	44.35 ± 1.47	46.08 ± 2.41	54.14 ± 7.07
Thinnest Pachymetry	µm	538.64 ± 31.20	528.64 ± 27.62	506.68 ± 29.13	473.71 ± 38.38
IS-Value	Diopter	0.21 ± 0.66	0.42 ± 0.46	1.52 ± 1.36	4.45 ± 3.25
bIOP	mmHg	15.95 ± 2.11	14.76 ± 2.20	14.93 ± 2.10	14.07 ± 2.34
SPA1	mmHg/mm	112.29 ± 17.10	98.64 ± 17.66	93.94 ± 19.26	73.31 ± 21.63
PRFI		0.13 ± 0.11	0.21 ± 0.16	0.66 ± 0.24	0.91 ± 0.19
BADD		1.18 ± 0.65	1.42 ± 0.63	2.94 ± 1.60	7.14 ± 3.79
CBI		0.23 ± 0.27	0.36 ± 0.32	0.56 ± 0.37	0.87 ± 0.27
SSI		0.87 ± 0.12	0.85 ± 0.15	0.85 ± 0.14	0.78 ± 0.16
TBI		0.26 ± 0.19	0.38 ± 0.26	0.87 ± 0.27	0.97 ± 0.13

FFKC, forme fruste keratoconus; EKC, early keratoconus; AKC, advanced keratoconus; IS-Value, the difference between average inferior and superior corneal powers 3 mm from the center of the cornea; bIOP, Biomechanically Corrected Intraocular Pressure; SPA1, stiffness parameter at first applanation; PRFI, Pentacam Random Forest Index; BADD, Belin-Ambrósio Deviation Index; CBI, Corvis Biomechanical Index; SSI, Stress-Strain Index; TBI, Tomographic and Biomechanical Index

Figure 1: The distributions and comparisons of patients' demographic characteristics among all groups



FFKC, forme fruste keratoconus; EKC, early keratoconus; AKC, advanced keratoconus; PRFI, the Pentacam random forest index; BADD, the Belin-Ambrósio deviation index; CBI, the Corvis biomechanical index; SSI, Stress-Strain Index; TBI, the tomographic and biomechanical index

ROC Analysis

The 10 highest-ranked parameters according to their AUC among those obtained from the SD-OCT (marked with ※), Corvis ST, and Pentacam (only PRFI, BADD, and TBI related with Pentacam) are shown in **Table 2** for the comparisons of the normal group with the three KC groups. In comparing the normal group with the AKC and EKC groups, the top three AUC ROC ranked parameters were the same in sequence: PRFI (AUC = 0.985 and 0.958, respectively), TBI (AUC = 0.983 and 0.925), and BADD (AUC = 0.981 and 0.922). When comparing the normal group with the FFKC group, the best AUC ROC greatly declined, and the top three AUC ROC ranked parameters switched from PRFI, TBI, and BADD to the following independent DCR parameters: A2_Deflection_Amp (AUC = 0.761), A2_Deflection_Area (AUC = 0.755), and A2_Deflection_Length (AUC = 0.701).

Table 2: The top 10 AUC parameters in all compared groups

Variable	AUC	95% CI	Cut-off Value	Sn	Sp
A: The Normal group vs. The AKC group					
PRFI	0.985	0.974-0.997	0.410	0.982	0.957
TBI	0.983	0.971-0.995	0.595	0.969	0.965
BADD	0.981	0.970-0.993	2.350	0.978	0.946
CBI	0.934	0.911-0.957	0.835	0.969	0.821
EPIOverallStdDev ※	0.906	0.879-0.932	2.665	0.834	0.833
Integrated_Radius_mm ⁻¹	0.880	0.850-0.911	10.480	0.883	0.755
Max_InverseRadius_mm ⁻¹	0.878	0.847-0.909	0.202	0.897	0.743
DA_Ratio_Max_2mm	0.877	0.846-0.908	5.170	0.951	0.685
PachyemtryOverallStdDev ※	0.863	0.831-0.896	22.075	0.848	0.774
EPI5mmSNIT ※	0.851	0.815-0.887	1.625	0.924	0.735
B: The Normal group vs. The EKC group					
PRFI	0.958	0.927-0.990	0.365	0.960	0.861
TBI	0.925	0.884-0.965	0.750	0.978	0.819
BADD	0.922	0.881-0.963	1.875	0.897	0.847
EPI5mmSNIT ※	0.761	0.690-0.832	1.325	0.901	0.597
CBI	0.758	0.687-0.829	0.465	0.798	0.639
EPI5mmSuperiorInferior ※	0.721	0.646-0.797	-0.130	0.767	0.583
Def_Amp_Max_mm	0.719	0.649-0.789	1.066	0.619	0.736

Table 2: The top 10 AUC parameters in all compared groups

Variable	AUC	95% CI	Cut-off Value	Sn	Sp
HC_Deformation_Amp_mm	0.719	0.649-0.789	1.066	0.619	0.736
EPI5mmSI ※	0.711	0.632-0.789	0.625	0.870	0.500
DA_Ratio_Max_2mm	0.697	0.627-0.767	4.491	0.596	0.750
C: The Normal group vs. The FFKC group					
A2_Deflection_Amp_mm	0.761	0.685-0.836	0.134	0.830	0.667
A2_Deflection_Area_mm ⁻¹	0.755	0.680-0.831	0.332	0.812	0.667
A2_Deflection_Length_mm	0.701	0.630-0.772	3.006	0.525	0.812
Def_Amp_Max_mm	0.676	0.600-0.752	1.062	0.587	0.710
HC_Deformation_Amp_mm	0.676	0.600-0.752	1.062	0.587	0.710
A2_Deformation_Amp_mm	0.674	0.604-0.744	0.373	0.475	0.783
BADD	0.654	0.579-0.729	1.465	0.740	0.580
HC_Deflection_Amp_mm	0.652	0.573-0.732	0.931	0.735	0.522
PRFI	0.652	0.575-0.729	0.165	0.717	0.536
DA_Ratio_Max_2mm	0.648	0.573-0.723	4.400	0.489	0.797
TBI	0.647	0.571-0.723	0.305	0.623	0.609
CBI	0.632	0.556-0.707	0.465	0.798	0.435

AUC, area under the curve ; CI, confidence interval; Sn, Sensitivity; Sp, specificity; AKC, advanced keratoconus; EKC, early keratoconus; FFKC, forme fruste keratoconus; PRFI, the Pentacam random forest index; TBI, the tomographic and biomechanical index; BADD, the Belin-Ambrósio deviation index; CBI, the Corvis biomechanical index; StdDev, standard deviation; EPI, epithelium; SNIT, superior-nasal minus inferior-temporal; ※, parameters obtained from OCT

Feature Selection and Artificial Intelligence Models

The results of feature selection from SD-OCT and Corvis ST are provided in **Table 3**.

For AI models' performance to discriminate between normal and FFKC eyes, based on the selected features from SD-OCT and Corvis ST, the RF and NN performed well, which far outperformed the existing clinical parameters PRFI, BADD, CBI, and TBI (**Figure 2**).

Table 3: Selected features from OCT and Corvis

Values	Mean Imp	MinImp- MaxImp	Norm Hits	Decision
A: Selected features from OCT				
EPI2mm	7.56	2.33-9.76	0.97	Confirmed
EPI5mmIT	6.56	1.35-8.54	0.95	Confirmed
EPI7mmIT	6.67	1.55-9.34	0.94	Confirmed
EPI9mmIT	6.18	0.84-8.73	0.94	Confirmed
EPI5mmT	5.31	2.03-7.45	0.91	Confirmed
EPI5mmIN	4.92	1.36-7.18	0.88	Confirmed
Pachyemtry9mmS	5.00	0.63-7.62	0.88	Confirmed
EPI7mmI	5.20	-0.09-7.63	0.87	Confirmed
EPI9mmT	4.43	0.57-6.89	0.83	Confirmed
EPIOverall.2.7mm.	4.50	0.55-7.67	0.82	Confirmed
EPI5mmN	4.48	0.69-6.73	0.81	Confirmed
EPI7mmT	4.42	0.46-7	0.81	Confirmed
EPI5mmSN	4.37	0.19-7.2	0.80	Confirmed
EPI5mmI	4.48	1.2-6.78	0.80	Confirmed
Stroma9mmS	4.26	1.32-6.91	0.77	Confirmed
EPI9mmN	4.09	-0.67-6.46	0.72	Confirmed
Stroma5mmST.IN	3.59	0.3-6.14	0.65	Confirmed
Pachyemtry9mmSN	3.46	0.09-5.79	0.60	Tentative
EPI9mmST.IN	3.39	0.38-6.02	0.59	Tentative
EPI5mmST.IN	3.25	0.17-6.3	0.58	Tentative
Stroma9mmSN	3.22	0.14-6.06	0.55	Tentative
EPI9mmST	3.01	-0.23-5.59	0.49	Tentative
Pachyemtry5mmST.IN	2.81	-0.25-6.27	0.45	Tentative
B: Selected features from Corvis ST				
A2_Velocity_m_s	24.59	18.97-27.53	1	Confirmed
A2_Time_ms	18.29	15.1-20.63	1	Confirmed
A1_Time_ms	10.85	8.75-12.61	1	Confirmed
A2_Deflection_Amp_mm	10.86	8.77-12.63	1	Confirmed
IOP_mmHg	8.52	6.28-10.93	1	Confirmed
SPA1	8.45	5.42-10.38	1	Confirmed
Whole_Eye_Movement_Max_ms	8.06	5.11-9.85	1	Confirmed
A2_Deflection_Area_mm1	10.11	7.38-12.16	1	Confirmed

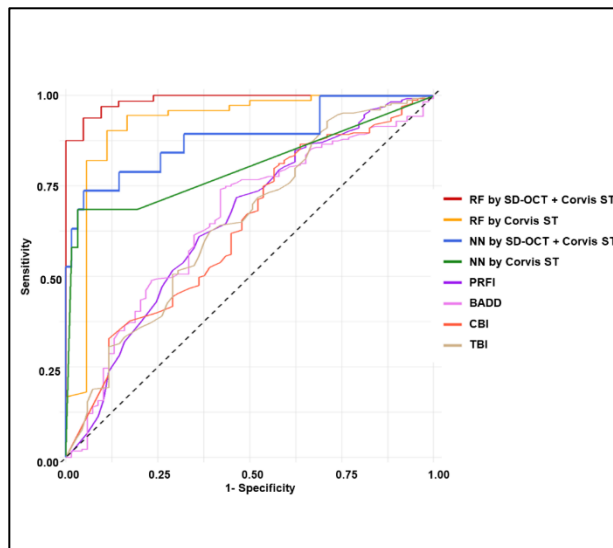
Table 3: Selected features from OCT and Corvis

Values	Mean Imp	MinImp- MaxImp	Norm Hits	Decision
blOP	7.65	5.14-9.61	1	Confirmed
HC_Deformation_Amp_mm	5.36	3.34-7.4	0.97	Confirmed
Def_Amp_Max_mm	5.35	3.01-7.55	0.97	Confirmed
HC_Deflection_Length_mm	4.67	1.67-6.99	0.91	Confirmed
A2_dArc_Length_mm	4.67	1.77-7.31	0.91	Confirmed
Peak_Dist_mm	4.39	1.95-6.82	0.89	Confirmed
Max_InverseRadius_mm..1	4.50	1.29-6.78	0.86	Confirmed
Radius_mm	3.93	0.9-6.23	0.79	Confirmed
A2_Deflection_Length_mm	3.87	0.71-6.21	0.79	Confirmed
HC_Deflection_Amp_mm	3.52	1.63-5.47	0.77	Confirmed
HC_Deflection_Area_mm1	3.46	1.77-6.8	0.74	Confirmed
DA_Ratio_Max_2mm	3.30	0.92-5.8	0.66	Confirmed
Deflection_Amp_Max_mm	3.07	0.77-5.19	0.63	Confirmed
Integrated_Radius_mm..1	3.10	0.87-5.18	0.62	Confirmed
A2_Deformation_Amp_mm	3.06	0.52-5.69	0.61	Confirmed
A1_Velocity_m_s	2.95	-0.11-5.26	0.58	Tentative
HC_dArc_Length_mm	2.58	-0.13-4.76	0.45	Tentative

OCT, optical coherence tomography; EPI, epithelium; I, inferior; S, superior; T, temporal; N, nasal

In detail, the best trained model was based on the RF by combining features from SD-OCT and Corvis ST (AUC = 0.99; 88.89% accuracy; 75.00% sensitivity; 94.74% specificity), following the RF-based model by only using Corvis ST features (AUC = 0.92; 90.00% accuracy; 72.22% sensitivity; 94.44% specificity). The performance of NN-based AI models was worse than that of RF-based AI models. However, the NN-based model that combined features from SD-OCT and Corvis ST (AUC = 0.88; 90.12% accuracy; 73.68% sensitivity; 87.10% specificity) was still better than the NN model that used the features from Corvis ST alone (AUC = 0.89; 90.12% accuracy; 63.16% sensitivity; 96.77% specificity).

Figure 2: Comparison of four artificial intelligence models and existing parameters with Receiver Operating Characteristic (ROC) curve analysis



RF, random forest; SD-OCT, Spectral-Domain optical coherence tomography; NN, neural network; PRFI, the Pentacam random forest index; BADD, the Belin-Ambrósio deviation index; SSI, the stress-strain index; CBI, the Corvis biomechanical index; TBI, the tomographic and biomechanical index

DISCUSSION

This diagnostic study represents the first attempt to innovative combine diagnostic information from SD-OCT and air-puff devices by AI to enhance clinicians' ability to detect KC and in particular, FFKC, the results were superior to using either of the devices individually.

As expected, the parameters already provided by the Pentacam, the Corvis ST, and the SD-OCT had an excellent ability to distinguish between normal and AKC corneas, reflecting normal clinical practice where they are already used to diagnose AKC using topography or tomography maps. The four most successful parameters in identifying AKC corneas were all AI parameters based on either RF (PRFI and TBI) or logistic regression (CBI and BADD), emphasizing the importance of AI-assisted KC diagnosis. The rest of the 10 best performing parameters included the overall standard deviation in epithelial

and overall corneal pachymetry thickness (obtained with SD-OCT imaging), which is compatible with the expectation that AKC corneas had undergone a major change in corneal thickness. It is worth noting that SSI, associated with the corneal material's biomechanical properties, did not appear in the list of best classifiers, which may be a confirmation of the idea that KC originates from a localized (rather than a global) decrease in corneal biomechanics ¹⁶.

In comparing the normal and the EKC groups, the three best performing parameters based on AUC were also AI parameters (PRFI, TBI, and BADD). Although the AUC values were lower than for the comparison with the AKC group, they still showed an outstanding diagnostic ability (**Table 2**). For the other parameters, the AUC was considerably lower compared to PRFI, TBI, and BADD, again confirming the importance of AI parameters. Further, the SD-OCT data showed a regional epithelial remodeling (**Table 2**), reported earlier by Silverman *et al.* ¹⁷, confirming epithelial thickness (ET) redistribution as one of the most critical AS-OCT parameters for detecting early-stage KC.

Finally, for discriminating between the normal and FFKC groups, a dramatic decrease in AUC was observed in all parameters measured, compared with the AKC and EKC analyses. Among the 10 top-scoring AUC parameters, independent DCR parameters replaced AI parameters and occupied dominant positions. These parameters, and particularly the first 3 parameters (A2_Deflection_Amp, A2_Deflection_Area, and A2_Deflection_Length), were more focused on the second applanation event, and were not independent variables that formed parts of the CBI and TBI. When compared with the DCR parameters, the tomographic parameters derived from OCT were less important, suggesting that the biomechanical change that takes place in KC occurs earlier than its morphological change in line with earlier literature ⁵. The BADD and PRFI, based on corneal tomography, are also relevant morphological parameters with some degree of ability to diagnose FFKC.

A literature review conducted by the authors of the present study identified six recent studies that focused on the detection of early-stage KC (including

subclinical KC, EKC, and FFKC) by various AI models (**Table 4**). Analysis of these studies identified several limitations. First, the number of early-stage KC eyes included was limited, especially for FFKC eyes; indeed, in three studies¹⁸⁻²⁰ no FFKC eyes were included. In another study by Xie *et al.*²¹, although a large number of EKC eyes were included, the EKC inclusion criteria were ambiguous. In addition, the inclusion criteria across studies were inconsistent,

Table 4: Recent studies using AI to differentiate subclinical KC and FFKC from normal eyes

Lead author and year	Devices (analyzed form)	Eyes Included	Algorithm Used	Performance
Cao et al. 2020 ¹⁸	Pentacam (parameters)	49 subclinical KC eyes, 39 control eyes	Eight different Algorithms	Highest AUC=0.97 with 89% precision by RF;
Shi et al. 2020 ¹⁹	Combine Pentacam and laboratorial UHR-OCT (parameters)	38 KC eyes, 33 subclinical KC eyes, and 50 normal eyes	NN	Highest AUC=0.93, 93% precision for subclinical KC eyes, and 99% precision for KC eyes by NN
Kuo et al. 2020 ²⁰	Pentacam (images)	170 KC eyes, 28 subclinical KC eyes, and 156 normal eyes	Three different convolutional NN models	Highest AUC=0.995 by ResNet152 model
Xie et al. 2020 ²¹	Pentacam (images)	389 KC eyes, 202 EKC eyes, and 1368 normal eyes	Convolutional NN	AUC=0.996 with 92% sensitivity, and 99.1% specificity for EKC
Pavlatos et al. 2020 ²²	Optovue SD-OCT (parameters)	91 KC eyes, 16 subclinical KC eyes, 26 FFKC eyes, and 82 normal eyes	Repeated five-fold cross-validation	56% sensitivity for FFKC and 100% sensitivity for subclinical KC
Toprak et al. 2021 ²³	MS-39 SD-OCT (parameters)	50 subclinical KC eyes, 27 FFKC eyes, and 66 normal eyes	Binary logistic regression	75% sensitivity and 94.3% specificity for FFKC

AI, artificial intelligence; AUC, the area under the curve; EKC, early keratoconus; FFKC, forme fruste keratoconus; KC, keratoconus; NN, neural network; OCT, optical coherence tomography; RF, random forest; SD-OCT, Spectral-Domain OCT; UHR-OCT, ultra-high-resolution OCT

making it difficult to compare the performance of the AI models used. Finally, no biomechanical information was included, which may have impacted the models' performance. To address these points, the current study included both FFKC and EKC eyes, and had the same inclusion criteria as the existing comprehensive parameters (PRFI, TBI, and CBI). In addition, both corneal structural and biomechanical information obtained from SD-OCT and Corvis ST were considered in the analyses.

Multinomial logistics regression (MLR) was not applied in the current study as MLR would delete features to get the minimal-optimal features. However, since MLR cannot optimally handle the relationship between the deleted and the reserved features, this process can result in a decrease in the model's performance. One limitation of this study was the relatively small size of the FFKC group due to the strict inclusion criteria. Since a larger FFKC patient's population may improve the performance of the AI models, we continue to search for more FFKC patients for future analyses.

In conclusion, this study confirms that earlier AI diagnostic tools that relied on PRFI, TBI, and BADD could accurately diagnose AKC and EKC patients, but struggle to diagnose FFKC patients. In contrast, the current Random Forest implementation combined corneal shape features obtained through SD-OCT with the biomechanical parameters of the air-puff device, which greatly improves healthcare professionals' ability to diagnose FFKC, leading to an overall improvement in the management of KC patients.

REFERENCES

1. Torres-Netto E, al-otaibi W, Hafezi N, et al. Prevalence of keratoconus in paediatric patients in Riyadh, Saudi Arabia. *British Journal of Ophthalmology* 2018;102:bjophthalmol-2017.
2. Li Y, Tan O, Brass R, Weiss JL, Huang D. Corneal epithelial thickness mapping by Fourier-domain optical coherence tomography in normal and keratoconic eyes. *Ophthalmology* 2012;119:2425-2433.
3. Hwang ES, Perez-Straziota CE, Kim SW, Santhiago MR, Randleman JB. Distinguishing Highly Asymmetric Keratoconus Eyes Using Combined Scheimpflug and Spectral-Domain OCT Analysis. *Ophthalmology* 2018;125:1862-1871.
4. Vinciguerra R, Ambrósio R, Elsheikh A, et al. Detection of Keratoconus With a New Biomechanical Index. *Journal of refractive surgery (Thorofare, NJ : 1995)* 2016;32:803-810.
5. Vinciguerra R, Ambrosio R, Jr., Roberts CJ, Azzolini C, Vinciguerra P. Biomechanical Characterization of Subclinical Keratoconus Without Topographic or Tomographic Abnormalities. *Journal of refractive surgery (Thorofare, NJ : 1995)* 2017;33:399-407.
6. Jr R, Lopes B, Faria-Correia F, et al. Integration of Scheimpflug-Based Corneal Tomography and Biomechanical Assessments for Enhancing Ectasia Detection. *Journal of Refractive Surgery* 2017;33:434-443.
7. Wardani M, Hashemi K, Aliferis K, Kymionis G. Topographic changes simulating keratoconus in patients with irregular inferior epithelial thickening documented by anterior segment optical coherence tomography. *Clinical Ophthalmology* 2019;Volume 13:2103-2110.
8. Reinstein DZ, Archer TJ, Gobbe M. Corneal epithelial thickness profile in the diagnosis of keratoconus. *Journal of refractive surgery (Thorofare, NJ : 1995)* 2009;25:604-610.
9. Vinciguerra R, Ambrósio RJ, Elsheikh A, et al. Detection of Post-Laser Vision Correction Ectasia with a new Combined Biomechanical Index. *Journal of Cataract & Refractive Surgery* 2021;Publish Ahead of Print.
10. Lu NJ, Chen D, Cui LL, Wang L, Chen SH, Wang QM. Repeatability of Cornea and Sublayer Thickness Measurements Using Optical Coherence Tomography in Corneas of Anomalous Refractive Status. *Journal of refractive surgery (Thorofare, NJ : 1995)* 2019;35:600-605.
11. Roberts CJ, Mahmoud AM, Bons JP, et al. Introduction of Two Novel Stiffness Parameters and Interpretation of Air Puff-Induced Biomechanical Deformation Parameters With a Dynamic Scheimpflug Analyzer. *Journal of refractive surgery (Thorofare, NJ : 1995)* 2017;33:266-273.
12. Kursa MB, Rudnicki WR. Feature selection with the Boruta package. *J Stat Softw*

- 2010;36:1-13.
13. Kohavi R, John GH. Wrappers for feature subset selection. *Artificial Intelligence* 1997;97:273-324.
 14. Liaw A, Wiener M. Classification and Regression by RandomForest. *Forest* 2001;23.
 15. Günther F, Fritsch S. neuralnet: Training of Neural Networks. *R Journal* 2010;2.
 16. Roberts CJ, Dupps WJ, Jr. Biomechanics of corneal ectasia and biomechanical treatments. *Journal of cataract and refractive surgery* 2014;40:991-998.
 17. Silverman RH, Urs R, Roychoudhury A, Archer TJ, Gobbe M, Reinstein DZ. Epithelial remodeling as basis for machine-based identification of keratoconus. *Investigative ophthalmology & visual science* 2014;55:1580-1587.
 18. Cao K, Verspoor K, Sahebjada S, Baird PN. Evaluating the Performance of Various Machine Learning Algorithms to Detect Subclinical Keratoconus. *Translational vision science & technology* 2020;9:24.
 19. Shi C, Wang M, Zhu T, et al. Machine learning helps improve diagnostic ability of subclinical keratoconus using Scheimpflug and OCT imaging modalities. *Eye and vision (London, England)* 2020;7:48.
 20. Kuo B-I, Chang W-Y, Liao T-S, et al. Keratoconus Screening Based on Deep Learning Approach of Corneal Topography. *Translational Vision Science & Technology* 2020;9:53-53.
 21. Xie Y, Zhao L, Yang X, et al. Screening Candidates for Refractive Surgery With Corneal Tomographic-Based Deep Learning. *JAMA Ophthalmol* 2020;138:519-526.

Chapter 5

Combinations of Scheimpflug Tomography, Ocular Coherence Tomography and Air-puff Tonometry Improve the Detection of Keratoconus

Nan-Ji Lu, Carina Koppen, Farhad Hafezi, Sorcha Ní Dhubhghaill, Ioannis M. Aslanides, Qin-Mei Wang, Le-Le Cui, Jos J. Rozema

Cont Lens Anterior Eye. 2023 Apr 12:101840

ABSTRACT

Purpose: To determine whether combinations of devices with different measuring principles, supported by artificial intelligence (AI), can improve the diagnosis of keratoconus (KC).

Methods: Scheimpflug tomography, spectral-domain optical coherence tomography (SD-OCT), and air-puff tonometry were performed in all eyes. The most relevant machine-derived parameters to diagnose KC were determined using feature selection. The normal and forme fruste KC (FFKC) eyes were divided into training and validation datasets. The selected features from a single device or different combinations of devices were used to develop models based on random forest (RF) or neural networks (NN) trained to distinguish FFKC from normal eyes. The accuracy was determined using receiver operating characteristic (ROC) curves, area under the curve (AUC), sensitivity, and specificity.

Results: 271 normal eyes, 84 FFKC eyes, 85 early KC eyes, and 159 advanced KC eyes were included. A total of 14 models were built. Air-puff tonometry had the highest AUC for detecting FFKC using a single device (AUC = 0.801). Among all two-device combinations, the highest AUC was accomplished using RF applied to selected features from SD-OCT and air-puff tonometry (AUC = 0.902), followed by the three-device combination with RF (AUC = 0.871) with the best accuracy.

Conclusion: Existing parameters can precisely diagnose early and advanced KC, but their diagnostic ability for FFKC could be optimized. Applying an AI algorithm to a combination of air-puff tonometry with Scheimpflug tomography or SD-OCT could improve FFKC diagnostic ability. The improvement in diagnostic ability by combining three devices is modest.

INTRODUCTION

Keratoconus (KC) is a bilateral, asymmetrical disorder characterized by the steepening and thinning of the cornea, leading to an irregular astigmatism that impairs vision ¹. Early diagnosis can help surgeons monitor the disease progression and perform corneal cross-linking (CXL) early to halt progression ². It also assists screening laser vision correction (LVC) candidates for ectasia risks.

Pathophysiologically, KC is thought to start as a regional impairment of the corneal biomechanics that leads to a remodelling of the shape ³. Over the past decades, diagnostic tools have become more diverse, from Placido ring topography, which precisely measures the anterior cornea curvature, to Scheimpflug tomography, which also provides posterior surface information. Other high resolution technologies, such as very high frequency (VHF) digital ultrasound and optical coherence tomography (OCT), enabled measurements of the corneal epithelial thickness ⁴, another parameter that may assist KC diagnosis ^{5, 6}. To capture the corneal biomechanical properties, the calibrated non-contact tonometer couples with an ultra-high-speed Scheimpflug camera and thus assesses the dynamic changes in corneal deformation ⁷⁻⁹. Most devices provide parameters for KC based on regression ¹⁰⁻¹³ or artificial intelligence ^{8, 14-17}, while others have parameters that combine data from two different measuring principles ¹⁸⁻²¹, each with claims of high diagnostic capabilities.

Although tomographic and biomechanical devices are capable of capturing different properties of the cornea, it is impractical and uneconomical to use every available device to make a diagnosis. It is therefore important to determine the value of the added information needed for diagnosis, whether provided by a single device or a combination of three devices with different working principles. To this end, this study compares the diagnostic performance of a number of combinations of clinical devices and their roles in the diagnosis for various degrees of KC.

METHODS

This retrospective study, conducted between June 2018 to December 2021, was approved by the Ethics Committee of the Eye Hospital of Wenzhou Medical University and adhered to the tenets of the Declaration of Helsinki.

Patients Groups and Inclusion Criteria

This study considered four patient groups: normal controls, forme fruste KC (FFKC), early-stage KC (EKC), and advanced KC (AKC) as defined by the criteria below ²¹.

Normal controls were recruited from patients seeking LVC surgery in the Hospital, excluding those with ocular or systemic abnormalities, prior ocular surgery. Inclusion criteria were a stable corrected distance visual acuity (CDVA) $\geq 20/20$ for 2 years with normal Scheimpflug tomography (Pentacam HR, Oculus Optikgeräte, Wetzlar, Germany, software version 1.25r12) confirmed by three doctors before LVC surgery. To exclude those developing post-LVC ectasia, patients were followed for at least 3 years postoperatively. Only one randomly selected eye was included per person in the control group.

The diagnosis of KC was clinical and confirmed by three doctors, which ordinarily required at least 1 typical slit lamp finding (Fleischer ring, Vogt striae, or central thinning) and/ or at least 1 typical sign of KC on Scheimpflug tomography, such as decreased thinnest pachymetry, abnormal pachymetry distribution, skewed asymmetric bowtie/inferior steep [SAB/IS], or increased inferior steepness. For the three KC groups, only the eye with mildest impairment was included in each KC patient.

The criteria for the FFKC group were: 1) a contralateral eye diagnosed with KC, 2) best CDVA $\geq 20/20$, 3) no KC signs at slit-lamp, 4) $K_{\max} < 47.4$ diopters (D), 5) thinnest pachymetry ≥ 480 μm obtained in Pentacam HR, "normal" tomography with the difference between the K_{\max} values in the inferior and superior areas at 3 mm (I-S Value) < 1.4 D, and no SAB/IS ^{21, 22}. For the EKC group, the criteria were: 1) $K_{\max} < 48.5$ D and smallest thickness > 480 μm , 2)

best CDVA $\geq 16/20$, and 3) no central scars and fewer than two slit lamp findings. Finally, the criteria for the AKC group were KC eyes with parameters exceeding those of the FFKC and EKC groups (*i.e.*, $K_{\max} \geq 48.5$ D, smallest thickness < 480 μm , best CDVA $< 16/20$).

Data Acquisition and Evaluated Parameters

Patients were asked to discontinue soft contact lenses for at least 2 weeks before the examination, or at least 4 weeks in cases of rigid gas-permeable contact lenses wear. Patients who could not comply were eliminated from the analysis.

Scheimpflug Tomography

Tomography measurements were performed with a Pentacam HR. The machine-derived parameters were exported, including the maximum/ average/ minimum pachymetry progression ($\text{RPI}_{\text{Max/Mid/Min}}$), averaged pachymetry ($D_{0\text{mm}} - D_{10\text{mm}}$ Pachy), index of surface variance (ISV), index of vertical asymmetry (IVA), keratoconus index (KI), central keratoconus index (CKI), index of height asymmetry (IHA), and index of height decentration (IHD).

Spectral-Domain OCT

The measurement was performed with the RTVue-XR Spectral-Domain OCT (Optovue, Inc., Fremont, CA, USA) ²³. The output consists of thickness maps for the whole cornea (CT), corneal epithelium (ET), and stroma (ST) in the central (2 mm diameter), paracentral (2 to 5 mm), midperipheral (5 to 7 mm), and peripheral regions (7 to 9 mm). In the latter three regions, thickness is monitored in 8 equally spaced points along the median circumference of the region, including the temporal (T), superior-temporal (ST), superior (S), superior-nasal (SN), nasal (N), inferior-nasal (IN), inferior (I) and inferior-temporal (IT) positions.

Air-puff Tonometry

Corneal biomechanics were measured by Corvis ST (Oculus Optikgeräte, Wetzlar, Germany, software version 1.6r2503), which recorded two categories' parameters: 1) independent parameters, including intraocular pressure (IOP),

biomechanically corrected IOP (bIOP), pachymetry, and 35 dynamic corneal response (DCR) parameters; 2) Comprehensive parameters, including the stress-strain index (SSI), the Corvis biomechanical index (CBI), the Corvis biomechanical factor (CBiF), and the tomographic and biomechanical index (TBI) developed from DCR and topography parameters.

Artificial Intelligence (AI)

The R software (version 4.2.0, R Foundation for Statistical Computing, Vienna, Austria) was used to develop AI models based on Random Forests (RF) and Neural Networks (NN). Before the training of AI models, feature selection was applied to the parameters exported from Pentacam HR, RTVue-XR, and Corvis ST using the *Boruta* package (Version 7.0.0) in R ²⁴. Two categories of parameters were excluded before feature selection: 1) parameters used in the groups' classification: K_{max} , thinnest pachymetry, and I-S Value; 2) existing machine-derived parameters: the Pentacam random forest index (PRFI), Belin-Ambrósio deviation index (BADD), CBI, CBI beta, CBiF, and TBI.

Models

After feature selection, two algorithms to distinguish the FFKC group from the normal group were developed based on RF using the *randomForest* package (Version 4.6-14) and NN using the *neuralnet* package (Version 1.44.2) ^{25, 26}. For the RF model, 600 decision trees were grown and combined to converge the out-of-bag error and improve prediction performance. For the NN model, an artificial NN was built on multi-layers of interconnected nodes, including 4 hidden layers and 5 hidden neurons, using a supervised learning algorithm. In each model, specific sub-models were developed based on the selected features representing combinations of the different devices: 1) only including features from Pentacam, RTVue-XR, or Corvis ST, respectively; 2) including features from device pairs (Pentacam with RTVue-XR, or Pentacam with Corvis ST, RTVue-XR with Corvis ST); 3) all three devices.

Validation

The dataset of normal and FFKC groups was randomly divided into a training and a validation set to determine the validity of the model. The training data constituted 60% of the total dataset and was used to train the models, whilst the remaining 40% of the total dataset formed the validation dataset used to evaluate the models' accuracy. The average value of the classification accuracy obtained after executing a 10-fold cross-validation in the validation dataset was recorded.

STATISTICAL ANALYSIS

The statistical analysis was performed in R. The normality of the data was veri-

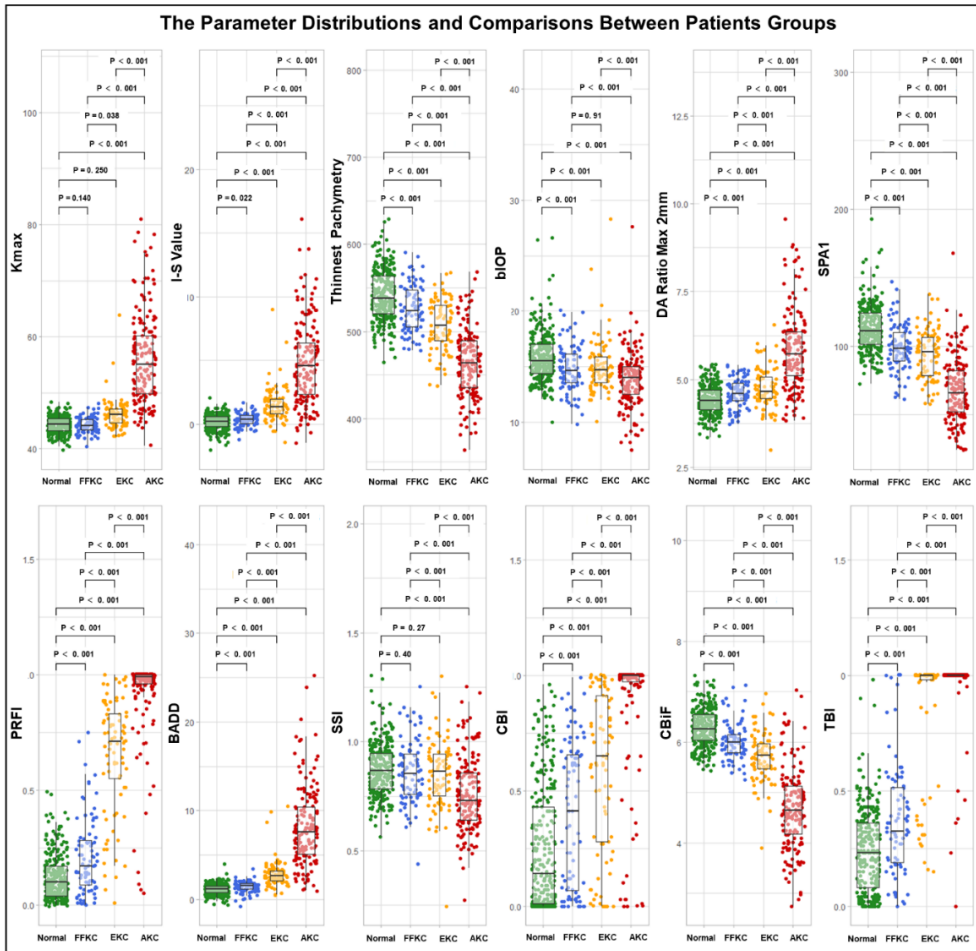
Table 1: Basic demographic information

	Unit	Normal	FFKC	EKC	AKC
Number	(OD/OS)	135/136	44/40	42/43	74/85
Gender	(M/F)	141/130	44/40	45/40	83/76
Age	Years	22.24 ± 6.05	23.58 ± 5.71	22.53 ± 7.22	21.79 ± 6.30
K _{max}	Diopter	44.33 ± 1.50	44.30 ± 1.41	46.15 ± 2.81	56.05 ± 8.11
Thinnest Pachy	µm	541.45 ± 29.19	526.46 ± 26.77	507.39 ± 29.36	463.06 ± 39.41
I-S Value	Diopter	0.19 ± 0.60	0.36 ± 0.51	1.53 ± 1.40	4.77 ± 3.22
bIOP	mmHg	15.83 ± 2.19	14.83 ± 2.09	15.03 ± 2.45	13.84 ± 2.46
DA Ratio Max 2mm	mm	4.42 ± 0.42	4.62 ± 0.41	4.76 ± 0.57	5.85 ± 1.11
SPA1	mmHg/mm	112.91 ± 17.17	99.18 ± 17.04	93.93 ± 17.99	67.91 ± 23.12
PRFI		0.12 ± 0.10	0.21 ± 0.17	0.66 ± 0.25	0.93 ± 0.18
BADD		1.12 ± 0.59	1.41 ± 0.63	2.90 ± 1.59	8.16 ± 4.39
SSI		0.87 ± 0.12	0.86 ± 0.15	0.85 ± 0.16	0.76 ± 0.17
CBI		0.25 ± 0.27	0.39 ± 0.31	0.59 ± 0.34	0.90 ± 0.26
CBiF		6.29 ± 0.38	6.03 ± 0.37	5.71 ± 0.48	4.68 ± 0.80
TBI		0.24 ± 0.18	0.38 ± 0.25	0.87 ± 0.27	0.97 ± 0.14

FFKC, forme fruste keratoconus; EKC, early keratoconus; AKC, advanced keratoconus; I-S Value, the difference between average inferior and superior corneal powers 3 mm from the center of the cornea; bIOP, biomechanically corrected intraocular pressure; DA Ratio Max 2mm, deformation amplitude measured at 2 mm from the center; SPA1, stiffness parameter at first applanation; PRFI, the Pentacam random forest index; BADD, the Belin-Ambrósio deviation index; SSI, the stress-strain index; CBI, the Corvis biomechanical index; CBiF, the Corvis biomechanical factor; TBI, the tomographic and biomechanical index

fied using the Shapiro-Wilks test. Descriptive statistics were presented as mean \pm standard deviation. Analysis of variance (ANOVA) and Kruskal-Wallis H tests were used to analyze the differences between the four groups, followed by post-

Figure 1: The distributions and comparisons of patients' demographic characteristics



I-S Value, the difference between average inferior and superior corneal powers 3 mm from the center of the cornea; biOP, biomechanically corrected intraocular pressure; DA ratio 2 mm, the ratio between the central deformation and the average of peripheral deformation at 2.0 mm from center; SPA1, stiffness parameter at first applanation; PRFI, the Pentacam random forest index; BADD, the Belin-Ambrósio deviation index; SSI, the stress-strain index; CBI, the Corvis biomechanical index; CBIF, the Corvis biomechanical factor; TBI, the tomographic and biomechanical index

hoc tests with a Bonferroni correction. The 95% confidence intervals (CI) were calculated by the binomial exact. A value of $P < 0.05$ was considered statistically significant. To determine the optimal cut-off values, sensitivity, and specificity, receiver operating characteristic (ROC) curves and area under the curve (AUC) as accuracy measures were used.

RESULTS

Demographics

Demographic information is shown in **Table 1**. The parameter distributions and comparisons between patient groups are shown in **Figure 1**. There were no significant differences in right eye/left eye ratios, sex distribution, or age among all groups ($P = 0.922, 0.999, \text{ and } 0.194$, respectively).

The Existing Parameters ROC Analysis

The comparisons of the normal group with the three KC groups, based on the parameters' AUC, TBI and the 3 highest-ranked parameters respectively obtained from Pentacam HR, RTVue-XR, and Corvis ST are listed in **Table 2**. Compared with the normal group vs. the AKC/EKC group, all parameters were far less performant in the normal group vs. the FFKC group.

Table 2: Top 3 AUC parameters from each device in the normal and KC groups

Device	Variable	AUC	95% CI	Cut-off	Sn	Sp
the Normal Group vs. the AKC Group						
Scheimpflug + tonometry	TBI	0.987	0.973-1.000	0.912	0.996	0.956
Scheimpflug	BAD-D	0.986	0.974-0.999	2.355	0.993	0.943
Scheimpflug	ISV	0.986	0.975-0.997	29.500	0.989	0.937
Scheimpflug	PRFI	0.985	0.971-0.999	0.505	1.000	0.956
SD-OCT	EPI Overall StDev	0.912	0.884-0.941	2.670	0.819	0.868
SD-OCT	EPI 5mm SN-IT	0.891	0.853-0.929	1.960	0.948	0.755
SD-OCT	Pachy Overall StDev	0.886	0.851-0.921	22.07	0.830	0.818
Tonometry	CBI beta	0.952	0.926-0.979	2.044	0.993	0.881
Tonometry	CBI	0.939	0.909-0.969	0.865	0.982	0.855
Tonometry	Max_InvRad_mm ⁻¹	0.915	0.885-0.945	0.204	0.919	0.786

Table 2: Top 3 AUC parameters from each device in the normal and KC groups

Device	Variable	AUC	95% CI	Cut-off	Sn	Sp
the Normal Group vs. the EKC Group						
Scheimpflug + tonometry	TBI	0.939	0.907-0.972	0.750	0.989	0.812
Scheimpflug	PRFI	0.957	0.927-0.988	0.365	0.974	0.847
Scheimpflug	BAD-D	0.927	0.888-0.967	1.875	0.919	0.847
Scheimpflug	RPIMax	0.887	0.842-0.933	1.555	0.911	0.765
SD-OCT	EPI 5mm SN-IT	0.765	0.703-0.827	1.325	0.904	0.553
SD-OCT	EPI 5mm Sup-Inf	0.718	0.651-0.786	-0.605	0.683	0.647
SD-OCT	EPI 5mm S-I	0.694	0.621-0.766	-0.620	0.734	0.588
Tonometry	CBI beta	0.823	0.767-0.879	0.343	0.823	0.718
Air-puff tonometry	CBI	0.774	0.712-0.837	0.463	0.771	0.682
Air-puff tonometry	DA_Ratio_Max_2mm	0.686	0.620-0.752	4.491	0.605	0.729
the Normal Group vs. the FFKC Group						
Scheimpflug + tonometry	TBI	0.665	0.598-0.733	0.265	0.561	0.679
Scheimpflug	PRFI	0.670	0.599-0.741	0.165	0.745	0.536
Scheimpflug	BAD-D	0.661	0.592-0.730	1.465	0.756	0.571
Scheimpflug	RPIMax	0.661	0.592-0.730	1.465	0.756	0.571
SD-OCT	EPI 5mm SN-IT	0.595	0.523-0.668	0.405	0.790	0.405
SD-OCT	EPI 5mm Sup-Infr	0.593	0.520-0.666	-0.605	0.683	0.500
SD-OCT	EPI 5mm S-I	0.575	0.502-0.647	-2.570	0.413	0.738
Tonometry	A2_Defl_Amp_mm	0.734	0.668-0.801	0.133	0.738	0.702
Tonometry	A2_Defl_Area_mm ⁻¹	0.736	0.669-0.803	0.332	0.727	0.714
Tonometry	CBI beta	0.692	0.626-0.758	-0.352	0.661	0.690

AUC, area under the receiver operating characteristic curve; AKC, advanced keratoconus; Sn, sensitivity; Sp, specificity; EKC, early keratoconus; SD-OCT, spectral domain optical coherence tomography; TBI, the tomographic and biomechanical index; BADD, the Belin-Ambrósio deviation index; ISV, the index of surface variance; PRFI, the Pentacam random forest index; IHD, the index of height decentration; IVA, the index of vertical asymmetry; RPIMax, the maximum pachymetric progression index; EPI, Epithelium; SN, superior nasal; IT, inferior temporal; S, Superior; I, Inferior; CBI beta, the linear Corvis biomechanical index; CBI, the Corvis biomechanical index

Feature Selection

Feature selection reduced the machine-derived parameters for Pentacam HR, RTVue-XR, and Corvis ST. These selected parameters are listed in **Table 3**.

Table 3: Selected features from each device

Feature	Mean Imp	Median Imp	Min Imp	Max Imp	Norm Hits	Decision
a: Selected features from Scheimpflug tomography (Pentacam)						
RPI.Max	7.12	7.14	2.04	10.33	0.97	Confirmed
Pachy.Apex	5.94	5.97	2.03	8.06	0.95	Confirmed
Pachy.Pupil	5.56	5.59	2.29	7.75	0.91	Confirmed
AlignXY	5.49	5.49	1.73	8.92	0.89	Confirmed
Iris.Convexity.Max	4.86	4.92	0.63	8.38	0.84	Confirmed
D8mm.Pachy	4.69	4.72	1.64	7.32	0.83	Confirmed
D2mm.Pachy	4.67	4.70	1.95	6.89	0.83	Confirmed
Pachy.Min	4.65	4.69	0.69	6.96	0.82	Confirmed
D0mm.Pachy	4.59	4.63	0.16	7.08	0.82	Confirmed
Thinnest_Pachy	4.63	4.64	1.96	7.03	0.82	Confirmed
C.Vol..D.7mm	4.35	4.40	0.83	6.47	0.79	Confirmed
Astig.B..D.	4.43	4.49	1.45	7.94	0.78	Confirmed
C.Vol.D.7mm	4.33	4.41	1.15	6.81	0.77	Confirmed
D4mm.Pachy	4.27	4.30	1.64	6.67	0.76	Confirmed
C.Vol.D.10mm	4.12	4.13	1.24	6.71	0.73	Confirmed
Iris.Convexity.Min	3.90	3.90	0.66	6.81	0.68	Confirmed
D6mm.Pachy	3.69	3.74	0.12	6.10	0.65	Confirmed
CKI	3.78	3.84	0.52	6.59	0.64	Confirmed
PRC..3mm.Zone.	3.68	3.68	0.92	6.30	0.63	Confirmed
LatShift	3.54	3.59	0.31	6.94	0.59	Confirmed
Rf.B..mm.	3.33	3.38	-0.56	6.14	0.54	Tentative
C.Vol.D.5mm	3.19	3.23	0.66	5.77	0.53	Tentative
C.Vol..D.5mm	3.14	3.19	-0.08	5.41	0.52	Tentative
b: Selected features from SD-OCT (RTVue-XR)						
Pachy9mmS	7.91	7.93	3.46	10.05	0.99	Confirmed
Pachy9mmSN	7.00	7.02	3.29	9.65	0.96	Confirmed
Stroma9mmSN	7.25	7.29	2.74	9.66	0.96	Confirmed
Stroma9mmS	6.43	6.54	2.81	8.56	0.95	Confirmed

Table 3: Selected features from each device

Feature	Mean Imp	Median Imp	Min Imp	Max Imp	Norm Hits	Decision
EPI5mmIT	5.96	6.00	2.24	8.42	0.92	Confirmed
EPI2mm	5.66	5.73	1.40	8.71	0.90	Confirmed
EPI9mmIT	5.09	5.17	1.61	7.64	0.85	Confirmed
EPI5mmSup.Infr	4.74	4.78	0.56	7.67	0.81	Confirmed
Stroma9mmST	4.53	4.56	0.07	6.97	0.78	Confirmed
EPI9mmN	4.51	4.57	0.17	7.40	0.77	Confirmed
EPI7mmI	4.26	4.35	-0.33	6.67	0.74	Confirmed
EPI5mmST.IN	4.20	4.22	0.97	6.77	0.73	Confirmed
StromaMax	4.25	4.32	-0.26	7.15	0.73	Confirmed
EPI5mmT	4.19	4.26	0.67	7.04	0.72	Confirmed
PachyOverallS.2.5mm.	4.08	4.09	0.70	7.10	0.72	Confirmed
Stroma5mmS	4.00	4.03	-0.78	6.77	0.70	Confirmed
EPI5mmSN.IT	3.88	3.86	-0.22	7.59	0.68	Confirmed
Pachyemtry9mmN	3.81	3.84	0.90	6.11	0.65	Confirmed
Stroma9mmN	3.69	3.74	0.38	6.29	0.63	Confirmed
Stroma2mm	3.68	3.71	0.76	6.04	0.62	Confirmed
Stroma7mmST	3.56	3.59	0.22	6.10	0.61	Confirmed
Pachy7mmN	3.58	3.63	0.54	5.95	0.61	Confirmed
PachyOverallyMin	3.31	3.31	0.50	6.23	0.54	Tentative
EPI9mmST	2.98	3.03	-0.65	6.05	0.45	Tentative

c: Selected features from air-puff device (Corvis ST)

A2_Velocity_m_s	19.88	19.88	16.94	22.42	1.00	Confirmed
A2_Time_ms	13.38	13.39	10.42	15.85	1.00	Confirmed
A2_Defl_Amp_mm	11.24	11.22	8.99	13.32	1.00	Confirmed
A2_Defl_Area_mm1	11.03	11.03	8.69	13.23	1.00	Confirmed
A1_Time_ms	9.37	9.37	7.38	11.40	1.00	Confirmed
SPA1	8.86	8.89	6.95	11.04	1.00	Confirmed
Pachy	7.19	7.19	4.74	10.18	1.00	Confirmed
IOP_mmHg	8.14	8.13	5.96	10.17	1.00	Confirmed
biOP	6.07	6.04	2.96	7.99	0.99	Confirmed
HC_Deform_Amp_mm	5.41	5.40	2.60	7.37	0.98	Confirmed
Def_Amp_Max_mm	5.39	5.36	2.86	8.02	0.97	Confirmed
A2_Defl_Length_mm	5.28	5.34	2.49	7.73	0.97	Confirmed
Whole_Eye_Mvmnt_Max_ms	5.07	5.05	2.63	8.20	0.97	Confirmed

Table 3: Selected features from each device

Feature	Mean Imp	Median Imp	Min Imp	Max Imp	Norm Hits	Decision
A2_dArc_Length_mm	4.84	4.90	2.55	7.08	0.95	Confirmed
Max_InverseRadius_mm..1	4.40	4.43	1.05	7.07	0.90	Confirmed
Radius_mm	4.11	4.09	1.08	6.95	0.86	Confirmed
Peak_Dist_mm	3.79	3.77	0.76	5.78	0.82	Confirmed
HC_Deflection_Length_mm	3.93	4.00	-0.26	6.69	0.82	Confirmed
A2_Deformation_Amp_mm	3.76	3.78	0.84	6.39	0.79	Confirmed
HC_Deflection_Amp_mm	3.24	3.27	-0.08	5.47	0.70	Confirmed
A1_Velocity_m_s	3.18	3.25	-0.22	5.43	0.65	Confirmed
Integrated_Radius_mm..1	2.91	3.01	0.42	5.43	0.59	Confirmed
HC_Deflection_Area_mm1	2.82	2.83	0.11	5.48	0.55	Tentative
Deflection_Amp_Max_mm	2.84	2.87	-0.23	5.27	0.54	Tentative
DA_Ratio_Max_2mm	2.84	2.85	-0.16	5.42	0.54	Tentative
HC_dArc_Length_mm	2.62	2.60	-1.56	5.72	0.45	Tentative

Mean Imp, mean importance; MinImp-MaxImp, the arrange between minimum importance and maximum importance; Norm Hits, the fraction of random forest runs

Artificial Intelligence Models and Performance

A total of 14 models were developed, including 7 models built by RF and 7 using NN. The models' features, accuracy, sensitivity, specificity, and AUC are presented in **Table 4**. The model with the highest AUC was Model 6 (AUC = 0.902), based on RF applied to RTVue-XR and Corvis ST, followed by Model 7 (RF applied to all three devices; AUC = 0.871) and Model 14 (NN applied to all three devices; AUC = 0.869). The most accurate models were Models 14 (85.07%), 7 (84.33%), and 6 (84.29%). Comparing the AUC and accuracy of single-device models (Models 1-3 and 8-10), Models 3 and 10 from the Corvis ST performed best, followed by the RTVue-XR and Pentacam HR. The AUC and accuracy of the two-devices models was best in models including features from the Corvis ST (Models 5, 6, 12 and 13).

Table 4: Current established artificial intelligence models' performance

No.	Included features	Accuracy	Sn	Sp	AUC
a: Models established by Random Forest					
6	RTVue-XR + Corvis ST	84.29%	73.53%	87.74%	0.902
7	Pentacam + RTVue-XR + Corvis ST	84.33%	68.57%	89.90%	0.871
5	Pentacam + Corvis ST	84.06%	59.26%	90.09%	0.867
3	Corvis ST only	77.46%	62.50%	81.82%	0.801
2	RTVue-XR only	74.83%	28.21%	91.07%	0.725
1	Pentacam only	72.00%	45.83%	78.22%	0.666
4	Pentacam + RTVue-XR	81.45%	42.86%	89.32%	0.658
b: Models established by Neutral Network					
14	Pentacam + RTVue-XR + Corvis ST	85.07%	71.43%	86.87%	0.869
12	Pentacam + Corvis ST	82.14%	56.67%	89.09%	0.842
13	RTVue-XR + Corvis ST	84.06%	63.89%	91.18%	0.832
10	Corvis ST only	77.40%	50.00%	87.04%	0.770
11	Pentacam + RTVue-XR	72.99%	40.74%	80.90%	0.681
9	RTVue-XR only	72.90%	36.84%	84.61%	0.625
8	Pentacam only	68.00%	30.00%	81.82%	0.620

No., number; Sn, sensitivity; Sp, specificity; AUC, area under the receiver operating characteristic curve

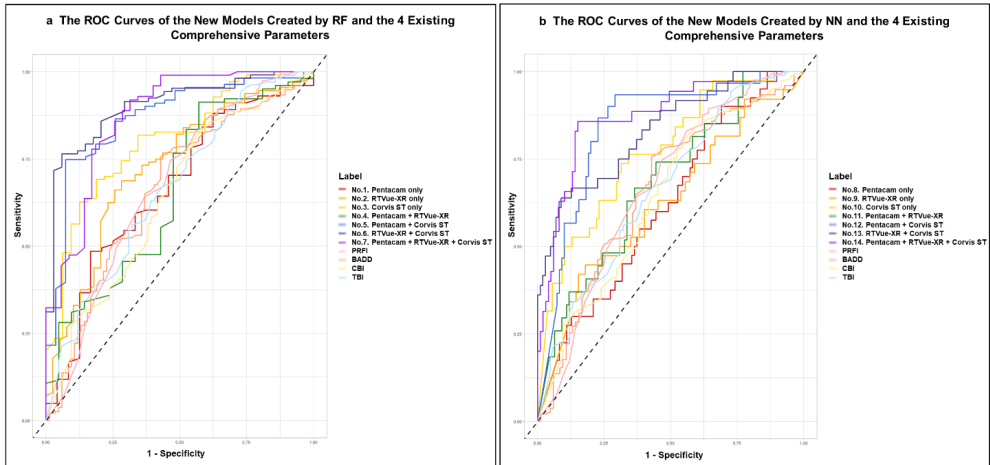
Comparisons of RF and NN

Comparing RF and NN applied to the same features, RF outperformed NN in all but two models: Model 11 had a higher AUC than Model 4 (0.681 vs. 0.658) and Model 14 had a higher accuracy and sensitivity than Model 7.

Comparisons between models and existing parameters

The ROC curves of the new models created by RF and NN and the 4 existing comprehensive parameters (PRFI, BADD, CBI, and TBI) to discriminate between normal and FFKC eyes are shown in **Figure 2a** and **Figure 2b**, respectively. Models 1 and 8 (selected features based on Pentacam HR only) performed similarly as PRFI and BADD; In contrast, Models 3 and 10 (selected

Figure 2: Comparison of seven Artificial Intelligence models created by Random Forest (a) and Neural Networks (b) and existing comprehensive parameters with Receiver Operating Characteristic (ROC) curve analysis



PRFI, the Pentacam random forest index; BADD, the Belin-Ambrósio deviation index; CBI, the Corvis biomechanical index; TBI, the tomographic and biomechanical index

features based on Corvis ST only), and Models 5 and 12 (selected features based on Pentacam HR and Corvis ST) outperformed CBI and TBI, respectively.

DISCUSSION

A review of the literature revealed eight previous studies that combined different measuring principles to diagnose KC (**Table 5**)^{18-21, 27-30}. Their combination approaches can be categorized as: 1) Placido topography plus aberrometer²⁸; 2) Scheimpflug tomography plus VHF digital ultrasound²⁰; 3) Placido topography/ Scheimpflug tomography plus OCT^{18, 29, 30}; 4) Scheimpflug tomography plus air-puff tonometry^{19, 27}; and 5) SD-OCT plus air-puff tonometry, as recently proposed by our research group using a different database²¹. The current study only considers the latter three for a number of reasons. Firstly, Scheimpflug tomography provides more information than Placido topography. Secondly, although VHF digital ultrasound may have high accuracy, it is slow and rarely used. Finally, aberrometers were eliminated as institutions without a refractive unit are less likely to have one, making it less useful.

Table 5: Studies combining devices to differentiate KC from normal eyes

Lead author	Devices	Eyes Included	Algorithm	Performance
Rabinowitz <i>et al.</i> ¹⁸ 2014	TMS-4 + Optovue SD-OCT	16 suspect eyes, 7 FFKC eyes, 54 EKC eyes, 46 moderate KC eyes, and 180 normal eyes	-	100% accuracy for EKC and FFKC eyes, with 2.7% misclassification of normal eyes
Luz <i>et al.</i> , ²⁷ 2016	Pentacam HR with ORA	21 FFKC eyes, 76 normal eyes	LR	Highest AUC = 0.95, 85.71% sensitivity, and 98.68% specificity
Saad <i>et al.</i> ²⁸ 2016	Orbscan IIz + OPD-Scan aberrometer	62 FFKC eyes, 114 normal eyes	LDA	Highest AUC = 0.97, 100% sensitivity, and 82% specificity
Silverman <i>et al.</i> ²⁰ 2016	Pentacam HR + Artemis-1 VHF digital ultrasound	30 clinical KC eyes, 111 normal eyes	Stepwise LDA	Highest AUC nearly =100%, 97.3% sensitivity and 100% specificity
Ambrósio <i>et al.</i> ¹⁹ 2017	Pentacam HR + Corvis ST	94 VAE-NT eyes, 72 VAE-E eyes, 204 KC eyes, and 480 normal eyes	RF, LR, and SVM	Highest AUC = 0.985, 90.4% sensitivity with 96% specificity for VAE-NT eyes by RF
Hwang <i>et al.</i> ²⁹ 2018	Pentacam HR + Optovue SD-OCT	30 highly asymmetric KC eyes, 60 normal eyes	Multivariable LR	Highest AUC = 1.00, 100% sensitivity and specificity
Shi <i>et al.</i> ³⁰ 2020	Pentacam HR + UHR-OCT	33 subclinical KC eyes, 38 KC eyes, and 50 normal eyes	NN	Highest AUC = 0.93, 93% precision for subclinical KC eyes, and 99% precision for KC eyes by NN
Lu <i>et al.</i> ²¹ 2022	Corvis ST + Optovue SD-OCT	69 FFKC eyes, 72 EKC eyes, 258 AKC eyes, and 223 normal eyes	RF, NN	Highest AUC = 0.99 for FFKC, with 75% sensitivity, 94.74% specificity by RF

AUC, area under the curve; KC, keratoconus; OCT, optical coherence tomography; FFKC, forme fruste keratoconus; EKC, early keratoconus; ORA, ocular response analyzer; LR, logistic regression; LDA, linear discriminant analysis; VHF digital ultrasound, very high frequency digital ultrasound; VAE-NT, very asymmetric ectasia-normal tomography; VAE-E, very asymmetric ectasia with clinical ectasia; RF, random forest; SVM, support vector machine; SD-OCT, spectral domain OCT; UHR-OCT, ultra-high-resolution OCT; NN, neural network

Here, three combinations of two devices with different measuring principles augmented by AI were reported. Combining Scheimpflug with SD-OCT (Models 4 and 11) did not improve the diagnostic ability for FFKC compared to Scheimpflug/ SD-OCT alone (Models 1, 2, 8, and 9). This might be because KC starts as a local weakening of the cornea, which does not show changes that can be detected by Scheimpflug/ SD-OCT. In contrast, when Hwang *et al.*, combined Scheimpflug tomography and SD-OCT using logistic regression, they obtained a highly performant model to distinguish asymmetric KC from normal eyes, which was superior to Scheimpflug or SD-OCT alone²⁹. This contradictory result could be due to the limited number of KC patients included in the study and the most of included highly asymmetric KC eyes were in the early KC stage but not in the forme fruste KC stage.

Among the two-device combinations, the FFKC diagnostic ability of Scheimpflug with air-puff tonometry (Models 5 and 12) and SD-OCT with air-puff tonometry (Models 6 and 13) was greatly improved compared to the single-device analyses. This again confirms the importance of biomechanical measurement in FFKC diagnosis, where corneal biomechanics abnormalities may occur in tomographically normal corneas³¹. The combination of air-puff tonometry with SD-OCT had a slightly better diagnostic ability for FFKC than the combination of air-puff tonometry with Scheimpflug, emphasizing the input of the epithelial and stromal profiles provided by OCT.

Various AI algorithms were built based on either a single device or combinations of devices, each claiming excellent KC diagnostic abilities³². The robustness of these approaches was unclear since studies rarely compare all available device types. For clinicians, it is difficult to determine the most useful tool for KC screening. Furthermore, diverse inclusion criteria between studies, the low number of early-stage KC patients included, and the wide range of devices and indices being used, highlight the need for comparative analyses. In this study, a large number of KC patients was included using the same inclusion criteria as the original studies that developed the PRFI, CBI, and TBI parameters.

Moreover, three different devices based on different measuring principles were differently combined to conduct a comprehensive and objective analysis.

The current results confirmed that existing parameters (PRFI, BADD, and CBI), based on a single device (Scheimpflug tomography or air-puff tonometry), can accurately diagnose EKC and AKC, but are less reliable for FFKC. Hence, our models focused mainly on distinguishing FFKC from normal eyes. Models 1 and 8 (Pentacam only) performed similarly to PRFI and BADD, suggesting the latter may have reached peak efficiency. Meanwhile, Models 3 and 10 (Corvis only) outperformed CBI, suggesting that CBI still has room for improvement. This may be because CBI was based on logistic regression rather than RF or NN, and the features of CBI were selected by forward stepwise inclusion⁸, which may have overlooked other potentially useful characteristics.

TBI, which combines Scheimpflug with air-puff tonometry, did not obtain superior FFKC diagnostic results compared to single-device parameters. This suggests that TBI, in its current iteration, is not yet fully optimised for FFKC diagnosis. However, Models 5 and 12 (based on Scheimpflug and air-puff tonometry) outperformed TBI, PRFI, BADD, CBI, as well as the single-device models in the current study (Models 1-3, Models 8-10). This also suggests that TBI may require further iterations to grasp forme fruste biomechanics. Although no detailed formula for TBI were provided in the original study¹⁹, it is known that TBI was built based on RF without feature selection, which might have left its diagnostic ability below potential.

To the best of our knowledge, this was the first attempt to combine three devices with different measuring principles to diagnose FFKC with the help of AI. This three-devices combination obtained the highest accuracy (Model 7), although it was only marginally better than air-puff tonometry with SD-OCT, which may be explained by the aforementioned fact: the combination of two corneal shape measuring devices did not improve FFKC diagnosis probably because they provide much the same information. While any of these devices could accurately diagnose EKC and AKC on their own, the combination of air-puff

tonometry with either Scheimpflug tomography or SD-OCT led to an obvious improvement in FFKC diagnostic ability. Combining all three devices, however, did not obviously improve the diagnostic ability for FFKC.

From health economics and efficiency perspective³³, clinicians are suggested to choose their KC examination devices based on their target population. For patients with high risk of KC, *e.g.*, age between 12-25, with KC family history, eye rubbing, LVC candidates, thin cornea, or corneal astigmatism more than 1.5 D^{34, 35}, a combination of air-puff tonometry with Scheimpflug tomography/SD-OCT to detect FFKC is recommended. For patients with low KC risk, the diagnostic ability of any single clinical device may be sufficient.

One limitation of the current study may be that it only included a selection of commercially available devices. As such, it is unclear whether combinations with other devices of the same type, *e.g.*, the self-combined Placido/SD-OCT device (MS-39, CSO Italia, Firenze, Italy), perform better. Further investigations need to be conducted in this regard: measuring the patients with all current commonly used clinical devices, and multicenter collaboration could speed up collection of early-stage KC patients.

In conclusion, existing AI methods can accurately diagnose EKC and AKC but their diagnostic ability of FFKC is low. Compared to using a single device, combining air-puff tonometry with Scheimpflug tomography or SD-OCT can vastly improve the diagnostic efficiency for FFKC but simultaneous use of three devices offers no additional advantages. Clinicians and optometrists are recommended to choose a combination of corneal biomechanical and morphological biometry, preferably including the epithelial profile, to improve their FFKC diagnosis in patients with high risk of KC.

REFERENCES

1. Ferdi AC, Nguyen V, Gore DM, Allan BD, Rozema JJ, Watson SL. Keratoconus Natural Progression: A Systematic Review and Meta-analysis of 11 529 Eyes. *Ophthalmology* 2019;126:935-945.
2. Larkin DFP, Chowdhury K, Burr JM, et al. Effect of Corneal Cross-linking versus Standard Care on Keratoconus Progression in Young Patients: The KERALINK Randomized Controlled Trial. *Ophthalmology* 2021;128:1516-1526.
3. Roberts CJ, Dupps WJJ. Biomechanics of corneal ectasia and biomechanical treatments. *Journal of Cataract & Refractive Surgery* 2014;40:991-998.
4. Reinstein DZ, Archer TJ, Gobbe M. Corneal epithelial thickness profile in the diagnosis of keratoconus. *Journal of refractive surgery (Thorofare, NJ: 1995)* 2009;25:604-610.
5. Reinstein DZ, Silverman RH, Rondeau MJ, Coleman DJ. Epithelial and Corneal Thickness Measurements by High-frequency Ultrasound Digital Signal Processing. *Ophthalmology* 1994;101:140-146.
6. Li Y, Meisler DM, Tang M, et al. Keratoconus Diagnosis with Optical Coherence Tomography Pachymetry Mapping. *Ophthalmology* 2008;115:2159-2166.
7. Luce DA. Determining in vivo biomechanical properties of the cornea with an ocular response analyzer. *Journal of Cataract & Refractive Surgery* 2005;31:156-162.
8. Vinciguerra R, Ambrósio R, Elsheikh A, et al. Detection of Keratoconus With a New Biomechanical Index. *Journal of Refractive Surgery* 2016;32:803-810.
9. Jr R, Ramos I, Luz A, et al. Dynamic ultra high speed Sheimpflug imaging for assessing corneal biomechanical properties. *Revista Brasileira de Oftalmologia* 2013;72:99-102.
10. Rabinowitz YS. Videokeratographic indices to aid in screening for keratoconus. *J Refract Surg* 1995;11:371-379.
11. Rabinowitz YS, Rasheed K. KISA% index: a quantitative videokeratography algorithm embodying minimal topographic criteria for diagnosing keratoconus. *J Cataract Refract Surg* 1999;25:1327-1335.
12. Auffarth GU, Wang L, Völcker HE. Keratoconus evaluation using the Orbscan Topography System. *J Cataract Refract Surg* 2000;26:222-228.
13. Ambrósio R, Jr., Alonso RS, Luz A, Coca Velarde LG. Corneal-thickness spatial profile and corneal-volume distribution: tomographic indices to detect keratoconus. *J Cataract Refract Surg* 2006;32:1851-1859.
14. Maeda N, Klyce SD, Smolek MK. Neural network classification of corneal topography. Preliminary demonstration. *Invest Ophthalmol Vis Sci* 1995;36:1327-1335.
15. Smolek MK, Klyce SD. Current keratoconus detection methods compared with a neural network approach. *Invest Ophthalmol Vis Sci* 1997;38:2290-2299.
16. Saad A, Gatinel D. Topographic and Tomographic Properties of Forme Fruste

- Keratoconus Corneas. *Investigative Ophthalmology & Visual Science* 2010;51:5546-5555.
17. Lopes BT, Ramos IC, Salomão MQ, et al. Enhanced Tomographic Assessment to Detect Corneal Ectasia Based on Artificial Intelligence. *Am J Ophthalmol* 2018;195:223-232.
 18. Rabinowitz YS, Li X, Canedo ALC, Ambrósio R, Jr., Bykhovskaya Y. Optical coherence tomography combined with videokeratography to differentiate mild keratoconus subtypes. *Journal of refractive surgery (Thorofare, NJ : 1995)* 2014;30:80-87.
 19. Ambrósio R, Lopes BT, Faria-Correia F, et al. Integration of Scheimpflug-Based Corneal Tomography and Biomechanical Assessments for Enhancing Ectasia Detection. *Journal of Refractive Surgery* 2017;33:434-443.
 20. Silverman RH, Urs R, RoyChoudhury A, Archer TJ, Gobbe M, Reinstein DZ. Combined tomography and epithelial thickness mapping for diagnosis of keratoconus. *Eur J Ophthalmol* 2017;27:129-134.
 21. Lu NJ, Elsheikh A, Rozema JJ, et al. Combining Spectral-Domain OCT and Air-Puff Tonometry Analysis to Diagnose Keratoconus. *J Refract Surg* 2022;38:374-380.
 22. Henriquez MA, Hadid M, Izquierdo L. A Systematic Review of Subclinical Keratoconus and Forme Fruste Keratoconus. *Journal of Refractive Surgery* 2020;36:270-279.
 23. Lu N-J, Chen D, Cui L-L, Wang L, Chen S-H, Wang Q-M. Repeatability of Cornea and Sublayer Thickness Measurements Using Optical Coherence Tomography in Corneas of Anomalous Refractive Status. *Journal of Refractive Surgery* 2019;35:600-605.
 24. Kursa MB, Rudnicki WR. Feature Selection with the Boruta Package. *Journal of Statistical Software* 2010;36:1 - 13.
 25. Liaw A, Wiener M. Classification and Regression by RandomForest. *Forest* 2001;23.
 26. Günther F, Fritsch S. Neuralnet: training of neural networks. *R J* 2010;2:30.
 27. Luz A, Lopes B, Hallahan KM, et al. Enhanced Combined Tomography and Biomechanics Data for Distinguishing Forme Fruste Keratoconus. *Journal of refractive surgery (Thorofare, NJ : 1995)* 2016;32:479-494.
 28. Saad A, Gatinel D. Combining Placido and Corneal Wavefront Data for the Detection of Forme Fruste Keratoconus. *Journal of Refractive Surgery* 2016;32:510-516.
 29. Hwang ES, Perez-Straziota CE, Kim SW, Santhiago MR, Randleman JB. Distinguishing Highly Asymmetric Keratoconus Eyes Using Combined Scheimpflug and Spectral-Domain OCT Analysis. *Ophthalmology* 2018;125:1862-1871.
 30. Shi C, Wang M, Zhu T, et al. Machine learning helps improve diagnostic ability of subclinical keratoconus using Scheimpflug and OCT imaging modalities. *Eye Vis (Lond)* 2020;7:48.
 31. Vinciguerra R, Ambrósio R, Jr., Roberts CJ, Azzolini C, Vinciguerra P. Biomechanical Characterization of Subclinical Keratoconus Without Topographic or Tomographic Abnormalities. *J Refract Surg* 2017;33:399-407.

32. Lin SR, Ladas JG, Bahadur GG, Al-Hashimi S, Pineda R. A Review of Machine Learning Techniques for Keratoconus Detection and Refractive Surgery Screening. *Seminars in Ophthalmology* 2019;34:317-326.
33. Kundu G, Shetty R, Khamar P, et al. Universal architecture of corneal segmental tomography biomarkers for artificial intelligence-driven diagnosis of early keratoconus. *British Journal of Ophthalmology* 2021;bjophthalmol-2021-319309.
34. Gomes JA, Tan D, Rapuano CJ, et al. Global consensus on keratoconus and ectatic diseases. *Cornea* 2015;34:359-369.
35. Santodomingo-Rubido J, Carracedo G, Suzaki A, Villa-Collar C, Vincent SJ, Wolffsohn JS. Keratoconus: An updated review. *Cont Lens Anterior Eye* 2022;45:101559.

Chapter 6

Performance of a New Biomechanical Index for Post-Laser Vision Correction Ectasia Diagnosis

Nan-Ji Lu, Carina Koppen, Jos J. Rozema, Ru-Yi Liu, Paolo Vinciguerra,
Qin-Mei Wang, Le-Le Cui, Riccardo Vinciguerra

In preparation

ABSTRACT

Purpose: To validate the performance of the Corvis Biomechanical Index for Laser Vision Correction (CBI-LVC), in distinguishing post-laser vision correction (LVC) ectasia from post-LVC stable patients.

Methods: Two groups of patients, post-LVC ectasia and post-LVC stable patients, were included. Corneal biomechanics was measured by an Ultra-high-speed Scheimpflug Camera (Corvis ST, Oculus Optikgeräte, Wetzlar, Germany) to provide the value of the CBI-LVC index. The sensitivity and specificity of the CBI-LVC were evaluated for the cut-off value of 0.50.

Results: Nineteen post-LVC ectasia patients (1 post sub-Bowman's keratomileusis [SBK], 1 post laser-assisted subepithelial keratectomy [LASEK], and 17 post laser assisted *in situ* keratomileusis [LASIK]) and 111 post-LVC stable patients with at least two years postoperative follow-up were included (42 post-transepithelial photorefractive keratectomy [TransPRK], 33 post femtosecond (FS)-LASIK, and 36 post-small incision lenticule extraction [SMILE]). The mean onset time for post-LVC ectasia was 10.74 ± 5.16 years. The sensitivity of CBI-LVC was 100.00% at the cutoff value of 0.20 and 0.50. At the cutoff value of 0.20, the specificity of CBI-LVC in the TransPRK, FS-LASIK, and SMILE was 90.48%, 93.94%, and 91.67%, respectively; At the cutoff value of 0.50, the specificity of CBI-LVC in the TransPRK, FS-LASIK, and SMILE was 95.24%, 96.97%, and 97.22%, respectively.

Conclusions: CBI-LVC is able to detect post-LVC ectasia, especially for post-LASIK eyes, making it a potentially useful tool in clinical practice. The post-LVC corneas with increased CBI-LVC that could not be confirmed by the tomography alone need closer follow-up.

INTRODUCTION

One of the most serious postoperative complications of Laser vision correction (LVC) is post-LVC ectasia. The rate of post-LVC ectasia is low and changes with the LVC technique used, with the incidence of post-laser assisted *in situ* keratomileusis (LASIK) ectasia being 4.5 times higher than that of post-photorefractive keratectomy (PRK) ectasia or small incision lenticule extraction (SMILE) ¹. The cause of post-LVC ectasia is a reduction in structural integrity and corneal biomechanics caused by the surgery ².

Post-LVC ectasia is typically diagnosed based on the progressive decline of the patients' vision and the characteristic manifestations of the patients' corneal tomography/topography ³. These signs are a consequence of the focal reduction of corneal biomechanics rather than a direct measurement of corneal elasticity itself. To address this issue, Corvis Biomechanical Index for Laser Vision Correction (CBI-LVC) was recently introduced based on the dynamic corneal response (DCR) parameters provided by the Corvis Scheimpflug tonometer (Oculus Optikgeräte, Wetzlar, Germany). This index allows distinguishing between post-LVC ectasia from post-LVC stable eyes ⁴.

This study aims to independently validate the performance and clinical application of CBI-LVC in diagnosing post-LVC ectasia by means of patients who underwent sub-Bowman's keratomileusis (SBK), laser-assisted subepithelial keratectomy (LASEK), transepithelial PRK (TransPRK), LASIK, and SMILE.

METHODS

This study enrolled patients from the Eye Hospital of Wenzhou Medical University (Wenzhou, China) and Humanitas Clinical and Research Center (Milano, Italy) between 2017 December to 2023 May. The study was approved by the ethical committee of the Eye Hospital of Wenzhou Medical University and adhered to the tenets of the Declaration of Helsinki. All participants provided informed consent before their data was used in this analysis.

Groups Setting and Patient Inclusion

Two groups of patients, the post-LVC ectasia group and the post-LVC stable group, were included in the study. The inclusion and exclusion criteria are mentioned below. At each visit patients underwent a comprehensive examination, including slit-lamp microscopy, subjective refraction, Scheimpflug-based tomography by Pentacam HR (Oculus Optikgeräte, Inc., Wetzlar, Germany), and corneal biomechanical examination by Corvis ST.

Post-LVC ectasia group patients

Patients were included if they had a history of LVC and were diagnosed for post-LVC ectasia by three independent corneal experts (CK, LLC, and RV) through anonymously exported data. Post-LVC ectasia was defined based on the evaluation of tomography over time and a history of proven progression over a minimum of 3 months and worsening after LVC.

In detail, the inclusion criteria for post-LVC ectasia diagnosis were taken from the literature^{3, 4} and required that they either showed (1) a decrease in uncorrected distance visual acuity (UDVA) of ≥ 2 lines on the Snellen chart and a refractive change of ≥ 2.00 D of spherical equivalent, or (2) a progressive inferior steepening of ≥ 5.00 D and a progressive local steepening of ≥ 1.50 D in the front sagittal curvature map. The exclusion criteria included systemic diseases, other ocular diseases, and prior ocular surgery other than LVC (e.g., cornea cross-linking [CXL]). The post-LVC ectasia patients included in the former original research were not included in this study⁴.

Post-LVC stable group patients

Patients enrolled in the Eye Hospital of Wenzhou Medical University and performed myopic LVC with at least 2 years postoperatively stable follow-up, including post-TransPRK, post-femtosecond (FS)-LASIK, and post-SMILE patients, were included in the post-LVC stable group.

Before the surgery, the corrected distance visual acuity (CDVA) of all patients was more than 20/20. After the comprehensive preoperative examination,

patients with any ocular surgery history or trauma, keratoconus, or iatrogenic diseases were excluded. Patients who received prophylactic CXL immediately after the LVC were also excluded ⁵.

During the surgical process, all patients were targeted at emmetropia based on their preoperative subjective refraction. In brief, for the post-TransPRK patients, all laser ablation was performed using the Amaris 750S Excimer Laser (Schwind eye-tech-solutions GmbH, Kleinostheim, Germany) in a single step. For the post-FS-LASIK patients, the corneal flap (range 90-110 µm) was formed by a femtosecond laser (iFS®, Johnson & Johnson Vision, USA) at first, and the same ablation protocol as the post-TransPRK patient was implemented later. For the post-SMILE patients, a VisuMax 500-kHz femtosecond laser (Carl Zeiss Meditec, Jena, Germany) was used to remove the designed stromal lenticule.

After surgery, a drop of tobramycin-dexamethasone (Tobradex®, Alcon) was instilled at the surgical site, and a soft bandage contact lens (Air Optix® Night & Day™ AQUA, Alcon) was placed in the TransPRK and FS-LASIK eyes. The soft bandage contact lenses were removed one day postoperatively in the FS-LASIK eyes, while in the TransPRK eyes, they were removed after complete re-epithelialization was observed. Artificial tears, antibiotics (0.5% levofloxacin, Cravit®, Santen, Osaka, Japan) and glucocorticoid drops were applied four times a day in all groups during the first postoperative week. The dosage of glucocorticoid drops was tapered over four months, and artificial tears were applied as needed.

All patients had at least 2 years follow-up after the LVC. At the last visit, no signs of post-LVC ectasia were found in any of them. In addition, the exclusion criteria of stable post-LVC patients included any other LVC-related intraoperative and postoperative complications, such as infectious keratitis, epithelium ingrowth and any types of corneal flap complications, trauma, or any other ocular surgeries (e.g., blepharoplasty).

Data Records and The Parameter Evaluation

To properly evaluate the performance of CBI-LVC, only randomly selected eye was included per patient. The data analysed consisted of a slit-lamp examination, UDVA, CDVA, and subjective refraction. The tomographic data from the Pentacam provided K_1 , K_2 , K_{max} , and thinnest pachymetry, while CBI-LVC was obtained from the Corvis ST.

Based on two different cut-off values, the calculation of sensitivity and specificity were calculated: (1) the CBI-LVC value of 0.20 set by the original study; (2) the value of 0.50 set by the current version of the software⁴. The calculation of the sensitivity of CBI-LVC was using:

$$\text{Sensitivity} = \frac{\text{The number of post - LVC ectasia eyes which CBI - LVC} \geq \text{cut - off value}}{\text{The number of post - LVC ectasia eyes}} \times 100 [\%]$$

the calculation of the specificity of CBI-LVC was using the following formula:

$$\text{Specificity} = \frac{\text{The number of post - LVC normal eyes which CBI - LVC} < \text{cut - off value}}{\text{The number of post - LVC normal eyes}} \times 100 [\%]$$

STATISTICAL ANALYSIS

The statistical analysis was performed in R (version 4.2.2, R Foundation for Statistical Computing, Vienna, Austria). The normality of the data was verified using the Shapiro-Wilks test. Descriptive statistics were presented as mean \pm standard deviation. Analysis of variance (ANOVA) and Kruskal-Wallis H tests were used to analyze the differences between the groups, followed by post-hoc tests with a Bonferroni correction. A P value of < 0.05 was considered statistically significant.

RESULTS

Demographics

Post LVC ectasia

Nineteen post-LVC ectasia patients were included (15 males and 4 females), more in details: 1 patient had undergone SBK, 1 patient had undergone LASEK,

and 17 patients had undergone LASIK; the mean surgical age was 22.95 ± 4.99 years old, the mean postoperative onset for post-LVC ectasia was 10.74 ± 5.16 years (range 6 to 20 years). The patients' basic information with their diagnoses are summarized in **Table 1** (Cases 1-16 from China, Cases 17-19 from Italy). For these post-LVC ectasia patients, post-LVC ectasia was diagnosed using Scheimpflug-based tomography, except for Cases 7OS, 13OS, and 14OS that were diagnosed based on vision decrease.

Stable post LVC

One hundred and eleven post-LVC stable patients with at least two years postoperative follow-up were included, including 42 eyes from 42 patients who underwent TransPRK, 33 eyes from 33 patients had undergone FS-LASIK, and 36 eyes from 36 patients had undergone SMILE. The demographic and operative information of these sub-groups and their comparison are presented in **Table 2**.

Validation of the performance of CBI-LVC

For the post-LVC ectasia group, in a total of 38 eyes of 19 patients, 10 patients had a bilateral post-LVC ectasia. The sensitivity of CBI-LVC was 100.00% using either the cut-off value of 0.20 or 0.50. There were 9 post-LVC stable eyes in the post-LVC ectasia group (these contralateral eyes were post-LVC ectasia), 2 of these 9 eyes (Cases 12OS and 18OD) had an increased CBI-LVC, although these 2 eyes had the remodeling of tomography but did not reach the post-LVC ectasia criteria. For the post-LVC stable group, in total of 111 eyes, the specificity of CBI-LVC in the TransPRK, FS-LASIK, and SMILE was of 90.48%, 93.94%, and 91.67%, respectively with a cut-off value of 0.2 (total specificity was 91.89%, 95% confidence interval [CI] = 0.495 - 0.831); while with a cut-off value of 0.5 was 95.24%, 96.97%, and 97.22%, respectively (total specificity was 96.40%, 95% confidence interval [CI] = 0.641 - 0.942).

Table 1: Current basic information of post-LVC ectasia patients

No.	Age (Y) At surg/current	Sex	Eye	Surgery	Ectasia	Sph (D)	Cyl (D)	UDVA	CDVA	P _{min} (μm)	K _{max} (D)	CBI- LVC
1	19/27	M	OD	SBK	Y	-2.50	-3.50	20/40	20/32	457	51.8	1.00
			OS	SBK	N	0.25	-0.75	20/20	20/20	491	44.4	0.00
2	21/30	F	OD	LASEK	Y	-0.25	-0.50	20/25	20/20	382	46.7	0.71
			OS	LASEK	Y	3.50	-7.00	20/50	20/40	347	66.1	1.00
3	20/40	M	OD	LASIK	Y	-2.00	-1.25	20/63	20/25	419	47.6	0.99
			OS	LASIK	Y	-1.75	-1.25	20/50	20/25	467	47.1	0.54
4	29/43	M	OD	LASIK	N	0.00	-0.75	20/20	20/16	482	43.1	0.00
			OS	LASIK	Y	-4.75	-6.25	20/100	20/32	438	58.9	1.00
5	22/32	M	OD	LASIK	N	0.25	-0.25	20/20	20/20	453	43.6	0.00
			OS	LASIK	Y	1.25	-1.00	20/32	20/20	452	47.1	1.00
6	19/29	M	OD	LASIK	Y	-6.00	-5.50	20/50	20/50	370	69.2	1.00
			OS	LASIK	Y	1.00	-1.50	20/32	20/32	472	47.5	0.99
7	19/41	M	OD	LASIK	Y	-3.00	-3.50	20/400	20/100	326	79.5	1.00
			OS	LASIK	Y	-3.25	-0.75	20/125	20/20	475	45.2	0.97
8	18/24	F	OD	FS-LASIK	N	0.50	-2.25	20/25	20/20	420	42.7	0.00
			OS	FS-LASIK	Y	-6.50	-3.75	20/125	18/20	379	54.2	1.00
9	21/31	M	OD	FS-LASIK	Y	-2.00	-6.25	20/200	20/25	434	51.2	1.00
			OS	FS-LASIK	Y	-2.50	-0.5	20/200	20/50	406	58.3	1.00
10	20/25	M	OD	FS-LASIK	Y	1.50	-4.5	20/32	20/25	401	48.9	1.00
			OS	FS-LASIK	Y	-1.25	-2.5	20/400	20/200	296	83.1	1.00
11	23/30	M	OD	FS-LASIK	N	-1.00	0.00	20/25	20/20	466	42.3	0.00
			OS	FS-LASIK	Y	-4.25	-2.75	20/200	20/32	405	52.3	1.00
12	21/27	M	OD	FS-LASIK	Y	3.00	-3.25	20/63	20/25	437	52.1	0.99
			OS	FS-LASIK	N	-0.25	-0.75	20/25	20/20	443	45.1	0.94
13	18/32	M	OD	LASIK	Y	2.25	-5.50	20/50	20/25	446	55.6	1.00
			OS	LASIK	Y	-1.50	-1.50	20/32	20/20	457	47.1	0.98
14	29/44	M	OD	LASIK	Y	-7.50	-7.00	20/2000	20/400	366	63.4	1.00
			OS	LASIK	Y	-1.75	-1.75	20/63	20/20	472	45.2	0.96
15	20/29	M	OD	FS-LASIK	N	0.25	-0.50	20/20	20/20	448	44.1	0.00
			OS	FS-LASIK	Y	1.50	-2.25	20/100	20/32	411	53	1.00
16	22/28	M	OD	FS-LASIK	Y	-0.25	-3.75	20/50	20/25	424	47.3	1.00
			OS	FS-LASIK	Y	1.75	-8.50	20/200	20/25	423	54	1.00
17	34/45	F	OD	LASIK	Y	-0.50	-0.75	20/32	20/20	451	48.2	0.99
			OS	LASIK	Y	1.50	-2.75	20/63	20/25	423	52.9	1.00

Table 1: Current basic information of post-LVC ectasia patients

18	32/50	M	OD	LASIK	N	-	-	20/20	-	485	45.0	0.60
			OS	LASIK	Y	-0.75	-4.00	20/200	20/20	447	51.3	1.00
19	29/33	F	OD	LASIK	N	-	-	20/20	-	409	43.7	0.06
			OS	LASIK	Y	-2.25	-2.75	20/200	20/32	332	49.3	1.00

Y, year; D, diopter; UDVA, uncorrected distance visual acuity; CDVA, corrected distance visual acuity; Pmin, thinnest pachymetry; CBI-LVC, Corvis biomechanical index-laser vision correction; M, male; F, female; SBK, sub-Bowman's keratomileusis; LASEK, laser-assisted subepithelial keratectomy; LASIK, laser assisted in situ keratomileusis; FS, femtosecond

Table 2: Basic demographic information of post-LVC stable group

	Unit	TransPRK	FS-LASIK	SMILE	TransPRK vs. FS-LASIK	TransPRK vs. SMILE	FS-LASIK vs. SMILE
Number	(OD/OS)	21/21	17/16	19/17	-	-	-
Gender	(M/F)	25/17	17/16	27/9	-	-	-
Age	Yrs	24.93±5.69	22.48±4.35	22.25±4.59	0.037*	0.019*	0.845
Pre-Kmax	D	44.40±2.38	44.32±1.66	44.02±1.61	0.876	0.402	0.522
PreThinnestPachy	µm	540.67±31.55	533.49±88.20	551.25±28.92	0.572	0.393	0.178
Pre-Sphere	D	-5.17±1.94	-5.32±1.85	-3.80±1.28	0.717	< 0.001*	< 0.001*
Pre-Cylinder	D	-0.63±0.48	-1.02±0.65	-0.68±0.51	0.003*	0.689	0.012*
Pre-SE	D	-5.49±1.96	-5.83±1.80	-4.14±1.38	0.407	0.001*	0.001*
Optical Zone	mm	6.53±0.43	6.53±0.34	6.77±0.17	0.982	0.002*	0.004*
Ablation Depth	µm	142.64±25.37	98.18±20.74	100.00±20.96	< 0.001*	< 0.001*	0.740
RSBThickness	µm	399.81±41.45	352.70±32.15	334.75±30.85	< 0.001*	< 0.001*	<0.039*
FUs Times	Yrs	3.00±1.81	3.86±2.11	2.51±0.79	0.028*	0.201	0.001*
Post-Kmax	D	43.42±1.89	43.96±1.72	43.19±1.99	0.215	0.586	0.088
PostThinnestPachy	µm	456.48±43.91	463.15±29.73	472.17±32.36	0.434	0.061	0.308
Post-Sphere	D	0.22±0.40	0.05±0.57	0.29±0.30	0.097	0.466	0.023*
Post-Cylinder	D	-0.29±0.36	-0.28±0.28	-0.35±0.33	0.883	0.406	0.355
Post-SE	D	0.07±0.40	-0.09±0.54	0.11±0.33	0.109	0.681	0.054
Post-	-	-0.05±0.06	-0.02±0.10	-0.07±0.03	0.029*	0.298	0.002*
UDVA(LogMAR)	-	-	-	-	-	-	-
CBI-LVCValue	-	0.06±0.19	0.06±0.22	0.05±0.16	0.909	0.801	0.727

LVC, laser vision correction; TransPRK, transepithelial photorefractive keratectomy; LASIK, laser assisted in situ keratomileusis; SMILE, small incision lenticule extraction; M, male; F, female; Pre, preoperative; SE, spherical equivalent; RSB, residual stromal bed; FUs, follow-up; Post, postoperative; UDVA, uncorrected distance visual acuity; LogMAR, Logarithm of the Minimum Angle of Resolution; CBI-LVC, Corvis Biomechanical Index for Laser Vision Correction; * P values < 0.05

DISCUSSION

The current study validated the performance of CBI-LVC in discriminating ectatic from stable post-LVC. The original study included 51 post-LVC ectasia eyes and reported a sensitivity of 93.3% and a specificity of 97.8% with a cut-off value of 0.20 ⁴. In the current study, all post-LVC ectasia eyes were correctly diagnosed by CBI-LVC, while 6 stable post-LVC fellow eyes (Cases 1 OS, 4 OD, 5 OD, 8OD, 11 OD, and 19 OD) showed CBI-LVC values of 0. The latter eyes had no signs of ectasia on the front sagittal curvature and elevation maps, confirming that CBI-LVC is able to discriminate post-LVC ectasia from post-LVC stable eyes.

In the current study, the cutoff values of 0.20 and 0.50 were both investigated, which both exhibited excellent sensitivity and specificity of post-LVC ectasia diagnosis. In the post-LVC ectasia group, not all cases exhibited equally clear signs of ectasia, however. Case 12 OS (CBI-LVC = 0.94), for example, showed an inferior region of steep curvature below 5.00 D, while Case 18 OD (CBI-LVC = 0.60) had a higher irregular front elevation. Hence, the increased values of CBI-LVC could perhaps be regarded as early diagnostic indication of post-LVC ectasia, even in absence of manifest tomographical signs. Such post-LVC patients should be scheduled for more frequent follow-up visits, and, if deemed necessary, timely CXL to halt the progression short after the diagnosis of post-LVC ectasia ⁶.

For the post-LVC ectasia occurrence time after the LVC, Seiler *et al.* first reported three post-LASIK ectasia case series with an ectasia development time between 1 and 8 months postoperatively ⁷. Randleman *et al.* reported that the mean onset time of post-LASIK ectasia was 16.3 months, while most of these cases occurred ectasia within 6 months postoperatively ⁸. In a recent review, Moshirfar *et al.* summarized that the mean onset time of post-LVC ectasia after PRK, LASIK, and SMILE was 41 ± 50 months, 35 ± 24 months, and 18 ± 13 months, respectively ¹. Based on a high-volume single center's data, Brar *et al.* recently found that the mean interval time from SMILE to post-SMILE ectasia occurrences was 21.3 months ⁹. In contrast, the current post-

LVC ectasia case series were mainly delayed-onset ectasia, which were largely late than the previous reported ectasia onset time.

The current study also included post-LVC stable patients to detect the specificity of CBI-LVC, which is the first study to test the specificity of CBI-LVC. The specificity of CBI-LVC was high in all three types of LVC. While there were also post-LVC stable cases with high values of CBI-LVC, which may also need close follow-up to prevent the late diagnosis of post-LVC ectasia.

According to the purpose of the design, the difference and application scope of CBI and CBI-LVC should be noticed. While both CBI and CBI-LVC were developed based on the DCR parameters using the logistic regression to build their algorithms ¹⁰, CBI can only be applied to the preoperative corneas screening to exclude the KC patients for the choice of proper LVC candidates and facilitate the timely diagnosis of KC. CBI-LVC, on the other hand, can be only applied to the postoperative corneas evaluation to diagnose post-LVC ectasia. It was recently confirmed that the corneal biomechanical properties on healthy Chinese and Caucasian corneas may be different ¹¹. The original algorithm of CBI was built based on Caucasian databases, requiring a Chinese CBI (cCBI) to bridge the gap and optimize the application of CBI for use in Chinese patients ¹². Similarly, the original study of CBI-LVC included post-LVC ectasia patients but not post-LVC stable patients from China. Hence, the inclusion of Chinese post-LVC stable patients in the CBI-LVC database would further improve the overall specificity of CBI-LVC.

To prevent post-LVC ectasia, the preoperative KC screening is continuously being improved based on corneal morphology, biomechanics ¹³⁻¹⁵, and different preoperative post-LVC ectasia risk systems, such as Ectasia Risk Score System and Percent Tissue Altered ¹⁶⁻¹⁸. For the patients who have high potential post-LVC risk, simultaneously performing prophylactic CXL with LVC may reinforce the corneal biomechanics during LVC to prevent later ectasia ¹⁹. Therefore, compared with routine post-LVC patients, it is important closely follow up the postoperative corneal biomechanics in these patients with a high

probability of post-LVC ectasia. However, the current CBI-LVC database did not include stable post-LVC patients that had undergone prophylactic CXL. Hence the inclusion of patients who combined LVC with prophylactic CXL that were proven stable could expand the applicability of CBI-LVC in clinical practice.

The current study has limitations, since it did not include post-PRK/SMILE ectasia patients. The ability of CBI-LVC to detect post-PRK/SMILE ectasia therefore needs further investigation. Although we tried to include the post-LVC ectasia and post-LVC stable patients as many as we can; still, the number of these included patients is relatively small. Including more patients may solidify this study result. Another limitation is that the follow-up time of the post-LVC stable patients was relatively short. It is unclear whether these initially stable corneas would not develop ectasia later on since the majority of the current post-LVC ectasia patients developed ectasia about 10 years after the procedure. The post-LVC stable group might therefore include several true-negative cases that could have affected the reported specificity of CBI-LVC.

In conclusion, the current study confirms that the CBI-LVC can be a useful clinical tool to detect post-LVC ectasia after LASIK. Some post-LVC eyes deemed stable, but with an increased CBI-LVC, could not be diagnosed as ectatic using tomography and need closer follow-up.

REFERENCES

1. Moshirfar M, Tukan AN, Bundogji N, et al. Ectasia After Corneal Refractive Surgery: A Systematic Review. *Ophthalmol Ther* 2021;10:753-776.
2. Salomão MQ, Hofling-Lima AL, Gomes Esporcatte LP, et al. The Role of Corneal Biomechanics for the Evaluation of Ectasia Patients. *Int J Environ Res Public Health* 2020;17.
3. Gomes JA, Tan D, Rapuano CJ, et al. Global consensus on keratoconus and ectatic diseases. *Cornea* 2015;34:359-369.
4. Vinciguerra R, Ambrósio RJ, Elsheikh A, et al. Detection of postlaser vision correction ectasia with a new combined biomechanical index. *Journal of Cataract & Refractive Surgery* 2021;47:1314-1318.
5. Lu NJ, Hafezi F, Torres-Netto EA, et al. Effect of fluence levels on prophylactic corneal cross-linking for laser in situ keratomileusis and transepithelial photorefractive keratectomy. *Acta Ophthalmol* 2023;101:e185-e196.
6. Hafezi F, Kanellopoulos J, Wiltfang R, Seiler T. Corneal collagen crosslinking with riboflavin and ultraviolet A to treat induced keratectasia after laser in situ keratomileusis. *J Cataract Refract Surg* 2007;33:2035-2040.
7. Seiler T, Koufala K, Richter G. Iatrogenic keratectasia after laser in situ keratomileusis. *J Refract Surg* 1998;14:312-317.
8. Randleman JB, Russell B, Ward MA, Thompson KP, Stulting RD. Risk factors and prognosis for corneal ectasia after LASIK. *Ophthalmology* 2003;110:267-275.
9. Brar S, Roopashree CR, Ganesh S. Incidence of Ectasia After SMILE From a High-Volume Refractive Surgery Center in India. *J Refract Surg* 2021;37:800-808.
10. Vinciguerra R, Ambrósio R, Jr., Elsheikh A, et al. Detection of Keratoconus With a New Biomechanical Index. *J Refract Surg* 2016;32:803-810.
11. Vinciguerra R, Herber R, Wang Y, et al. Corneal Biomechanics Differences Between Chinese and Caucasian Healthy Subjects. *Front Med (Lausanne)* 2022;9:834663.
12. Vinciguerra R, Ambrosio R, Wang Y, et al. Detection of Keratoconus with a new Corvis Biomechanical Index Optimized for Chinese Population (cCBI). *Am J Ophthalmol* 2023.
13. Ambrósio R, Randleman JB. Screening for Ectasia Risk: What Are We Screening For and How Should We Screen For It? *Journal of Refractive Surgery* 2013;29:230-232.
14. Asroui L, Dupps WJ, Jr., Randleman JB. Determining the Utility of Epithelial Thickness Mapping in Refractive Surgery Evaluations. *Am J Ophthalmol* 2022;240:125-134.
15. Lu N-J, Koppen C, Hafezi F, et al. Combinations of Scheimpflug tomography, ocular coherence tomography and air-puff tonometry improve the detection of keratoconus. *Contact Lens and Anterior Eye* 2023;101840.
16. Randleman JB, Woodward M, Lynn MJ, Stulting RD. Risk Assessment for Ectasia after

Corneal Refractive Surgery. *Ophthalmology* 2008;115:37-50.e34.

17. Santhiago MR, Smadja D, Gomes BF, et al. Association between the percent tissue altered and post-laser in situ keratomileusis ectasia in eyes with normal preoperative topography. *Am J Ophthalmol* 2014;158:87-95.e81.
18. Santhiago MR, Smadja D, Wilson SE, Krueger RR, Monteiro ML, Randleman JB. Role of percent tissue altered on ectasia after LASIK in eyes with suspicious topography. *J Refract Surg* 2015;31:258-265.
19. Kanellopoulos AJ. Long-term safety and efficacy follow-up of prophylactic higher fluence collagen cross-linking in high myopic laser-assisted in situ keratomileusis. *Clin Ophthalmol* 2012;6:1125-1130.

Chapter 7

Epithelium-on CXL Provides a Similar Biomechanical Effect as Accelerated Epithelium-off CXL

Nan-Ji Lu, Emilio A. Torres-Netto, M Enes Aydemir, Sabine Kling, Nikki Hafezi, Farhad Hafezi

In preparation

ABSTRACT

Purpose: To compare the corneal biomechanical stiffening effect of a new epithelium-on corneal cross-linking (epi-on CXL) protocol without iontophoresis and without additional oxygen with a broadly used epithelium-off (epi-off) CXL.

Methods: One hundred and fifty porcine eyes were assigned equally into three study groups: epi-on, epi-off, and controls. A manual abrasion was performed in the epi-off CXL group. For the epi-on and control groups: a penetration enhancer solution was applied to the corneal surface before soaking with 0.1% hypo-osmolar riboflavin solution without a carrier. In the epi-off group, the same riboflavin solution was applied directly. The epi-on and epi-off groups were irradiated at 365 nm UV-A light: in the epi-on group, 18 mW/cm² pulsed UV-A light for 15 mins was applied (fluence 8.1 J/cm²); in the epi-off group, 9 mW/cm² continuous UV-A light for 10 mins was applied (fluence 5.4 J/cm²). Stress-strain extensimetry was performed to assess the corneal biomechanics.

Results: The mean elastic modulus (Young's modulus) as a function between 5% and 10% of strain was 5.21 ± 1.58 , 4.95 ± 1.50 , and 4.01 ± 1.41 N/mm in epi-on, epi-off, and controls, respectively. There were no significant differences in the elastic modulus between two cross-linked groups ($P = 0.45$), but significant differences were found between the two cross-linked groups and controls ($P < 0.001$ and $= 0.001$, respectively).

Conclusion: This new epi-on CXL protocol provides a stiffening effect similar to the most commonly used epi-off CXL protocol and has the potential to clinically replace the latter.

INTRODUCTION

Keratoconus (KC) is a corneal biomechanics decreasing disease, characterized by progressive thinning and steepening of the cornea with corneal astigmatism¹. As the disease progresses, corneal hydrops occurs, resulting in further vision impairment and eventually in corneal blindness. Corneal cross-linking (CXL), the application of ultraviolet A (UV-A) light and riboflavin to create covalent bonds between collagen and the proteoglycans of the extracellular matrix to increase corneal biomechanics, is currently the only technique to halt the progression of KC².

The first established CXL protocol was the Dresden protocol, which applies 3 mW/cm² UV-A light for continuous 30 minutes irradiation after the epithelium removal (epithelium-off)³. Although its long-term success rate is high⁴, it is time-consuming and limited to the application of corneas with a stromal thickness of more than 400 μ m. Therefore, other accelerated epithelium-off CXL protocols were proposed when considering the limitation of oxygen on cross-linking efficiency⁵. However, the epithelium-off CXL may cause potential complications, such as serious postoperative pain, delayed epithelium recovery, serious haze, and infection⁶⁻⁸. Therefore, the protocols of CXL without epithelium removal (epithelium-on) were proposed.

The transmission of UV-A light, the saturation of riboflavin, and the diffusion of oxygen are three key elements of CXL⁹. While the intact epithelium in epithelium-on CXL decreases the penetration of riboflavin, consumes oxygen, and prevents the UV-A light irradiation, to address these limitations, riboflavin with different concentration or solutions¹⁰, the iontophoresis-CXL (I-CXL)¹¹, and the oxygen-boost CXL were developed and even implemented collaboratively^{12, 13}. However, the requirements for additional devices and the preparation of various forms of riboflavin for different stages and status of KC increase the complexity of CXL operations and the cost of CXL treatment. Therefore, after sorting out the relationship between the above three elements, we invented an independent epithelium penetration enhancer while using the

same riboflavin (0.1% hypo-osmolar without carriers) as the epithelium-off CXL and proposed a new combined epithelium-on CXL protocol.

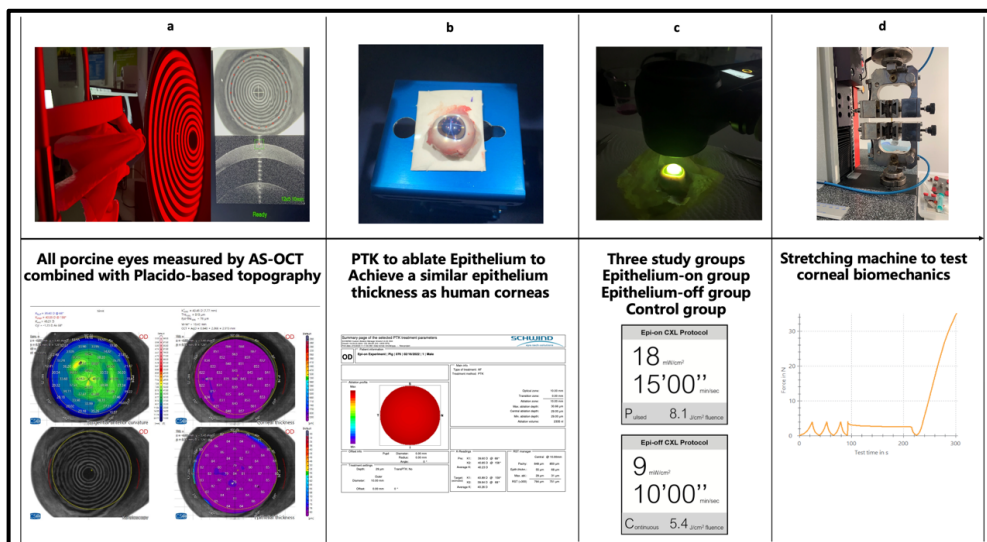
The aim of this study was to investigate whether this new epithelium-on CXL protocol facilitated with the epithelium penetration enhancer can achieve an equivalent corneal biomechanical stiffening effect as an accelerated epithelium-off CXL protocol which being widely applied now.

MATERIALS and METHODS

Groups Setting and Cornea Preparation

One hundred fifty freshly enucleated porcine eyes with an intact epithelium and no scars were obtained from a local slaughterhouse (Zurich, Switzerland) and used within 8 hours. Eyes were randomly assorted into three study groups (n = 50 for each group) and named them respectively as the epithelium-on group,

Figure 1: Main experimental steps



(a) AS-OCT combined with corneal Placido-based topography was performed to measure porcine corneas; (b) PTK was conducted to ablate porcine eyes in Epithelium-on and Control groups; (c) Two different CXL protocols were applied in Epithelium-on and Epithelium-off groups; (d) Corneal biomechanics was tested in all porcine corneas by a stress-strain extensometer. AS-OCT, anterior-segment optical coherence tomography; PTK, phototherapeutic keratectomy; CXL, corneal cross-linking

epithelium-off group, and control group. For all the eyes, anterior segment optical coherence tomography (AS-OCT) combined with corneal Placido-based topography was performed (MS-39, CSO Italia, Firenze, Italy) (**Figure 1a**); the corneal epithelial and total thickness, as well as the corneal curvature information, were recorded.

For porcine eyes in the epithelium-on and control groups, the excimer laser phototherapeutic keratectomy (PTK) was performed using the Amaris 750S excimer laser (Schwind eye-tech solutions GmbH, Kleinostheim, Germany) (**Figure 1b**). Based on the measured epithelial thickness, the epithelium ablation depth of PTK was calculated, resulting in the remaining central epithelial thickness reaching at 55 μm . The PTK ablation scope was set at a maximum of 10 mm for all ablated eyes. For all eyes in epithelium-off group, the hocky knife was used to remove the epithelium.

CXL Procedures and Protocols

After the preparation of all the porcine corneas, 0.4% Oxybuprocaine (Théa Pharma, Schaffhausen, Switzerland) once a minute for 3 minutes was applied. For the epithelium-on and control groups, the penetration enhancer (Bichsel AG, Interlaken, Switzerland) was applied to the corneal surface every 30 seconds for total 10 minutes. Then, after waiting for 5 minutes, the corneal surface was rinsed off with balanced salt solution (BSS), and 0.1% hypo-osmolar riboflavin solution without carrier (Ribo-Ker, EMAGine, Zug, Switzerland) was applied to the corneal surface every 20 seconds for 20 minutes. While for the epithelium-off group, without the application of the penetration enhancer, the same riboflavin-dropping protocol was directly applied.

All corneas (except for the corneas in the control group) were then irradiated with 365 nm UV-A light using a same cross-linking device (C-eye; EMAGine AG, Zug, Switzerland). For the epithelium-on group, 18 mW/cm^2 pulsed UV-A light (1 second on/ 1 second off) for 15 minutes was applied, resulting in a total irradiation energy of 8.1 J/cm^2 ; While for the epithelium-off group, 9 mW/cm^2

continuous UV-A light for 10 minutes was applied, resulting in a total irradiation energy of 5.4 J/cm² (**Figure 1c**).

Before the biomechanical measurements, the corneoscleral button was taken in all the corneas. In each cornea, two corneoscleral strips of 5 mm width were prepared centrally in the horizontal axis. To standardize the hydration of all corneas, all the corneoscleral strips were put in 400 mOsmol/L phosphate buffered saline (PBS) solution for 15 minutes.

Biomechanical Stress-Strain Measurements

Stress-strain extensometry was performed as described previously^{14, 15}. In brief, 4 mm of the ends of each corneoscleral strip were dedicated to fixation, leaving approximately 11 mm of central corneal strip length to undergo extensometry. A stress-strain extensometer (Z0.5; Zwick GmbH & Co., Ulm, Germany) was used to perform tensile strength measurements (**Figure 1d**), calibrated with a distance accuracy of 2 mm and a tensile sensor with $\leq 0.21\%$ of measurement uncertainty between 0.25 Newton (N) and 50 N. The extensometer has a linear holder extension arm that moved with a controllable speed, and the instrument was able to measure the real-time force in N exerted by the arm on the held specimen. The force to stress conversion was calculated from the width and thickness of the specimen. In the conditioning cycles, the arm speed was 2 mm/minute; during the test phase, the position was controlled at the point where load was applied.

The biomechanical characterization included elastic testing up to 4 N standard force. For the analysis, the stress-strain curve was considered, as its slope corresponds to the tangent elastic modulus and was determined between 5% to 10% of strain. Data analysis was performed using the Xpert II-Testing Software (Zwick GmbH & Co., Ulm, Germany).

Statistical Analysis

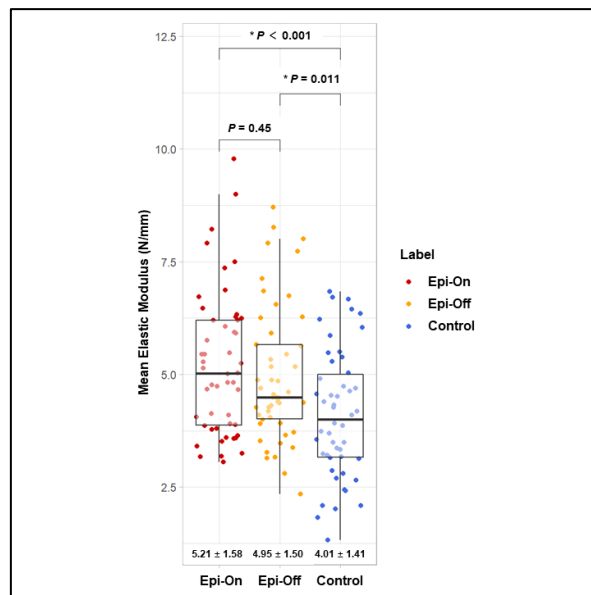
Statistical analysis was conducted using R software (version 4.2.0, R Foundation for Statistical Computing, Vienna, Austria). A Shapiro-Wilks test

was applied to verify the normality of data distribution. Descriptive statistics were described as mean \pm standard deviation. Either a one-way analysis of variance (ANOVA) or a Kruskal-Wallis H test was conducted for continuous variables to analyze the equivalence among all groups. A value of $P < 0.05$ was considered statistically significant.

RESULTS

The mean elastic modulus (Young's modulus) as a function between 5% and 10% of strain was 5.21 ± 1.58 N/mm, 4.95 ± 1.50 N/mm, and 4.01 ± 1.41 N/mm in the epithelium-on, epithelium-off, and control groups, respectively. The distributions and comparisons between groups are shown in **Figure 2**. There were no significant differences in the elastic modulus between the epithelium-on and epithelium-off groups ($P = 0.45$), but significant differences were found between two cross-linked groups with the control group ($P < 0.001$ and $= 0.001$, respectively).

Figure 2: The distributions and comparisons of porcine corneas' mean elastic modulus (Young's modulus) among three study groups



Epi-on, epithelium-on; Epi-off, epithelium-off

DISCUSSION

The current study proves that, without the application of iontophoresis and oxygen-boost devices, by using the epithelium penetration enhancer only, the epithelium-on CXL protocol could achieve a similar biomechanical effect as the currently wide applied accelerated epithelium-off CXL protocol. These results hold the promise of unifying and simplifying the current complex epithelium-on CXL protocols.

The corneal epithelium is composed of 5-6 layers of epithelial cells with its hydrophobic properties, it also has different types of tight junctions between them to act as a barrier of water-soluble solutions¹⁶. The CXL chromophore riboflavin is a large hydrophilic molecule and therefore difficult to penetrate through the epithelial barrier. To overcome the barrier limitation of epithelium in epithelium-on CXL, previous studies have made efforts in the following aspects: (1) the chemical method by adding tetracaine before riboflavin dropping or by modifying riboflavin solutions, such as by adding benzalkonium chloride (BAC) or ethylenediaminetetraacetic acid (EDTA) without containing dextran¹⁷, although the clinical studies showed that the long-term results are unstable^{18, 19}. (2) the mechanical methods, such as by creating stromal channels and corneal flaps^{20, 21}, which need to be validated in large scale clinical trials. (3) the I-CXL, which uses a low electrical current to create a low electric gradient to improve the riboflavin transportation. However, compared with the epithelium-off protocol, it still does not achieve a similar riboflavin concentration in the stroma, and it was less effective^{22, 23}. In addition, the iontophoresis method is also difficult to operate and there is a risk of the loss suction of corneal applicator. Therefore, based on the above experience, we developed a new independent penetration enhancer of riboflavin solution, which does not require the preparation of various riboflavin and other additional equipment.

After the limitation for the penetration of riboflavin has been solved, another limitation point that we need to consider is that the epithelium accounts for 40% of the total oxygen consumption in the cornea and blocks 20% of UV-A light transmission^{9, 24}, while the CXL efficiency is oxygen-dependent and oxygen

diffusion in the cornea is a passive process^{5, 25}, thus more oxygen is required to replenish its consumption by the epithelium during CXL. To overcome these limitations, (1) pulsed UV-A light with high-fluence CXL protocol aimed at supplying oxygen during the irradiation-off phrase and (2) oxygen goggles that deliver 100% oxygen to increase the oxygen concentration of the cornea surface were proposed. However, the epithelium-on CXL needs less exposure time to protect the intact epithelium and thus requires accelerated protocols; in addition, the oxygen-boost CXL requires additional equipment and the actual oxygen gain in the corneal stroma is also undetermined. Therefore, without the application of the oxygen boost, the irradiation mode and total energy of CXL protocols should be reconsidered.

In viewing the previous epithelium-on CXL with long-term clinical follow-ups, Mazzotta *et al.* applied I-CXL to deliver riboflavin with pulsed UV-A light and enhanced irradiation energy (18 mW/cm², 1 second on/ 1 second off, 7 J/cm²) and reported stable results after 3 years follow-up²⁶. Later, the same group of authors applied the same irradiation protocols by only using chemically enhanced riboflavin without iontophoresis and oxygen-boost and found that it could effectively halt the progression of early-stage young progressive KC patients with 3 years follow-up²⁷. For the design of the current epithelium-on CXL protocol, it comprehensively considered the three key elements during CXL and thus the total irradiation energy was optimized at 50% (from 5.4 to 8.1J/cm²) to fully compensate the consumption of oxygen and the block of UV-A light transmission by epithelium.

For the stress-strain extensimetry test, the current epithelium-on CXL showed a similar stiffing effect with the most commonly used epithelium-off protocol (9 mW/cm², 10 minutes, 5.4 J/cm²). Previous clinical studies proved that this epithelium-off protocol had long-term stable results²⁸, which was comparable with the Dresden protocol from functional outcomes perspective²⁹. In this means, the current epithelium-on CXL protocol has the potential to replace the accelerated epithelium-off protocol in the near future, although the long-term clinical study is required to test its demarcation line depth and the stability of the

keratoconic cornea after CXL. In addition, the safety of the current epithelium-on CXL protocol evaluated by the corneal endothelial cell density is also needed.

Our study has limitations. The first is the *ex-vivo* setting of this study, although its approach has been widely used methodologically, our extensimetry findings may not be fully equivalent to the *in-vivo* response. The second limitation is the structural differences between human and porcine eyes. Although porcine eyes do not have Bowman's layer, since Bowman's layer is a thin acellular layer with a random arrangement of collagen fibrils and proteoglycans³⁰, so it should be no effect on riboflavin penetration. In addition, our group's *ex-vivo* study showed that Bowman's layer does not contribute to corneal biomechanics in human corneas³¹. While the epithelial thickness of porcine eyes is much thicker than humans³², in this study, PTK was applied for ablating the porcine eyes to best simulate the epithelial profile of the humans.

In conclusion, after comprehensively considering the three key elements during CXL, this new epi-on CXL protocol provides a stiffening effect equivalent to the most commonly used epi-off CXL protocol and has the potential to clinically replace the latter.

REFERENCES

1. Roberts CJ, Dupps WJ, Jr. Biomechanics of corneal ectasia and biomechanical treatments. *J Cataract Refract Surg* 2014;40:991-998.
2. Randleman JB, Khandelwal SS, Hafezi F. Corneal cross-linking. *Surv Ophthalmol* 2015;60:509-523.
3. Wollensak G, Spoerl E, Seiler T. Riboflavin/ultraviolet-a-induced collagen crosslinking for the treatment of keratoconus. *Am J Ophthalmol* 2003;135:620-627.
4. Raiskup F, Herber R, Lenk J, et al. Corneal Crosslinking With Riboflavin and UVA Light in Progressive Keratoconus: Fifteen-Year Results. *Am J Ophthalmol* 2023;250:95-102.
5. Richoz O, Hammer A, Tabibian D, Gatziofias Z, Hafezi F. The Biomechanical Effect of Corneal Collagen Cross-Linking (CXL) With Riboflavin and UV-A is Oxygen Dependent. *Transl Vis Sci Technol* 2013;2:6.
6. Murchison CE, Petroll WM, Robertson DM. Infectious keratitis after corneal crosslinking: systematic review. *J Cataract Refract Surg* 2021;47:1075-1080.
7. Mazzotta C, Balestrazzi A, Baiocchi S, Traversi C, Caporossi A. Stromal haze after combined riboflavin-UVA corneal collagen cross-linking in keratoconus: in vivo confocal microscopic evaluation. *Clin Exp Ophthalmol* 2007;35:580-582.
8. Koller T, Mrochen M, Seiler T. Complication and failure rates after corneal crosslinking. *J Cataract Refract Surg* 2009;35:1358-1362.
9. Hafezi F. Corneal Cross-Linking: Epi-On. *Cornea* 2022;41:1203-1204.
10. Gatziofias Z, Raiskup F, O'Brart D, Spoerl E, Panos GD, Hafezi F. Transepithelial Corneal Cross-linking Using an Enhanced Riboflavin Solution. *J Refract Surg* 2016;32:372-377.
11. Vinciguerra P, Randleman JB, Romano V, et al. Transepithelial iontophoresis corneal collagen cross-linking for progressive keratoconus: initial clinical outcomes. *J Refract Surg* 2014;30:746-753.
12. Mazzotta C, Sgheri A, Bagaglia SA, Rechichi M, Di Maggio A. Customized corneal crosslinking for treatment of progressive keratoconus: Clinical and OCT outcomes using a transepithelial approach with supplemental oxygen. *Journal of Cataract & Refractive Surgery* 2020;46:1582-1587.
13. Matthys A, Cassagne M, Galiacy SD, El Hout S, Fournié P, Malecaze F. Transepithelial Corneal Cross-linking With Supplemental Oxygen in Keratoconus: 1-Year Clinical Results. *J Refract Surg* 2021;37:42-48.
14. Abdshahzadeh H, Abrishamchi R, Aydemir ME, et al. Repeated application of riboflavin during corneal cross-linking does not improve the biomechanical stiffening effect ex vivo. *Experimental Eye Research* 2022;224:109267.
15. Abrishamchi R, Abdshahzadeh H, Hillen M, et al. High-Fluence Accelerated

- Epithelium-Off Corneal Cross-Linking Protocol Provides Dresden Protocol-Like Corneal Strengthening. *Translational Vision Science & Technology* 2021;10:10.
16. Yi X-j, Wang Y, Yu F-SX. Corneal Epithelial Tight Junctions and Their Response to Lipopolysaccharide Challenge. *Investigative Ophthalmology & Visual Science* 2000;41:4093-4100.
 17. Raiskup F, Pinelli R, Spoerl E. Riboflavin osmolar modification for transepithelial corneal cross-linking. *Curr Eye Res* 2012;37:234-238.
 18. Koppen C, Wouters K, Mathysen D, Rozema J, Tassignon MJ. Refractive and topographic results of benzalkonium chloride-assisted transepithelial crosslinking. *J Cataract Refract Surg* 2012;38:1000-1005.
 19. Caporossi A, Mazzotta C, Paradiso AL, Baiocchi S, Marigliani D, Caporossi T. Transepithelial corneal collagen crosslinking for progressive keratoconus: 24-month clinical results. *Journal of Cataract & Refractive Surgery* 2013;39:1157-1163.
 20. Seiler TG, Fischinger I, Senfft T, Schmidinger G, Seiler T. Intrastromal Application of Riboflavin for Corneal Crosslinking. *Investigative Ophthalmology & Visual Science* 2014;55:4261-4265.
 21. Armstrong BK, Lin MP, Ford MR, et al. Biological and Biomechanical Responses to Traditional Epithelium-Off and Transepithelial Riboflavin-UVA CXL Techniques in Rabbits. *Journal of Refractive Surgery* 2013;29:332-341.
 22. Mastropasqua L, Nubile M, Calienno R, et al. Corneal cross-linking: intrastromal riboflavin concentration in iontophoresis-assisted imbibition versus traditional and transepithelial techniques. *Am J Ophthalmol* 2014;157:623-630.e621.
 23. Bikbova G, Bikbov M. Standard corneal collagen crosslinking versus transepithelial iontophoresis-assisted corneal crosslinking, 24 months follow-up: randomized control trial. *Acta Ophthalmol* 2016;94:e600-e606.
 24. Freeman RD. Oxygen consumption by the component layers of the cornea. *J Physiol* 1972;225:15-32.
 25. Kling S, Richoz O, Hammer A, et al. Increased Biomechanical Efficacy of Corneal Cross-linking in Thin Corneas Due to Higher Oxygen Availability. *J Refract Surg* 2015;31:840-846.
 26. Mazzotta C, Bagaglia SA, Sgheri A, et al. Iontophoresis Corneal Cross-linking With Enhanced Fluence and Pulsed UV-A Light: 3-Year Clinical Results. *Journal of Refractive Surgery* 2020;36:286-292.
 27. Mazzotta C, Balamoun AA, Chabib A, et al. Transepithelial Enhanced Fluence Pulsed Light M Accelerated Crosslinking for Early Progressive Keratoconus with Chemically Enhanced Riboflavin Solutions and Air Room Oxygen. *Journal of Clinical Medicine* 2022;11:5039.
 28. Mazzotta C, Raiskup F, Hafezi F, et al. Long term results of accelerated 9 mW corneal

crosslinking for early progressive keratoconus: the Siena Eye-Cross Study 2. *Eye and Vision* 2021;8:1-12.

29. Lang PZ, Hafezi NL, Khandelwal SS, Torres-Netto EA, Hafezi F, Randleman JB. Comparative functional outcomes after corneal crosslinking using standard, accelerated, and accelerated with higher total fluence protocols. *Cornea* 2019;38:433-441.
30. Wilson SE. Bowman's layer in the cornea- structure and function and regeneration. *Exp Eye Res* 2020;195:108033.
31. Torres-Netto EA, Hafezi F, Spuru B, et al. Contribution of Bowman layer to corneal biomechanics. *J Cataract Refract Surg* 2021;47:927-932.
32. Kling S, Remon L, Pérez-Escudero A, Merayo-Llodes J, Marcos S. Corneal Biomechanical Changes after Collagen Cross-Linking from Porcine Eye Inflation Experiments. *Investigative Ophthalmology & Visual Science* 2010;51:3961-3968.

Chapter 8

The Antibacterial Efficacy of High-Fluence PACK Cross-Linking can be Accelerated

Nan-Ji Lu, Hendrik Koliwer-Brandl, Francesca Gilardoni, Nikki Hafezi, Boris Knyazer, Asaf Achiron, Reinhard Zbinden, Adrian Egli, Farhad Hafezi

Transl Vis Sci Technol. 2023 Feb 1;12(2):12

ABSTRACT

Purpose: To determine whether high-fluence photoactivated chromophore for keratitis cross-linking (PACK-CXL) can be accelerated.

Methods: Solutions of *Staphylococcus aureus* and *Pseudomonas aeruginosa* with 0.1% riboflavin were prepared and exposed to 365 nm ultraviolet (UV)-A irradiation of intensities and fluences from 9 to 30 mW/cm² and from 5.4 to 15.0 J/cm², respectively, representing nine different accelerated PACK-CXL protocols. Irradiated solutions and unirradiated controls were diluted, plated, and inoculated on agar plates so that bacterial killing ratios (BKR) could be calculated. Additionally, strains of *Achromobacter xylosoxidans*, *Staphylococcus epidermidis*, and *Stenotrophomonas maltophilia* were exposed to a single accelerated PACK-CXL protocol (intensity: 30 mW/cm², total fluence: 15.0 J/cm²).

Results: With total fluences of 5.4, 10.0, and 15.0 J/cm², the range of mean BKR for *S. aureus* was 45.78%-50.91%, 84.13%-88.16%, and 97.50%-99.90%, respectively; the mean BKR for *P. aeruginosa* was 69.09%-70.86%, 75.37%-77.93%, and 82.27%-91.44%, respectively. Mean BKR was 41.97% for *A. xylosoxidans*, 65.38% for *S. epidermidis*, and 78.04% for *S. maltophilia* for the accelerated PACK-CXL protocol (30 mW/cm², 15 J/cm²).

Conclusion: The BKR of high-fluence PACK-CXL protocols can be accelerated while maintaining a high, but species-dependent BKR. The Bunsen-Roscoe law is respected in fluences up to 10 J/cm² in *S. aureus* and *P. aeruginosa*, whereas fluences above 10 J/cm² show strain dependence.

Translational Relevance: The high-fluence PACK-CXL protocols can be accelerated in clinical practice while maintaining high levels of BKR.

INTRODUCTION

Infectious keratitis is a significant and frequent cause of ocular morbidity ^{1,2}. Typically, the infection requires urgent and repeated treatment, which involves the intense and continuous application of antimicrobial agents ^{3,4}. Most cases are bacterial, fungal, or mixed (bacterial/fungal) in origin, however, the timely identification of the causative organism(s) and selection of the most appropriate antimicrobial agent(s) sometimes can be challenging ⁵. Unfortunately, increasing antimicrobial resistance (AMR) continues to reduce the number of effective treatment options, leading to a growing need for new infectious keratitis treatments to overcome the challenge of AMR. Photoactivated chromophore for keratitis-corneal cross-linking (PACK-CXL) represents one such approach ⁶.

Corneal cross-linking (CXL), originally developed for the treatment of corneal ectasia, involves the saturation of the cornea with a chromophore, which is then photoactivated *in situ*. Typically, the chromophore is riboflavin, which is photoactivated with 365 nm ultraviolet-A (UV-A) light, generating riboflavin radicals and reactive oxygen species (ROS). The latter has multiple effects: (1) the covalent bonds between collagen molecules and proteoglycans of the extracellular matrix increase biomechanical stiffness to prevent the corneal penetration; (2) increased steric hindrance and altered access to metalloproteinase cleavage sites render the corneal stroma more resistant to enzymatic digestion generated by various pathogens, thus decreasing the size of corneal scars after the end of infectious course; and (3) increased oxidative stress induces a direct damaging effect on the cell membranes and nucleic acids of any bacterial and fungal pathogens present ⁷. PACK-CXL has been successfully applied for killing bacteria and fungi in experiments, it has also been shown to be effective alone, and in combination with standard-of-care antimicrobial therapy in clinical practices ⁸⁻¹².

We have previously shown *in-vitro* that high-fluence PACK-CXL distinctly increases the BKR ¹³. The purpose of this study was to determine whether high-fluence PACK-CXL can be accelerated while maintaining its similar anti-

bacterial efficacy, as accelerated high-fluence protocols are not only more time-saving but also more suitable to be applied at the slit lamp, giving more convenient access to the treatments and a better and more comfortable treatment experience for patients.

MATERIALS and METHODS

Bacterial Strains and UV-A Light Device

Bacterial strains are independent clinical isolates of corneal infections: *Staphylococcus aureus* (methicillin-sensitive), *Pseudomonas aeruginosa*, *Achromobacter xylosoxidans*, *Staphylococcus epidermidis*, and *Stenotrophomonas maltophilia*, isolated at the Institute of Medical Microbiology, University of Zurich. The same portable 365 nm UV-light source with a fixed 12 mm irradiation spot, which covered each single 96 empty plate aperture (C-Eye; EMAGine AG, Zug, Switzerland), was used to perform all UV-A irradiations.

Preparation of Bacterial Solutions

Colonies of all bacterial strains from overnight subcultures on Colombia agar + 5% sheep blood (COS, bioMérieux, Marcy l'Etoile, France) were suspended in sterile 0.9% NaCl and adjusted to McFarland 0.5, corresponding to approximately 10^8 colony forming units (CFU)/mL, in the tubes. Then, the bacterial solutions were diluted 10-fold to 10^7 CFU/mL in the 96-well microtiter plates (Costar Assay Plate, Corning Incorporated, NY, USA) that contained a final concentration of 0.1% (w/v) riboflavin (hypo-osmolar 0.1% riboflavin without carriers, Ribo-Ker, EMAGine, Zug, Switzerland) or not in order to generate two kinds of standard samples, which were named as Control-Blank and Control-Riboflavin, respectively.

Design of PACK-CXL Protocols

Nine PACK-CXL protocols, named from **Protocol 1** to **Protocol 9**, were established. As shown in **Table 1**, three different total fluences were set, including 5.4, 10.0, and 15.0 J/cm², while these fluences were reached by variable UV-A intensities (9, 18, and 30 mW/cm², respectively). All protocols

were tested for *S. aureus* and *P. aeruginosa*, while only **Protocol 9** was tested for the remaining three bacterial strains, *A. xylosoxidans*, *S. epidermidis*, and *S. maltophilia*.

Table 1: The technical details of each PACK-CXL protocol

Protocols	Total Fluence (J/cm ²)	Irradiance Intensity (mW/cm ²)	Irradiance Time (mm' ss'')
Protocol 1	5.4	9	10'00''
Protocol 2	5.4	18	5'00''
Protocol 3	5.4	30	3'00''
Protocol 4	10.0	9	18'31''
Protocol 5	10.0	18	9'15''
Protocol 6	10.0	30	5'33''
Protocol 7	15.0	9	27'46''
Protocol 8	15.0	18	13'53''
Protocol 9	15.0	30	8'20''

PACK-CXL, photoactivated chromophore for keratitis-corneal cross-linking;
mm, minutes; ss, seconds

Experimental Procedures and Group Settings

For all bacterial strains, 11 µL of the two standard samples (Control-Blank and Control-Riboflavin) were transferred into two separate new 96-well microtiter plates and either exposed to the experimental PACK-CXL protocols or left unirradiated. Accordingly, four study groups were generated for all bacterial strains: (1) **Group A:** Control-Blank without PACK-CXL; (2) **Group B:** Control-Riboflavin without PACK-CXL; (3) **Group C:** Control-Blank with PACK-CXL; (4) **Group D:** Control-Riboflavin with PACK-CXL. For Groups C and D, based on the PACK-CXL protocols, various protocols were applied correspondingly for all bacterial strains.

After performing PACK-CXL or not, the suspensions of all groups were 10-fold diluted three times to a concentration of approximately 10⁵ CFU/mL. Ten µL of the final dilution were then plated on the COS agar and incubated at 37°C for 24 hours to determine the bacterial reduction after irradiation. In order to

address both biological and experimental variability to obtain reliable and stable results, all experiments were repeated using multiple independent bacterial solutions, each irradiation was repeated three times (technical replicate) and the whole experiment was repeated on three different days (biological replicate), resulting in a total of nine irradiations.

Bacterial CFUs: Counting and Analysis

After incubation, all agar plates were photographed and the number of CFUs was counted. Since the load of the prepared bacterial solutions was set to McFarland 0.5, corresponding to 10^8 CFU/mL for most bacteria, when 10 μ L of the final resulting dilutions were plated, this meant that the untreated bacterial solutions (Group A and Group B) reached approximately 10^3 CFU/10 μ L on agar plates.

As described previously¹³, the BKR was calculated by comparing the CFU of each PACK-CXL irradiated plate ($CFU_{With\ PACK-CXL}$) to its corresponding control plate ($CFU_{Without\ PACK-CXL}$) (Group B vs. Group D), using the following formula:

$$BKR = \left(1 - \frac{CFU_{With\ PACK-CXL}}{CFU_{Without\ PACK-CXL}}\right) \times 100 [\%]$$

The BKRs of all bacteria strains were then compared under the same series of PACK-CXL protocols.

Statistical Analysis

Statistical analysis was conducted using SPSS version 24 (IBM Corp., Armonk, NY, USA) and the graphs were created in R software (version 4.2.0, R Foundation for Statistical Computing, Vienna, Austria). A Shapiro-Wilks test was applied to verify the normality of data distribution. Descriptive statistics were described as mean \pm standard deviation. Either a one-way analysis of variance (ANOVA) or a Kruskal-Wallis H test was conducted for continuous variables to analyze the equivalence among all groups, and post hoc tests were performed with Bonferroni correction. A p -value < 0.05 was considered as the threshold for statistical significance.

RESULTS

Quantification of Bacteria

All five strains in Groups A, B, C, and D were repeated nine times with stable results and included in the analyses. The repetitions include three biological replicates on independent days, each with three technical triplicates. For Group A (Control-Blank without PACK-CXL), the mean CFU/10 μ L were 945.22 \pm 98.83, 965.11 \pm 36.69, 994.22 \pm 30.48, 277.11 \pm 22.42, and 915.44 \pm 55.46 in *S. aureus*, *P. aeruginosa*, *A. xylosoxidans*, *S. epidermidis*, and *S. maltophilia*, respectively. For Group B (Control-Riboflavin without PACK-CXL), the average CFU/10 μ L were 932.78 \pm 64.70, 956.22 \pm 76.66, 979.33 \pm 18.23, 282.44 \pm 29.81, and 932.11 \pm 51.94 in *S. aureus*, *P. aeruginosa*, *A. xylosoxidans*, *S. epidermidis*, and *S. maltophilia*, respectively. There was no significant difference between Group A and Group B for all bacterial strains (all *p*-values > 0.05), meaning riboflavin itself has no significant bactericidal activity.

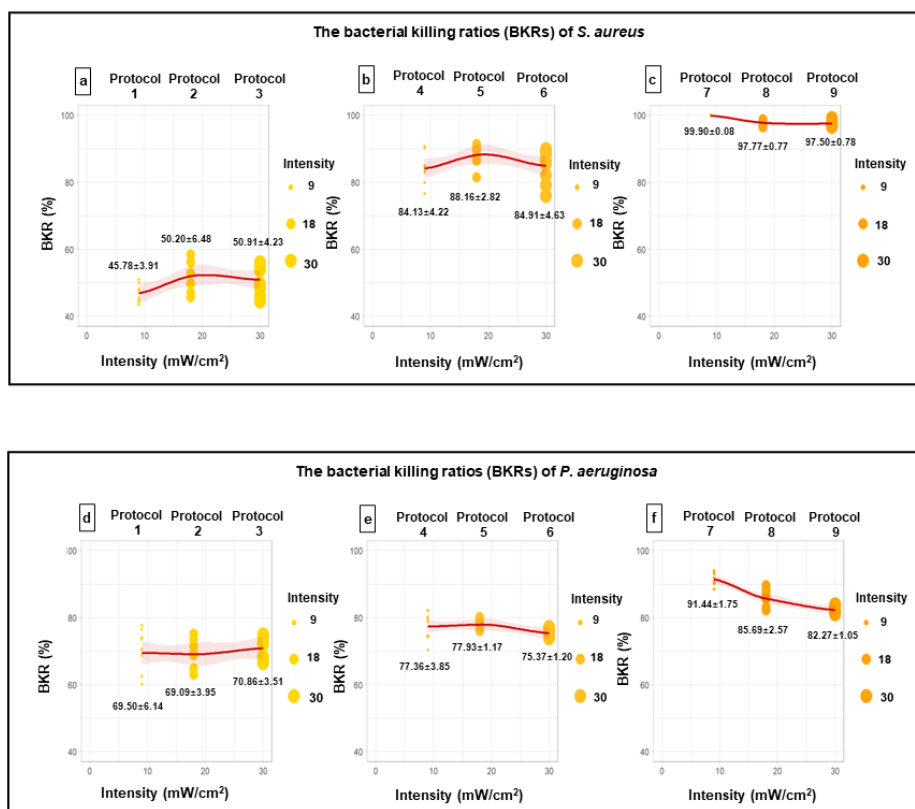
Table 2: Quantification of bacteria in CFU before and after *v* PACK-CXL protocols

	S. A	P. A	S. A	P. A	S. A	P. A
	Protocol 1		Protocol 4		Protocol 7	
Group C	787.3 \pm 16.3	333.4 \pm 37.7	703.4 \pm 20.5	252.8 \pm 23.7	360.3 \pm 39.3	172.7 \pm 16.0
Group D	505.8 \pm 36.5	279.4 \pm 56.3	148.0 \pm 39.3	207.4 \pm 35.3	0.89 \pm 0.74	78.4 \pm 16.0
<i>p</i>	< 0.001	0.038	< 0.001	0.007	< 0.001	< 0.001
	Protocol 2		Protocol 5		Protocol 8	
Group C	779.6 \pm 28.8	346.78 \pm 32.1	533.7 \pm 46.1	259.6 \pm 44.41	290.6 \pm 45.0	223.2 \pm 58.43
Group D	464.6 \pm 60.5	283.2 \pm 36.2	110.4 \pm 26.3	202.2 \pm 11.3	26.00 \pm 19.92	131.1 \pm 23.4
<i>p</i>	< 0.001	0.002	< 0.001	0.003	< 0.001	< 0.001
	Protocol 3		Protocol 6		Protocol 9	
Group C	764.2 \pm 35.1	346.3 \pm 68.4	529.9 \pm 97.7	275.1 \pm 34.1	366.8 \pm 47.0	239.8 \pm 35.4
Group D	457.9 \pm 39.4	267.0 \pm 32.1	140.8 \pm 43.2	225.67 \pm 10.95	23.3 \pm 7.3	162.4 \pm 9.7
<i>p</i>	< 0.001	0.007	< 0.001	0.001	< 0.001	< 0.001

After PACK-CXL, the bacterial solutions were diluted to reach at the maximum approximately 10^3 CFU on agar for CFU determination. S. A., *S. aureus*; P.A., *P. aeruginosa*; CFU, colony-forming units; PACK-CXL, photoactivated chromophore for keratitis-corneal cross-linking

For Group C (Control-Blank with PACK-CXL; without Riboflavin) and Group D (Control-Riboflavin with PACK-CXL), the average CFU/10 μ L and comparisons of *S. aureus* and *P. aeruginosa* for all protocols are shown in **Table 2**. For Group C, the average CFU/10 μ L was 825.89 ± 37.54 , 230.67 ± 20.83 , and 612.44 ± 21.87 in *A. xylosoxidans*, *S. epidermidis*, and *S. maltophilia*, respectively; for Group D, the average CFU/10 μ L was 568.44 ± 43.66 , 97.78 ± 16.80 , and 204.67 ± 10.39 in *A. xylosoxidans*, *S. epidermidis*, and *S. maltophilia*, respectively. Statistical differences were found between Group C and Group D in *A. xylosoxidans*, *S. epidermidis*, and *S. maltophilia* (all p -values < 0.001), showing that the bactericidal activity was enhanced by the addition of riboflavin (Group D) compared to the UV-A light irradiation (Group C).

Figure 1: The Bacterial Killing Ratios (BKR) of *S. aureus* (a, b, c) and *P. aeruginosa* (d, e, f) under the same total fluence of 5.4 J/cm² (Protocols 1-3), 10.0 J/cm² (Protocols 4-6), and 15.0 J/cm² (Protocols 7-9) with different irradiation intensity

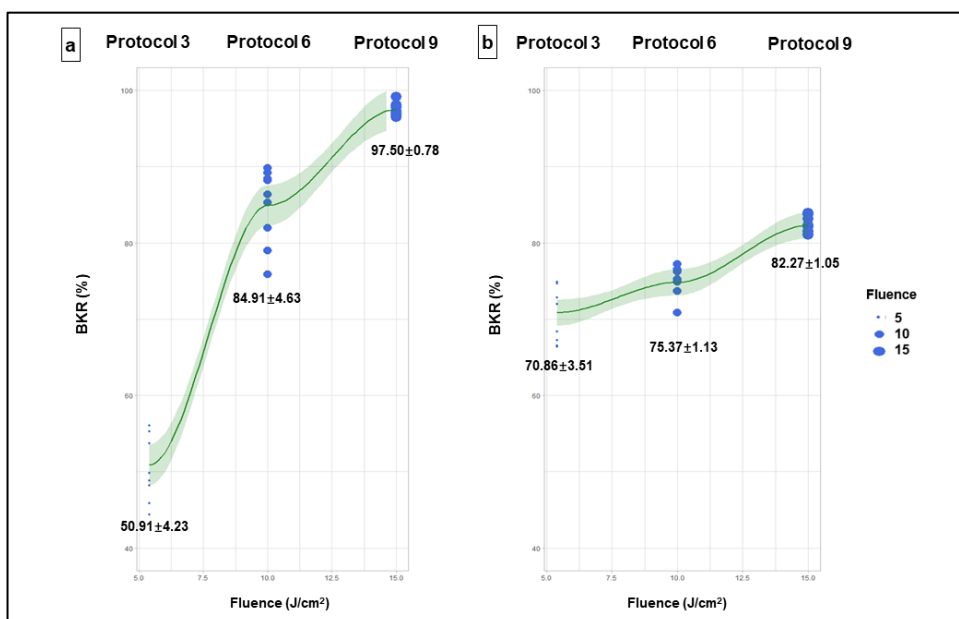


BKRs in *S. aureus* and *P. aeruginosa*

As shown in **Figure 1a, 1b, 1d, and 1e**, shorter irradiation time maintaining a total fluence of 5.4 or 10.0 J/cm² did not appear to have a negative effect on the BKR ($p = 0.106, 0.120, 0.284,$ and $0.105,$ respectively). In the 15.0 J/cm² total fluence protocols (Protocols 7-9), increasing acceleration (higher UV intensity, shorter duration) resulted in a statistically significant decrease of BKR in both *S. aureus* (Protocol 7 vs. Protocols 8 and 9, both $p < 0.001$; Protocol 8 vs. Protocol 9, $p = 0.404$) (**Figure 1c**) and *P. aeruginosa* (Protocol 7 vs. Protocols 8 and 9, Protocol 8 vs. Protocol 9, all p -values < 0.001) (**Figure 1f**).

Using an irradiation intensity of 30 mW/cm² with fluences of 5.4 (Protocol 3), 10.0 (Protocol 6), and 15.0 J/cm² (Protocol 9), the mean BKR of *S. aureus* was 50.91%, 84.91%, and 97.50%, respectively (**Figure 2a**); while the mean BKR of *P. aeruginosa* was 70.86%, 75.34%, and 82.27%, respectively (**Figure 2b**). The statistical analyses showed that the increase in BKR was significant with increasing fluences (all p -values < 0.001).

Figure 2: The bacterial killing ratios (BKRs) of *S. aureus* (a) and *P. aeruginosa* (b) under the same irradiation intensity (30 mW/cm²) with three different total fluences (Protocol 3, Protocol 6, and Protocol 9)



Comparisons of PACK-CXL Induced BKR Under Protocol 9

The average PACK-CXL induced BKR was 97.50% for *S. aureus*, compared to 82.27%, 41.97%, 65.38%, and 78.04% for *P. aeruginosa*, *A. xylosoxidans*, *S. epidermidis*, and *S. maltophilia*, respectively. Across all strains, a statistical difference was found between every two strains (all p -values < 0.001).

DISCUSSION

This *in-vitro* study tried to prove that, besides the bactericidal effect of UV-A light itself, the bacterial killing effect induced by accelerated high-fluence PACK-CXL could effectively reduce the bacterial concentration of several clinically significant bacterial strains obtained from the clinical corneal infection samples, while the Bunsen-Roscoe law of reciprocity was still simultaneously followed at the relatively high total fluence level.

For the bacterial strains investigated in the current study, in bacterial keratitis and more specifically in contact lens-associated keratitis, *S. aureus* represents the most common Gram-positive organism, while *P. aeruginosa* is the most common Gram-negative organism. Both strains might rapidly lead to vision-threatening keratitis^{14, 15}. In addition, *S. epidermidis* is one of the most commonly implicated pathogens in polymicrobial keratitis¹⁴. The other strains (*A. xylosoxidans* and *S. maltophilia*) investigated here were chosen as the references for emerging, multidrug-resistant pathogens¹⁶⁻¹⁸.

In the current study, in order to objectively investigate the bacterial killing effect induced by PACK-CXL, we have first proven that the chromophore itself - riboflavin - did not influence bacterial growth. We also noticed that, except for *S. epidermidis*, the number of the CFUs in all other bacterial strains without PACK-CXL (in Group A and Group B) was close to 10^3 in the final diluted solutions. This may be explained by the fact that some strains, especially Gram-positive bacteria, form strong clusters that have an influence on turbidity measurements¹⁹. Therefore, it seems to be true for this certain *S. epidermidis* strain, where the McFarland 0.5 solution reached only approximately 0.25×10^8

CFU/mL. Then, the UV-A light irradiation was applied in the bacteria solution which contains riboflavin (Group D) or not (Group C) to directly confirm that these bacterial killing effects were not induced by UV-A light only and the PACK-CXL induced bacterial killing effects were relevant (**Table 2**). Interestingly, neither Gram status (Gram-positive: *S. aureus* and *S. epidermidis*) nor the aerobic/anaerobic state of the bacterial strains seemed to be predictive of PACK-CXL BKR efficacy, postulating rather a protective effect due to the properties of the bacterial cell wall, e.g., molecular composition, thickness or charge. This composition is often not only bacterial species-dependent, but might even be different between strains of the same species ²⁰.

For the PACK-CXL protocol settings, as per our previous study findings ¹³, we once again found that, when higher total fluence PACK-CXL protocols were applied in all bacterial strains, the BKR would correspondingly increase. One potential concern might be if the higher total fluence PACK-CXL protocols were applied in clinical practice, the high fluence might potentially risk causing damage to the corneal endothelium. However, for CXL in transparent keratoconic and myopic corneas, previous studies have investigated the safety of the endothelium ^{21, 22}, showing that accelerated CXL protocols with total fluences of up to 15J/cm² did not affect endothelial cell density. Similarly, Seiler *et al.* have recently shown that the damage threshold of the corneal endothelium in transparent corneas might be substantially higher than previously anticipated ²³. Unlike keratoconic and myopic corneas, corneas with bacterial keratitis usually display edema and are opaque, reducing UV-A transmission through the stroma. This should further lower the potential risk of endothelial cell damage caused by PACK-CXL with a total fluence of 15 J/cm² ²⁴.

The Bunsen-Roscoe law of reciprocity states that the same photochemical effect can be achieved with a reduced irradiation time and increased radiation intensity if the total dose remains the same ²⁵. Originating from photochemistry, this theoretical law should not be steadily used in biological systems. In the context of CXL research, however, this law has been discussed numerous times

in publications over the past decade²⁶. In the current study, up to a total fluence of 10 J/cm², lower irradiation intensity protocols (Protocol 1 and 4) achieved similar *S. aureus* and *P. aeruginosa* BKR to higher irradiation intensity protocols (Protocols 2 and 3 vs. Protocol 1; Protocols 6 and 7 vs. Protocol 4). However, at total fluences of 15 J/cm², when both *S. aureus* and *P. aeruginosa* were irradiated with higher intensities in a shorter time (Protocol 8 and 9), a slight decrease in BKR was observed, relative to the low-intensity protocol (Protocol 7), indicating that the Bunsen-Roscoe law was not fully respected. Nevertheless, the BKR was still highly satisfactory as it exceeded 95% in *S. aureus* and 80% in *P. aeruginosa*. Moreover, faster irradiation protocols are more easily applied in clinical practice, especially when performed in an office-based slit lamp procedure²⁷. Such an approach can allow ophthalmologists to perform a timely intervention upon the diagnosis of bacterial keratitis, which may improve patients' prognosis, relative to the normal practice of arranging the bacterial keratitis patients to be at the end of the operating room schedule to avoid introducing the pathogen to the operating room and thus delaying treatments.

The slight decrease of BKR with the 15.0 J/cm² total fluence accelerated protocols might be due to some potential rate-limiting effects that we considered: 1) the lower rate at which oxygen diffuses from the atmosphere into the reaction well plates, which may have reduced the rate of the UV-A-riboflavin photooxidative reaction²⁸; 2) the bacteria are able to survive ROS for a short while, meaning PACK-CXL treatment is too short to reach a linear kill-curve; 3) radicals are not produced fast enough in the accelerated PACK-CXL procedures. We know from CXL for ectasia that is corneal biomechanical stiffening effect decreases significantly when 5.4 J/cm² total fluence UV irradiation protocols are accelerated (18 mW/cm²)²⁹, whereas accelerated PACK-CXL-induced bacterial killing effects are similar across fluences up to 10.0 J/cm² and remain at promising levels up to at least 15.0 J/cm² fluence.

It is worth noting in this study that the chosen amount of bacteria in the wells of the microtiter plate differs from the amount present in infected corneas. However, the choice to irradiate a volume of 11 μL in a well of a 96-well plate corresponds, as previously described, to a corneal thickness of around 285 μm , which is within the known CXL penetration depth of approximately 300 μm ¹³. Moreover, we chose a very high initial bacterial load ($10^7/\text{mL}$). As shown by Badenoch *et al.*³⁰, in a rat model for bacterial keratitis, the maximum bacterial count of 10^7 was found 48 hours after infection.

The *in-vitro* setting is a limitation of this study, because it does neither consider the role of the extracellular matrix, nor the eventual immune response. At the same time, the presence of an immune response and the concomitant use of antibiotics might enhance the positive effect of PACK-CXL. The *ex-vivo* study is indicated for us to validate the results of the current study. In addition, further experiments are required to investigate the safety of high-fluence PACK-CXL in infected corneas and the actual role of oxygen in PACK-CXL. After these experiments are completed, we will conduct a multi-center large-scale clinical randomized trial based on the results of these experiments.

In conclusion, our study showed that high-fluence accelerated PACK-CXL is effective in reducing the bacterial concentration *in-vitro* in several of the strains that are most commonly responsible for keratitis, and that PACK-CXL is associated with different BKR depending on the bacterial strain. With regards to the clinical setting, high-fluence accelerated PACK-CXL holds the potential to significantly improve infectious keratitis treatment outcomes. Further research is needed to optimize the specific PACK-CXL protocol for distinct bacterial strains.

REFERENCES

1. Thylefors B. Epidemiological patterns of ocular trauma. *Aust N Z J Ophthalmol* 1992;20:95-98.
2. Whitcher JP, Srinivasan M, Upadhyay MP. Corneal blindness: a global perspective. *Bull World Health Organ* 2001;79:214-221.
3. Srinivasan M, Gonzales CA, George C, et al. Epidemiology and aetiological diagnosis of corneal ulceration in Madurai, south India. *Br J Ophthalmol* 1997;81:965-971.
4. Whitcher JP, Srinivasan M. Corneal ulceration in the developing world--a silent epidemic. *Br J Ophthalmol* 1997;81:622-623.
5. Upadhyay MP, Karmacharya PC, Koirala S, et al. Epidemiologic characteristics, predisposing factors, and etiologic diagnosis of corneal ulceration in Nepal. *Am J Ophthalmol* 1991;111:92-99.
6. Tabibian D, Mazzotta C, Hafezi F. PACK-CXL: Corneal cross-linking in infectious keratitis. *Eye and vision (London, England)* 2016;3:11.
7. Kumar V, Lockerbie O, Keil SD, et al. Riboflavin and UV-light based pathogen reduction: extent and consequence of DNA damage at the molecular level. *Photochem Photobiol* 2004;80:15-21.
8. Makdoui K, Bäckman A, Mortensen J, Crafoord S. Evaluation of antibacterial efficacy of photo-activated riboflavin using ultraviolet light (UVA). *Graefes Arch Clin Exp Ophthalmol* 2010;248:207-212.
9. Knyazer B, Krakauer Y, Baumfeld Y, Lifshitz T, Kling S, Hafezi F. Accelerated Corneal Cross-Linking With Photoactivated Chromophore for Moderate Therapy-Resistant Infectious Keratitis. *Cornea* 2018;37:1.
10. Iseli HP, Thiel MA, Hafezi F, Kampmeier J, Seiler T. Ultraviolet A/riboflavin corneal cross-linking for infectious keratitis associated with corneal melts. *Cornea* 2008;27:590-594.
11. Knyazer B, Krakauer Y, Tailakh MA, et al. Accelerated Corneal Cross-linking as an Adjunct Therapy in the Management of Presumed Bacterial Keratitis: A Cohort Study. *J Refract Surg* 2020;36:258-264.
12. Achiron A, Elhaddad O, Regev T, et al. PACK Cross-Linking as Adjuvant Therapy Improves Clinical Outcomes in Culture-Confirmed Bacterial Keratitis. *Cornea* 2021.
13. Kling S, Hufschmid FS, Torres-Netto EA, et al. High Fluence Increases the Antibacterial Efficacy of PACK Cross-Linking. *Cornea* 2020;39:1020-1026.
14. Lin A, Rhee MK, Akpek EK, et al. Bacterial Keratitis Preferred Practice Pattern. *Ophthalmology* 2019;126:P1-P55.
15. Enzor R, Bowers EMR, Perzia B, et al. Comparison of Clinical Features and Treatment Outcomes of Pseudomonas aeruginosa Keratitis in Contact Lens and Non-Contact Lens

- Wearers. *Am J Ophthalmol* 2021;227:1-11.
16. Spierer O, Monsalve PF, O'Brien TP, Alfonso EC, Gologorsky D, Miller D. Clinical Features, Antibiotic Susceptibility Profiles, and Outcomes of Infectious Keratitis Caused by *Achromobacter xylosoxidans*. *Cornea* 2016;35:626-630.
 17. Penland RL, Wilhelmus KR. *Stenotrophomonas maltophilia* Ocular Infections. *Archives of Ophthalmology* 1996;114:433-436.
 18. Brooke JS. *Stenotrophomonas maltophilia*: an emerging global opportunistic pathogen. *Clin Microbiol Rev* 2012;25:2-41.
 19. Rohde M. The Gram-Positive Bacterial Cell Wall. *Microbiol Spectr* 2019;7.
 20. Egan AJ, Cleverley RM, Peters K, Lewis RJ, Vollmer W. Regulation of bacterial cell wall growth. *Febs j* 2017;284:851-867.
 21. Mazzotta C, Moramarco A, Traversi C, Baiocchi S, Iovieno A, Fontana L. Accelerated Corneal Collagen Cross-Linking Using Topography-Guided UV-A Energy Emission: Preliminary Clinical and Morphological Outcomes. *J Ophthalmol* 2016;2016:2031031-2031031.
 22. Elling M, Kersten-Gomez I, Dick HB. Photorefractive intrastromal corneal crosslinking for treatment of myopic refractive error: Findings from 12-month prospective study using an epithelium-off protocol. *J Cataract Refract Surg* 2018;44:487-495.
 23. Seiler TG, Batista A, Frueh BE, Koenig K. Riboflavin Concentrations at the Endothelium During Corneal Cross-Linking in Humans. *Invest Ophthalmol Vis Sci* 2019;60:2140-2145.
 24. Spillmann L. Density, light scatter, and spectral transmission of a scarred human cornea. *Albrecht Von Graefes Arch Klin Exp Ophthalmol* 1972;184:278-286.
 25. Bunsen R, Roscoe H. Photochemische Untersuchungen. *Journal für Praktische Chemie* 1857;71:129-144.
 26. Wernli J, Schumacher S, Spoerl E, Mrochen M. The Efficacy of Corneal Cross-Linking Shows a Sudden Decrease with Very High Intensity UV Light and Short Treatment Time. *Investigative Ophthalmology & Visual Science* 2013;54:1176-1180.
 27. Hafezi F, Richo O, Torres-Netto EA, Hillen M, Hafezi NL. Corneal Cross-linking at the Slit Lamp. *Journal of Refractive Surgery* 2021;37:78-82.
 28. Kamaev P, Friedman MD, Sherr E, Muller D. Photochemical Kinetics of Corneal Cross-Linking with Riboflavin. *Investigative Ophthalmology & Visual Science* 2012;53:2360-2367.
 29. Hammer A, Richo O, Mosquera SA, Tabibian D, Hoogewoud F, Hafezi F. Corneal Biomechanical Properties at Different Corneal Cross-Linking (CXL) Irradiances. *Investigative Ophthalmology & Visual Science* 2014;55:2881-2884.
 30. Badenoch PR, Hay GJ, McDonald PJ, Coster DJ. A rat model of bacterial keratitis. Effect of antibiotics and corticosteroid. *Arch Ophthalmol* 1985;103:718-722.

Chapter 9

High-Fluence Accelerated PACK-CXL for Bacterial Keratitis Using Riboflavin/UV-A or Rose Bengal/Green in the Ex-Vivo Porcine Cornea

Nan-Ji Lu, Hendrik Koliwer-Brandl, Mark Hillen, Adrian Egli, Farhad Hafezi

Transl Vis Sci Technol. 2023 Sep 1;12(9):14

ABSTRACT

Purpose: To investigate and compare the efficacy of high-fluence accelerated photoactivated chromophore for keratitis cross-linking (PACK-CXL) using either riboflavin/UV-A light or rose bengal/green light to treat *Staphylococcus aureus* or *Pseudomonas aeruginosa* infections in an *ex-vivo* porcine cornea model.

Methods: One hundred and seventeen *ex-vivo* porcine corneas were injected with clinical isolates of *S. aureus* or *P. aeruginosa* into 8 groups and cultured for 24 hours. Then, either riboflavin with UV-A light irradiation (30 mW/cm², 8 min 20 secs, 15 J/cm²) or rose bengal with green light irradiation (15 mW/cm², 16 min 40 secs, 15 J/cm²) was applied while unirradiated infected groups served as controls. All corneas were incubated for another 24 hours. Next, corneal buttons were obtained and vortexed to release the bacterial cells. The irradiated and unirradiated solutions were then plated and incubated on agar plates. The amount of colony forming units was quantified and the bacterial killing ratios (BKR) resulting from different PACK-CXL protocols relative to non-treated controls were calculated.

Results: riboflavin/UV-A light PACK-CXL resulted in median BKRs of 52.8% and 45.8% in *S. aureus* and *P. aeruginosa*, respectively, whereas rose bengal/green light PACK-CXL resulted in significantly greater BKRs of 76.7% and 81.0%, respectively (both *p*-values < 0.01).

Conclusion: Both accelerated PACK-CXL protocols significantly decrease *S. aureus* and *P. aeruginosa* bacterial loads. Comparing riboflavin/UV-A light and rose Bengal/green light PACK-CXL approaches in the same experimental setup may help develop strain-specific and depth-dependent PACK-CXL approaches that could be used alongside the current standard of care.

INTRODUCTION

Infectious keratitis is an ophthalmic condition that can rapidly impair vision and requires immediate and effective treatment to avoid complications and minimize vision loss. Moreover, the incidence of infectious keratitis is increasing with the widespread use of contact lenses ¹. Although the principal causative organisms of infectious keratitis vary by geographical region, a bacterial infection is the most common cause ², and the increasing global prevalence of antibiotic-resistant bacteria adds an important challenge to effectively treat bacterial keratitis with traditional topical antibiotic eyedrops ^{3,4}, highlighting the need for new treatments to overcome this challenge.

Corneal cross-linking (CXL) was initially developed to treat corneal ectasias like keratoconus. The procedure starts with saturation of the stroma using riboflavin, followed by a 30-minute period of ultraviolet-A (UV-A) irradiation ⁵. In the presence of oxygen, UV-A photons photoactivate riboflavin to create Reactive Oxygen Species (ROS), which covalently cross-bind collagen and proteoglycans in the stroma and increase the biomechanical strength. In 2008, the antimicrobial effects of CXL were described ⁶. Later, other wavelength/chromophore combinations such as green light/rose bengal, were proposed ⁷. Accordingly, the term “photoactivated chromophore for keratitis-corneal cross-linking (PACK-CXL)” was introduced to describe this indication of CXL ⁸.

The antimicrobial mechanism of PACK-CXL can be explained by two effects: (1) the direct killing effects of microorganisms through UV-A light and chromophores via generation of ROS, which impair the structural integrity of bacterial membranes and their replication; and (2) the development of collagenase resistance through steric hindrance ⁹.

In-vitro experiments show that riboflavin/UV-A light (rf) PACK-CXL can effectively kill antibiotic-resistant bacteria ¹⁰. In clinical studies, rf PACK-CXL with irradiation fluences between 5.4-7.2 J/cm² has already been used to treat bacterial keratitis of varying severity ¹¹⁻¹³. In a recent *in-vitro* study, we have

shown that high-fluence rf PACK-CXL can be accelerated while maintaining the bacterial killing effect¹⁴. The purpose of this study was therefore to transfer the conclusions of the previously published *in-vitro* study into an *ex-vivo* model and to compare the bacterial killing effects of rf PACK-CXL with rose Bengal/green light (rb) PACK-CXL.

MATERIALS and METHODS

Bacteria and Solution Preparation

Two species of clinically relevant bacteria, *Staphylococcus aureus* and *Pseudomonas aeruginosa*, were chosen from independent clinical isolates of corneal infections for the following experiments. The bacterial strains were obtained from the Institute of Medical Microbiology, University of Zurich, Switzerland. Both bacterial species were cultured on Columbia agar + 5% sheep blood (COS, bioMérieux, Marcy l'Etoile, France) for 24 hours at 37°C. Colonies were suspended in sterile 0.9% NaCl and adjusted to McFarland 0.5, which corresponds to approximately 10⁸ colony forming units (CFU)/mL. The solutions were diluted 100-fold to 10⁶ CFU/mL in 96-well microtiter plates (Costar Assay Plate, Corning Incorporated, NY, USA).

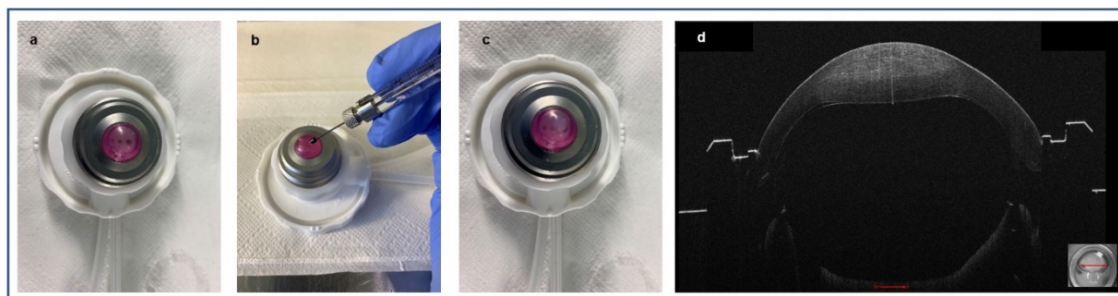
Ex-vivo Infectious Keratitis Model

Freshly enucleated porcine eyes were obtained from a local slaughterhouse and used within 4 hours. The corneas were excised with a 3-mm scleral rim individually immersed in povidone iodinate solution (Betadine[®], Basel, Switzerland) for 10 minutes, rinsed 10 times in distilled water, and individually placed in 6-well plates (Costar Assay Plate, Corning Incorporated) containing 4 mL of Dulbecco's Modified Eagle's Medium (DMEM, Sigma-Aldrich Ltd, Poole, UK) each. Plates were kept at 37 °C with 5% CO₂ for 24 hours.

The culture medium was removed after incubation. Before that, the culture medium was plated on COS agar to check for potential bacterial contaminations. If bacteria were detected, the corresponding corneas were discarded. Bacteria free corneas were individually mounted on an artificial chamber (Moria, Antony, France) (**Figure 1a**). A 33-gauge micro syringe (Hamilton[®], USA) with a fixed 2

mm needle containing 10 μ L of the bacterial solution diluted to 10^6 CFU/mL was prepared and the solution injected into each cornea at a 45-degree angle (**Figure 1b**). After the injection, corneas formed a localized bulge (**Figure 1c**); Anterior segment optical coherence tomography (MS-39, CSO Italia, Firenze, Italy) was used to determine the deepest part of the formed bulge that was located at approximately 60% of stromal depth (**Figure 1d**). All the corneas were individually placed in new 6-well plates containing 1 mL of DMEM medium and kept at 37 °C with 5% CO₂ for another 24 hours. Corneal opacity, edema, and beginning ulceration was observed in all corneas at 24 hours after inoculation. This indicated the successful establishment of the *ex-vivo* infection keratitis model. The loose epithelium over the site of inoculation was removed using triangular sponges (Eye spears, EYETEC[®], Network Medical Products LTD, UK).

Figure 1: *The injection steps*



Corneas were mounted on an artificial chamber (a) and a micro syringe was injected into the cornea at a 45-degree angle (b); After the injection, all the corneas formed a localized bulge (c); The bulge could be observed by the sectional scan of anterior segment optical coherence tomography (d)

Irradiation Settings and PACK-CXL Protocols

Two different light sources were used: a commercially available UV-A LED light source (C-eye; EMAGine AG, Zug, Switzerland) and an experimental green light LED source (CSO Italia, Scandicci, Italy). Both light sources had a fixed 12 mm irradiation spot and performed two different types of PACK-CXL irradiation. The settings for rf PACK-CXL were: UV-A light at 365 nm using 0.1% [w/v]

riboflavin solution without carriers (Ribo-Ker, EMAGine, Zug, Switzerland) and irradiation settings of 30 mW/cm² for 8 min 20 secs, corresponding to a fluence of 15 J/cm². The settings for rb PACK-CXL were: green light at 522 nm using 0.1% rose bengal solution (Bichsel Pharmacy, Interlaken, Switzerland) and irradiation settings of 15 mW/cm² for 16 min 40 secs, corresponding to a fluence of 15 J/cm².

Groups Setting and PACK-CXL Procedures

The inoculated corneas were randomly assigned to the experimental (irradiated) or control groups. **Table 1** provides an overview of the experimental and control groups; as indicate, we conducted rb PACK-CXL or rf PACK-CXL in corneas inoculated with one of two bacterial strains.

Table 1: The study groups and PACK-CXL technical details

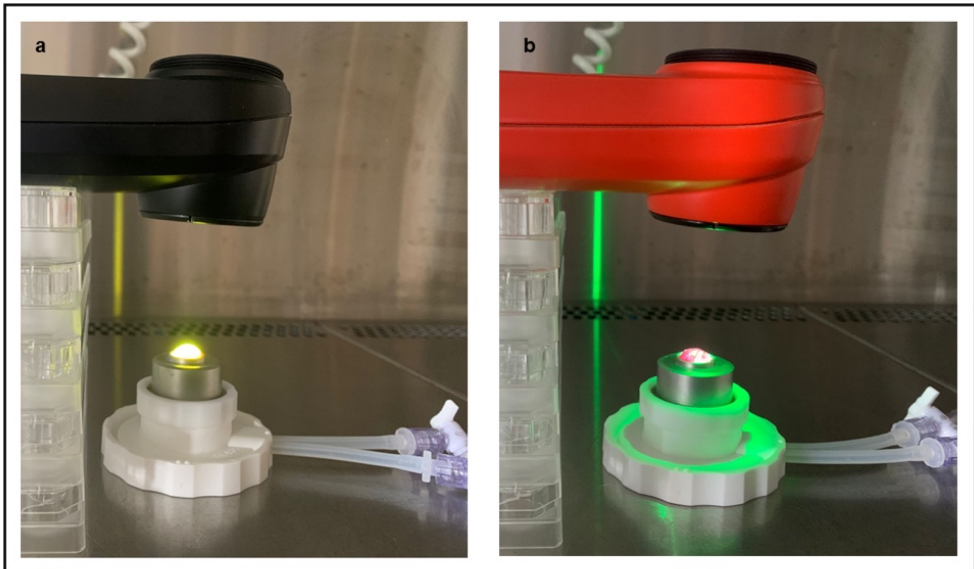
Group	Injected Bacteria	Light source and Chromophore	Total Fluence (J/cm ²)	Irradiance Intensity (mW/cm ²)	Irradiance Time (mm' ss'')
Group 1-control	<i>S. aureus</i>	riboflavin			
Group 1-PACK-CXL	<i>S. aureus</i>	UV-A light + riboflavin	15	30	8'20''
Group 2-control	<i>S. aureus</i>	Rose Bengal			
Group 2-PACK-CXL	<i>S. aureus</i>	Green light + Rose Bengal	15	15	16'40''
Group 3-control	<i>P. aeruginosa</i>	riboflavin			
Group 3-PACK-CXL	<i>P. aeruginosa</i>	UV-A light + riboflavin	15	30	8'20''
Group 4-control	<i>P. aeruginosa</i>	Rose Bengal			
Group 4-PACK-CXL	<i>P. aeruginosa</i>	Green light + Rose Bengal	15	15	16'40''

PACK-CXL, photoactivated chromophore for keratitis cross-linking; mm, minutes; ss, seconds; S. aureus, Staphylococcus aureus; P. aeruginosa, Pseudomonas aeruginosa

Corneas in the experimental groups were mounted on an artificial chamber, and riboflavin or rose bengal was dropped every 20 seconds for 20 minutes, followed by irradiation with the aforementioned protocols (**Figures 2a and 2b**).

After irradiation, the corneas were placed into new 6-well plates filled with 1 mL of fresh DMEM medium and incubated for 24 hours at 37°C with 5% CO₂. Corneas in the control groups were treated similarly to the experimental groups: applied chromophore but were not irradiated.

Figure 2: During the PACK-CXL irradiation



PACK-CXL treatment of a porcine cornea mounted in an artificial chamber using (a) UV-A light/riboflavin (rf) and (b) green light/rose bengal (rb)

Bacterial CFUs: Counting and Analysis

To address both biological and experimental variability and to obtain reliable and stable results, experiments were performed as follows: each irradiation was repeated at least three times (technical replicate), and the whole experiment was repeated at least on three different days (biological replicate). For every irradiation, fresh bacterial solutions were used. Corneal buttons were prepared using an 8 mm corneal punch (SMI AG, Brussels, Belgium). The buttons were placed in 2 mL tubes (Eppendorf AG, Hamburg, Germany) containing 1 mL 0.9% NaCl solution, vortexed and then centrifuged for 10 minutes at 15,000 revolutions per minute (rpm) to release the bacteria from the cornea. Following centrifugation, the solutions were vortexed again, then aspirated and mixed with

a 1 mL pipette (Eppendorf AG, Hamburg, Germany). The solutions then underwent three 10-fold dilutions, and 10 µL of the final dilution was plated on COS agar using its whole surface to get single bacterial colonies and incubated at 37°C for 24 hours.

After incubation, all agar plates were photographed and the number of CFUs was counted as described previously¹⁵. Based on each CFUs result, the BKR of three technical replicates was calculated by comparing the median CFU of each PACK-CXL irradiated plate (CFU_{PACK-CXL}) to its corresponding control plate (CFU_{control}), using the following formula:

$$BKR = \left(1 - \frac{CFU_{PACK-CXL}}{CFU_{control}}\right) \times 100 [\%]$$

For two investigated bacteria, *S. aureus* and *P. aeruginosa*, the BKRs achieved by the two PACK-CXL protocols (rf PACK-CXL vs. rb PACK-CXL) were then compared.

Statistical Analysis

Statistical analysis and graph preparation were conducted using GraphPad Prism (version 5, San Diego, CA). In the case of determination of BKRs, descriptive statistics were calculated as median with interquartile range. A t-test was conducted followed by a non-parametric Mann-Whitney test to analyze the differences among all groups. Mean and standard deviations were used to calculate CFUs. A *p*-value < 0.05 was considered as the threshold for statistical significance.

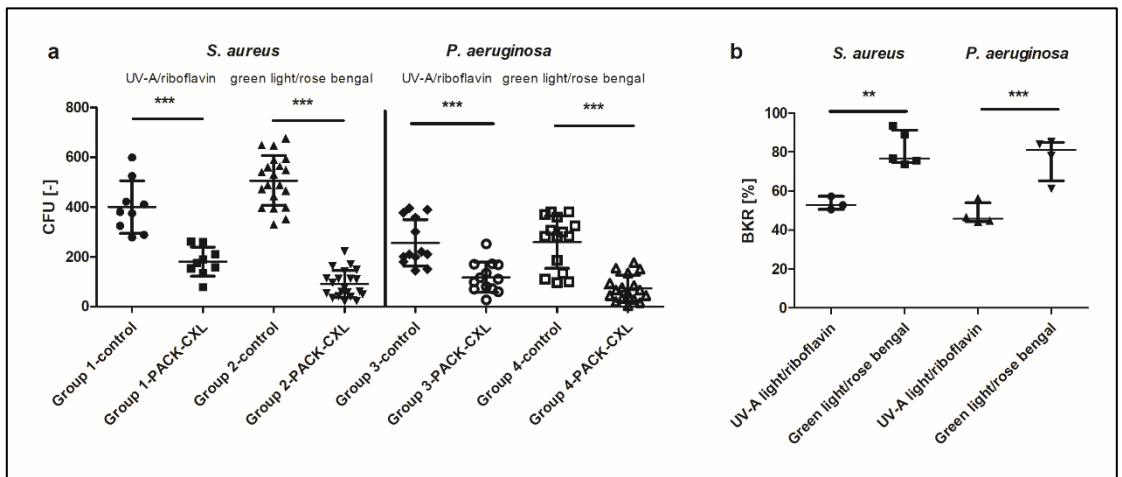
RESULTS

Overall, one hundred and seventeen porcine corneas were used in our *ex-vivo* model and included in the analyses. For *S. aureus*, the application of rf PACK-CXL yielded in a mean CFU of 400 ± 106 for Group 1-control (n = 9) and 181 ± 59 for Group 1-PACK-CXL (n = 9), while rb PACK-CXL yielded in a mean CFU of 507 ± 100 for Group 2-control (n = 20) and 91 ± 55 for Group 2-PACK-CXL (n = 21). For *P. aeruginosa*, rb PACK-CXL yielded in a mean of CFU 257 ± 94

for Group 3-control (n = 13) and 118 ± 61 Group 3-PACK-CXL (n = 13), while rb PACK-CXL yielded in a mean CFUs of 260 ± 106 for Group 4-control (n = 15) and 74 ± 53 for Group 4-PACK-CXL (n = 17). The mean CFUs of all control groups were significantly higher (all p -values < 0.001) compared to the mean CFUs of all corresponding experimental groups (**Figure 3a**).

The median BKR of high-fluence rf PACK-CXL of *S. aureus* and *P. aeruginosa* were $52.8\% \pm 3.4$ and $45.8\% \pm 5.7$, respectively, whereas median BKR with high-fluence rb PACK-CXL for *S. aureus* and *P. aeruginosa* were $76.7\% \pm 8.9$ and $81.0\% \pm 11.1$, respectively (**Figure 3b**). The higher BKR were achieved by rb bengal PACK-CXL for both bacteria (both p -values < 0.01).

Figure 3: The CFU and BKR results



(a) The colony forming units (CFUs) of *S. aureus* and *P. aeruginosa* with or without two different protocols (UV-A light/riboflavin or green light/rose bengal) of PACK-CXL treatment were determined. The scatters represent each single experiments with the bars showing the means (***) $P < 0.001$); **(b)** Bacterial killing rates (BKRs) are calculated from independent biological replicates. Higher BKRs were achieved when PACK-CXL was applied with green light/rose bengal (** $P < 0.01$, *** $P < 0.001$)

DISCUSSION

This *ex-vivo* study demonstrates that accelerated high-fluence PACK-CXL can effectively reduce the bacterial concentration in a model for infectious keratitis using two clinically relevant bacterial species. These results suggest that a timely application of accelerated high-fluence PACK-CXL, potentially at the slit lamp, may effectively treat bacterial keratitis by decreasing the bacterial load at the lesion site and by increasing the stroma's resistance to digestion¹⁶. Furthermore, this decrease in bacterial load and with the combined application of antibiotic treatment may shorten the duration of infection, and enhance the effects of concomitantly applied antimicrobial drugs, improving patients' outcomes^{16, 17}.

Two main *ex-vivo* models of bacterial cornea infection are commonly used in the literature: (1) direct injection of bacterial solutions into the stroma with a needle and (2) scratching the corneal surface and applying a bacterial solution over the surface^{18, 19}. In this study, we chose the first method because it is highly reproducible, whereas the depth of a corneal scratch can be difficult to control. Additionally, applying bacterial solution to the cornea surface does not guarantee that the bacteria will fully penetrate the cornea. To investigate the bacterial killing effects of PACK-CXL to the maximum extent, a high initial bacterial count of 10^6 CFU/mL was used, which is consistent with a rat model for bacterial keratitis, in which the maximum bacterial count of 10^7 CFU/mL was found 48 hours after infection²⁰.

Currently, the most widely used PACK-CXL protocol in UV-A light/riboflavin still is the classic "Dresden protocol" (3 mW/cm^2 , 30 minutes, 5.4 J/cm^2)²¹. This 20-year-old protocol may be appropriate for biomechanically strengthening ectatic corneas. However, the protocol is slow, assumes a transparent cornea, and has a limited depth of killing effect due to a low fluence of 5.4 J/cm^2 . This constrains the efficacy of the procedure, as in infectious keratitis, the infected tissue is opaque and the depth of infection may be far beyond the $330 \mu\text{m}$ which Dresden protocol was designed for²².

Our group has previously shown *in-vitro* that fluences of 10 and 15 J/cm², significantly greater than the Dresden protocol's 5.4 J/cm², improve the antimicrobial efficacy of rf PACK-CXL¹⁵. Previous clinical studies, using 15 J/cm² accelerated rf CXL did not decrease the endothelial cell density in transparent keratoconic and myopic corneas^{23,24}. We therefore applied 15 J/cm² using high LED intensities for both UV-A light (30 mW/cm²) and green light (15 mW/cm²).

The current *ex-vivo* study and our previous *in-vitro* study used the same rf PACK-CXL irradiation protocols (UV-A light plus riboflavin, 30 mW/cm², 8 min 20 secs, 15 J/cm²). Although we achieved lower BKR than in the *in-vitro* study (BKR of *S. aureus* and *P. aeruginosa* were 97.50% and 82.27%, respectively), BKR were still substantial. Potential reasons for this include the fact that in the *ex-vivo* model, the remaining bacteria continued to replicate in the corneas during the incubation after rf PACK-CXL, while in the *in-vitro* experiments, the remaining bacteria were directly plated on the agar plates. Further, opaque corneas act to prevent the penetration of UV-A light whereas in the *in-vitro* experiments, the solutions present in 96-well plates were almost transparent.

In this study, we evaluated two PACK-CXL protocols with a similar irradiation fluence delivered via different chromophores. For both bacterial species, the rb PACK-CXL BKR were higher than rf PACK-CXL BKR. This is similar to the resistance to enzymatic digestion that rb PACK-CXL provides more resistance than rf PACK-CXL using the same fluence. In contrast, the biomechanical cross-linking effect of rb PACK-CXL was lower than the effect of rf PACK-CXL²⁵.

The depth of the infection plays a critical role in the cornea's response to PACK-CXL and effective bacterial killing in deep keratitis is essential, since the continuing bacterial growth in the depth will impair corneal structure and may lead to corneal perforation. Therefore, while higher BKR were achieved by rb PACK-CXL, the potential benefits of deep killing induced by rf PACK-CXL may be crucial. Accordingly, the application of both rf PACK-CXL and rb PACK-CXL

protocols in the same session would appear to offer several advantages over either technique performed separately.

In the current study, we count the remaining bacteria after PACK-CXL treatment by plating bacterial dilutions to agar, which is still the gold standard in microbiology for quantification of living bacteria. Thereby, the location of the bacteria in the cornea, that survived the treatment, cannot be determined. In a following study, we like to address the question by infecting cornea with green fluorescent protein (GFP) expressing bacteria and the application of confocal laser scanning microscopy, which may help us to identify the location of remaining active bacteria in the cornea after PACK-CXL treatment²⁶.

In conclusion, the results from our *ex-vivo* model presented here confirm the findings of our previous *in-vitro* study, showing that high-fluence accelerated rf and rb PACK-CXL effectively reduce the concentration of *S. aureus* and *P. aeruginosa* in the cornea. In a clinical setting, the use of both chromophores simultaneously may have the potential to improve the outcomes of bacterial keratitis treatment significantly.

REFERENCES

1. Stapleton F, Shrestha GS, Vijay AK, Carnt N. Epidemiology, Microbiology, and Genetics of Contact Lens-Related and Non-Contact Lens-Related Infectious Keratitis. *Eye & Contact Lens* 2022;48:127-133.
2. Cabrera-Aguas M, Khoo P, Watson SL. Infectious keratitis: A review. *Clin Exp Ophthalmol* 2022;50:543-562.
3. Willcox MDP. Antibiotics and Microbial Keratitis: Do We Need to Test for Resistance? *Eye Contact Lens* 2020;46:1-2.
4. Ting DSJ, Ho CS, Deshmukh R, Said DG, Dua HS. Infectious keratitis: an update on epidemiology, causative microorganisms, risk factors, and antimicrobial resistance. *Eye* 2021;35:1084-1101.
5. Randleman JB, Khandelwal SS, Hafezi F. Corneal cross-linking. *Survey of Ophthalmology* 2015;60:509-523.
6. Martins SAR, Combs JC, Noguera G, et al. Antimicrobial Efficacy of Riboflavin/UVA Combination (365 nm) In Vitro for Bacterial and Fungal Isolates: A Potential New Treatment for Infectious Keratitis. *Investigative Ophthalmology & Visual Science* 2008;49:3402-3408.
7. Halili F, Arboleda A, Durkee H, et al. Rose Bengal- and Riboflavin-Mediated Photodynamic Therapy to Inhibit Methicillin-Resistant Staphylococcus aureus Keratitis Isolates. *Am J Ophthalmol* 2016;166:194-202.
8. Hafezi F, Randleman JB. PACK-CXL: defining CXL for infectious keratitis. *J Refract Surg* 2014;30:438-439.
9. Richoz O, Kling S, Hoogewoud F, et al. Antibacterial efficacy of accelerated photoactivated chromophore for keratitis-corneal collagen cross-linking (PACK-CXL). *J Refract Surg* 2014;30:850-854.
10. Makdoui K, Bäckman A. Photodynamic UVA-riboflavin bacterial elimination in antibiotic-resistant bacteria. *Clinical & Experimental Ophthalmology* 2016;44:582-586.
11. Said DG, Elalfy MS, Gatziofufas Z, et al. Collagen cross-linking with photoactivated riboflavin (PACK-CXL) for the treatment of advanced infectious keratitis with corneal melting. *Ophthalmology* 2014;121:1377-1382.
12. Naranjo A, Arboleda A, Martinez JD, et al. Rose Bengal Photodynamic Antimicrobial Therapy for Patients With Progressive Infectious Keratitis: A Pilot Clinical Study. *Am J Ophthalmol* 2019;208:387-396.

13. Hafezi F, Hosny M, Shetty R, et al. PACK-CXL vs. antimicrobial therapy for bacterial, fungal, and mixed infectious keratitis: a prospective randomized phase 3 trial. *Eye and Vision* 2022;9:2.
14. Lu N-J, Koliwer-Brandl H, Gilardoni F, et al. The Antibacterial Efficacy of High-Fluence PACK Cross-Linking Can Be Accelerated. *Translational Vision Science & Technology* 2023;12:12-12.
15. Kling S, Hufschmid FS, Torres-Netto EA, et al. High Fluence Increases the Antibacterial Efficacy of PACK Cross-Linking. *Cornea* 2020;39:1020-1026.
16. Achiron A, Elhaddad O, Regev T, et al. PACK Cross-Linking as Adjuvant Therapy Improves Clinical Outcomes in Culture-Confirmed Bacterial Keratitis. *Cornea* 2022;41:1069-1073.
17. Sepulveda-Beltran PA, Levine H, Altamirano DS, et al. Rose Bengal Photodynamic Antimicrobial Therapy: A Review of the Intermediate-Term Clinical and Surgical Outcomes. *Am J Ophthalmol* 2022;243:125-134.
18. Pinnock A, Shivshetty N, Roy S, et al. Ex vivo rabbit and human corneas as models for bacterial and fungal keratitis. *Graefes Arch Clin Exp Ophthalmol* 2017;255:333-342.
19. Marquart ME. Animal models of bacterial keratitis. *J Biomed Biotechnol* 2011;2011:680642.
20. Badenoch PR, Hay GJ, McDonald PJ, Coster DJ. A rat model of bacterial keratitis. Effect of antibiotics and corticosteroid. *Arch Ophthalmol* 1985;103:718-722.
21. Wollensak G, Spoerl E, Seiler T. Riboflavin/ultraviolet-a-induced collagen crosslinking for the treatment of keratoconus. *Am J Ophthalmol* 2003;135:620-627.
22. Hafezi F, Torres-Netto EA, Hillen MJP. Re: Prajna et al.: Cross-Linking-Assisted Infection Reduction: a randomized clinical trial evaluating the effect of adjuvant cross-linking on outcomes in fungal keratitis (Ophthalmology. 2020;127:159-166). *Ophthalmology* 2021;128:e6.
23. Mazzotta C, Moramarco A, Traversi C, Baiocchi S, Iovieno A, Fontana L. Accelerated Corneal Collagen Cross-Linking Using Topography-Guided UV-A Energy Emission: Preliminary Clinical and Morphological Outcomes. *J Ophthalmol* 2016;2016:2031031.
24. Elling M, Kersten-Gomez I, Dick HB. Photorefractive intrastromal corneal crosslinking for treatment of myopic refractive error: Findings from 12-month prospective study using an epithelium-off protocol. *J Cataract Refract Surg* 2018;44:487-495.
25. Cherfan D, Verter EE, Melki S, et al. Collagen cross-linking using rose bengal and

- green light to increase corneal stiffness. *Invest Ophthalmol Vis Sci* 2013;54:3426-3433.
26. Alshehri JM, Caballero-Lima D, Hillarby MC, et al. Evaluation of Corneal Cross-Linking for Treatment of Fungal Keratitis: Using Confocal Laser Scanning Microscopy on an Ex Vivo Human Corneal Model. *Invest Ophthalmol Vis Sci* 2016;57:6367-6373.

Chapter 10

Summary, Discussion and Future Directions

This thesis proposes and evaluates new methods to diagnose and prevent the postoperative complications of laser refractive surgery. In addition, new protocols for the treatment of postoperative complications of laser refractive surgery, including postoperative corneal ectasia and infection, were established.

Laser Refractive Surgery Complications: Prevention and Diagnosis

Currently, the main focus of preoperative screenings for laser refractive surgery candidates is to timely and accurately diagnose corneal diseases such as keratoconus to prevent triggering postoperative corneal ectasia ¹. Keratoconus was regarded as a rare disease before; however, the prevalence of keratoconus is usually being underestimated due to the methods of diagnosis. The prevalence of keratoconus is estimated to range from 0.2 to 4,790 per 100 thousand people, with a higher prevalence in the Middle East ².

Typically, the diagnosis of keratoconus was based on corneal morphology, the most currently used system for staging keratoconus is the Belin ABCD staging system, which is based on an upgrade of the Amsler-Krumeich staging system. Compared with Placido-based topography and Scheimpflug-based tomography, optical coherence tomography (OCT) can characteristically measure the different layers of cornea profile in a higher resolution ³. Using OCT, the new STEP keratoconus staging system (**Chapter 2**) and WISE index to diagnose keratoconus based on artificial intelligence (**Chapter 3**) were proposed. The STEP staging system is based on Stromal Overall Minimum Thickness (ST) and Epithelium Overall Standard Deviation (EP) ⁴, and has a similar performance as the Belin ABCD system to stage keratoconus ⁵. Meanwhile, the WISE index considers all parameters that describe the corneal profile, rather than just local epithelial tor stromal thickness, thus improving the diagnostic ability of the algorithm formed by principal component analyses and logistic regression. Nowadays, the most commonly used Scheimpflug-based keratoconus diagnosis parameters include Belin/Ambrósio enhanced ectasia display (BADD) and Pentacam random forest index (PRFI) ^{6,7}, WISE has a similar diagnostic ability as these two parameters.

After the successful establishment of STEP and WISE, it is important to note that both were developed based on the same commercial OCT system and on the Chinese database. Hence, in future work, both need to be validated clinically on other OCT devices and on other races' databases: 1) other commercially available OCT devices also can provide the stroma and epithelium thickness profile; collecting a cohort of normal and keratoconus patients by other OCT devices for the validation is needed; 2) For the race difference, collecting a cohort of normal patients by using the same OCT device and comparing it with the current normal group patients will be the first step. Furthermore, the functions of the STEP system need to be continuously improved. In its current form it functions as a staging system, but may be developed further to describe the epithelial and stromal remodeling due to keratoconic progression or corneal cross-linking (CXL) treatment ⁸, allowing for progression tracking and assessment of CXL effectiveness. In addition, to maximize the use of the information that OCT can provide, combining the STEP system with the structural OCT-based keratoconus system to carry out comprehensive management of keratoconus is also another future work. The WISE index may be improved by incorporating additional early-stage keratoconus patients to further optimize the algorithm and improve its diagnostic ability.

Keratoconus can be not only diagnosed by assessing the corneal morphology, but also by evaluation of the corneal biomechanical properties ⁹. While the software of each type of device is continually optimized, the diagnostic efficiency of each device is still limited by its technical specifications. Therefore, it was proposed to combine devices of different measurement principles. Previous studies considered combinations of Scheimpflug-based tomography and corneal biomechanical measurement or combinations of Scheimpflug-based tomography and OCT to diagnose keratoconus ^{10, 11}. In clinical practice, one of the most frequently commercially used parameters generated by the combination of devices (Scheimpflug-based tomography and air-puff device) is the tomographic and biomechanical index (TBI). Instead, we were the first to innovatively combine OCT with a corneal biomechanical measurement using an ultra-high-speed Scheimpflug camera for this task (**Chapter 4**) ¹². After we

proposed this new diagnostic model, a similar parameter like TBI can be generated, which could be called the OCT and biomechanical index (OBI). Future work can work in this direction.

Although topographic, tomographic, and biomechanical devices each consider different cornea characteristics, it is neither practical nor cost-effective to use each device to reach a diagnosis. We therefore firstly assessed the diagnostic efficacy of various combinations of all combinations of devices and their ability to diagnose keratoconus of various degrees (**Chapter 5**)¹³. These results showed that, with the help of artificial intelligence, existing algorithms can accurately diagnose both early and advanced keratoconus, but their diagnostic ability of forme fruste keratoconus (FFKC) is low, but can be improved by combining corneal biomechanical measurements with Scheimpflug-based tomography or OCT. This study is of health-economic value since in laser refractive surgery candidates, who have a high risk of postoperative ectasia, combining devices can improve preoperative screening, thus reducing the incidence of post-laser refractive surgery ectasia and the corresponding financial burden.

While combining devices using different measuring principles has been confirmed to improve the diagnosis of keratoconus, future work could see such combinations integrated into a single device. Recently, optical coherence elastography (OCE) was developed¹⁴, which performs corneal biomechanical measurements *in situ*. and may become a future diagnostic method for keratoconus or other corneal diseases. Combining the OCT-based STEP system with the corneal biomechanical information obtained from OCE could further improvement keratoconus management.

Ectasia after laser refractive surgery ectasia still may occur despite careful preoperative evaluation and the selection of proper surgery candidates. The actual incidence of post-LVC ectasia is undetermined. Based on the literature, for PRK, LASIK, and SMILE, the incidence of post-LVC ectasia in eyes without recognizable preoperative risk factors is 20 per 100,000, 90 per 100,000, and

11 per 100,000 patients, respectively ¹⁵. The diagnosis of postoperative ectasia is typically based on the postoperative corneal morphology, while post-laser refractive surgery ectasia is caused by the decompensation of corneal biomechanics. To this end, based on corneal biomechanical measurements, we established the corneal biomechanical index-laser vision correction index (CBI-LVC) to diagnose the disease ¹⁶. After the establishment of CBI-LVC, due to a limited inclusion number of post-laser refractive surgery ectasia cases in the original study, we evaluated the parameter with a new independent database, confirming its high sensitivity and specificity (**Chapter 6**). For the limitations of this study, we should notice that the post-SMILE ectasia patients still were not included in the study due to their rarity; besides, the follow-up time of post-laser refractive surgery normal patients could be extended to avoid include post-laser refractive surgery ectasia patients in the control groups. In the future, the inclusion of post-laser refractive surgery patients that simultaneously received prophylactic CXL with a long follow-up can broaden the scope of application of CBI-LVC. Similar to the diagnosis of keratoconus, the diagnosis of post-laser refractive surgery ectasia using OCT could be developed in the future, that is, artificial intelligence is used to diagnose post-laser refractive surgery ectasia based on postoperative corneal epithelial and stromal thickness profile measured by OCT.

Laser Refractive Surgery Complications: Treatment

Although the pathogenesis of keratoconus and post-laser refractive surgery ectasia may differ, they both exhibit a decline in corneal biomechanics ¹⁷ requiring CXL to stiffen the cornea, thereby delaying disease progression ¹⁸. Compared with epithelium-off CXL, epithelium-on CXL reduces the incidence of postoperative complications. However, the epithelium partially blocks the penetration of riboflavin and increases the consumption of oxygen, after the founding of iontophoresis-CXL and oxygen-boost CXL ^{19,20}, requiring additional equipment to perform the procedures. We invented an independent epithelium penetration enhancer that uses the same riboflavin as the epithelium-off CXL without additional equipment, accompanied by a new epithelium-on CXL protocol (**Chapter 7**). Our results show that this new protocol (18 mW/cm², 1

sec on/ 1 sec off for 15 mins, 8.1 J/cm²) accomplishes a similar stiffening as the most commonly used epithelium-off CXL protocol (9 mW/cm², 10 mins, 5.4 J/cm²)²¹. The *ex-vivo* results are promising and have the potential to replace the existing protocols that require more equipment, are more complicated, and have a larger spectrum of potential complications.

Based on these results, several clinical multicenter studies are currently being conducted that are awaiting long-term results to validate the stiffening effect, the safety for the corneal endothelium, and the occur rates of potential post-CXL complications. Similar to the establishment of the sub400 protocol²², an updated version of the Dresden protocol that allows treating patients with a stromal thickness less than 400 µm after epithelial removal²³, the current epithelium-on CXL protocol also could be updated after its postoperative demarcation line depth and long-term results is determined. This is particularly important for post-laser refractive surgery patients as their stromal thickness is usually thinner after the laser ablation. Still, this epithelium-on protocol itself has the potential to be optimized, as the total procedure time is still long, the adjustment of the corneal enhancer components, the application time of the corneal enhancer and riboflavin, and the CXL irradiation intensity and fluence is the direction of our future work.

After laser refractive surgery infections may occur, of which bacterial infectious keratitis is the most common²⁴. Such corneal infections are more challenging than common corneal infection due to the routine use of postoperative steroids and the thinner postoperative stroma. Photoactivated chromophore for keratitis-corneal cross-linking (PACK-CXL) is a treatment method that can directly kill the bacteria, while increasing corneal stiffness and increasing stromal resistance to enzymatic degradation through steric hindrance. The protocols of PACK-CXL were based on the CXL protocols for the treatment of keratoconus, however, requiring the existing protocols of PACK-CXL to be updated to be more in line with its treatment purpose. Based on our previous *in-vitro* results that by increasing the total irradiation energy used in the PACK-CXL protocol a higher bacterial killing rate (BKR) could be achieved²⁵, we investigated whether

a high BKR can still be maintained while increasing the irradiation fluence to reduce the total treatment time (**Chapter 8**)²⁶. In this *in-vitro* study two common bacteria, *Staphylococcus aureus* and *Pseudomonas aeruginosa*, were exposed to nine accelerated protocols with the total irradiation energy of 15 J/cm². These results showed that for a total irradiation fluence of up to 10 J/cm², the high-fluence PACK-CXL protocols can be accelerated while maintaining a high but species-dependent BKR.

The *in-vitro* study did not consider the role of the corneal extracellular matrix or the opacity of infectious corneas, however, affecting the penetration of the UV-A radiation. Hence, a corresponding *ex-vivo* study was conducted to validate these *in-vitro* results. This study also considered another combination of chromophore and light source for PACK-CXL consisting of Rose Bengal with 522 nm green light²⁷ (**Chapter 9**). These results confirmed the *in-vitro* findings that accelerated PACK-CXL significantly decreases *S. aureus* and *P. aeruginosa* bacterial loads, while suggesting that Rose Bengal combined with green light may have an even better BKR²⁸.

The current two PACK-CXL studies mainly focused on two common bacteria and the results demonstrated that the BKR is species dependent. Therefore, more strains of these two common bacteria, especially for resistant strains such as Methicillin-resistant *Staphylococcus aureus* (MRSA) and clinical strains collected from contact lens-related infections, could solidify the study conclusion, and more types of bacteria need to be investigated to confirm the variation of BKR, which is especially important for resistant strains. While the protocol may be accelerated to a certain degree, an independent experiment study is still needed to clarify the relationship between oxygen and PACK-CXL. Furthermore, the BKR of PACK-CXL is currently the main parameter used to evaluate the efficacy, which is the golden standard in medical microbiology. In bacterial infectious keratitis, however, the role of corneal extracellular matrix and the eventual immune response should also be considered. The application of green fluorescent protein (GFP) expressed bacteria and related immunohistochemistry will help us understand other potential functions and reaction of

PACK-CXL in the treatment of bacterial infectious keratitis. In the future, under the permission of the ethical committee, the in-vivo infectious keratitis model based on rabbits could be established and the PACK-CXL can be performed to further investigate the effectiveness of PACK-CXL while the immunity reaction of the animal model exists. While fungal keratitis is more challenging than bacterial keratitis, the fungus has two existing forms -colony and hypha- which makes the difficulties of quantifying them, thus it is difficult to accurately evaluate the killing effect of PACK-CXL on fungus; future works should start with the in-vitro experiments to find an objective way to evaluate the number of fungi in a certain volume of solution.

In summary, new instruments and treatment techniques have emerged in recent years, including OCT, corneal biomechanical measurements, CXL, etc., that helped prevent complications in laser refractive surgery and improved the diagnosis and treatment of complications after they occur. The results of this thesis may also be applied to the diagnosis and treatment of keratoconus and improve the treatment of infectious keratitis.

REFERENCES

1. Ambrósio R, Jr., Randleman JB. Screening for ectasia risk: what are we screening for and how should we screen for it? *J Refract Surg* 2013;29:230-232.
2. Santodomingo-Rubido J, Carracedo G, Suzaki A, Villa-Collar C, Vincent SJ, Wolffsohn JS. Keratoconus: An updated review. *Contact Lens and Anterior Eye* 2022;45.
3. Li Y, Tan O, Brass R, Weiss JL, Huang D. Corneal epithelial thickness mapping by Fourier-domain optical coherence tomography in normal and keratoconic eyes. *Ophthalmology* 2012;119:2425-2433.
4. Lu NJ, Hafezi F, Koppen C, et al. A Novel Keratoconus Staging System Based on Optical Coherence Tomography. *J Cataract Refract Surg* 2023.
5. Belin MW, Kundu G, Shetty N, Gupta K, Mullick R, Thakur P. ABCD: A new classification for keratoconus. *Indian J Ophthalmol* 2020;68:2831-2834.
6. Jr R, Belin M. Enhanced Screening for Ectasia Risk prior to Laser Vision Correction. *International Journal of Keratoconus and Ectatic Corneal Diseases* 2017;6:23-33.
7. Lopes BT, Ramos IC, Salomão MQ, et al. Enhanced Tomographic Assessment to Detect Corneal Ectasia Based on Artificial Intelligence. *Am J Ophthalmol* 2018;195:223-232.
8. Hwang ES, Schallhorn JM, Randleman JB. Utility of regional epithelial thickness measurements in corneal evaluations. *Surv Ophthalmol* 2020;65:187-204.
9. Luz A, Salomão MQ, Ambrósio R. Corneal Biomechanics in Keratoconus Diagnosis. In: Almodin E, Nassaralla BA, Sandes J (eds), *Keratoconus : A Comprehensive Guide to Diagnosis and Treatment*. Cham: Springer International Publishing; 2022:133-145.
10. Ambrósio R, Jr., Lopes BT, Faria-Correia F, et al. Integration of Scheimpflug-Based Corneal Tomography and Biomechanical Assessments for Enhancing Ectasia Detection. *J Refract Surg* 2017;33:434-443.
11. Hwang ES, Perez-Straziota CE, Kim SW, Santhiago MR, Randleman JB. Distinguishing Highly Asymmetric Keratoconus Eyes Using Combined Scheimpflug and Spectral-Domain OCT Analysis. *Ophthalmology* 2018;125:1862-1871.
12. Lu NJ, Elsheikh A, Rozema JJ, et al. Combining Spectral-Domain OCT and Air-Puff Tonometry Analysis to Diagnose Keratoconus. *J Refract Surg* 2022;38:374-380.
13. Lu NJ, Koppen C, Hafezi F, et al. Combinations of Scheimpflug tomography, ocular coherence tomography and air-puff tonometry improve the detection of keratoconus. *Cont Lens Anterior Eye* 2023;101840.
14. Larin KV, Sampson DD. Optical coherence elastography - OCT at work in tissue biomechanics [Invited]. *Biomed Opt Express* 2017;8:1172-1202.
15. Moshirfar M, Tukan AN, Bundogji N, et al. Ectasia After Corneal Refractive Surgery: A Systematic Review. *Ophthalmol Ther* 2021;10:753-776.

16. Vinciguerra R, Ambrósio R, Jr., Elsheikh A, et al. Detection of postlaser vision correction ectasia with a new combined biomechanical index. *Journal of Cataract & Refractive Surgery* 2021;47.
17. Dawson DG, Randleman JB, Grossniklaus HE, et al. Corneal ectasia after excimer laser keratorefractive surgery: histopathology, ultrastructure, and pathophysiology. *Ophthalmology* 2008;115:2181-2191.e2181.
18. Richoz O, Mavranakas N, Pajic B, Hafezi F. Corneal collagen cross-linking for ectasia after LASIK and photorefractive keratectomy: long-term results. *Ophthalmology* 2013;120:1354-1359.
19. Vinciguerra P, Randleman JB, Romano V, et al. Transepithelial iontophoresis corneal collagen cross-linking for progressive keratoconus: initial clinical outcomes. *J Refract Surg* 2014;30:746-753.
20. Mazzotta C, Sgheri A, Bagaglia SA, Rechichi M, Di Maggio A. Customized corneal crosslinking for treatment of progressive keratoconus: Clinical and OCT outcomes using a transepithelial approach with supplemental oxygen. *J Cataract Refract Surg* 2020;46:1582-1587.
21. Mazzotta C, Raiskup F, Hafezi F, et al. Long term results of accelerated 9 mW corneal crosslinking for early progressive keratoconus: the Siena Eye-Cross Study 2. *Eye Vis (Lond)* 2021;8:16.
22. Hafezi F, Kling S, Gilardoni F, et al. Individualized Corneal Cross-linking With Riboflavin and UV-A in Ultrathin Corneas: The Sub400 Protocol. *Am J Ophthalmol* 2021;224:133-142.
23. Wollensak G, Spoerl E, Seiler T. Riboflavin/ultraviolet-a-induced collagen crosslinking for the treatment of keratoconus. *Am J Ophthalmol* 2003;135:620-627.
24. Donnenfeld ED, O'Brien TP, Solomon R, Perry HD, Speaker MG, Wittpenn J. Infectious keratitis after photorefractive keratectomy. *Ophthalmology* 2003;110:743-747.
25. Kling S, Hufschmid FS, Torres-Netto EA, et al. High Fluence Increases the Antibacterial Efficacy of PACK Cross-Linking. *Cornea* 2020;39:1020-1026.
26. Lu N-J, Koliwer-Brandl H, Gilardoni F, et al. The Antibacterial Efficacy of High-Fluence PACK Cross-Linking Can Be Accelerated. *Translational Vision Science & Technology* 2023;12:12-12.
27. Cherfan D, Verter EE, Melki S, et al. Collagen Cross-Linking Using Rose Bengal and Green Light to Increase Corneal Stiffness. *Investigative Ophthalmology & Visual Science* 2013;54:3426-3433.
28. Lu NJ, Koliwer-Brandl H, Hillen M, Egli A, Hafezi F. High-Fluence Accelerated PACK-CXL for Bacterial Keratitis Using Riboflavin/UV-A or Rose Bengal/Green in the Ex Vivo Porcine Cornea. *Transl Vis Sci Technol* 2023;12:14.

English Abstract

Laser refractive surgery helps patients with refraction errors to correct their vision acuity without spectacles or contact lenses. By applying a high-powered laser beam to the cornea, the tissue can be remodeled, altering the corneal refraction to allow a clear image to be projected on the retina. Although these techniques have been continuously improved over the past three decades, laser refractive surgery still sees some complications. The most serious complications are postoperative ectasia and postoperative infectious keratitis.

Keratoconus is a strong contraindication for laser refractive surgery as the laser ablation can trigger postoperative ectasia. This ectasia is caused by the decompensation of the corneal material properties and is diagnosed based on postoperative tomography. The main purpose of preoperative examinations is therefore to screen for keratoconus using devices based such as Scheimpflug tomography, optical coherence tomography (OCT), and air-puff tonometry. These devices use different techniques to assess the in-vivo shape and material properties of the cornea for signs of early keratoconus.

OCT provides higher resolution images than Scheimpflug tomography, which allows studying the corneal epithelial layer thickness. This can be used to detect keratoconus early and to stage the condition using artificial intelligence (AI). Although OCT only provides morphological information, its abilities can be extended by combining it with an air-puff device and AI to achieve a very high diagnostic sensitivity for the earliest form of keratoconus, referred to as forme fruste keratoconus (FFKC).

Postoperative ectasia is typically treated using corneal cross-linking (CXL), which strengthens the impaired mechanical properties of the cornea. This technique comes in two variants in which the corneal epithelium is either removed (epi-off) or left in place (epi-on). Although epi-off was considered more effective, modern epi-on protocols have overcome limitations such as oxygen diffusion, riboflavin penetration, and UV-A light blocks to ensure a similar biomechanical effect as the accelerated epithelium-off CXL protocol.

Postoperative infectious keratitis is rare and is caused by the laser ablation that makes the cornea thinner and more susceptible to perforation. Photo-activated chromophore for keratitis-CXL (PACK-CXL) treats infectious keratitis from different perspectives, but the protocols should be updated based on our keratoconus-oriented treatment experience. The PACK-CXL protocols may be accelerated while maintaining the same bacterial killing rate.

In conclusion, the focus of laser refractive surgery complications should still be on prevention, both for ectasia and infectious keratitis. Both can seriously threaten vision, but properly adjusted protocols for CXL and PACK-CXL can help to improve prognosis.

Dutch Abstract

Refractieve laserchirurgie helpt patiënten met refractieafwijkingen om hun gezichtsscherpte te corrigeren zonder bril of contactlenzen. Door een laserstraal te schijnen op het hoornvlies, kan de vorm en de lichtbreking van het hoornvlies worden aangepast om zo een duidelijk beeld op het netvlies te vormen. Hoewel de deze technieken voortdurend worden verfijnd, kunnen er nog steeds complicaties optreden. De ernstigste complicaties zijn postoperatieve ectasie en postoperatieve infectieuze keratitis.

Keratoconus is een duidelijke contra-indicatie voor refractieve laserchirurgie aangezien dit kan leiden tot postoperatieve ectasie veroorzaakt door een decompensatie van het corneaal weefsel. Ectasie wordt typisch gedetecteerd aan de hand van postoperatieve Scheimpflug-tomografie, optische coherentie tomografie (OCT) of luchtpuf-tonometrie. Deze toestellen gebruiken verschillende meetmethoden om de vorm en materiaaleigenschappen van het hoornvlies in-vivo te screenen op tekens van vroege keratoconus.

OCT verschaft een hogere resolutie dan Scheimpflug-tomografie, zodat het een de dikte van epitheellaag van het hoornvlies in kaart kan brengen. Dit laat toe om een stadium toe te wijzen aan de keratoconus en om de ziekte in een vroeg stadium te detecteren diagnosticeren met behulp van kunstmatige intelligentie (AI). Hoewel OCT alleen de informatie geeft over de vorm van het hoornvlies, kan het worden gecombineerd met luchtpuf-tonometer en AI om zo de zeer hoge diagnostische gevoeligheid capaciteit te behalen voor het detecteren van de vroegste vorm van keratoconus, forme fruste keratoconus (FFKC) genaamd.

Postoperatieve ectasie wordt doorgaans behandeld met corneale crosslinking (CXL), een techniek om de verzwakte mechanische eigenschappen van het hoornvlies te verstevigen. CXL komt in twee varianten, waarbij het epitheel van het hoornvlies ofwel is verwijderd (epi-off) of op zijn plaats blijft (epi-on). Hoewel epi-off door de band effectiever is, hebben de moderne epi-on protocollen de belangrijkste beperkingen opgelost, zoals zuurstofdiffusie, riboflavine-penetratie en UV-A-lichtblokkering, waardoor het nu een vergelijkbaar biomechanisch effect heeft als het versnelde epithelium-off CXL-protocol.

Postoperatieve infectieuze keratitis is een zeldzame aandoening die ontstaat doordat de laserablatie het hoornvlies dunner en gevoeliger maakt voor perforaties. Dit kan worden behandeld met Photo-activated chromophore for keratitis-CXL (PACK-CXL), die de ziekte benadert vanuit verschillende perspectieven. De protocollen worden best eerste aangepast op basis van onze op keratoconus gerichte experimenten. De PACK-CXL-protocollen bleken sneller te werken met behoud van dezelfde bacteriedodende werking.

In conclusie, ligt de nadruk bij complicaties door refractieve laserchirurgie nog steeds op preventie, zowel voor ectasie als bij infectieuze keratitis. Beide complicaties kunnen het zicht ernstig aantasten, maar kunnen worden behandeld met aangepaste protocollen voor CXL en PACK-CXL.

List of Abbreviations

AKC	Advanced Keratoconus
ASLA	All Surface Laser Ablation
ANOVA	Analysis of Variance
ARC	Anterior Radius of Curvature
AS-OCT	Anterior Segment Optical Coherence Tomography
AMR	Antimicrobial Resistance
AUC	Area Under the Curve
AI	Artificial Intelligence
AAI	Asphericity Asymmetry Index
BKR	Bacterial Killing Rate
BSS	Balanced Salt Solution
BAD-D	Belin-Ambrósio Deviation Index
BAC	Benzalkonium Chloride
biOP	Biomechanically Corrected Intraocular Pressure
CCT	Central Corneal Thickness
CKI	Central Keratoconus Index
CFU	Colony Forming Unit (s)
CI	Confidence Interval
CL	Contact Lenses
CBI-LVC	Corneal Biomechanical Index-Laser Vision Correction Index
CXL	Corneal Cross-linking
CDVA	Corrected Distance Visual Acuity
CBiF	Corvis Biomechanical Factor
CBI	Corvis Biomechanical Index
D	Diopter (s)
DMEM	Dulbecco's Modified Eagle's Medium
DCR	Dynamic Corneal Response
EKC	Early Keratoconus
ERSS	Ectasia Risk Score System
ET	Epithelial Thickness
EPI	Epithelium
EP	Epithelium Overall Standard Deviation
EDTA	Ethylenediaminetetraacetic Acid

K1	Flat Keratometry
K2	Steep Keratometry
FFKC	Forme Fruste Keratoconus
GFP	Green Fluorescent Protein
IHA	Index of Height Asymmetry
IHD	Index of Height Decentration
ISV	Index of Surface Variance
IVA	Index of Vertical Asymmetry
I	Inferior
IN	Inferior Nasal
IT	Inferior Temporal
IL	Interleukin
I-CXL	Iontophoresis-CXL
KC	Keratoconus
KI	Keratoconus Index
KISA%	Keratoconus Percentage Index
K	Keratometry
KNN	K-nearest Neighbors
LASIK	Laser Assisted <i>in situ</i> Keratomileusis
LVC	Laser Vision Correction
LASEK	Laser-assisted Subepithelial Keratectomy
CBI beta	Linear Corvis Biomechanical Index
LDA	Linear Discriminant Analysis
LR	Logistic Regression
Kmax	Maximal Anterior Keratometry
RPIMax	Maximum Pachymetric Progression Index
Mean Imp	Mean Importance
MRSA	Methicillin-resistant Staphylococcus aureus
MMC	Mitomycin C
MLR	Multinomial Logistics Regression
N	Nasal
NN	Neutral Network
N	Newton

NA	Not Available
ORA	Ocular Response Analyzer
OCE	Optical Coherence Elastography
OCT	Optical Coherence Tomography
Pachy	Pachymetry
PRFI	Pentacam Random Forest Index
PBS	Phosphate Buffered Saline
PACK-CXL	Photo-activated Chromophore for Keratitis-CXL
PRK	Photorefractive Keratectomy
PTK	Phototherapeutic Keratectomy
PRC	Posterior Radius of Curvature
PCA	Principal Component Analysis
<i>P. aeruginosa</i>	<i>Pseudomonas aeruginosa</i>
RF	Random Forest
ROS	Reactive Oxygen Species
ROC	Receiver Operating Characteristic
rf	Riboflavin
RMS	Root Mean Square
rb	Rose Bengal
Sn	Sensitivity
SAB/IS	Skewed Asymmetric Bowtie/Inferior Steep
SMILE	Small Incision Lenticule Extraction
Sp	Specificity
StdDev	Standard Deviation
<i>S. aureus</i>	<i>Staphylococcus aureus</i>
K2	Steep Keratometry
SPA1	Stiffness Parameter at First Applanation
SSI	Stress-Strain Index
ECM	Stromal Extracellular Matrix
ST	Stromal Overall Minimum Thickness
SBK	Sub-Bowman's Keratomileusis
S	Superior
SN	Superior Nasal

SN-IT	Superior Nasal minus Inferior Temporal
ST	Superior Temporal
SL	Supervised Learning
SVM	Support Vector Machine
T	Temporal
I-S Value	The difference between average inferior and superior corneal powers 3 mm from the center of the cornea
DA ratio 2 mm	The ratio between the central deformation and the average of peripheral deformation at 2.0 mm from center
TBI	Tomographic and Biomechanical Index
TransPRK	Transepithelial PRK
TGF	Transforming Growth Factor
TNF	Tumor Necrosis Factor
UV-A	Ultraviolet-A
UHR-OCT	Ultra-high-resolution OCT
UDVA	Uncorrected Distance Visual Acuity
USL	Unsupervised Learning
VAE-E	Very Asymmetric Ectasia with Clinical Ectasia
VAE-NT	Very Asymmetric Ectasia-Normal Tomography
VHF	Very High Frequency

Appendix

CV and Publication Lists

BASIC INFORMATION

First Name: Nanji

Last Name: Lu

Gender: Male

DOB: 1994-Aug-04

Nationality: China

Language: Chinese (mother tongue), English (C1), German (A2)

EDUCATION

09/2020 - 09/2023

PhD, University of Antwerp, Antwerp, Belgium

Supervisors: Carina Koppen, Farhad Hafezi, Jos J. Rozema

09/2017 - 06/2020

MSc (Ophthalmology), Wenzhou Medical University, Zhejiang, China

Supervisors: Qin-Mei Wang, Ioannis M. Aslanides

09/2012 - 06/2017

MD, Southwest Medical University, Sichuan, China

REVIEWER of INDEXED JOURNALS

- Experimental Eye Research
- Ophthalmology and Therapy
- Journal of Refractive Surgery (“2021 and 2022 Golden Reviewer”)
- Cornea
- Cornea Open
- European Journal of Ophthalmology
- International Ophthalmology
- BMC Ophthalmology
- Frontiers in Pharmacology
- Computers in Biology and Medicine

GUEST EDITOR of INDEXED JOURNALS

Frontiers in Pharmacology

AWARDS

- Third Place at the Ophthalmology Star Awards VSY Biotechnology, 2023 Sep
- European Society of Cataract & Refractive Surgeons (ESCRS) Trainee Bursary, 2023 Jun
- European Society of Cataract & Refractive Surgeons (ESCRS) Young Ophthalmologist Observership Award, 2022 Dec
- 40th European Society of Cataract & Refractive Surgeons (ESCRS) Best Poster Prize, 2022 Sep, Milan, Italy
- China Scholarship Council (CSC) National High-level University Scholarship Program 2020 Jun

RESEARCH EXPERIENCE

09/2021 - 09/2023

Institute of Medical Microbiology, University of Zurich, Zurich, Switzerland

· Co-cultivation PhD student followed with Professor Adrian Egli and Dr. Hendrik Koliwer-Brandl: focus on basic microbiology diagnosis and experimental technology (bacteria, fungus, and Acanthamoeba)

08/2019 - 07/2020

Emmetropia Mediterranean Eye Institute, Heraklion, Greece

Foundation for Research and Technology-Hellas (FORTH), Heraklion, Greece

· Master student followed with Professor Ioannis M. Aslanides: focus on dyslexia and eye moment monitor, contact lenses loaded with medicine, and clinical ophthalmology

· Research Assistant followed with Professor Emmanuel Stratakis: focus on laser development and graphene research

09/2017 - 06/2020

State Key Laboratory of Optometry, Ophthalmology and Vision Science, Eye Hospital of Wenzhou Medical University, Wenzhou, China

· Master student followed with Professor Qin-Mei Wang: focus on corneal biomechanics, clinical and basic experiments of refractive surgery, keratoconus diagnosis, and corneal cross-linking

PUBLICATIONS

Peer-reviewed articles

1. **Lu Nan-Ji**, Koliwer-Brandl Hendrik, Hillen Mark, Egli Adrian, Hafezi Farhad. High-Fluence Accelerated PACK-CXL for Bacterial Keratitis Using Riboflavin/UV-A or Rose Bengal/Green in the Ex Vivo Porcine Cornea. *Translational Vision Science & Technology*. 2023 Sep 1;12(9):14
2. Olshaker Hagar, Achiron Asaf, Chorny Alexander, Hafezi Farhad, Yahalomi Tal, Kratz Assaf, Tsumi Erez, **Lu Nan-Ji**, Knyazer Boris. Accelerated high fluence photoactivated chromophore for infectious keratitis-corneal cross-linking (PACK-CXL) at the slit lamp: a pilot study. *Frontiers in Pharmacology*. 2023 Sep 7; 14:1229095
3. Hafezi Farhad, Torres-Netto Emilio, Kollros Leonard, **Lu Nan-Ji**, Hafezi Nikki, Mazzotta Cosimo, Aydemir M Enes, Hillen Mark. Rates of infectious keratitis and other ocular surface adverse events in corneal cross-linking for keratoconus and corneal ectasias performed in an office-based setting: a retrospective cohort study. *Eye and Vision*. 2023 Sep
4. **Lu Nan-Ji**, Hafezi Farhad, Koppen Carina, Alió Del Barrio Jorge L, Aslanides Ioannis M, Awwad Shady T, Dhubhghaill Sorcha Ni, Pineda Roberto 2nd, Torres-Netto Emilio A, Wang Lin, Chen Shi-Hao, Cui Le-Le, Rozema Jos. A Novel Keratoconus Staging System Based on Optical Coherence Tomography. *Journal of Cataract and Refractive Surgery*. 2023 Aug
5. Torres-Netto Emilio A, Abdshahzadeh Hormoz, **Lu Nan-Ji**, Kling Sabine, Abrishamchi Reyhaneh, Hillen Mark, Hafezi Nikki, Koppen Carina, Hafezi Farhad.

Corneal Cross-Linking with Riboflavin Using Sunlight. *Journal of Cataract and Refractive Surgery*. 2023 Jun

6. **Lu Nan-Ji**, Koppen Carina, Hafezi Farhad, Dhuhghaill Sorcha Ní, Aslanides Ioannis, Wang Qin-Mei, Cui Le-Le, Rozema Jos. Combinations of Scheimpflug Tomography, Ocular Coherence Tomography and Air-puff Tonometry Improve the Detection of Keratoconus. *Contact lens and Anterior Eye*. 2023; 46(3):101840
7. Kollros Léonard, Torres-Netto Emilio A, Rodriguez-Villalobos Carmen, Hafezi Nikki L, Hillen Mark, **Lu Nan-Ji**, Hafezi Farhad. Progressive keratoconus in patients older than 48 years. *Contact Lens and Anterior Eye*. 2023 Apr; 46(2):101792
8. **Lu Nan-Ji**, Koliwer-Brandl Hendrik, Gilardoni Francesca, Hafezi Nikki, Knyazer Boris, Achiron Asaf, Zbinden Reinhard, Adrian Egli, Hafezi Farhad. The Antibacterial Efficacy of High-Fluence PACK Cross-Linking can be Accelerated. *Translational Vision Science & Technology*. 2023;12(2):12
9. Renato Ambrósio Jr, Aydano P Machado, Edileuza Leão, João Marcelo G Lyra, Marcella Q Salomão, Louise G Pellegrino Esporcatte, João B R da Fonseca Filho, Erica Ferreira-Meneses, Nelson B Sena Jr, Jorge S Haddad, Alexandre Costa Neto, Gildasio Castelo de Almeida Jr, Cynthia J Roberts, Ahmed Elsheikh, Riccardo Vinciguerra, Paolo Vinciguerra, Jens Bühren, Thomas Kohlen, Guy M Kezirian, Farhad Hafezi, Nikki L Hafezi, Emilio A Torres-Netto, **Nan-Ji Lu**, David Sung Yong Kang, Omid Kermani, Shizuka Koh, Prema Padmanabhan, Suphi Taneri, William Trattler, Luca Gualdi, José Salgado-Borges, Fernando Faria-Correia, Elias Flockerzi, Berthold Seitz, Vishal Jhanji, Tommy C Y Chan, Pedro Manuel Baptista, Dan Z Reinstein, Timothy J Archer, Karolinne M Rocha, George O Waring 4th, Ronald R Krueger, William J Dupps, Ramin Khoramnia, Hassan Hashemi, Soheila Asgari, Hamed Momeni-Moghaddam, Siamak Zarei-Ghanavati, Rohit Shetty, Pooja Khamar, Michael W Belin, Bernardo T Lopes; International Corneal and Ocular and Biomechanics Study Group. Optimized artificial intelligence for enhanced ectasia detection using Scheimpflug-based corneal tomography and biomechanical data. *American Journal of Ophthalmology*. 2023; 251:126-142

10. Kollros Léonard, **Lu Nan-Ji**, Hillen Mark, Torres-Netto Emilio A., Hafezi Farhad. Scleral contact lenses fitted to extremely steep corneas. *Journal Français d'Ophtalmologie*. 2023;46(2): e70-e74
11. **Lu Nan-Ji**, Hafezi Farhad, Torres-Netto Emilio A., Assaf Jad F., Aslanides Ioannis M., Awwad Shady T., Chen Shi-Hao, Cui Le-Le, Koppen Carina. Effect of fluence levels on prophylactic corneal cross-linking for laser in situ keratomileusis and transepithelial photorefractive keratectomy. *Acta Ophthalmologica*. 2023;101(2): e185-e196
12. Hafezi Farhad, **Lu Nan-Ji**, Assaf Jad F., Hafezi Nikki L., Koppen Carina, Vinciguerra Riccardo, Vinciguerra Paolo, Hillen Mark, Awwad Shady. Demarcation Line Depth in Epithelium-Off Corneal Cross-Linking Performed at the Slit Lamp. *Journal of Clinical Medicine*. *Journal of Clinical Medicine*. 2022;11(19):5873
13. Abdshahzadeh Hormoz, Abrishamchi Reyhaneh, Aydemir M Enes, Hafezi Nikki, Hillen Mark, Torres-Netto Emilio A, **Lu Nan-Ji**, Hafezi Farhad. Repeated application of riboflavin during corneal cross-linking does not improve the biomechanical stiffening effect ex vivo. *Experimental Eye Research*. 2022; 224:109267
14. **Lu Nan-Ji**, Kang Qian, Ní Dhubhghaill Sorcha. Acanthamoeba Keratitis After Corneal Refractive Surgery: A Case Series and Literature Review. *Journal of Refractive Surgery Case Reports*. 2022; 2 (2), e32-e37
15. **Lu Nan-Ji**, Elsheikh Ahmed, Rozema Jos J, Hafezi Nikki, Aslanides Ioannis M, Hillen Mark, Eckert Daniel, Funck Christian, Koppen Carina, Cui Le-Le, Hafezi Farhad. Combining Spectral-Domain OCT and Air-puff Tonometry Analysis to Diagnose Keratoconus. *Journal of Refractive Surgery*. 2022;38(6):374-380
16. **Lu Nan-Ji**, Hafezi Farhad, Rozema Jos J, Hillen Mark, Hafezi Nikki, Zhang Jia, Koppen Carina. Repeatability of Corvis ST to Measure Biomechanical Parameters Before and After Myopic Refractive Surgery. *Journal of Cataract and Refractive Surgery*. 2022;48(9):1057-1062
17. Vinciguerra Riccardo, Ambrósio Renato Jr, Elsheikh Ahmed, Hafezi Farhad, Yong Kang David Sung, Kermani Omid, Koh Shizuka, **Lu Nan-Ji**, Padmanabhan Prema,

Roberts Cynthia J, Taneri Suphi, Trattler William, Vinciguerra Paolo. Detection of post laser vision correction ectasia with a new combined biomechanical index, *Journal of Cataract and Refractive Surgery*. 2021;47(10):1314-1318

18. **Lu Nan-Ji**, Koppen Carina, Awwad Shady, Aslanides Minas, Aslanides Ioannis, Chen Shi-Hao. Effect of intraoperative mitomycin-C application on epithelial regeneration after transepithelial photorefractive keratectomy. *Journal of Cataract and Refractive Surgery*. 2021;47(2):227-232
19. Zhang Jia, Aslanides Ioannis, Selimis Vasileios, **Lu Nan-Ji**, Liu Wei-Jie, Jiang Hong-Xiao, Zhang Chao, Xu Chen-Chen, Wang Qin-Mei, Qu Jia, Chen Shi-Hao. A Comprehensive Strategy for Laser Corneal Refractive Surgery during the COVID-19 Epidemic in a Tertiary Teaching Hospital in Wenzhou, China. *Journal of Ophthalmology*. 2020 Jul 15; 2020:4835630
20. Aslanides Ioannis, Hafezi Farhad, Chen Shi-Hao, Mukherjee Hatch, Selimis Vasileios, **Lu Nan-Ji**, Kymionis George. 5-year efficacy of All Surface Laser Ablation with Cross linking (ASLA-XTRA) for the treatment of myopia. *Eye and Vision*. 2020 Jun 11; 7:31
21. Bao Fang-Jun, Huang Wei, Zhu Rong, **Lu Nan-Ji**, Wang Yuan, Li Hechen Li, Wu Songan, Lin Huini, Wang Junjie, Zheng Xiaobo Zheng, Huang JinHai, Li Yiyu, Wang Qinmei Wang, Ahmed Elsheikh. Effectiveness of the Goldmann Applanation Tonometer, the Dynamic Contour Tonometer, the Ocular Response Analyzer and the Corvis ST in measuring intraocular pressure following FS-LASIK. *Current Eye Research*. 2019 Dec 26:1-9
22. **Lu Nan-Ji**, Chen Ding, Cui Le-Le, Wang Lin, Chen Shi-Hao, Wang Qin-Mei. Repeatability of Cornea and Sublayer Thickness Measurements Using Optical Coherence Tomography in Corneas of Anomalous Refractive Status. *Journal of Refractive Surgery*. 2019;35(9):600-605

Acknowledgements

I would like to express my gratitude to all the mentors, teachers, classmates, friends and family who helped and supported me during my PhD study.